Dissertation

submitted to the
Combined Faculties of the Natural Sciences and Mathematics
of the Ruperto-Carola-University of Heidelberg, Germany,
for the degree of

Doctor of Natural Sciences

Put forward by
Daniel Schmidt
born in: Saarbrücken

Oral examination: December, 18th 2013

Novel Frameworks for Dark Matter and Neutrino Masses

Referees:
Prof. Dr. Manfred Lindner
Prof. Dr. Tilman Plehn

Novel Frameworks for Dark Matter and Neutrino Masses

The established light neutrino masses and the Dark Matter of the Universe both require physics beyond the Standard Model for their theoretical explanation. Models that provide a common framework for these two issues are very attractive. In particular, radiative mechanisms naturally yield light neutrino masses due to loop suppression factors. These corrections can comprise a link to the physics of Dark Matter. In most considerations, the Dark Matter relic density is produced by freeze-out. This thesis contributes to the fields of radiative neutrino masses and frozen-out Dark Matter. In detail, it is shown that in the Ma-model, right-handed neutrino Dark Matter can be directly detected by photon exchange at one-loop level. The Zee–Babu-model is extended such that it enjoys a global symmetry based on baryon and lepton number. This symmetry generates light neutrino masses and a mass for a stable Dark Matter particle by its spontaneous breaking. Moreover, this thesis provides a new production mechanism for keV sterile neutrino Dark Mattetr, which is based on the freeze-in scenario. In particular, keV sterile neutrino Dark Matter produced by the decay of a frozen-in scalar is investigated.

Neue Erklärungsrahmen für Dunkle Materie und Neutrinomassen

Die festgestellten leichten Neutrinomassen und die Dunkle Materie im Universum erfordern Physik jenseits des Standardmodells für eine theoretische Erklärung. Modelle, die einen gemeinsamen Erklärungsrahmen für diese zwei Probleme bereitstellen, sind besonders attraktiv. Insbesondere liefern Mechanismen mit Korrekturen höherer Ordnung leichte Neutrinomassen bedingt durch Korrekturfaktoren, die Neutrinomassen auf natürliche Weise unterdrücken. Diese Korrekturen können eine Verbindung zur Physik der Dunklen Materie darstellen. In den meisten Betrachtungen wird die Restdichte der Dunklen Materie durch Ausfrieren von Teilchenreaktionen erzeugt. Diese Doktorarbeit leistet einen Beitrag zu Neutrinomassen, die über Korrekturen höherer Ordnung erzeugt werden, und zu Dunkler Materie, die ausfriert. Im Einzelnen wird gezeigt, dass im Ma-Model ein rechtshändiges Neutrino als Dunkle Materie in direkten Nachweisexperimenten durch Photonenaustausch in erster Strahlungskorrektur nachgewiesen werden kann. Das Zee–Babu-Model wird mit einer globalen Symmetrie erweitert, die auf Baryon- und Leptonzahl basiert. Spontane Brechung dieser Symmetrie erzeugt leichte Neutrinomassen und eine Masse für stabile Dunkle Materie Teilchen. Darüber hinaus stellt diese Doktorarbeit einen neuen Produktionsmechanismus bereit, der keV sterile Neutrinos erzeugt. Dieser Mechanismus basiert auf Erzeugungs-und Vernichtungsreaktionen eines Teilchens, die mit Reaktionen anderer Teilchen einfrieren. Insbesondere werden keV sterile Neutrinos untersucht, die durch den Zerfall eines skalaren Teilchens entstehen, das eingefroren ist.

To My Grandmother

Lucie Schmidt
(* 1930 - † 2013)

Contents

List of Figures

List of Tables

per aspera ad astra

(Seneca, *Hercules furens*)

Acknowledgments

My first and candid appreciation goes to my supervisor Manfred Lindner: I am cordially thankful for your grand guidance, your enduring encouragement and for the self-esteem I gained in the numerous private communications with you. I am also deeply grateful to you for granting me permission to attend all the conferences where I could improve my knowledge and present my work, most notably the conference in Beijing and in Kanazawa.

I thank Manfred Lindner and Tilman Plehn for rendering referee reports. Aloha!

If I have seen further it is by standing on ye sholders of [1] my collaborators, which I list in order of the corresponding projects, starting with the first one: Besides Manfred Lindner, these are Thomas Schwetz, Takashi Toma, Alexander Merle, Viviana Niro, He Zhang and Atsushi Watanabe. I benefitted a lot from Thomas's insights and ideas in projects. Discussions with Takashi have always been very fruitful and enlightening for me. I thank Alexander Merle and Viviana Niro for their many instructive online conversations. Thank you for not giving up a project in a seemingly hopeless situation. Thank you for your permanent support. Beyond that, Alexander proofread parts of this thesis. I give He Zhang and Atsushi Watanabe props for two projects in progress.

For me, the pleasant working atmosphere in Manfred Lindner's division for Particle and Astroparticle Physics is a result of the pleasant company of colleagues. I specially thank James Barry and Julian Heeck for proofreading parts of this thesis. I have really enjoyed sharing an office with Michael Dürr. It was Michael who brought some variation into our everyday work life, especially with his conference trip counter, which he is leading.

I thank the AHEP group in Valencia for inviting me to a seminar talk and the organizers of the Japanese-German-Symposium for giving me the chance to present part of my work in Kanazawa.

My sincerest thanks is addressed to the people who are closest to my heart: my parents Rita and Michael and my fiancée Christine Dorothea Lutz. Rita and Michael, thank you so much for stimulating my interests. You are always there when your help is needed. In the last two years, Christine has been asking me about my time in office expressing her interest towards my work. Even when I was grumpy due to problems which I could not solve straightforwardly she was heartening me. Thank you for being at my side.

[1] Sir Isaac Newton, Letter to Robert Hooke, 1676

1. Introduction

Then I felt like some watcher of the skies/ When a new planet swims into his ken; [1] With these lines the English poet John Keats referred to the discovery of Uranus in 1781 by Sir William Herschel. What have *a watcher of the skies* and *a new planet* that *swims into his ken* in common with Dark Matter (DM) and neutrinos? A lot!

Going back into 1821, the French astronomer M. A. Bouvard had published astronomical tables for Jupiter, Saturn and Uranus predicting their future positions by using celestial mechanics based on Newton's gravitational law [2]: whereas the predicted positions of Jupiter and Saturn were confirmed, the prediction for Uranus was wrong. The irregularities in the orbit of Uranus could have been explained by the assumptions that Newton's gravitational law had to be changed or that there was an additional source of gravitation perturbing the orbit of Uranus. With the first observation of Neptune by the German astronomer J. G. Galle in 1846, the irregularities in the orbit of Uranus were explained by the assumption of an additional source of gravity in form of a new planet.

Another irregularity was found studying the planet Mercury. The observed perihelion precession of Mercury equals 5599.74 ± 0.41 arcs per Julian century of 36,525 mean solar days. However, using Newton's law of gravity and taking into account all the effects from the other planets, the predicted perihelion precession of Mercury equals 5557.18 ± 0.85 arcs per Julian century [3]. To explain this discrepancy, one can look for an additional planet or use a modification to Newton's law of gravity. So far, an additional planet inside the orbit of Mercury has not been found, however, using Einstein's theory of general relativity instead of Newton's law of gravity, a shift of 42.98 ± 0.0023 arcs per Julian century results [4], which added to the predicted perihelion precession yields the observed value.

The discovery of Neptune and the advance of the perihelion of Mercury illustrate the possible solutions to verify observations based on gravitational effects; either there is an additional source of gravity, such as Neptune leading to the observed irregularities in the orbit of Uranus, or the gravitational law has to be changed, as done for the correct description of the perihelion precession of Mercury.

By today, we still watch the sky. Besides many new extrasolar planets, we have discovered an additional source of gravity that leads to the observed large scale structure of the Universe. The impact of the baryonic matter alone, which makes up only 4.9% of the energy density of the Universe, cannot explain the structures of the Universe formed under the influence of gravity. The main part of the matter in the Universe,

which in the framework of Einstein's theory of general relativity makes up 26.8% of the energy density of the Universe as revealed by the *Planck* satellite [5], does not interact electromagnetically and is called Dark Matter (DM). Since a candidate for a particle-like DM has not been discovered yet, the question arises whether this DM, being the main ingredient to explain the observed structure of the Universe, is Neptune-like, i.e., whether it is an additional kind of matter constituted of particles, or it is Mercury-like, i.e., it needs the framework of Einstein's theory of general relativity to be changed.

Already in 1932, the investigation of *the force exerted by the stellar system in the direction perpendicular to the galactic plane* led the Dutch astronomer J. H. Oort to the conclusion that *it would appear from the comparison that the dark mass must be relatively more frequent near the galactic plane than far from it, but the data are too uncertain to derive numerical results.* [6] Based on the measured dispersion of the velocities of individual galaxies in the Coma Cluster, and applying the virial theorem, the Swiss astronomer F. Zwicky [7] discovered in 1933 that the mean matter density of the Coma Cluster has to be at least 400 times larger than the mass derived from the observed luminous matter. Zwicky conjectured that non-luminous matter, i.e., DM, must exist in the Universe in an amount much larger than that of luminous matter. On the scale of an individual galaxy, V. C. Rubin and W. K. Ford Jr. determined in 1970 the circular velocities v_c of several emitting regions inside the Andromeda nebula from 3-24 kpc distance r to the core of the galaxy. In an equilibrium between the centripetal and Newtonian gravitational forces, one expects that v_c should decrease as $1/\sqrt{r}$ with increasing distance to the center. However, a more or less constant circular velocity profile was found [8]. Rubin's and Ford's conclusion was that the best-fit value of the the mean matter density of the Andromeda nebula, which can be inferred from the circular velocity profile, has to be twelve times larger than the one resulting from the observed luminous matter. These first observations, ranging from the small scales of a galaxy to the large scales of a galaxy cluster, show that, in the framework of Einstein's theory of general relativity, there must be an additional matter component added to the gravitational potential.

Contrary to these observations, the Israeli physicist M. Milgrom proposed in 1983 a modified Newtonian dynamics MOND, which equals Newtonian dynamics for gravitational acceleration $a \gg a_0 = 1.2 \times 0^{-8}\,\mathrm{cm^2 s^{-1}}$, and for $a \ll a_0$, Newtonian dynamics with gravitational acceleration $\sqrt{aa_0}$ [9]. This theory, in its original formulation, is a fundamentally non-covariant theory, but it could be formulated as a relativistic covariant theory in the framework of a tensor-vector-scalar model [10]. Although the embedding of MOND into a relativistically covariant theory is able to solve the structure problem of the Universe without particle-like DM, it cannot describe the shape of the matter power spectrum [1] [11]. The motivation for MOND was to find an explanation for the

[1] The matter power spectrum is the power spectrum, i.e., the Fourier transformation, of the averaged

observed constant circular velocity profile without introducing a DM particle. Indeed, MOND can correctly describe the observed small scale effects without particle-like DM, however, only on really small scales. For example, MOND predicts an r independent circular velocity profile, which is more or less true for $r \lesssim 20\,\mathrm{kpc}$. But for distances in the range $50\,\mathrm{kpc} \lesssim r \lesssim 500\,\mathrm{kpc}$, the velocity declines excluding constant velocity profiles at a 10σ level, as the observation of 9500 satellite galaxies within a projected distance of $r < 1000$ kpc within a number of 215000 observed galaxies in total revealed [12]. Given these problems, which MOND and more elaborated modifications to the gravitational law, like tensor-vector-scalar models, fail to solve, we must abandon the idea of changing the gravitational law and thus do not follow a Mercury-like DM. What we will do in the following is to start from a Neptune-like DM, i.e., DM made up of some type of particle.

The Standard Model (SM) of Particle Physics, which describes very well the baryonic matter and whose long-missing Higgs boson has been confidently found at the Large Hadron Collider (LHC) by the ATLAS [13] and CMS [14] collaborations, has no viable DM candidate particle: the electromagnetically neutral particles of the SM are the neutrinos, the Higgs boson and the Z gauge boson. The SM neutrinos are hot at freeze-out, which would lead to inconsistent structure formation if they would be the DM. Also, the coupling of the SM neutrinos to the Z gauge boson is too large: neutrino annihilations into Z bosons would yield a DM relic density much smaller than the observed one. In analogy, the weak interactions of the Z boson and the Yukawa interactions of the Higgs boson are too strong to produce the correct DM relic density. In addition, due to t-channel Z boson exchange, SM neutrinos as DM particles would have been already detected in direct detection experiments. As we will point out, there are three possibilities to detect interactions of a DM particle: either indirectly, directly or by collider production. We will pay special attention to direct detection experiments that probe non-gravitational, i.e., direct interactions, of a possible DM particle. They have already set stringent upper limits on the interaction strength of DM, and are currently advancing to even lower upper limits, such that a positive signal may be announced very soon.

The neutrino is another object we can learn about when we watch the sky with appropriate instruments. In the SM, the neutrino has left-handed chirality. There is neither a right-handed counter part that could generate a Dirac mass nor a Majorana mass term; the latter would break the global lepton number symmetry of the SM Lagrangian. However, observing in particular the neutrino flux coming from the Sun, we have learned that neutrinos oscillate between different flavor states. Our knowledge on neutrino oscillations has been considerably improved by the latest measurement of a non-zero leptonic mixing angle θ_{13}, e.g., by the Double Chooz [15] experiment. The neutrino oscillation experiments proved that neutrinos are indeed massive. So, in addition to the mysterious DM, the neutrino mass, which can also be inferred from watching the sky, is

matter density fluctuations.

a fact that cannot be explained with the *ken* of the SM.

Given the experimental state of the art and its developments, it is very interesting to study particle DM and neutrino physics at the same time. Our aim is to connect descriptions for particle DM with neutrino mass generation mechanisms to finally host particle DM and massive neutrinos in one unified framework.

To achieve our aim, we build on the idea of right-handed neutrinos. Right-handed neutrinos could be a possible DM particle and at the same time help to explain light neutrino masses. One of the pioneering questions asked in this field concerns the realization of light neutrino masses by right-handed neutrinos and the characteristics and production of right-handed neutrinos as particulate DM.

With this thesis, we aim to broaden our *ken* about DM and neutrinos. To do so, we first illustrate the importance of neutrinos and DM in chapter 2. We already distinguish between freeze-out production of DM, which is the relevant mechanism in part I of this thesis, and freeze-in production, which is the relevant mechanism in part II. We proceed with studying a radiative seesaw mechanisms in which a right-handed neutrino is linked in a specific way to the loop processes involved. In detail, we investigate radiative neutrino mass generation at one-loop level in section 3.1. The right-handed neutrino runs inside the loop giving mass to the light neutrinos, and simultaneously acts as the DM particle. We focus on the possible direct detection of that DM particle by an effective three-point interaction with a photon. In section 3.4, we increase the number of loops involved in the neutrino mass generation and discuss a $B - L$ symmetric two-loop model. The masses of the right-handed neutrino DM and of the light neutrinos are linked by spontaneous symmetry breaking. Chapter 4 presents a new production mechanism for keV right-handed neutrinos. A scalar particle freezes-in and produces by its decays keV right-handed neutrinos. The freeze-in production opens up a new and previously unknown region in the allowed parameter space. For specific masses of the scalar and of the keV right-handed neutrinos, the latter can act as warm DM. Warm DM is believed to describe structure formation on small scales even better than the cold DM discussed so far.

2. Importance of Neutrinos and Illuminating Dark Matter

Before starting the discussion of DM and radiative neutrino masses in part I and of keV sterile neutrino DM produced by freeze-in in part II, we emphasize the importance of neutrinos and DM in this chapter. We shortly review the SM in section 2.1, from which we build on neutrino physics in section 2.2. Having discussed the particle physics part, we proceed with the cosmological part in section 2.3, which will lead to DM physics in section 2.4. Throughout this thesis, we use the units $\hbar = c = 1$ and Heaviside-Lorentz units for electromagnetism, i.e., we write the fine structure constant α_{EM} as $\alpha_{EM} = {}^{e^2}/_{4\pi}$. In section 2.5, the production of the DM relic density is paid special attention to: the concepts of the freeze-out and freeze-in mechanisms are explained. We also review the experimental situation concerning the evidences for neutrino masses and DM, and in particular, the possibilities for the detection of a DM particle in section 2.6.

2.1. Prelude I: The Glashow–Weinberg–Salam Theory of Weak Interactions

Back in 1960, S. L. Glashow studied the parallels between electromagnetic effects and phenomena associated with weak interactions. His remarkable result was that both interactions are unified supposing the existence of unstable bosons that would mediate the weak interactions [16]. In a three-page note published in 1967, S. Weinberg imagined that the symmetries, which relate the electromagnetic and the weak interactions, are exact symmetries of the Lagrangian but broken by the vacuum. The corresponding massless Goldstone bosons are avoided by introducing intermediate boson fields as gauge fields [17]. The idea of broken symmetries was already discussed in the paper [18], of which Weinberg and A. Salam are co-authors. Salam also dreamed of the synthesis between the electromagnetic and weak interactions and worked on an $SU(2) \times U(1)$ transformation. Besides the weak interaction gauge fields W^+ and W^-, he introduced in 1964 a neutral gauge field X^0. He assumed that this boson has a mass in order to be different from the photon [19]. For these and other 1960's papers, the Nobel Prize in Physics 1979 was awarded jointly to S. L. Glashow, S. Weinberg and A. Salam *for their*

contributions to the theory of the unified weak and electromagnetic interaction between elementary particles, including, inter alia, the prediction of the weak neutral current.[1]

Today, the $SU(2)_L \times U(1)_Y$ theory [2] is confirmed as the SM of electroweak interactions. It is a relativistic quantum field theory that characterizes leptons and quarks as the fundamental building blocks of ordinary matter. Their non-gravitational interactions are described through the exchange of gauge bosons. The chiral fermions of the theory are arranged into left-handed $SU(2)_L$ doublets and right-handed $SU(2)_L$ singlets. There are three ($\alpha = e$, μ, τ) flavor copies of the $SU(2)_L$ doublet and singlet representations. In each representation, the flavor copies have the same charges.

The generation of masses in the SM for charged leptons, quarks and gauge bosons is based on spontaneous symmetry breaking of $SU(2)_L \times U(1)_Y$ to $U(1)_{\mathrm{EM}}$ described by the already in 1964 proposed Higgs [20]–Englert–Brout [21]–Guralnik–Hagen–Kibble [22] mechanism, in the following called Higgs-mechanism for shorthand. The key ingredient for that mechanism to work is a complex scalar $SU(2)_L$ doublet field:

$$H(x) = \begin{pmatrix} H^+(x) \\ H^0(x) \end{pmatrix} , \tag{2.1.1}$$

called the Higgs $SU(2)_L$ doublet in the following, where each component is a complex field by itself. The Higgs potential, which drives spontaneous symmetry breaking, is the following:

$$V[(H(x))] = \mu_H^2 H(x)^\dagger H(x) + \lambda_H \left(H(x)^\dagger H(x)\right)^2 \tag{2.1.2}$$

In the SM, μ_H^2 is the only dimensionful coupling.

After the spontaneous breaking of the electroweak theory, we parametrize the Higgs double in the unitary gauge as:

$$H(x) = \frac{1}{\sqrt{2}} \begin{pmatrix} 0 \\ v + h(x) \end{pmatrix} . \tag{2.1.3}$$

We use a linear representation, where $h(x)$ is the real Higgs boson. The vacuum expectation value v, VEV for shorthand, equals $v = 246$ GeV. It is the global minimum of the potential (2.1.2). The minimum condition sets:

$$\mu_H^2 = -\lambda_H v^2 . \tag{2.1.4}$$

Equation (2.1.4) shows that μ_H^2 is given by the VEV of the Higgs $SU(2)_L$ doublet. Thus the only physical scale in the SM is the scale of spontaneous breaking of the electroweak symmetry.

[1] http://www.nobelprize.org/nobel_prizes/physics/laureates/1979/

[2] Including strong interactions, the full gauge group is $SU(3)_C \times SU(2)_L \times U(1)_Y$.

The leptons in the SM consist of the left-handed $SU(2)_L$ doublets $L^{(\alpha)}$ with hypercharge $q_Y = -1/2$ and the right-handed $SU(2)_L$ singlets $e^{(\alpha)}$ with hypercharge $q_Y = -1$:

$$L^{(e)} = \begin{pmatrix} \nu_e \\ e^- \end{pmatrix}_L \,,\; L^{(\mu)} = \begin{pmatrix} \nu_\mu \\ \mu^- \end{pmatrix}_L \,,\; L^{(\tau)} = \begin{pmatrix} \nu_\tau \\ \tau^- \end{pmatrix}_L \tag{2.1.5}$$

$$e^{(\alpha)} = e_R, \mu_R, \tau_R \,. \tag{2.1.6}$$

We denote the chirality as $L = L_L = P_L L$ and $e = e_R = P_R e$, where P_L and P_R are the left- and right-handed projection operators. Here and in the following description we have omitted the flavor indices. The charge conjugation operator C acts as $(L_L)^C = (L^C)_R$. The bar notation for the $SU(2)_L$ doublets is $\overline{L} = (\overline{\nu}, \overline{e})_L$. For a single component u, the bar acts as $\overline{u} = u^\dagger \gamma^0$. It follows that $\overline{(L_L)^C} = \overline{L^C} P_L$ and $\overline{(e_R)^C} = \overline{e^C} P_R$.

Accordingly, the quarks consist of the left-handed $SU(2)_L$ doublets $Q^{(\alpha)}$ with hypercharge $q_Y = 1/6$ and the right-handed $SU(2)_L$ singlets $u^{(\alpha)}$ and $d^{(\alpha)}$ with hypercharges $q_{Y,u} = 2/3$ and $q_{Y,d} = -1/3$, respectively:

$$Q^{(u)} = \begin{pmatrix} u \\ d' \end{pmatrix}_L \,,\; Q^{(c)} = \begin{pmatrix} c \\ s' \end{pmatrix}_L \,,\; Q^{(t)} = \begin{pmatrix} t \\ b' \end{pmatrix}_L \,, \tag{2.1.7}$$

$$u^{(\alpha)} = u_R, c_R, t_R \tag{2.1.8}$$

$$d^{(\alpha)} = d_R, s_R, b_R \,. \tag{2.1.9}$$

The $SU(2)_L$ gauge bosons are W^1_μ, W^2_μ, W^3_μ with coupling constant g and the $U(1)_Y$ gauge boson is B_μ with coupling constant g'. The field strength tensors are:

$$F_{1,\mu\nu} = \partial_\mu B_\nu - \partial_\nu B_\mu \,, \tag{2.1.10}$$

$$F^a_{2,\mu\nu} = \partial_\mu W^a_\nu - \partial_\nu W^a_\mu + g\epsilon^{abc} W^b_\mu W^c_\nu \,. \tag{2.1.11}$$

The dual tensor is given by:

$$\tilde{F}_{\mu\nu} = \frac{1}{2}\epsilon_{\mu\nu\rho\sigma} F^{\rho\sigma} \,, \tag{2.1.12}$$

which is used in equation (3.4.17). The SM gauge terms involving the field strength tensors read:

$$\mathcal{L}_{\text{gauge}} = -\frac{1}{4} F_{1,\mu\nu} F_1^{\mu\nu} - \frac{1}{4} F^a_{2,\mu\nu} F_2^{a,\mu\nu} \,. \tag{2.1.13}$$

The masses of the charged leptons and quarks, respectively, arise from the following Yukawa interactions:

$$\mathcal{L}_y = -y_L \overline{L^{(\alpha)}} H e^{(\alpha)} - y_d \overline{Q^{(\alpha)}} H d^{(\alpha)} - y_u \overline{Q^{(\alpha)}} \tilde{H} u^{(\alpha)} + \text{h.c.} \,, \tag{2.1.14}$$

with dimensionless Yukawa coupling constants y_i and $\tilde{H} = i\sigma_2 H^*$. When the Higgs $SU(2)_L$ doublet H obtains its VEV, the Yukawa interactions induce mass terms for the corresponding fields. The masses are hence proportional to y_i and v

For quarks, there are two types of Yukawa terms: y_u, which forms a mass term for the upper component of the $SU(2)_L$ doublets, and y_d, which forms a mass term for the lower component. Thus there are two corresponding mass matrices, however, they can not be diagonalized at the same time. In general, each type mixes the flavors of the $SU(2)_L$ doublets and the singlets. We conventionally choose the basis in such a way that the upper components are the mass eigenstates. Then the lower components are a linear combination of lower $SU(2)_L$ doublet flavor fields, indicated by a prime:

$$\begin{pmatrix} d' \\ s' \\ b' \end{pmatrix} = \begin{pmatrix} V_{ud} & V_{us} & V_{ub} \\ V_{cd} & V_{cs} & V_{cb} \\ V_{td} & V_{ts} & V_{tb} \end{pmatrix} \begin{pmatrix} d \\ s \\ b \end{pmatrix} \equiv \mathbf{V} \begin{pmatrix} d \\ s \\ b \end{pmatrix} \quad . \tag{2.1.15}$$

This means that in the quark sector, there is a flavor mixing expressed by the 3×3 unitary Cabibbo [23]-Kobayashi-Maskawa-matrix [24] $\mathbf{V}$.

The masses for the gauge bosons arise from their covariant derivative terms, which couple them to the Higgs $SU(2)_L$ doublet. After spontaneous symmetry breaking, we can write the gauge bosons and their corresponding masses as:

$$W_\mu^\pm = \frac{1}{\sqrt{2}} \left(W_\mu^1 \mp i W_\mu^2 \right) \quad ; \quad m_{W_\mu^\pm} = \frac{1}{2} g v \tag{2.1.16}$$

$$Z_\mu = -\sin\Theta_W B_\mu + \cos\Theta_W W_\mu^3 \quad ; \quad m_{Z_\mu} = \frac{1}{2}\sqrt{g^2 + g'^2}\, v \tag{2.1.17}$$

$$A_\mu = \cos\Theta_W B_\mu + \sin\Theta_W W_\mu^3 \quad ; \quad m_{A_\mu} = 0\,. \tag{2.1.18}$$

In the expressions above, $\cos\Theta_W \equiv g/\sqrt{g^2+g'^2}$ and $\sin\Theta_W \equiv g'/\sqrt{g^2+g'^2}$, where the angle Θ_W that expresses the weak-mixing is called the Weinberg angle. The photon A_μ is massless because after spontaneous symmetry breaking, $U(1)_{\mathrm{EM}}$ is preserved.

Clearly, for leptons, the above Yukawa interactions generate only a mass term for the lower component of the $SU(2)_L$ doublets because right-handed neutrinos are absent in the SM. In that sense, neutrinos are special in the framework of the SM. We will look at the peculiarities of neutrinos in the next section.

2.2. Neutrinos

To save the law of conservation of energy in β decay processes, the Austrian physicist W. Pauli *hit upon the desperate remedy* to postulate in 1930 the existence of *electrically neutral particles that have spin ½ and obey the exclusion principle.* [25] These neutral particles are known as neutrinos by today. Neutrinos are special compared to the other

fermions of the SM. The particle spectrum of the SM does not contain a right-handed neutrino. So there is no Dirac mass m_D for neutrinos. A Majorana mass M_M, in turn, would violate the global accidental $U(1)_{B-L}$ symmetry of the SM by two units. Therefore, in the framework of the SM, the left-handed neutrinos, which take part in the weak interactions, are massless.

2.2.1. Flavor Oscillations

It is by now a fact that the neutrino weak interaction states perform flavor oscillations, e.g., an electron neutrino can oscillate into an muon neutrino, thus violating lepton flavor conservation. Flavor oscillations rely on the fact that neutrinos are massive and mix with each other. Studying neutrino flavor oscillations, one can learn about the differences of the squared mass eigenvalues and about the mixing angles that parametrize neutrino mixing. We focus on three environments where neutrino flavor oscillations are manifest: the Sun, the atmosphere of the Earth and terrestrial nuclear reactors. Inside the Sun, boron-8 is produced. According to the standard solar model, the production reactions are:

$$ {}^{3}_{2}\mathrm{He} + {}^{4}_{2}\mathrm{He} \longrightarrow {}^{7}_{4}\mathrm{Be} + \gamma \,, \tag{2.2.1} $$

$$ {}^{7}_{4}\mathrm{Be} + p \longrightarrow {}^{8}_{5}\mathrm{B} + \gamma \,. \tag{2.2.2} $$

With a half-life time of 770 ms, boron-8 decays into electron neutrinos:

$$ {}^{8}_{5}\mathrm{B} \longrightarrow {}^{8}_{4}\mathrm{Be} + e^{+}\nu_e \,. \tag{2.2.3} $$

The first calculation of the expected electron neutrino flux from boron-8 decays resulted in $3.6 \times 10^7\,\mathrm{cm^{-2}s^{-1}}$ [26]. As current theoretically calculated value, we take $5.05 \times 10^6\,\mathrm{cm^{-2}s^{-1}}$ [27] .

The first experiment measuring the neutrino flux from the Sun has used the following detection reaction:

$$ {}^{37}_{17}\mathrm{Cl} + \nu_e \longrightarrow {}^{37}_{18}\mathrm{Ar} + e^{-} \,. \tag{2.2.4} $$

The measured value for the neutrino flux from boron-8 decays was $1.3 \times 10^7\,\mathrm{cm^{-2}s^{-1}}$ [28], in disagreement with the theoretical calculation at that time. The current measured value of the neutrino flux from boron-8 decays is $2.35 \pm 0.02 \pm 0.08 \times 10^6\,\mathrm{cm^{-2}s^{-1}}$ [29], in disagreement with the theoretical calculation.

In the atmosphere of the Earth, cosmic rays create showers of particles of which many are unstable and decay into neutrinos. For example, due to the interactions of cosmic rays in the atmosphere of the Earth, pions are produced. With a branching ratio of almost 100%, the negative charged pions decay into muons and anti-muon neutrinos. The

muons produced by the decay of the pions decay with a branching ratio of almost 100% into electrons, anti-electron neutrinos muon neutrinos, such that finally, two different neutrino flavors result from the pion decays:

$$\pi^- \longrightarrow \mu^- + \overline{\nu_\mu} \longrightarrow e^- + \overline{\nu_e} + \nu_\mu + \overline{\nu_\mu}\,. \tag{2.2.5}$$

The first measurement studying the atmospheric neutrino spectrum from muon decays counted 85 muon-like events, whereas 144 events were expected [30]. At that time, the collaboration was *unable to explain the data as the result of systematic detector effects or uncertainties in the atmospheric neutrino flux. Neutrino oscillations between muon-neutrino and ν_x or between electron-neutrinos and muon-neutrinos might be one of the possibilities that could explain the data.* [30]

In terrestrial nuclear reactors, anti-electron neutrinos are produced. For example, the Double Chooz experiment [31] observed an electron antineutrino disappearance in the following reaction:

$$\overline{\nu_e} + p \longrightarrow e^+ + n\,. \tag{2.2.6}$$

The experimental discoveries listed above led to the concept of neutrino flavor oscillations. The observed and measured oscillations are driven by neutrino mixing. The neutrino weak interaction states ν_e, ν_μ, ν_τ are linear superpositions of the neutrino mass eigenstates ν_1, ν_2, ν_3. As eigenstate of a mass operator with a mass eigenvalue different from zero, a neutrino mass eigenstate is a stationary state, i.e., its time evolution depends only on its energy. Thus, the time evolution of a given neutrino weak interaction state depends on the time evolution of its comprising neutrino mass eigenstates. Different mass eigenstates evolve differently in time due to their different masses according to:

$$|\nu_i(t)\rangle = e^{-\sqrt{p_i^2+m_i^2}\,t}|\nu_i\rangle\,. \tag{2.2.7}$$

Taking massive neutrinos with different masses as a fact, neutrino flavor oscillations are then simply given by the time evolution of the mass eigenstates. The neutrino weak interaction states ν_e, ν_μ, ν_τ as superpositions of mass eigenstates ν_1, ν_2, ν_3 can be written as follows:

$$\begin{pmatrix} \nu_e \\ \nu_\mu \\ \nu_\tau \end{pmatrix} = \mathbf{U} \begin{pmatrix} \nu_1 \\ \nu_2 \\ \nu_3 \end{pmatrix}\,, \tag{2.2.8}$$

where $\mathbf{U}$ is a 3×3 unitary matrix. For two neutrino flavor states, this matrix was introduced by the Japanese physicists Z. Maki, M. Nakagawa and S. Sakata. They assumed that *some orthogonal transformation applied to the representation of weak neutrinos*, which enter into leptonic currents, *defines the true neutrinos* [32]. However,

Maki–Nakagawa–Sakata did not consider neutrino flavor oscillation. It was B. Pontecorvo who opened the field of neutrino flavor oscillations by studying particle $\leftrightarrow$ antiparticle transitions [33]. To pay tribute to the pioneering works of all of these authors, the matrix $\mathbf{U}$ is called the Pontecorvo–Maki–Nakagawa–Sakata (PMNS)-matrix. The independent parameters of $\mathbf{U}$ are three mixing angle θ_{12}, θ_{23} and θ_{13} and one CP violating phase δ_{CP}. Taking the three mixing angles as Euler angles of a rotation in three dimensional Euclidean space, $\mathbf{U}$ can be written as:

$$\mathbf{U} = \underbrace{\begin{pmatrix} 1 & 0 & 0 \\ 0 & c_{23} & s_{23} \\ 0 & -s_{23} & c_{23} \end{pmatrix}}_{\text{atmospheric}} \cdot \underbrace{\begin{pmatrix} c_{13} & 0 & s_{13}e^{-i\delta_{CP}} \\ 0 & 1 & 0 \\ -s_{13}e^{-i\delta_{CP}} & 0 & c_{13} \end{pmatrix}}_{\text{reactor}} \cdot \underbrace{\begin{pmatrix} c_{12} & s_{12} & 0 \\ -s_{12} & c_{12} & 0 \\ 0 & 0 & 1 \end{pmatrix}}_{\text{solar}} \cdot \underbrace{\begin{pmatrix} e^{\mathrm{i}\frac{\alpha_1}{2}} & 0 & 0 \\ 0 & e^{\mathrm{i}\frac{\alpha_2}{2}} & 0 \\ 0 & 0 & 1 \end{pmatrix}}_{\text{Majorana phases}}, \tag{2.2.9}$$

where $c_{ij} \mathrel{\widehat{=}} \cos\theta_{ij}$ and $s_{ij} \mathrel{\widehat{=}} \sin\theta_{ij}$. The Majorana phases α_1 and α_2 take into account the nature of a Majorana spinor with a mass term being not invariant under a $U(1)$ symmetry. For three flavors, there are two squared mass differences Δm^2_{21} and Δm^2_{32}, referred to as the solar and atmospheric neutrino mass splittings. The experimental measurements of neutrino fluxes from the Sun, the atmosphere of the Earth and terrestrial nuclear reactors can be understood in the framework of oscillations of three active neutrino flavors.[3]

The present day neutrino oscillation data are given in table 2.1, which is taken from [37]. In the SM, the manifest neutrino masses cannot be explained at a renormalizable level. The importance of neutrinos is thus that, by their flavor oscillations and therefore mass terms, the existence of and the need for physics beyond the SM becomes inevitable.

2.2.2. Mass Generation

One can introduce a higher dimensional operator that generates neutrino masses. At dimension five, there is the operator:

$$\overline{L^C_{ai}} L_{bj} H_c H_d \epsilon_{ac} \epsilon_{bd} \,. \tag{2.2.10}$$

This operator was first discussed by Weinberg, who conjectured that the resulting produced neutrino mass *might perhaps be observable in neutrino oscillation experiments* [38].

[3] In the measured neutrino fluxes, anomalies have been discovered, e.g., [34] and [35] report an excess in the $\overline{\nu_\mu} \to \overline{\nu_e}$ transition, and [36] discusses an anomaly in reactor antineutrinos. An investigation of these anomalies is beyond the scope of this thesis.

	Free Fluxes + RSBL	
	Best fit $\pm 1\sigma$	3σ range
$\sin^2\theta_{12}$	$0.302^{+0.013}_{-0.012}$	$0.267 \to 0.344$
$\theta_{12}/^\circ$	$33.36^{+0.81}_{-0.78}$	$31.09 \to 35.89$
$\sin^2\theta_{23}$	$0.413^{+0.037}_{-0.025} \oplus 0.594^{+0.021}_{-0.022}$	$0.342 \to 0.667$
$\theta_{23}/^\circ$	$40.0^{+2.1}_{-1.5} \oplus 50.4^{+1.3}_{-1.3}$	$35.8 \to 54.8$
$\sin^2\theta_{13}$	$0.0227^{+0.0023}_{-0.0024}$	$0.0156 \to 0.0299$
$\theta_{13}/^\circ$	$8.66^{+0.44}_{-0.46}$	$7.19 \to 9.96$
$\delta_{\rm CP}/^\circ$	300^{+66}_{-138}	$0 \to 360$
$\frac{\Delta m^2_{21}}{10^{-5}\ \text{eV}^2}$	$7.50^{+0.18}_{-0.19}$	$7.00 \to 8.09$
$\frac{\Delta m^2_{31}}{10^{-3}\ \text{eV}^2}$ (N)	$+2.473^{+0.070}_{-0.067}$	$+2.276 \to +2.695$
$\frac{\Delta m^2_{32}}{10^{-3}\ \text{eV}^2}$ (I)	$-2.427^{+0.042}_{-0.065}$	$-2.649 \to -2.242$

Table 2.1.: Three-flavor oscillation parameters to global data after the Neutrino 2012 conference. The "Free Fluxes + RSBL" reactor fluxes have been left free in the fit and short baseline reactor data (RSBL) with an oscillation length of $L \lesssim 100\,\text{m}$ are included.

With this operator, which is obviously gauge invariant because the tensor product of four $SU(2)_L$ doublets contains a $SU(2)_L$ singlet representation, the theory is predictive only below the scale that suppresses the dimension five. To ensure a predictive theory at all scales, this operator as any higher dimensional operator has to be viewed as an effective operator at low energies; it is realized at higher energies through renormalizable interactions. It turns out that there are three and only three realizations of the Weinberg operator at tree-level [39], which are known as seesaw type-I [40], type-II [41] and type-III [42]. In type-I seesaw, the Weinberg operator is generated after integrating out three fermion singlets, in type-II seesaw a scalar triplet is integrated out and in type-III seesaw a fermion triplet is integrated out. The type-I seesaw mass matrix is:

$$m_\nu = -m_D M_M^{-1} m_D^T \,. \tag{2.2.11}$$

In the type-I seesaw framework, the light neutrino masses are proportional to the product of the corresponding Yukawa couplings $y_{\alpha i}$ squared times the vacuum expectation value v of the SM Higgs $SU(2)_L$ doublet squared divided by the mass M_i of the fermion singlet. M_i is the scale of new physics generating the effective low energy theory for neutrino masses, see equation (2.2.12).

A simple estimate shows that, taking $y_{\alpha i} \sim 1$ and $v \sim 100\,\text{GeV}$, the scale M_i of new physics has to be as high as $M_i \sim 10^{14}\,\text{GeV}$ in order to generate a light neutrino mass scale of 0.1 eV, as is suggested by the upper limit on the summed neutrino masses obtained by *Planck* in 2013 [5]. To have the scale of new physics in the TeV range as desired for LHC, i.e., $M_i \sim 1\,\text{TeV}$, the Yukawa couplings $y_{\alpha i}$ have to be as tiny as $y_{\alpha i} \sim 10^{-6}$. There is nothing wrong about such a tiny Yukawa, given that the Yukawa coupling of the electron is also of order $\mathcal{O}(10^{-6})$. However, apart from tree level realizations, the Weinberg operator can also be generated at loop level. If there are no tree level contributions to light neutrino masses at all, i.e., neutrinos are massless at tree level, the light neutrino masses are naturally explained by loop-suppressions, which naturally decrease the scale of new physics compared to tree level realizations due to loop factors of $1/16\pi^2$ per loop and additional coupling constants involved in the loops.

We will study neutrino mass generation at loop level. In chapter 3, we make contributions to two well-known radiative neutrino mass models, i.e., the one-loop model proposed by E. Ma and the two-loop model named after A. Zee and K. S. Babu. Before we put these loop models up for discussion, we first concentrate on the mixing between SM neutrinos and right-handed neutrinos, which are sterile under the SM gauge interactions. Sterile neutrinos are then further studied in part II of this thesis.

2.2.3. Sterile Neutrinos

As we have outlined, the SM particle spectrum does not contain right-handed neutrinos.

In the models we have built and will discuss, including the freeze-in production mechanism in chapter 4, right-handed neutrinos are included in the particle spectrum. They are neutral fermion $SU(2)_L$ singlets under the gauge group of the SM. If there existed such a fermion singlet, light neutrino masses could be generated already in the framework of the type-I seesaw, as pointed out above. A singlet does not take part in weak interactions. It is almost completely blind to the SM weak interactions, or in other words, sterile.

We have put emphasize on almost blind. Their mass eigenstates do mix with the SM left-handed neutrinos, which are called active neutrinos in this context.

Following the argumentation of [43], the relevant interactions for left- and right-handed neutrinos are:

$$\mathcal{L} = y_{\alpha i}\,\overline{L_\alpha}\,H\,N_i + \frac{1}{2} y_i\,S\,\overline{N_i^C}\,N_i + \text{h.c.} \tag{2.2.12}$$

N_i are right-handed neutrinos ($i = 1, 2, 3$) and S is a complex scalar singlet.

The Majorana and Dirac masses are, respectively:

$$[M_M]_{ij} = M_i \delta_{ij} = y_i \langle S \rangle \delta_{ij}\,, \tag{2.2.13}$$

$$[m_D]_{\alpha i} = y_{\alpha i} \langle H \rangle\,. \tag{2.2.14}$$

In the basis $(\nu_e, \nu_\mu, \nu_\tau, N_1, N_2, N_3)^T$, the 6×6 symmetric mass matrix reads:

$$\hat{m} = \begin{pmatrix} 0 & m_D \\ m_D^T & M_M\,. \end{pmatrix} \tag{2.2.15}$$

The PMNS matrix $\mathbf{U}$ diagonalizing the seesaw mass matrix $m_\nu = -m_D M_M^{-1} m_D^T$, see equation (2.2.11):

$$\mathbf{U}^\dagger m_\nu \mathbf{U}^* = \text{diag}\,(m_1, m_2, m_3)\,. \tag{2.2.16}$$

The corresponding mass eigenstates are again denoted as ν_1, ν_2, ν_3. The PMNS matrix as a product of three Euler rotations is written in equation (2.2.8). It has the standard form:

$$\mathbf{U} = \begin{pmatrix} c_{12}c_{13} & s_{12}c_{13} & s_{13}e^{-i\delta} \\ -c_{23}s_{12} - s_{23}c_{12}s_{13}e^{i\delta} & c_{23}c_{12} - s_{23}s_{12}s_{13}e^{i\delta} & s_{23}c_{13} \\ s_{23}s_{12} - c_{23}c_{12}s_{13}e^{i\delta} & -s_{23}c_{12} - c_{23}s_{12}s_{13}e^{i\delta} & c_{23}c_{13} \end{pmatrix}, \tag{2.2.17}$$

where the Majorana phase is neglected.

For three generations of neutrinos, there are two differences of squared light neutrino mass eigenvalues. There are three neutrino flavor states and three neutrino mass eigenstates, i.e., six neutrino states. This gives five relative phases between the six neutrino

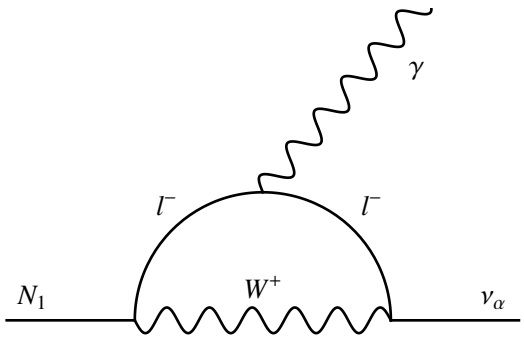

Figure 2.1.: Decay of a sterile neutrino into an active neutrino and a photon. A similar diagram exists in which the lepton line and the W boson line are interchanged such that the photon couples to the W boson.

states. Conventionally, these phases are chosen such that from the nine parameters of $\mathbf{U}$, four parameters remain as free parameters. The free parameters can be counted as $(3-1)^2 = 1/2 \cdot 3\,(3-1) + 1/2 \cdot (3-1) \cdot (3-2)$. The first summand gives the three weak mixing angles θ_{ij}, the second summand gives the CP violating phase δ.

The neutrino flavor states that enter the weak interaction are then equal:

$$\nu_{L\alpha} = U_{\alpha_i}\nu_i + \Theta_{\alpha i}\tilde{N_i}^C\,, \tag{2.2.18}$$

with $\tilde{N_i}$ the mass eigenstates of the right-handed neutrinos N_i. The active-sterile mixing $\Theta_{\alpha i}$ is given by:

$$\Theta_{\alpha i} = \frac{|m_D|_{\alpha i}}{M_i} = \frac{y_{\alpha i}\langle H\rangle}{y_i\langle S\rangle}\,. \tag{2.2.19}$$

For convenience, we define:

$$\Theta_i^2 = \sum_{\alpha=e,\mu,\tau} |\Theta_{\alpha i}|^2\,. \tag{2.2.20}$$

Because the active-sterile mixing angle is non-zero, N_1 can decay into an active neutrino and a photon at one-loop level with a W boson and a charged lepton running in the loop, see figure 2.1. The total decay width of this channel is the sum over all contributing lepton flavors, and it is given by:

$$\Gamma_{N_1\to\nu_{L\alpha}\gamma} = \frac{9\alpha G_F^2}{1024\pi^2}\sin^2(2\Theta_1)M_1^5\,. \tag{2.2.21}$$

Using the numerical values for the electromagnetic fine-structure constant, i.e., $\alpha_{\mathrm{EM}} = 1/137$, the Fermi coupling constant $G_F = 1.166 \times 10^{-5}\,\mathrm{GeV}^{-2}$ and the Taylor expansion $\sin^2 2\Theta_1 = 4\Theta_1^2 + \mathcal{O}[\Theta_1]^3$, we find:

$$\Gamma_{N_1 \to \nu_{L\alpha}\gamma} \approx 8.954 \times 10^{-17} 4\Theta_1^2 \left(\frac{M_1}{\mathrm{keV}}\right)^5 \times 1.519 \times 10^{-6}\,\mathrm{s}^{-1} \tag{2.2.22}$$

$$\approx 5.440 \times 10^{-22} \Theta_1^2 \left(\frac{M_1}{\mathrm{keV}}\right)^5 \mathrm{s}^{-1}\,. \tag{2.2.23}$$

If there is such a decay, the photon leaves its mark in the diffuse photon background radiation at the energy $E_\gamma = M_1/2$.

To be short, the flux of photons resulting from this decay of N_1 is calculable. It is inversely proportional to the lifetime of N_1 for that decay channel, which is given by the decay width. The flux F depends on the sterile neutrino mass M_1 and the mixing angle Θ_1 as $F \sim \Theta_1^2 M_1^5$ [44]. The upper limit on the flux finally translates into an upper limit on Θ_1^2:

$$\Theta_1^2 \lesssim 1.8 \times 10^{-5} \left(\frac{\mathrm{keV}}{M_1}\right)^5\,. \tag{2.2.24}$$

The bound on the active-sterile mixing angle is used to obtain an upper bound for the mass of the sterile neutrino. In section 4.4, this bound then constrains the relic density of a keV sterile neutrino as DM particle.

In the following section, we will provide a basis for DM physics.

2.3. Prelude II: Cosmological Equations

In section 2.1, we briefly described the fundamental concepts of the SM of particle physics before we proceeded with a discussion of neutrinos. Before we move on to a general discussion of DM, we begin with a short presentation of the fundamental principles of the standard model of Cosmology.

The basic equations of the standard model of Cosmology [45] rely on Einstein's equations of General Relativity, which we take as granted as mentioned in the introduction. These equations are differential equations for a metric tensor $g^{\mu\nu}$, which characterizes the geometry of space time. They can be derived from the principle of least action. The geometry of four-dimensional space time is encoded in the Riemann curvature tensor $\mathcal{R}_{\mu\nu\rho\sigma}$, which is a unique expression derived from combinations of the metric tensor $g^{\mu\nu}$. Since an action S is given by integrating over a scalar, we have to construct a scalar from the Riemann curvature tensor to obtain a candidate action for gravity. This is done by first contracting the indices of the Riemann curvature tensor with the metric tensor

$g^{\mu\nu}$ yielding the Ricci tensor $\mathcal{R}_{\mu\rho} \equiv \mathcal{R}_{\mu\nu\rho\sigma} \cdot g^{\nu\sigma} = \mathcal{R}_{\mu\nu\rho}{}^{\nu}$. In a second step we calculate the trace of the Ricci tensor resulting in the curvature scalar $\mathcal{R} = \mathcal{R}_{\mu\nu} \cdot g^{\mu\nu} = \mathcal{R}_{\mu}{}^{\mu}$.

The action S for General Relativity has to lead to the same physics after transforming the coordinates through a diffeomorphism. The rule for integration by substitution assigns the following diffeomorphism-invariant integral for any integrable function $f(x)$:

$$\int d^4x \sqrt{-g}\, f(x) \quad , \tag{2.3.1}$$

with $g \equiv$ det $(g^{\mu\nu})$. The minus sign arises because, locally, $g^{\mu\nu}$ must be equal to the Minkowski metric $g^{\mu\nu} = \text{diag}(-,+,+,+)$, for which $g = -1$. The action S for General Relativity is:

$$S = \int d^4x \sqrt{-g} \left(\frac{1}{2\sqrt{8\pi}G_N} \cdot \mathcal{R} + \mathcal{L}_{\text{matter}} \right) . \tag{2.3.2}$$

$\mathcal{L}_{\text{matter}}$ contains the energy momentum tensor $T_{\mu\nu}$ and the cosmological constant Λ. Applying the principle of least action [46], the outcome are Einstein's equations of General Relativity :

$$\mathcal{R}_{\mu\nu} - \frac{1}{2} g_{\mu\nu} \mathcal{R} = 8\pi G_N T_{\mu\nu} + \Lambda g_{\mu\nu}. \tag{2.3.3}$$

On scales larger than 10^8 pc, cosmological observations suggest that the Universe is homogeneous and isotropic (compare [47]), i.e., characterized by translational and rotational invariance. The only time-dependent four-dimensional space-time that preserves homogeneity and isotropy of space is the Robertson–Walker metric, i.e.:

$$ds^2 = x^\mu x^\nu g_{\mu\nu} = dt^2 - a^2(t) \left[\frac{dr^2}{1 - kr^2} + r^2(d\theta^2 + \sin^2\theta d\phi^2) \right] , \tag{2.3.4}$$

with comoving radial coordinate r. The scale factor $a(t)$ expresses the physical distance $x(t)$ as:

$$x(t) = a(t) \cdot r \, . \tag{2.3.5}$$

The curvature constant $k \in \{+1, -1, 0\}$ corresponds to closed $k = +1$, open $k = -1$ or spatially flat $k = 0$ geometries.

The energy momentum tensor $T_{\mu\nu}$ has to be diagonal in a homogeneous universe and its spatial components have to be equal due to isotropy. If we assume that the matter content of the Universe behaves like a perfect fluid with energy density ρ and pressure p, then:

$$T_{\mu\nu} = \text{diag}(\rho, p, p, p). \tag{2.3.6}$$

With equation (2.3.4) and equation (2.3.6), the (00) component of equation (2.3.3) is evaluated to

$$H^2(t) \equiv \left(\frac{\dot{a}(t)}{a(t)}\right)^2 = \frac{8\pi G_N \rho(t)}{3} - \frac{k}{a(t)^2} + \frac{\Lambda}{3} \quad . \tag{2.3.7}$$

Dividing by the present day Hubble expansion rate $H_0 = H(t = t_0)$ and introducing the critical energy density

$$\rho_c \equiv \frac{3H_0^2}{8\pi G_N} \quad , \tag{2.3.8}$$

equation (2.3.7) is equivalent to

$$\frac{\rho(t)}{\rho_c} - \frac{k}{H_0^2 a(t)^2} + \frac{\Lambda}{8\pi G_N \rho_c} = \frac{H^2(t)}{H_0^2} \quad . \tag{2.3.9}$$

The critical energy density ρ_c is the total energy density of a spatially flat universe. The (ii) components of equation (2.3.3) are:

$$\left(\frac{\ddot{a}(t)}{a(t)}\right) = \frac{\Lambda}{3} - \frac{4\pi G_N}{3}\left(\rho(t) + 3p(t)\right). \tag{2.3.10}$$

Equation (2.3.7) and equation (2.3.10) are the Friedmann. From these, it follows:

$$\dot{\rho}(t) = -3H(t)\left(\rho(t) + p(t)\right) \tag{2.3.11}$$

To solve equation (2.3.11), we can use the general equation of state

$$p = \omega\rho \quad . \tag{2.3.12}$$

For this case, equation (2.3.11) is integrated to:

$$\rho(t) \propto a^{-3(1+\omega)}(t) \quad . \tag{2.3.13}$$

Putting equation (2.3.13) into equation (2.3.7), and neglecting the curvature term, the time dependence of the scale factor results up to an integration constant into:

$$a(t) \propto t^{\frac{2}{3(1+\omega)}} . \tag{2.3.14}$$

The solutions of equation (2.3.13) and equation (2.3.14), respectively, are classified according to their equation of state parameter, see table 2.2. In section 4.3.3, where we calculate the free streaming horizon, we have to use the different time dependence of the scale factor $a(t)$ in each era of the Universe. We introduce the cosmological density

	ω	$a(t)$	$\rho(t)$
radiation-dominated	$\frac{1}{3}$	$t^{\frac{1}{2}}$	$a^{-4}(t)$
matter-dominated	0	$t^{\frac{2}{3}}$	$a^{-3}(t)$
Λ-dominated	-1	$e^{\sqrt{\Lambda/3t}}$	const.

Table 2.2.: Time dependence of the scale factor $a(t)$ for different eras of the Universe.

parameter:

$$\Omega_{\text{tot}} = \Omega_\gamma + \Omega_m + \Omega_\Lambda = \frac{\rho_{\text{tot}}}{\rho_c}\,, \tag{2.3.15}$$

with the total energy density $\rho_{\text{tot}} = ((\rho_0)_\gamma + (\rho_0)_m) + \rho_\Lambda = \rho + \rho_\Lambda$. Ω_m contains baryonic (b) matter and Dark Matter (DM):

$$\Omega_m = \Omega_b + \Omega_{\text{DM}} \quad . \tag{2.3.16}$$

The current most precise measurement of the cosmological parameters is performed by *Planck*, a space observatory of the European Space Agency. We present the relevant best fit values [5] in table 2.3.

The energy density $\rho_{0,\text{DM}}$ of DM today is $\rho_{0,\text{DM}} = m_{\text{DM}} n_{0,\text{DM}}$. m_{DM} is the mass of the DM particle and $n_{0,\text{DM}}$ is its number density by today. The number density $n(t)$ of a particle species i with g_i internal degrees of freedom results from the phase-space integration:

$$n(t) = \frac{g_i}{(2\pi^3)} \int d^3p\, f(p,t) \tag{2.3.17}$$

with $f(p,t)$ the phase-space distribution function. The DM relic density, which can be written as

$$\Omega_{\text{DM}} = \frac{m_{\text{DM}} n_{0,\text{DM}}}{\rho_c}\,, \tag{2.3.18}$$

then follows after phase-space integration of the phase-space distribution function, once the mass of the DM is known. The phase-space distribution function is thus the decisive quantity that we will further discuss. By definition of the abundance Y, see equation (D.0.6), the number density of a particle species can also be written as the product of its abundance Y and the entropy density s. Both factors are comoving quantities, i.e., there is no dependence on the scale factor $a(t)$. The entropy density s of a particle species i is defined in appendix C.0.5.

If one assumes that the expansion of the Universe is isentropic, the entropy $S = sa^3(t)$ is conserved, where the entropy density s is given in equation (D.0.7). Conservation

of entropy is in particular important when a particle species decouples from chemical equilibrium, see section 2.5 for details. For example, we briefly review the decoupling of neutrinos, which is also discussed in section 3.4.2.

The neutrino interactions are weak interaction. For temperatures $T \lesssim 1\,\mathrm{MeV}$, the weak interaction rate is smaller than the Hubble expansion rate at that time, and the neutrinos are no longer in chemical equilibrium. Shortly after the neutrinos have decoupled, but still for temperatures above the electron mass, electrons and positrons are in chemical equilibrium with photons. Using equation (C.0.12), where we can set $T_B = T_F = T$, because the masses of the electron, positron and photon are much smaller than the actual photon temperature T, the number of degrees of freedom equals $2 + {}^{7}/_{8} \cdot (2+2) = {}^{11}/_{2}$. When the temperature of the photons has fallen below the mass of the electron, the number of degrees of freedom decreases to 2, only including photons. Due to entropy conservation, the product $(a(t_{\mathrm{after}})T_\gamma(t_{\mathrm{after}}))^3$ must therefore be larger than the product $(a(t_{\mathrm{before}})T_\gamma(t_{\mathrm{before}}))^3$: at the time t_{after}, when the electrons and positrons have left the thermal bath, the number of degrees of freedom is by a factor of ${}^{4}/_{11}$ smaller than the number of degrees of freedom at the time t_{before} just before electron-positron decoupling. These electron-positron annihilations transfer entropy to the photons, but not to the neutrinos, which have already left chemical equilibrium. Therefore the temperature T_γ of photons is increased by the entropy transfer relative to the temperature T_ν of neutrinos. For the present day time t_0, the metric scale factor $a(t_0)$ equals one and the ratio of T_ν and T_γ follows to be:

$$\frac{T_\nu(t_0)}{T_\gamma(t_0)} = \left(\frac{2}{\frac{11}{2}}\right)^{\frac{1}{3}} = \left(\frac{4}{11}\right)^{\frac{1}{3}} . \tag{2.3.19}$$

The present day entropy density s_0 can be expressed in terms of the photon temperature T_γ as $s_0 = 2969.5\,(T_\gamma/2.75)^3\ \mathrm{cm}^{-3}$. We take $T_\gamma = 2.7255\,\mathrm{K}$. We can therefore write $\rho_{0,\mathrm{DM}} = m_{\mathrm{DM}} s_0 Y_0$. The relic density of DM in comoving quantities then follows to:

$$\Omega_{\mathrm{DM}} = \frac{s_0}{\rho_c} m_{\mathrm{DM}} Y_0 \,. \tag{2.3.20}$$

Inserting the relevant *Planck* 2013 data [5] yields:

$$\Omega_{\mathrm{DM}} h^2 = 2.717 \times 10^8 m_{\mathrm{DM}}[\mathrm{GeV}] Y_0 \,. \tag{2.3.21}$$

In chapter 4, we explicitly use equation (2.3.21) to find the mass of our DM particle that leads to the correct relic density. The best fit values in table 2.3 suggest that 84.50% of the matter content of the Universe is DM.

In the following section, we briefly emphasize the importance of DM on the structure formation of the Universe.

	Cosmological parameters and N_{eff}	
	Best fit	68% limits
H_0	67.11	67.4 ± 1.4
Ω_Λ	0.6825	0.686 ± 0.020
Ω_m	0.3175	0.314 ± 0.020
$\Omega_b h^2$	0.022068	0.02207 ± 0.00033
$\Omega_{\text{DM}} h^2$	0.12029	0.1196 ± 0.0031
N_{eff}	$3.36^{+0.68}_{-0.64}$	$\leftarrow$ 95 % limit

Table 2.3.: Cosmological parameter values and the effective neutrino number.

2.4. Dark Matter in the Universe

Observations of individual galaxies and superclusters of galaxies reveal that individual galaxies tend to be older than superclusters [48]. We thus conclude that structures of the Universe observed today formed in a bottom-up approach.

In the common understanding of the Universe, its structure originates from gravitational perturbations in the metric as an aftermath of the Big Bang. The gravitational perturbations are present in the energy and matter densities. It is believed that the time evolution of these perturbations have formed the structures of the Universe as observed today.

The characteristic scale to explore the time evolution of perturbations is the Jeans scale k_J named after the British physicist J. H. Jeans. The matter energy density $\rho = \rho_0 + \rho_p$ has to satisfy the equation of an expanding universe governed by general relativity, see equation (2.3.7). ρ_0 is a static contribution, and ρ_p is the perturbation. The solution for ρ_p can be Fourier expanded with wavenumber k and frequency ω. The frequency ω can be expressed by the wavenumber k and the static solution ρ_0 via a dispersion relation. The Jeans scale k_J is the wavenumber for which $\omega = 0$ [45]. If $k < k_J$, the perturbation related to k is exponential growing, if $k > k_J$, the perturbation oscillates. The mass inside a sphere of radius $r_J = \pi/k_J$ is called the Jeans mass. Masses smaller than the Jeans mass are stable against gravitational perturbations, i.e., there is no gravitational collapse, whereas masses larger than the Jeans mass must undergo a gravitational collapse.

In the early Universe, the coupling of the radiation fluid to electrons can be approximated by Thomson scattering because the energy of the electrons with a rest mass of 511 keV is larger than the energy of the massless photons. Due to Coulomb scattering, electrons couple to protons, such that there is the photon-baryon fluid. The

photon-baryon fluid, the DM fluid and the neutrino fluid all interact with each other gravitationally. In the radiation dominated era, the Jeans mass of baryons is larger than the mass of baryons within the sphere of radius r_J, i.e., the gravitational perturbations in the photon-baryon fluid are stable and do not grow: the radiation pressure counteracts the gravitational contraction, and the baryon acoustic oscillations starts.

At matter-radiation equality, the matter content starts to dominate over the radiation content. Cold DM is pressure-less and if cold DM dominates in the matter dominated era, there is no pressure left that could counteract the gravitational contraction, such that the baryon acoustic oscillations stop. Gravitational perturbations grow in the DM, and small and large scales clump together.

When the baryons have decoupled from the photons, the Jeans mass of baryons decreases and gravitational perturbations start growing in the baryon fluid. Small scale clumps in the baryons fall into the gravitational potentials generated by the DM. Existing scale clumps attract further small scale clumps. This is the evolution of individual galaxies attracting more and more galaxies, resulting in the formation of galaxy clusters.

The *Millenium Simulation* [49], which assumed DM to be cold and collision-free, numerically describes how the structures of the Universe evolve from perturbations, and it shows that the resulting large scale structures match the ones observed.

If the DM was hot, i.e.,, if it would have behaved as a radiation fluid, this evolution would have been completely different. The structures would have formed in a top-down manner, which does not agree with observations. DM can therefore not be hot. However, between hot and cold there is warm. On large scales warm DM works as well as cold DM. On small scales, cold DM models seem to over-predict the number of satellite galaxies, as already pointed out in [50]. However, warm DM erases small scale structures relative to cold DM. Therefore, warm DM describes even better the structure formation of the Universe on large and on small scales compared to cold DM. The specifications hot, warm and cold refer to the distribution function of the DM particle in velocity space [51]. For a fermionic DM particle X with mass m_{DM}, the distribution function $f_X(v)$ can be parametrized as

$$f_X(v) = \frac{\beta}{e^{\frac{p}{\alpha T_\gamma}} + 1}\,. \tag{2.4.1}$$

Here, T_γ is the temperature of photons, and the velocity v equals $v = {}^{p}\!/\!\sqrt{p^2+m_{\mathrm{DM}}^2}$. The expected mean velocity is:

$$E[v] = \int_0^\infty dv\, v f_X(v)\,, \tag{2.4.2}$$

where we consider only one dimension for simplicity. The velocity dispersion σ that is important for structure formation then follows to:

$$\sigma = \sqrt{E[v^2] - (E[v])^2}\,. \tag{2.4.3}$$

The distribution function in momentum space of hot DM in the form of SM neutrinos equals:

$$f_\nu(p) = \frac{1}{e^{\frac{p}{T_\nu}} + 1}\,, \tag{2.4.4}$$

where we have used entropy conversation, ${}^{T_\nu}\!/_{T_\gamma} = ({}^4\!/_{11})^{1/3}$, i.e., $\beta = 1$ and $\alpha = ({}^4\!/_{11})^{1/3}$, see equation (2.3.19). Since the phase-space distribution function determines the relic density as discussed below equation (2.3.17), the phase-space integration of equation (2.4.4) then yields:

$$\Omega_\nu h^2 = \frac{m_\nu}{93\,\mathrm{eV}}\,, \tag{2.4.5}$$

see [45] and references therein. With the upper limit [5] on the neutrino mass of

$$\sum m_\nu < 0.23\,\mathrm{eV}\,, \tag{2.4.6}$$

$\Omega_\nu h^2 \approx 0.002$, which is thus by a factor of 60 too small to solely account for the DM relic density.

For a particle X that decouples when it is still relativistic, entropy conversation yields:

$$\frac{T_X}{T_\gamma} = \left(\frac{4}{11}\right)^{\frac{1}{3}} \left(\frac{10.75}{g(T_D)}\right)^{\frac{1}{3}}\,, \tag{2.4.7}$$

where T_D is the temperature at the time the particle X decouples, T_X is the temperature of the particle X and the decoupling happens before the neutrino decoupling. The earlier the particle X decouples, the higher the number $g(T_D)$ of relativistic degrees of freedom is and, therefore, the lower the temperature of the particle X will be. Since the particle X is still relativistic when it decouples, its number density scales like T_X^3 and thus also decreases for increasing T_D. For a fixed relic density, which is basically the product of the number density and the mass, this implies a higher mass for the particle X, which decouples earlier than the SM neutrinos. A higher mass results in a lower velocity dispersion σ. In that sense, hot DM has a large velocity dispersion at the time of matter-radiation equality when gravitational perturbations start to grow in the DM, whereas cold DM, which is already non-relativistic at the time of decoupling, has a negligible velocity dispersion. Warm DM has a velocity dispersion that is much smaller than that for hot DM, but non-negligible at the time of matter-radiation equality.

Warm DM suppresses small scale power due to free streaming r_{FS} resulting from its non-negligible velocity dispersion, and thus it can explain the observed small scale structures even better than cold DM. A freely propagating particle with velocity v propagates on a geodesic satisfying $v(t)dt = a(t)dr$. The comoving distance that a freely

	Freeze-Out	Freeze-In
interactions	in thermal equilibrium	not in thermal equilibrium
initial abundance	thermal abundance	negligible
evolution	out of equilibrium	increasing abundance
representative	WIMP	FIMP
Y_0	$\propto 1/\lambda^2$	$\propto \lambda^2$

Table 2.4.: Freeze-out versus freeze-in.

moving particle propagates between a time $t_{\rm in}$ and t_0 follows to:

$$r_{\rm FS} = \int_{t_{\rm in}}^{t_0} dt\, \frac{v(t)}{a(t)}\,. \tag{2.4.8}$$

It is called the free streaming horizon and is used to distinguish between hot, warm and cold DM. Generically, hot DM has $r_{\rm FS} > 0.1\,\text{Mpc}$ and warm DM $r_{\rm FS} < 0.1\,\text{Mpc}$, see the discussion of equation (4.3.31). For cold DM, $r_{\rm FS}$ is one order of magnitude smaller.[4] The free streaming horizon is discussed in detail in equation (4.3.20) and following.

In chapter 3, we investigate cold DM models with radiative neutrino mass generation at one and at two loop level. In chapter 4, we focus on warm DM and introduce a new production mechanism for keV sterile neutrinos as DM particles. Next, we explain the freeze-out and freeze-in mechanisms.

2.5. The Relic Density of Dark Matter: Freeze-Out vs. Freeze-In

Now that we have shown the importance of DM on the structure formation of the Universe, we move on to production mechanism for particle DM, which is one of the main topics of this thesis.

Throughout this work we hold the view that the DM particle is stable and is connected to an initial thermal equilibrium.

There are two opposite production mechanisms, freeze-out and freeze-in, see [45] and references therein. In the freeze-out scenario, the initial abundance of DM is the equilibrium abundance. For a given temperature, the DM interactions leave thermal equilibrium and the DM abundance remains constant. In the freeze-in scenario, the initial DM abundance is almost zero, and it later freezes in to its final abundance.

[4] The free streaming horizon gives only a hint on the kind of DM. To clearly determine whether a DM particle is hot, cold or warm, one has to consider its velocity dispersion and judge from the resulting power spectrum the nature of DM, which is out of focus for this work.

In the freeze-out scenario, concentrated studies on DM particles falling into the class of weakly interacting massive particles (WIMPs) are conducted. With equation (2.5.9), the relic density in equation (2.3.21) of a frozen out DM particle can be written as:

$$\Omega_{\mathrm{DM}}h^2 \approx \frac{3\times 10^{-27}\,\mathrm{cm^3 s^{-1}}}{\langle\sigma v_r\rangle}\,. \tag{2.5.1}$$

To obtain the measured DM relic density $\Omega_{\mathrm{DM}}h^2 \sim \mathcal{O}(10^{-1})$, the thermal average of the annihilation cross section times relative velocity has to be of order $\langle\sigma v_r\rangle = 3\times 10^{-26}\,\mathrm{cm^3 s^{-1}} = 1\,\mathrm{pb}$, which is the scale of weak interaction strengths. In that sense, the term *weakly interacting* refers to the fact that a stable particle associated with new physics at the electroweak scale can contribute the necessary DM relic density. In the freeze-in scenario, the class of feebly interacting massive particles (FIMPs) is commonly investigated.

In two of the three models we analyze, the DM particle has a Yukawa interaction to a scalar singlet particle S beyond the particle content of the SM. When S obtains a vacuum expectation value, the renormalizable interaction $\lambda(S^*S)(H^\dagger H)$, which is invariant under SM gauge transformations, becomes a portal, called Higgs portal, for DM annihilations into SM particles through the mixing of the mass eigenstates of S and the SM Higgs $SU(2)_L$ doublet H. [5] In the model presented in section 3.1, there is no s-channel Higgs portal. In that case, DM annihilations can proceed via t-channel exchange of an inert Higgs $SU(2)_L$ doublet. But the DM relic density is still achieved by thermal freeze-out. In addition to DM annihilations, co-annihilations are important in that model. We briefly discuss co-annihilations in the following.

In general, the thermally averaged annihilation cross section times relative velocity, i.e., $\langle\sigma v_r\rangle$, for DM annihilations through the Higgs portal are proportional to ${}^{\lambda^2 m_{\mathrm{SM}}^2}/_{(4m_{\mathrm{DM}}^2 - m_H^2)^2}$.

[5] One should remark that, for the number density n of the DM particle, annihilation and creation processes driven by SM particles are relevant. For example, in SUSY theories, given that R-parity is an exact symmetry, all SUSY partners decay into the LSP, which is natural DM particle, if electrically neutral. Therefore, the number density n of the LSP is the sum of the number densities n of all heavier SUSY particles.

For this number density being the sum of the number densities n of all heavier SUSY particles, the thermal average of the total annihilation cross section of the LSP equals the thermal average of the sum of the annihilation cross sections of the heavier SUSY particles into SM particles. Through scattering processes with SM particles, the SUSY particles are kept in kinetic equilibrium. However, when the temperature T falls below the mass of the heavier SUSY particles due to the expansion of the Universe, the heavier SUSY particles become non-relativistic. Their number densities n become Boltzmann suppressed. The number densities n of the SM particles, which, in kinetic equilibrium, follow a T^3 power law as long as the particles are relativistic, are therefore larger. This means that, for LSP DM, the scattering processes with SM particles are much more frequent that with heavier SUSY particles and the SM particles ensure that the LSP remains in kinetic equilibrium. Also for other theories beyond the SM in which the DM particle is the lightest particle of the new particle sector, the SM particles ensure the kinetic equilibrium for the DM particle.

In the freeze-out scenario, the number density n of the DM particle at a high temperature T traces the equilibrium distribution, which is proportional to T^3. For a temperature at which the interaction rate $n\langle\sigma v_r\rangle$ of the DM particle is smaller than the Hubble expansion rate H, the DM particle leaves the chemical equilibrium, and its number density n_0 observed today is inversely proportional to the thermally averaged annihilation cross section times relative velocity, i.e., $n_0 \propto {}^1\!/\!_{\lambda^2} \cdot {}^{(4m_{\mathrm{DM}}^2 - m_H^2)^2}\!/\!_{m_{\mathrm{SM}}^2}$. Thus, the larger the coupling constant λ, i.e., the larger the interaction strength, the smaller the number density n_0 observed today is in the freeze-out scenario. Since experiments have measured the DM relic density, which is essentially its number density observed today, the coupling constant λ is constrained to be of order $\mathcal{O}(10^{-1})$ far from Higgs resonances. Note that in the vicinity of a Higgs resonance, which is at $m_{\mathrm{DM}} = {}^1\!/\!_2 \cdot m_H$, the coupling constant λ has to smaller than $\mathcal{O}(10^{-1})$ to compensate for the pole in the scalar propagator [52]. The numerical treatment of freeze-out was already developed in [53].

In the freeze-in scenario, the number density n of the DM particle at a high temperature T is assumed to be negligible small in contrast to the T^3 dependence in the freeze-out scenario. In that case, the DM particle is never in chemical equilibrium, which is satisfied if $n\langle\sigma v_r\rangle < H$, even at high temperatures. The condition $n\langle\sigma v_r\rangle < H$ translates into an upper bound for the coupling λ if the Higgs portal is the dominant communication channel between the DM particle and the particles in chemical equilibrium, which is $\lambda \lesssim 10^{-6}$. For such a small coupling constant, the DM particle is only feebly coupled to the particles in chemical equilibrium, from which it is only gradually being produced by annihilations or decays as the temperature of the Universe decreases. When the temperature of the particles in chemical equilibrium falls below the mass of the DM particle, the production of the DM particle from the particles in chemical equilibrium becomes kinematically forbidden and the number density n of the DM particle freezes in to a constant value. So the general evolution of the DM number density in the freeze-in scenario is characterized by an initial negligible number density. This then increases by the production channels of the particles in chemical equilibrium until the freeze-in temperature. For smaller temperatures the number density remains constant. The larger the coupling constant λ, the larger the number density n_0 observed today will be in the freeze-in scenario, which is opposite to the behavior for the freeze-out case. The idea to generate a particle abundance with an initial abundance equal to zero via the Higgs portal with a very tiny coupling constant was expressed in [54]. It was then summarized and systematized in [55]. We provide an overview about freeze-out and freeze-in in table 2.4. Although we do not know the particle nature of DM neither its non-gravitational interactions, we know the present day amount of DM expressed in terms of the relic density Ω_{DM}.The key quantity, which, apart from the mass of the DM particle, determines its relic density, is the present day abundance Y_0. Y_0 depends on the expansion history of the Universe and on the interactions of the particle under consideration with other particles in the thermal bath. The interactions with other

thermal bath particles produce the present day DM abundance, which depends on the two scenarios freeze-in and freeze-out. In general, one has to start with a Boltzmann equation, which is a rate equation describing the evolution of a phase-space distribution function $f_i(E,t)$ for a particle species i due to the expansion of the Universe and due to interaction processes:

$$\mathbf{L}[f] = \mathbf{C}[f]\,. \tag{2.5.2}$$

Here, $\mathbf{L}$ is the Liouville operator and $\mathbf{C}$ is the collision operator.

Applying $\mathbf{L}$ in the Robertson–Walker metric on the number density n as defined in equation (2.3.17), i.e., the outcome is:

$$\mathbf{L}[n] = \dot{n}(t) + 3Hn(t)\,. \tag{2.5.3}$$

To write this in comoving quantities, one has to use that $\dot{s} = -3Hs$, which results in $\dot{n}(t) + 3Hn(t) = s\dot{Y}$. The collision operator takes into account the interactions of the particle with particles of the thermal bath. For the case of annihilations of a particle-antiparticle pair 1 and 2 into a particle pair 3 and 4 with $|\mathcal{M}_{1+2\to3+4}|^2$ being the squared matrix element for the forward reaction and $|\mathcal{M}_{3+4\to1+2}|^2$ for the backward reaction the collision operator is the following phase space integral:

$$\begin{aligned} -\int \frac{d^3p_1}{(2\pi)^3\,2E_1}\,\frac{d^3p_2}{(2\pi)^3\,2E_2}\,\frac{d^3p_3}{(2\pi)^3\,2E_3}\,\frac{d^3p_4}{(2\pi)^3\,2E_4}\,(2\pi)^4\,\delta^{(4)}\left(p_1+p_2-p_3-p_4\right) \\ \cdot\left(f_1f_2(1\pm f_3)(1\pm f_4)|\mathcal{M}_{1+2\to3+4}|^2 - f_3f_4(1\pm f_1)(1\pm f_2)|\mathcal{M}_{3+4\to1+2}|^2\right)\,. \end{aligned} \tag{2.5.4}$$

Under CPT invariance we have $|\mathcal{M}_{1+2\to3+4}|^2 = |\mathcal{M}_{3+4\to1+2}|^2 \equiv |\mathcal{M}|^2$. We further approximate the Pauli blocking and enhancing factors to one; the error of this approximation is negligibly small. Thus we can write:

$$\begin{aligned} -\int \frac{d^3p_1}{(2\pi)^3\,2E_1}\,\frac{d^3p_2}{(2\pi)^3\,2E_2}\,\frac{d^3p_3}{(2\pi)^3\,2E_3}\,\frac{d^3p_4}{(2\pi)^3\,2E_4}\,(2\pi)^4\,\delta^{(4)}\left(p_1+p_2-p_3-p_4\right) \\ \cdot\left(f_1f_2 - f_3f_4\right)|\mathcal{M}|^2\,. \end{aligned} \tag{2.5.5}$$

Note that we have taken into account the backward reactions, which is only relevant if the particles 3 and 4 produced in the forward reaction have already a non-negligible abundance compared to the chemical equilibrium abundance. This is the case in the freeze-out, however, in the freeze-in scenario, one could in principle neglect the backward reactions if the particles 3 and 4 have an negligible abundance.

2.5.1. Freeze-Out

In fact, if the particles 3 and 4 are in chemical equilibrium and if they are lighter than the particles 1 and 2, 3 and 4 will stay in chemical equilibrium even after particles 1 and

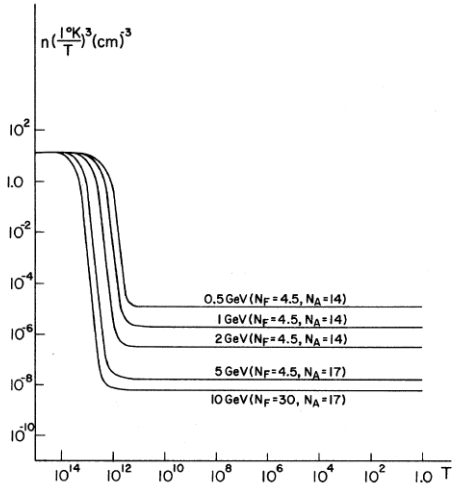

Figure 2.2.: Evolution of the abundance in the freeze-out scenario of a possible neutral lepton for the lepton masses m_L=0.5 GeV, 1 GeV, 2 GeV, 5 GeV and 10 GeV. N_F is the effective number of degrees of freedom and N_A is the number of annihilation channels.

2 have left it. In the determination of the final abundance of the particles 1 and 2 we can therefore use the equilibrium phase-space distribution functions for the particles 3 and 4, which we approximate as Maxwell–Boltzmann distributions. Energy momentum conservation leads to $f_3^{\mathrm{eq}} f_4^{\mathrm{eq}} = f_1^{\mathrm{eq}} f_2^{\mathrm{eq}}$ such that the collision operator becomes

$$-\int \frac{d^3p_1}{(2\pi)^3\,2E_1}\,\frac{d^3p_2}{(2\pi)^3\,2E_2}\,\frac{d^3p_3}{(2\pi)^3\,2E_3}\,\frac{d^3p_4}{(2\pi)^3\,2E_4}\,(2\pi)^4\,\delta^{(4)}\left(p_1+p_2-p_3-p_4\right) \cdot \left(f_1 f_2 - f_1^{\mathrm{eq}} f_2^{\mathrm{eq}}\right)|\mathcal{M}|^2\,. \tag{2.5.6}$$

Using $n_1 = n_2$ for the particle-antiparticle pair 1 and 2, the resulting Boltzmann equation finally simplifies to:

$$\dot{n}_1 = -3Hn_1 - \langle\sigma v_r\rangle(n_1^2 - n_{1,\mathrm{eq}}^2)\,. \tag{2.5.7}$$

Here, v_r is the relative velocity and n_{eq} is the chemical equilibrium number density, see appendix D for details. Equation (2.5.7) was already used in [58]. Exemplary solutions to equation (2.5.7) are shown in figure 2.2, which is taken from [58].

$\langle\sigma v_r\rangle$ is the thermal average of the annihilation cross section σ times relative velocity v_r:

$$\langle\sigma v_r\rangle = \frac{1}{8m^4TK_2^2\left(\frac{m}{T}\right)}\int_{4m^2}^{\infty} ds\,\sigma\left(s-4m^2\right)\sqrt{s}K_1\left(\frac{\sqrt{s}}{T}\right)\,. \tag{2.5.8}$$

In terms of the abundance Y, equation (2.5.7) reads:

$$\dot{Y} = -s\langle\sigma v_r\rangle(Y^2 - Y_{eq}^2)\,. \tag{2.5.9}$$

In the most general case, the annihilation cross section for a $2 \to 2$ process depends on the Mandelstam variables s, t and u. Since u can be written as $\sum_{i=1}^{i=4} m_i^2 - s - t$, where the sum runs over all external particles, it is sufficient to expand s and t in terms of the center of mass velocity v_{cm}, which than results in a v_{cm} expansion for the whole annihilation cross section times v_{cm}. Due to the definitions of s and t, the expansion of s only involves even powers of v_{cm}, whereas the expansion of t involves even and odd powers of v_{cm} with the odd powers of v_{cm} having the cosine of the center of mass system angle θ as a common factor in linear power. The only θ dependence in the expansion of the squared amplitude for the annihilation cross section times v_{cm} in the variables s and t is manifest in the t derivative terms, which are multiplied by powers of t. The integration of odd powers of $\cos\theta$ yields zero. Since $\cos\theta$ enters only linear into the v_{cm} expansion of t as factor of the odd powers in v_{cm}, the annihilation cross section finally does not depend on odd powers of v_{cm} and can be expressed as $\sigma v_{\text{cm}} = a + b v_{\text{cm}}^2 + \mathcal{O}(v_{\text{cm}}^4)$. The coefficients a, b and c follow from the square amplitude [59]. A detailed discussion of the expansion of σv_{cm} in terms of v_{cm} is provided in appendix A.

In the radiation dominated era, the expansion time t in a flat universe equals $1/2H$, where the Hubble expansion rate H is proportional to the temperature T squared. Introducing the variable $x = m/T$, the derivative with respect to t can be translated into a derivative with respect to T. At very early times, the freezing-out particle is in chemical equilibrium with all the other bath particles, i.e., its number density n is equal to the equilibrium number density, which is proportional to T^3. The entropy density is also proportional to T^3. Therefore, at very early times, the abundance Y is independent of T. The Boltzmann equation then forces $Y^2 = Y_{eq}^2$, or, in other words, in the freeze-out scenario, the initial abundance of the freezing-out particle is independent of T and follows the equilibrium abundance, as already noted.

Co-Annihilations

So far, we have considered annihilations of a particle-antiparticle pair 1 and 2, meaning that particle 2 is the antiparticle of particle. Therefore, in the cases of scalar or Majorana particles, only annihilations of one and the same particle are considered. As already noted, in section 3.1 we consider also co-annihilations, which we briefly discuss in this section. We rely on [60].

Suppose in a model beyond the SM there exist particles X_i that are charged under a discrete symmetry such that they are not allowed to decay into SM particles. Let the lightest of them be the DM particle X_1. The particles X_i are assumed to be degenerated in mass. If the mass difference $\delta m \equiv m - m_1$ to X_1 does not exceed

the temperature at freeze-out of X_1, then the additional particles X_i are thermally accessible and have to be included into the freeze-out calculation; not only the annihilation reactions $X_1\,X_1 \to SM\,SM'$ contribute to the total $\langle\sigma v_r\rangle$, where SM and SM' denote SM particles; also the annihilation reaction $X_1\,X_{i\neq 1} \to SM\,SM'$, which is called co-annihilation reaction, has to be included. If the cross sections of these individual reactions are similar, then the effect of co-annihilations is not significant. However, if the cross sections of the individual reactions are different, than co-annihilations can significantly increase the total $\langle\sigma v_r\rangle$ and therefore decrease the relic density of the DM particle X_1 in the freeze-out scenario.

This effect of co-annihilations is in particular important in models where DM annihilations are driven by Yukawa couplings, which by themselves are constrained by lepton flavor violation (LFV) processes. Such models have in general the problem that the relevant Yukawa coupling constants have to be tiny in order not to violate constraints from LFV processes. On the other hand, in the freeze-out scenario, tiny Yukawa coupling constants relevant for DM annihilations yield a DM relic density that is above the current bound. DM co-annihilations can then simultaneously satisfy the constraints from LFV processes and DM relic density.

In section 3.1, we will exploit from the co-annihilations $N_1\,N_2$ and $N_1\,\eta$; the first one contribute to s-wave annihilations for which the cross sections are relatively large because they are not suppressed by v_r, the second one has a completely different cross section.

2.5.2. Freeze-In

To obtain the final abundance in the freeze-in scenario, one again has to start with a Boltzmann equation. The Liouville term is the same as in the freeze-out scenario, however, the collision term is different in the freeze-in scenario. It depends on the production process of the frozen-in particle; in the literature, the most frequently studied processes are those in which the frozen-in particle can be produced by decays of heavier particles that are in chemical equilibrium, by inverse decays or by scattering processes [55].

To illustrate the general behavior of the freeze-in scenario, we consider the freeze-in of a real scalar singlet by annihilations mediated by the Higgs portal. The Lagrangian is that of [61] and [62]:

$$\begin{aligned}\mathcal{L} =& \frac{1}{2}\left(\partial_\mu S\right)\left(\partial^\mu S\right) - \frac{m_0^2}{2}S^2 - \frac{1}{4}\lambda_S S^4 \\ &+ \left(D_\mu H\right)^\dagger\left(D^\mu H\right) - \lambda_H (H^\dagger H)^2 - \lambda S^2 H^\dagger H\,. \end{aligned} \tag{2.5.10}$$

The relic density of the real scalar singlet S in the freeze-in regime was determined in [56].

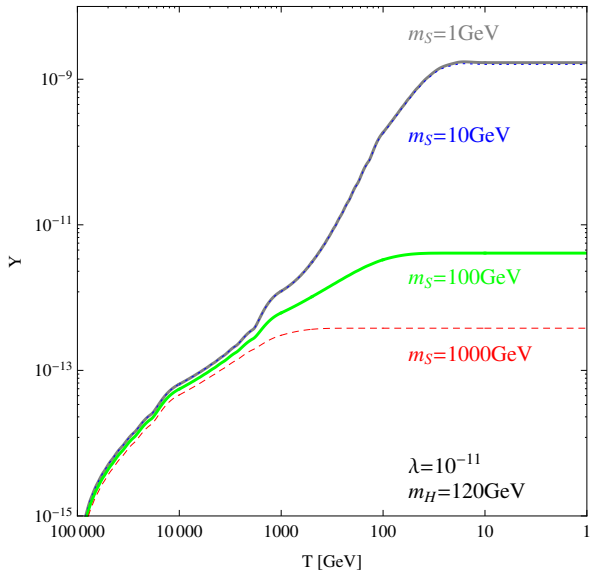

Figure 2.3.: Evolution of the abundance in the freeze-in scenario of a real scalar particle for different scalar masses. The Higgs portal coupling is set to $\lambda = 10^{-11}$ and the mass of the SM Higgs $SU(2)_L$ doublet is set to $m_H = 120\,\mathrm{GeV}$.

The collision term of the Boltzmann equation is:

$$-\int \frac{d^3p_1}{(2\pi)^3\,2E_1}\,\frac{d^3p_2}{(2\pi)^3\,2E_2}\,\frac{d^3p_3}{(2\pi)^3\,2E_3}\,\frac{d^3p_4}{(2\pi)^3\,2E_4}\,(2\pi)^4\,\delta^{(4)}\left(p_1+p_2-p_3-p_4\right) \cdot \left(f_1 f_2 - f_3 f_4\right)|\mathcal{M}|^2\,. \tag{2.5.11}$$

Contrary to the freeze-out process, the initial abundance of the scalar singlet, which corresponds to the particles 1 and 2 in the above expression, is always much smaller than the equilibrium abundance. At very early times, we can therefore approximate $f_1 = f_2 \approx 0$ yielding:

$$\int \frac{d^3p_1}{(2\pi)^3\,2E_1}\,\frac{d^3p_2}{(2\pi)^3\,2E_2}\,\frac{d^3p_3}{(2\pi)^3\,2E_3}\,\frac{d^3p_4}{(2\pi)^3\,2E_4}\,(2\pi)^4\,\delta^{(4)}\left(p_1+p_2-p_3-p_4\right) \cdot f_3 f_4 |\mathcal{M}|^2\,. \tag{2.5.12}$$

Again we can use the Maxwell–Boltzmann distributions for the bath particles 3 and 4 at very early times and by using energy conservation, we have:

$$f_3^{\mathrm{eq}} f_4^{\mathrm{eq}} = e^{-\frac{E_3+E_4}{T}} = e^{-\frac{E_1+E_2}{T}} = f_1^{\mathrm{eq}} f_2^{\mathrm{eq}}\,. \tag{2.5.13}$$

The outcome is:

$$\int \frac{d^3p_1}{(2\pi)^3\,2E_1}\,\frac{d^3p_2}{(2\pi)^3\,2E_2}\,\frac{d^3p_3}{(2\pi)^3\,2E_3}\,\frac{d^3p_4}{(2\pi)^3\,2E_4}\,(2\pi)^4\,\delta^{(4)}\left(p_1+p_2-p_3-p_4\right) \cdot\; f_1^{\mathrm{eq}} f_2^{\mathrm{eq}} |\mathcal{M}|^2\,. \tag{2.5.14}$$

Observe that the equilibrium distributions for particles 1 and 2 enter only by using energy momentum conservation in the equilibrium distributions of the particles 3 and 4, however, the scalar singlet is never in thermal equilibrium.

The Boltzmann equation reads:

$$\dot{Y} = s\langle\sigma v_r\rangle Y_{eq}^2\,, \tag{2.5.15}$$

compare to equation (2.5.9).

We have implemented the model of the freeze-in of a scalar singlet into LanHEP [63]. The thermal average of the annihilation cross section times relative velocity has then been calculated numerically using the micrOMEGAs package [64]. We have developed a procedure in the computer algebra system Mathematica to solve the differential equation (2.5.15). The result we obtain for the evolution of the abundance in the freeze-in scenario of a real scalar particle is shown in figure 2.3, which is obviously different from the freeze-out scenario displayed in figure 2.2: Initially, Y_{eq} is constant, such that in the freeze-in scenario the abundance Y increases. After the temperature T of the thermal bath has fallen below the mass of the real singlet scalar, the production channels for the real scalar singlet particle close due to the kinematics. From then on, the abundance Y of the singlet scalar reaches a plateau and remains constant. It is frozen-in. Our result is in accordance with [56]. Comparing our figure 2.3 with figure 1 of [56], our implementation and numerical treatment of the freeze-in scenario appears to be quite accurate. As figure 2.3 shows, the abundance Y reaches a plateau at a temperature $T \sim m_S$. For temperatures $T > 1\,\mathrm{TeV}$ the singlet scalar particle is relativistic for all the different cases. Therefore, $\langle\sigma v_r\rangle \sim T^2$ in equation (2.5.15). The equilibrium abundance Y_{eq} is independent of T for high temperatures, as explained above. From equation (2.5.15) it follows that $Y \propto 1/T$, as shown in the logarithmic plot of figure 2.3. For both singlet masses $m_S = 10\,\mathrm{GeV}$ and $m_S = 1\,\mathrm{GeV}$, the plateau is reached at $T \sim 10\,\mathrm{GeV}$, which is well below 100 GeV. At temperatures $T \sim 100\,\mathrm{GeV}$, $\langle\sigma v_r\rangle$ has a resonance for the fixed Higgs mass $m_H = 120\,\mathrm{GeV}$. We keep the value for the Higgs mass as given in [56]. The resonance increases $\langle\sigma v_r\rangle$, which is the reason why for the singlet masses $m_S = 10\,\mathrm{GeV}$ and $m_S = 1\,\mathrm{GeV}$, the abundance Y increases around $T \sim 100\,\mathrm{GeV}$, as already pointed out in [56]. For $m_S = 1\,\mathrm{GeV}$, the abundance does not increase until 1 GeV. The reason for this behavior is related to the dominant production channel of the singlet scalar, which is W^+W^- annihilation. W^+W^-, however, are not anymore in chemical equilibrium for temperatures well above $1\,\mathrm{GeV}$, which is also pointed out in [56]. We build on our

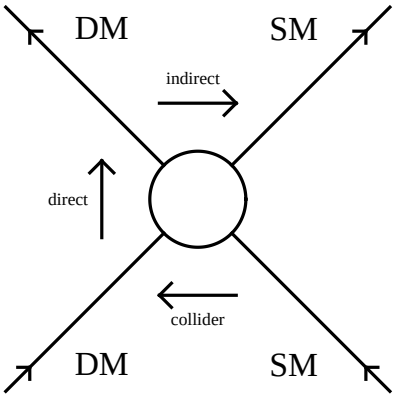

Figure 2.4.: Illuminating DM: Indirect detection experiments probe final SM products through DM s-channel annihilation. Direct detection experiments aim to observe the t-channel scattering of DM off SM nuclei. At colliders, DM could be produced through s-channel annihilation of SM particles.

numerics in chapter 4, where we study the production of keV sterile neutrinos by the decays of a frozen-in scalar.

In the model we consider, the abundance of a scalar singlet σ is produced by freeze-in mediated by the Higgs portal. When the singlet scalar is frozen in, it can in principle still scatter off particles that are in the thermal heat bath.

2.6. Detection of Dark Matter

We know that DM constitutes the major part of the matter of the Universe, however, we have not yet detected a DM particle. If one assumes that there is an interaction besides gravity between a DM particle and SM particles, then this interaction, whatever its underlying nature is, can be represented by a Feynman diagram that has as external legs the DM particle on the one side and SM particles on the other side, which are connected by a yet unknown interaction vertex. Depending on in which direction this representative diagram is read, one can distinguish between three possible methods of how to detect a DM particle if the interaction strength is strong enough, see figure 2.4. The s-channel read out represents annihilation of DM into SM particles. Through this channel, DM may be indirectly detected as an excess signal in cosmic rays. A possible DM signal in cosmic rays could also be expected from a decaying DM particle.

The difficulty off indirect DM searches is the lack of a complete understanding of the astrophysical sources for the production of cosmic rays. In that sense, a not completely understood or even an unknown astrophysical source could mimic a possible signal

expected from DM annihilations and/or decays. For example, the AMS-02 experiment precisely measured the positron fraction in primary cosmic rays in the energy interval $[0.5; 350]$GeV based on $6.8{\times}10^6$ positron and electron events [65]. The overall cosmic ray flux decreases with increasing particle energy. If all of the positrons observed in cosmic rays have the same origin as all of the other particles in cosmic rays, then the flux of the positron fraction should also decrease with increasing energy of the positrons. Instead, the AMS-02 experiment determined a steady increase of the positron fraction from 10 GeV to $\sim$ 250 GeV. This and other *observations show the existence of new physical phenomena, whether from a particle physics*, e.g., DM annihilation or decay, *or an astrophysical origin* [65]. Apart from that, if the DM annihilation or decay products are charged particles, they will be deflected in intergalactic magnetic fields, and thus the information about their production position will be lost.

The situation is better if DM dominantly annihilates or decays into photons, which do not experience any deflection in magnetic fields and can thus provide local information about the galactic DM distribution for which only fit-models exist. For a DM particle with a mass larger than 1 GeV, the produced photons contribute to gamma ray emission. The background for indirect DM searches in galactic gamma rays is the diffuse galactic gamma ray emission [66]. Known sources are cosmic ray nucleons interacting with the interstellar gas, Bremsstrahlung by cosmic ray electrons, inverse Compton scattering of cosmic ray electrons with low energy interstellar photons, π^0 decays into two photons and point sources like pulsars, which are also a source of high energetic electrons and positrons. However, there might be additional unknown sources.

Nevertheless, given DM particles were responsible for excesses in the energy spectra of gamma rays, the energy at which such an excess would be observed is directly correlated to the mass of the DM particle: for DM annihilations or direct decays into photons, the photons are monochromatic such that there will be the clear spectral signature of a line. If the DM particle decays into a photon γ and a particle X, the energy E_γ of the photon in the rest frame of the DM particle equals $E_\gamma = {}^{m^2_{\mathrm{DM}}-m^2_X}/_{2m_{\mathrm{DM}}} = {}^1/_2 \cdot m_{\mathrm{DM}}\,(1 - {}^{m^2_X}/_{m^2_{\mathrm{DM}}})$. For the DM annihilation process, one has to replace $m_{\mathrm{DM}} \to 2m_{\mathrm{DM}}$, i.e.,

$$E_\gamma = m_{\mathrm{DM}} \left(1 - \frac{m_X^2}{4m_{\mathrm{DM}}^2}\right) . \tag{2.6.1}$$

The t-channel read out makes the direct detection of DM possible if the interaction is strong enough. For example, a feebly interacting DM particle will probably not be detected directly.

The concept for direct detection of DM, which was already formed in 1985 by M. W. Goodman and E. Witten [67], is that a DM particle can scatter off a nucleus. The scattering process can be elastic or inelastic. Furthermore, the scattering can be spin-dependent or spin-independent, depending on whether the target nucleus has a net spin or not.

In spin-independent interactions, the mediated interaction particle between the DM and the nucleus interacts coherently with all the nucleons inside the nucleus. Hence, the cross section is enhanced by the squared mass number A^2 of the nucleus and thus the detection rate is larger for heavier nuclei.

For spin-dependent interactions, it has to be taken into account that the spins of the nucleons occupying the inner shells cancel in pairs.

If a DM particle of mass m_{DM} and velocity v_0 elastically scatters of a nucleus of mass m_A at rest, conservation of momentum yields a recoil velocity v_R for the nucleus given by $v_R = {}^{2m_{\mathrm{DM}}\cdot v_0}/_{(m_{\mathrm{DM}}+m_A)}$, and hence a recoil energy of:

$$E_R = \frac{2\mu_{\mathrm{DM}}^2}{m_A} v_0^2 \,, \tag{2.6.2}$$

with the reduced mass $\mu_{\mathrm{DM}} = {}^{m_{\mathrm{DM}}\cdot m_A}/_{m_{\mathrm{DM}}+m_A}$.

But, as in the indirect searches, a not well understood or not even known background can mimick a possible DM signal. For direct DM searches, the backgrounds can be better controlled than for indirect searches.

For $m_{\mathrm{DM}} = m_A \sim 100\,\mathrm{GeV}$ and $v_0 = 10^{-3}\,\mathrm{c}$, $E_R \sim 50\,\mathrm{keV}$. The nuclear recoil energy does depend by definition on the velocity of the colliding DM particle. The above expression fixes the minimal velocity v_{min} of a DM particle needed to reveal a nuclear recoil energy with an amount of E_R in an elastic scattering process:

$$v_{\mathrm{min}} = \frac{1}{\sqrt{2m_A E_R}} \left(\frac{m_A E_R}{\mu_{\mathrm{DM}}} \right) . \tag{2.6.3}$$

In an inelastic scattering process, the initial state DM particle is different from the final state DM particle. If the mass difference between the initial and the final state DM particle is δ, than the minimal velocity v_{min} of a DM particle needed to reveal a nuclear recoil energy with an amount of E_R equals:

$$v_{\mathrm{min}} = \frac{1}{\sqrt{2m_A E_R}} \left(\frac{m_A E_R}{\mu_{\mathrm{DM}}} + \delta \right) . \tag{2.6.4}$$

General inelastic scattering of DM has been discussed in [68], and inelastic scattering due to the magnetic moment interactions in ref. [69].

For our discussion, the relevant facts about inelastic DM scattering follow directly from equation (2.6.4): the higher the level of inelasticity δ in a scattering process is, the larger the minimal velocity becomes. For fixed δ, m_{DM} and E_R, the minimal velocity decreases for increasing nuclear masses up to 126 GeV, which is the mass of ${}^{136}_{54}\mathrm{Xe}$, see figure 2.5. The decisive point in DM direct detection experiments is that the velocity of the DM particles is distributed. To predict an event rate for a DM direct detection experiment, that is the number of counted signals in a given recoil energy interval, it

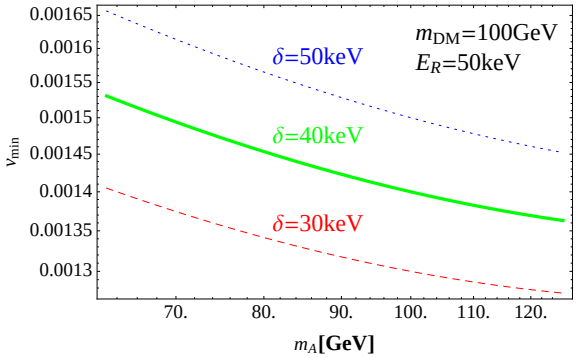

Figure 2.5.: Minimal velocity for a given DM mass of $m_{\mathrm{DM}} = 100\,\mathrm{GeV}$ and a recoil energy of $E_R = 50\,\mathrm{keV}$ as a function of the nuclear mass m_N. Three different choices for the level of inelasticity δ are shown.

is therefore necessarily to assume a velocity distribution for the DM particles. With a given velocity distribution of DM particles, the measurable recoil energy of a nucleus with a specific mass then determines the mass of the DM particle.

All direct detection experiments are designed for measuring this nuclear recoil energy. The various experiments distinguish in the read out of the nuclear recoil energy. Current techniques are based on the read out of phonons in crystals excited by the recoil energy like the CRESST I experiment [70], of light like the DAMA/LIBRA experiment [71] and of charges using p-type point contact Germanium detectors like CoGeNT [72]. Beyond that, several experiments combine two of these read out techniques. For example, the XENON100 experiment [73] and the KIMS experiment [74] use the read out of light and charges. The CDMS experiment [75] reads out phonons and charges.

In this thesis, we compare the predictions of our models for DM direct detection with data from the experiments DAMA, KIMS and XENON100 in section 3.2, and CDMS and XENON100 in section 3.4.5. These experiments are described in dedicated sections.

Reading the s-channel in figure 2.4 from the opposite direction leads to the possible creation of DM at colliders, where the DM particle may show up as missing transverse energy. From the reconstructed missing energy, the mass of a DM particle, if it is the particle that produces the missing energy, can be determined. Again, the difficulty is that one wants to detect something, here a weakly interacting DM particle, which does not leave its tracks directly in the detectors. In indirect DM searches, final state products in cosmic rays are the judges over the nature of DM, although other astrophysical sources could generate the detectable final products as well. In the DM direct detection experiments, it is the read out of nuclear recoil energy that might be produced by the DM particle and then used to pin down a DM particle, although backgrounds or other

sources could produce the same amount of nuclear recoil energy. In a collider experiment, there could be other particles than DM be produced beyond the SM particles, which would also only show up as missing energy.

To really claim the detection of a DM particle, the three possible methods have to be combined. If the mass inferred from the energy spectrum of cosmic rays in DM indirect detection experiments, the mass inferred from the nuclear recoil energy in DM direct detection experiments and the mass inferred from the missing energy at DM creation experiments all agree with each other, then the particle produced at a collider might be indeed the particle that makes up the DM of the Universe, see, e.g., [76].

The three possible detection methods are directly related to each other in models with a Higgs portal. The portal coupling constant λ controls the s-channel annihilation of DM particles and thus is responsible for a possible signal in indirect detection experiments. Besides, the Higgs portal in the t-channel realizes spin-independent nuclear scattering cross sections and it can therefore give a signal in direct detection experiments. In addition, at colliders, the Higgs portal in the s-channel can create DM particles.

In the following subsections we will address each of the three detection possibilities. All of these detection possibilities rely on the fact that there is a distribution of DM particles in our Galaxy. Therefore, before addressing each of the three detection possibilities in the following subsection, one first has to specify the actual distribution of DM particles. To do so, the Universe is simulated as an ΛCDM Universe. In that framework, large N-body simulations produce DM halos of galaxies that depend on the DM density profiles $\rho(r)$. Simulating several systems ranging from dwarf galaxies to galaxy clusters, J. F. Navarro, C. S. Frenk and S. D. M. White (NFW) obtained the following fit to the DM density profile [77]:

$$\frac{\rho(r)}{\rho_c} = \frac{\delta_c}{\frac{r}{r_s}\left(1+\frac{r}{r_s}\right)^2}\,, \tag{2.6.5}$$

where ρ_c is the critical density of the Universe, see equation (2.3.8), δ_c is a dimensionless parameter characterizing the overdensity of the halo and r_s is the scale radius of the halo, which for our Galaxy equals $r_s = 20\,\mathrm{kpc}$.

The NFW profile leads to a smooth distribution of DM particles in the simulated halos. The quantity $\rho_{\mathrm{crit}}\delta_c$ is determined by fixing the DM density $\rho(r_\odot)$ at the Solar distance $r_\odot = 8.4\,\mathrm{kpc}$ from the Galactic center. For the NFW profile, a determination yields $\rho(r_\odot) = 0.389 \pm 0.025\,\mathrm{GeVcm}^{-3}$ [78], whereas a model independent analysis yields $\rho(r_\odot) = 0.430 \pm 0.113 \pm 0.096\,\mathrm{GeVcm}^{-3}$ [79].

2.6.1. Indirect Detection

The best chance to detect DM particles indirectly in cosmic rays is the annihilation of DM particles into a photon γ and a particle X. The final state photons would show up

as a monochromatic line signature above the diffuse gamma ray background.

The photon flux Φ_γ per photon energy E_γ is written as [80]

$$\frac{d\Phi_\gamma}{dE_\gamma} = \frac{1}{8\pi}\frac{\langle\sigma v\rangle}{m_{DM}^2}\frac{dN_\gamma}{dE_\gamma} r_\odot \rho(r_\odot)^2 J\,. \tag{2.6.6}$$

$\langle\sigma v\rangle$ is the partial cross section for the annihilation of a DM particle, m_{DM}^2 is the mass of the DM particle, ${}^{dN_\gamma}/_{dE_\gamma}$ is the photon energy spectrum, $\rho(r_\odot)$ is the DM density at the Solar distance $r_\odot = 8.4\,\mathrm{kpc}$ from the Galactic center and J is the integral over the region of interest expressed in galactic coordinates:

$$J = \int db \int dl \int \frac{ds}{r_\odot}\,\cos b \left(\frac{\rho(r)}{\rho_\odot}\right)^2\,. \tag{2.6.7}$$

Here, b is the Galactic latitude, l is the Galactic longitude, s is the line of sight and r is the distance from the Galactic center, which equals $r^2 = r_\odot^2 + s^2 - 2r_\odot^2 s\cos b\cos l$.

The dependence of the photon flux on the DM density to the power of two is characteristic for DM annihilations, because two DM particles are in the initial state. For DM decay, only one DM particle is in the initial state and the photon flux depends linearly on the DM density.

The photon energy spectrum follows to be:

$$\frac{dN_\gamma}{dE_\gamma} = N_\gamma \delta\left(E_\gamma - m_{\mathrm{DM}}\left(1 - \frac{m_X^2}{4m_{DM}^2}\right)\right)\,, \tag{2.6.8}$$

with $N_\gamma = 2$ (1) if $X = \gamma$ ($X \neq \gamma$).

In its 3.7 years of data taking the *Fermi* Large Area Telescope did not find any globally significant lines in their search regions, which translates into limits for the DM annihilation cross section into photons. The limits for the DM annihilation cross section into two photons times velocity are in the range $(10^{-29} - 10^{-27})\,\mathrm{cm^3 s^{-1}}$, depending on the DM mass and on the DM density profile assumed for the Milky Way [81] and thus by a factor of approximately 5–5000 smaller than the thermal average of the annihilation cross section times velocity needed to produce the correct amount of DM relic density by freeze-out, which equals $3 \times 10^{-26}\,\mathrm{cm^3 s^{-1}}$. In particular, with a global significance of only 1.6 σ for a line-like feature at a DM mass of 133 GeV, recent claims of a line-like feature at a DM mass near 130 GeV [82, 83] seem to be killed.

Given the above arguments, in particular possible and yet unknown astrophysical sources, we do not discuss the prospects for indirect detection of DM annihilations in the course of this thesis, but we do discuss direct detection.

2.6.2. Direct Detection

The event rate is written as:

$$\frac{dR}{dE_R} = \sum_{\text{nuclei}} \frac{\rho_\odot}{m_{\text{DM}}} \frac{1}{M_{\text{det}}} \int_{v>v_{\min}} \frac{d\sigma}{dE_R}\, v f_\oplus(\boldsymbol{v}) d^3v \,, \tag{2.6.9}$$

where $\rho_\odot \simeq 0.3\,\text{GeVcm}^{-3}$ is the local DM density, taken as the mean density of elementary particles trapped in the galactic gravitational field at the position of the Sun, M_{det} is the mass of target material. $v_{\min}$ is the minimum velocity required for DM to scatter off a nucleus with recoil energy E_R and $f_\oplus(\boldsymbol{v})$ is the local DM velocity distribution function in the rest frame of the Earth.

The matrix element of the DM-nucleus scattering cross section σ involves the expectation values $\langle n|\overline{q}\Gamma q|n\rangle$ of quark bilinear operators $\overline{q}\Gamma q$ inside a nucleon n. Under Lorentz transformation, these operators transform as scalar $\overline{q}q$, pseudo-scalar $\overline{q}\gamma_5 q$, vector $\overline{q}\gamma_\mu q$, axial-vector $\overline{q}\gamma_5\gamma_\mu q$ and tensor $\overline{q}\sigma_{\mu\nu}q$. Under charge conjugation, these operators are even, even, odd, even and odd, respectively. Note that, for a Majorana field that is even under charge conjugation, the odd operators vanish. As noted above, the present velocity v_0 of a DM particle is about three orders of magnitude smaller than the speed c of light, which justifies a non-relativistic approximation. In the non-relativistic limit, the vector operator transforms as a scalar and the tensor operator as an axial vector. In that limit, the remaining interactions are the scalar and the axial vector interactions. It is the axial vector interaction that contains the spin operator $\xi^\dagger\sigma_i\xi$ with ξ the two-component spinors and σ_i the Pauli matrices. We discuss effective scalar interactions in the model of section 3.4, and effective vector and tensor interactions, respectively, in the model of section 3.1. Therefore, in section 3.4, spin-independent interactions lead to DM direct detections, whereas in section 3.1, spin-independent and spin-dependent interactions contribute.

In [84], the effective DM direct detection cross sections resulting from scalar and axial vector interactions are calculated. For the scalar interaction, the matrix element of the operator $\overline{q}q$, where the light quarks $q = u, d, s$ enter with masses m_q, in a nucleon n with mass m_n is written as:

$$\langle n|m_q\overline{q}q|n\rangle = m_n f_q^{(n)} \,. \tag{2.6.10}$$

The nucleon parameters $f_q^{(n)}$ are associated with hadronic uncertainties in the computation of the pion-nucleon-sigma term $\sigma_{\pi n}$, that is $\sigma_{\pi n} = {}^1\!/_2\,(m_u + m_d)\,\langle n|\overline{u}u + \overline{d}d|n\rangle$, and of the quantity $\sigma_0 = {}^1\!/_2 \cdot (m_u + m_d)\,\langle n|\overline{u}u + \overline{d}d - 2\overline{s}s|n\rangle$, see [84] and [85]. In section 3.4, we use the values from table 2.5, which follow from $\sigma_{\pi n} = 55\,\text{MeV}$ and $\sigma_0 = 35\,\text{MeV}$. The contribution of the heavy quarks $Q = c, b, t$ is obtained in the heavy quark expansion:

$$\langle n|m_Q\overline{Q}Q|n\rangle = \frac{2}{27} m_n \left(1 - \sum_{q=u,d,s} f_q^{(n)}\right) . \tag{2.6.11}$$

	neutron$^{(n)}$	proton$^{(n)}$
f_u	0.018	0.023
f_d	0.042	0.033
f_s	0.26	0.26

Table 2.5.: Nucleon Parameters.

Equations (2.6.10) and (2.6.11) yield the effective scalar coupling $g_{S(n)}$ for DM spin-independent scattering on a nucleon n:

$$g_{S(n)} = \frac{m_n}{v}\left[\sum_{q=u,d,s} f_q^{(n)} + \frac{2}{27} m_n \left(1 - \sum_{q=u,d,s} f_q^{(n)}\right)\right], \tag{2.6.12}$$

see equation (3.4.67).

For the axial vector interaction, the matrix element of the operator $\overline{q}\gamma_\mu\gamma_5$ in a nucleon n is proportional to the spin of the nucleon. The differential cross section for spin-dependent DM scattering is proportional to [84]:

$$\frac{d\sigma}{dE_R} \propto \left(a_p\langle S_p\rangle + a_n\langle S_n\rangle\right)^2 \frac{J+1}{J} F^2(E_R)\,. \tag{2.6.13}$$

In equation (2.6.13), J is the total angular momentum of the nucleus. $\langle S_p\rangle = \langle N|S_p|N\rangle$ is the expectation value of the spin content of the proton group inside a nucleus N, and in analogy, $\langle S_n\rangle$ is the expectation value of the spin content of the neutron group. a_p and a_n are parametrization factors. The term in brackets in equation (2.6.13) corresponds to equation (3.2.11), where we also take the orbital angular momentum into account. $F^2(E_R)$ is a form factor. Form factors are discussed in detail in section 3.2.1.

In the rest frame of the Galaxy, the local DM velocity distribution follows from the DM density distribution and its phase-space density, which both depend on the Galactic gravitational potential. Taking the standard DM halo model in which the DM density distribution is an isotropic isothermal sphere and assuming that the Galactic gravitational potential is spherically symmetric, the local DM velocity distribution is the Maxwell–Boltzmann distribution [86] for velocities $v < v_{\text{esc}}$ and zero for velocities $v \geqq v_{\text{esc}}$ with the local escape velocity v_{esc}. v_{esc} is related to the local gravitational potential and set to $v_{\text{esc}} = 544\,\text{kms}^{-1}$. The Maxwell–Boltzmann distribution is normalized if the local velocity dispersion,

$$\sigma_v^2(r_\odot) = \int d^3v\,|\mathbf{v}|^2 f_{r_\odot}(\mathbf{v})\,, \tag{2.6.14}$$

equals $\sigma_v = \sqrt{3/2}v_0$, where $v_0 = 220\,\text{kms}^{-1}$ is the circular velocity at the position of the Sun assuming that the rotation curve of the Galaxy is flat down to the position of the Sun.

The velocities involved are smaller than the speed of light by a factor 10^{-3}, and therefore a coordinate transformation is well approximated by a non-relativistic Galilean transformation, which has to be applied from the DM velocity in the Galactic rest frame into the rest frame $\oplus$ of the Earth where the detector of a DM direct detection experiment is located. The underlying transformation reads: $f_\oplus(\mathbf{v}, v_e) = f(\mathbf{v}+v_e)$, where v_e is the velocity of the detector relative to the Galaxy taking into account the galactic rotation v_0, the mean velocity of the Sun relative to nearby stars, which we set equal to $12\,\mathrm{kms}^{-1}$, and the orbital velocity $v_{\mathrm{orb}} = 30\,\mathrm{kms}^{-1}$ of the Earth relative to the Sun [87]: $v_e = v_0{+}12\,\mathrm{kms}^{-1}{+}v_{\mathrm{orb}}\cos\gamma\cos\left[2\pi(t-t_0)/\mathrm{year}\right]$ with $\cos\gamma = 0.51$ and $t_0 =$ June 2nd. The measurable quantity depends on the product of the differential cross section, the DM velocity and the DM velocity distribution.

Since we will investigate differential cross sections that are independent of v and proportional to $1/v^2$, respectively, we must evaluate the following velocity integrals to predict the event rate:

$$\zeta_1(v_{\mathrm{min}}, v_e) = \int_{v_{\mathrm{min}}}^{\infty} d^3v\, \frac{f(\boldsymbol{v}+\boldsymbol{v}_e)}{v}, \tag{2.6.15}$$

$$\zeta_2(v_{\mathrm{min}}, v_e) = \int_{v_{\mathrm{min}}}^{\infty} d^3v\, v f(\boldsymbol{v}+\boldsymbol{v}_e). \tag{2.6.16}$$

The analytic formulas for the DM velocity integrals given in refs. [88, 89] are used.

The total predicted event rate in the DM direct detection experiments is obtained by integrating the differential event rate with respect to an appropriate recoil energy range. However, due to energy losses in the detection material, the nuclei in the detection materials do not transfer the total recoil energies into the measurable energies, i.e., the actual measured energies are only fractions of the incident transferred energies by the scattering process. These fractions are known as nuclear quenching factors, which were already discussed in [90].

In section 3.2, we compare the event rates predicted in a specific model with the data from the XENON100, DAMA, and KIMS direct detection experiments. The energy range and the quenching factors are taken from [74, 91, 92] and shown in Tab. 2.6. For XENON100 we use the same light-yield function L_{eff} as in ref. [91] that corresponds to an effective quenching factor.

DAMA

The DAMA experiment has 25 sodium-iodine crystals doped with thallium as detector material. They are arranged in five rows by five columns. Each crystal has a mass of 9.70 kg and a volume of $10.2 \times 10.2 \times 25.4\,\mathrm{cm}^3$. Each detector has two photomultiplier tubes at opposite sides [71].

A possible DM-NaI(TI)-scattering process can induce light emission after recoil of the nuclei of the crystals. Due to the photoelectric effect, photoelectrons are ejected. The photomultipliers measure the resulting electric charge, which is proportional to the recoil energy.

To obtain a model-independent result on the mass of the DM particle, the DAMA collaboration measures an annual modulation signal [93]. In fact, since the Earth orbits around the Sun and the Sun itself moves relative to the center of the Galactic rest frame, once a year on June 2nd, the orbital velocity of the Earth is parallel to the velocity of the Sun around the Galactic center. Then the flux of DM particles crossing the Earth should have a maximum. Hence, the event rate measured in the NaI(Tl) crystals should have a maximum. The DAMA collaboration claims to have measured such an annual modulation signal.

In the energy interval $[2; 6]$keV, the modulation amplitude is measured with an event rate of 0.0166 ± 0.0013 at a confidence level of 8.9σ [93]. Having investigated several sources that could also generate an annual modulation signal, the DAMA collaboration claims to have evidence for DM particles in our Galactic halo at 8.9σ confidence level.

KIMS

The KIMS experiment consists of an array of 3×4 cesium-iodine crystals that are doped with thallium. The crystals have a mass of 8.6 kg each and a volume of $8 \times 8 \times 30\,\mathrm{cm}^3$. To each crystal, two photomultiplier tubes are attached at opposite sides. Having also iodine as target material, the KIMS measurement is competitive to the DAMA measurement.

In the energy interval $[3.6; 5.8]$keV, the KIMS collaboration obtains an event rate for nuclear recoil events of 0.0098 counts day^{-1} kg^{-1} keV^{-1} at 90% confidence level [74].

CDMS

The CDMS experiment has 19 germanium and 11 silicon detectors. Each germanium detector has a mass of approximately 230 g, and each silicon detector has a mass of approximately 100 g [75]. The detectors are cooled to temperatures below 50 mK. On top of each detector, phonon sensors measure the recoil energy and position of a possible DM scattering event. In addition, the phonon sensors are used as reference for the ionization measurement.

$^{28}_{14}$Si is lighter than $^{72}_{32}$Ge; therefore the spin-independent scattering cross section, which is proportional to the squared mass number A^2 of the nucleus, is enhanced for germanium relative to silicon.

In section 3.4.5 we use the data detected by 14 germanium detectors with a total exposure of 612 kg-days, which set the upper limit on the DM-nucleon elastic-scattering spin-independent cross section of $7.0 \times 10^{-44}\,\mathrm{cm}^2$ for a DM mass of 70 GeV at 90%

	Energy range	Quenching factor
XENON100	$8.4 - 44.6\,\text{keV}$	L_{eff}
KIMS	$3.6 - 5.8\,\text{keV}$	0.1 (Cs), 0.1 (I)
DAMA	$2 - 8\,\text{keV}$	0.3 (Na), 0.09 (I)

Table 2.6.: The energy range and the quenching factor for the experiments XENON100, KIMS and DAMA.

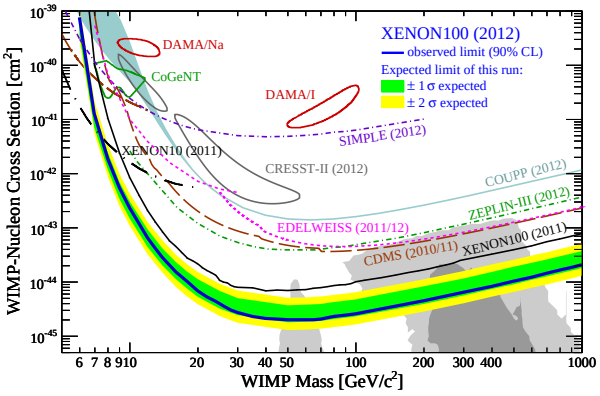

Figure 2.6.: Limit on the spin-independent WIMP-nucleon scattering cross section from XENON100. The green and yellow bands show the expected sensitivity at 1σ and 2σ, respectively. The resulting exclusion limit at 90% confidence level is shown in blue. Other experimental limits are shown for comparison.

confidence level.

XENON100

The XENON experiment is a two phase time projection chamber, which is almost cylindrical with a height of 30.5 cm and a radius of 15.3 cm. The time projection chamber contains 62 kg of liquid xenon. On the bottom, the time projection chamber is closed by a cathode below which an array of photomultiplier tubes is installed. On top of the time projection chamber, there is a gate grid. Cathode and gate grid generate an electric drift field. Above the gate grid, there is a liquid gas interface followed by a gaseous phase of xenon. An anode with a stronger electric field than the gate grid is placed a few mm above the liquid gas interface. At the top end cap of the chamber, xenon is present in the gaseous phase. The top end of the whole detector is closed by an array of photomultiplier tubes. The coordinate system to locate the interaction point has its z-axis aligned along the electric drift field. The brief description of the geometry of the XENON detector as

well as the following details on the signal read-out are taken from [73].

The melting point of xenon is $-111.7\,^{\circ}\mathrm{C}$ and its boiling point is $-108.12\,^{\circ}\mathrm{C}$, both referring to a pressure of 1.01325 bar. With an atomic mass number of 54 and a density of $3\,\mathrm{g cm}^{-3}$, liquid xenon is very efficient in stopping radiation. Being liquid, it is not an expensive task to stop radiation in a large and homogeneous volume of liquid xenon. Experiments based on crystals like sodium-iodine or semiconductors such as germanium have to face engineering and economic problems when operating on relatively large and homogeneous volumes. Compared to other liquid rare gases, liquid xenon has the highest ionization and scintillation yield.

It is a unique feature of liquid rare noble gases to produce both charged particles and scintillation photons in response to radiation. In liquid xenon, the scintillation photons have a wavelength centered around 177.6 nm. These photons are emitted when the excited dimer Xe_2^* decays into the ground state:

$$\mathrm{Xe}_2^* \longrightarrow 2\,\mathrm{Xe} + \gamma\,. \tag{2.6.17}$$

Xe_2^* is created directly through excitation of atoms and indirectly through electron-ion recombination.

In liquid xenon, isotopes with an even number of neutrons can be found, i.e., ${}^{124}_{54}\mathrm{Xe}$, ${}^{126}_{54}\mathrm{Xe}$, ${}^{128}_{54}\mathrm{Xe}$, ${}^{130}_{54}\mathrm{Xe}$, ${}^{132}_{54}\mathrm{Xe}$, ${}^{134}_{54}\mathrm{Xe}$ and ${}^{136}_{54}\mathrm{Xe}$, as well as isotopes with an odd number of neutrons, i.e., ${}^{129}_{54}\mathrm{Xe}$ and ${}^{131}_{54}\mathrm{Xe}$. Therefore, liquid xenon can probe spin-dependent and spin-independent interactions. The listed features of liquid xenon are extracted from [94].

Typically, when a possible weakly interacting massive particle scatters off a xenon nucleus from the liquid xenon inside the time projection chamber, a prompt scintillation signal S1 is generated during the nuclear recoil when a xenon atom is excited to the dimer Xe_2^*. S1 is detected by the photomultiplier tubes at the bottom of the time projection chamber. In the scattering process, xenon atoms are also ionized. The resulting free electrons drift through the liquid xenon to the gate grid. The anode above the gate grid with its stronger electric field extracts the electrons into the gaseous phase where the proportional light signal S2 is generated. S2 is detected in the top array of photomultiplier tubes. Knowing the drift velocity of the electrons, the time between the detection of S1 and S2 yields the z-coordinate of the interaction point. The x- and y-coordinates can be inferred from the single photomultiplier tubes in the array that detected a light signal for the scattering process under consideration.

The current analysis is based on a data set corresponding to 224.6 live days$\times$34 kg exposure [95] . There are no evidences on DM interactions. The exclusion limit on the spin-independent DM-nucleon scattering cross section is taken from [95] and shown in figure 2.6. The limit on the spin-independent DM-nucleon scattering cross section is $2 \times 10^{-45}\,\mathrm{cm}^2$ for a DM mass of 55 GeV at 90% confidence level. At the time when we made predictions on the DM direct detection possibilities in the models we present in chapter 3, we had to rely and on data sets with less exposure time. In section 3.1 we use

the data set corresponding to 100.9 live days×48 kg exposure [91]. At that time, the limit on the spin-independent DM-nucleon scattering cross section was $7 \times 10^{-45}\,\mathrm{cm}^2$ for a DM mass of 50 GeV at 90% confidence level. We account for the increase of sensitivity in direct detection by presenting the planned sensitivity of XENON1T [96], see figure 3.9. In section 3.4 we use the data set corresponding to 11.17 live days×40 kg exposure [97]. At that time, the limit on the spin-independent DM-nucleon scattering cross section was $3.4 \times 10^{-44}\,\mathrm{cm}^2$ for a DM mass of 55 GeV at 90% confidence level. We can simply make a prediction on the cross section without being in conflict with the present bounds, because we can always make the relevant mixing angle small, see figure 3.11.

2.6.3. Collider Production

Although DM particles could be directly pair created in proton-proton collisions, they are invisible to the detectors, which only measure electromagnetic and hadronic interactions. Nevertheless, events in which DM particles are pair produced could be detected if there is an additional SM particle emerging from initial-state radiation. For example, in the collision of an up quark with an anti-down quark, a pair of DM particles could be produced that will not be directly detectable in the detectors. However, if the initial up quark or the anti-down quark radiates off a W^+ gauge boson, than the calorimeters could measure the energy of the W^+ decay products. The missing transverse momentum from the not directly detected DM particles can then be reconstructed from the center-of-mass energy and the measured energies of the W^+ decay products. The search for DM pair production in events with a hadronically decaying W or Z boson and missing transverse momentum in proton-proton collisions is reviewed in [98]. The data analysis is based on data recorded with the ATLAS detector corresponding to $20.3\,\mathrm{fb}^{-1}$ at $\sqrt{s} = 8\,\mathrm{TeV}$. The data very well agree with the estimated backgrounds and are thus consistent with the SM expectations.

2.7. Neutrinos Have Mass and the Universe Has Dark Matter

As outlined above, neutrino masses and DM in the Universe in form of a new particle are two very interesting but yet unresolved problems in particle physics.

Experiments have proven their existence and thus have directly born the younger generation of particle physicist into the doorway of physics beyond the SM. Precision measurements in the neutrino and in the DM sectors have already led to the discoveries of their main characteristics, respectively, and therefore we already have entered into the realm of non-standard physics.

Believing in the present and future experimental development, it is thus very well motivated to study further neutrino masses and DM. The investigations in this thesis combine neutrino masses and DM, providing a common framework.

Part I.

Radiative Neutrino Masses and Frozen-Out Dark Matter

3. Neutrino Masses at Loop-Level Connected to Dark Matter

In section 2.2, we have advertised neutrino mass generation at the loop level. If one assumes that the Yukawa coupling constants $y_{\alpha i}$ of the terms

$$y_{\alpha i}\,\overline{L_\alpha}\,H\,N_i + \text{h.c.} \tag{3.0.1}$$

in equation (2.2.12) are of order one, then the Majorana mass scale M_M in leading order type-I seesaw has to be as large as $M_M \sim 10^{14}\,\text{GeV}$. Such a high scale is needed to generate light neutrino masses of order 0.1 eV according to the seesaw mass matrix

$$m_\nu = -m_D M_M^{-1} m_D^T\,, \tag{3.0.2}$$

see equation (2.2.11) for further discussion.

In terrestrial experiments, energies of the order of $10^4\,\text{GeV}$ are accessible. To probe nevertheless directly the scale needed for neutrino masses, one could force the relevant Yukawa couplings to be as tiny as 10^{-6}, which would decrease M_M to an accessible order of $M_M \sim 10^3\,\text{GeV}$. However, one may wonder about the origin of such tiny Yukawa couplings.

A way out of correctly matching a Yukawa coupling constant and Majorana mass in type-I seesaw mechanism could be to think about neutrinos being massless at tree level. The light mass scale could then be explained by loop effects. In addition, loops can naturally combine the light neutrino mass generation with DM physics.
In this chapter, we study frameworks that simultaneously explain light neutrino masses by radiative mass mechanisms and DM by freeze-out of a stable particle. We consider models at the one-loop and two-loop level. Even at three-loop level, there is an available model discussed by Krauss et al. [99] and by Aoki et al. [100], which, however, is beyond the scope of this thesis.

We start in section 3.1 by reviewing the Ma-model [101], which generates light neutrino masses at the one-loop level. Despite the leptophilic nature of the DM with no direct couplings to quarks and gluons, scattering with nuclei is induced at the one-loop level through photon exchange, for which we explore for the first time in literature the expected event rate in DM direct detection experiments.

This section is the result of the work based on collaboration with Thomas Schwetz and Takashi Toma. The subsequent publication is [102], of which the author of the present thesis is a co-author. The author of the present thesis contributed to the calculation of the DM relic density, the DM direct detection, effects of θ_{13} and was partly involved in the loop integration.

Next we review the Zee–Babu-model [103], which generates light neutrino masses at two-loop level. Although the scale of new physics is at the accessible TeV range due to two loop suppression factors and relative small coupling constants in the loops, the drawback of this model is the introduction of a lepton number violating trilinear scalar term by hand with a dimensionful coupling constant μ, see equation (3.4.5). In the SM, the dimensionful coupling constant μ_H^2 is fixed by spontaneous symmetry breaking such that the symmetry breaking scale is the remaining physical scale, see equation (2.1.4). Motivated by the demand that any new physical scale beyond the SM should arise dynamically from the general concept of spontaneous symmetry breaking, the original Zee–Babu-model is augmented by a scalar $SU(2)_L$ singlet in section 3.4.1 such that the potential enjoys a global $U(1)_{B-L}$ symmetry. It is then the spontaneous symmetry breaking of the global symmetry that generates dynamically the trilinear term needed for neutrino masses. In order to obtain a DM particle we introduce two SM fermion $SU(2)_L$ singlets. Neutrino masses and DM are then related by the global $U(1)_{B-L}$ symmetry; most noticeably, a remnant $\mathbb{Z}_2$ symmetry automatically guarantees the stability of the DM particle. The DM phenomenology of the model is discussed and similar models based on a gauged $U(1)_{B-L}$ symmetry are commented on.

The work done in collaboration with Manfred Lindner and Thomas Schwetz added up to this section. The subsequent publication is [104], of which the author of the present thesis is the corresponding author. The author of the present thesis determined the mass spectrum of the model, calculated the annihilation cross sections and direct detection cross section.

3.1. One-Loop Example: The Ma-Model

3.1.1. Neutrino Masses and Mixing

At one-loop level, a very well studied model to generate neutrino masses radiatively is the model proposed by E. Ma in 2006 [101]. It represents a mechanism to realize the dimension-five Weinberg operator at one-loop level.

The particles beyond the particle content of the SM are three right-handed neutrinos N_i $(i = 1, 2, 3)$ and one scalar $SU(2)_L$ doublet η. In addition to the SM gauge group there is a $\mathbb{Z}_2$ symmetry under which the new particles change sign and the SM particles transform trivially. The $\mathbb{Z}_2$ charges are assigned such that the right-handed neutrinos N_i

only have Yukawa couplings with the scalar $SU(2)_L$ doublet η. Yukawa couplings of η to SM fermions are forbidden, thus η is called an inert $SU(2)_L$ doublet.

The new invariant Lagrangian expressed in Dirac spinors is:

$$\mathcal{L}_N = \overline{N_i} i\partial\!\!\!/ P_R N_i + (D_\mu \eta)^\dagger (D^\mu \eta) - \frac{1}{2} M_i \overline{N_i{}^c} P_R N_i + h_{\alpha i} \overline{L_\alpha} \tilde{\eta} P_R N_i + \text{h.c.}\,, \tag{3.1.1}$$

and the scalar potential V_{scalar} is:

$$\begin{aligned} V_{\text{scalar}} =& m_H^2 H^\dagger H + m_\eta^2 \eta^\dagger \eta + \frac{1}{2}\lambda_1 \left(H^\dagger H\right)^2 + \frac{1}{2}\lambda_2 \left(\eta^\dagger \eta\right)^2 \\ &+ \lambda_3 \left(H^\dagger H\right)\left(\eta^\dagger \eta\right) + \lambda_4 \left(H^\dagger \eta\right)\left(\eta^\dagger H\right) + \frac{1}{2}\lambda_5 \left(\left(H^\dagger \eta\right)^2 + \text{h.c.}\right)\,, \end{aligned} \tag{3.1.2}$$

where H is the SM Higgs $SU(2)_L$ doublet and $\tilde{\eta} = i\sigma_2 \eta^*$. This is the most general $SU(2)_L \times U(1)_Y$ gauge invariant renormalizable scalar potential for two $SU(2)_L$ doublets that also enjoys the discrete $\mathbb{Z}_2$ symmetry introduced above.

The symmetry breaking pattern of this potential with all of the possible combinations of the two vacuum expectation values being zero or different from zero, respectively, was analyzed in [105].

In the following, the vacuum expectation value $\langle \eta \rangle$ of η is assumed to be zero, so that the discrete $\mathbb{Z}_2$ symmetry is an unbroken symmetry of the vacuum state.

The combination $\langle H \rangle = {}^1\!/\!_{\sqrt{2}} \cdot v \neq 0$ and $\langle \eta \rangle = 0$ is one of the four combinations analyzed in [105]. Because $\langle \eta \rangle = 0$, Dirac neutrino masses are not generated through the Yukawa couplings in equation (3.1.1), and neutrinos remain massless at tree level.

We parametrize the SM Higgs $SU(2)_L$ doublet H and the inert $SU(2)_L$ doublet η in the unitary gauge as:

$$H = \begin{pmatrix} 0 \\ \frac{1}{\sqrt{2}}(v+h) \end{pmatrix}\,, \quad \eta = \begin{pmatrix} \eta^+ \\ \eta_{\text{R}}^0 + i\eta_{\text{I}}^0 \end{pmatrix}\,, \tag{3.1.3}$$

see equation (2.1.3). The mass eigenvalues of the potential are then:

$$m^2(h) = \frac{1}{4}\lambda_1 v^2\,, \tag{3.1.4}$$

$$m^2\left(\eta^\pm\right) = m_\eta^2 + \frac{1}{2}\lambda_3 v^2\,, \tag{3.1.5}$$

$$m^2\left(\eta_{\text{R}}^0\right) = m_\eta^2 + \frac{1}{2}\left(\lambda_3 + \lambda_4 + \lambda_5\right) v^2\,, \tag{3.1.6}$$

$$m^2\left(\eta_{\text{I}}^0\right) = m_\eta^2 + \frac{1}{2}\left(\lambda_3 + \lambda_4 - \lambda_5\right) v^2\,. \tag{3.1.7}$$

The addition of three right-handed neutrinos N_i $(i = 1, 2, 3)$ to [105] then allows for radiative neutrino masses, see figure 3.1. The relevant couplings that enter into the

neutrino mass generation are the Yukawa couplings $h_{\alpha i}$ of the inert Higgs $SU(2)_L$ doublet η and the scalar coupling λ_5.

The amplitude for the diagram in figure 3.1 equals:

$$i\mathcal{M} = h_{\alpha i} h^{\dagger}_{\beta i} \int \frac{d^d k}{(2\pi)^d} P_R \frac{\not{p} + \not{k} + M_i}{(p+k)^2 - M_i^2} P_R \frac{i}{k^2 - m^2(\eta^0)} \,. \tag{3.1.8}$$

Here and in the following a summation over the index i is implied.

$m^2(\eta^0)$ represents the mass eigenvalue of either the real or the imaginary part of η^0. We will point out the distinction between $m^2(\eta^0_{\mathrm{R}})$ and $m^2(\eta^0_{\mathrm{I}})$ where needed.

With the projection operator P_R of the right-handed Majorana neutrino N_i involved in the loop integral in equation (3.1.8), one sees that only the mass M_i in the numerator contributes because $P_R(\not{p} + \not{k})P_R = (\not{p} + \not{k})P_L P_R = 0$.

We obtain the denominator of the one-loop integral in Feynman parametrization:

$$\frac{1}{\{x[(p+k)^2 - M_i^2] + (1-x)(k^2 - m^2(\eta^0))\}^2} \,. \tag{3.1.9}$$

We define $k' \equiv k + xp$ and $\overline{\Lambda_i} = (M_i^2 - m^2(\eta^0))x + m^2(\eta^0)$. We neglect the light neutrino mass p^2 in equation (3.1.9) as well as in the numerator of the one-loop integral. The one-loop integral in $d = 4$ dimensions can now be calculated:

$$\int_0^1 dx \int \frac{d^d k'}{(2\pi)^d} \frac{M_i}{(k'^2 - \overline{\Lambda_i})^2} \tag{3.1.10}$$

$$= -\frac{M_i}{16\pi^2} \int_0^1 dx \, \log \frac{\overline{\Lambda_i}}{M_i^2} \tag{3.1.11}$$

$$= -\frac{M_i}{16\pi^2} \int_0^1 dx \, \log[(1-a_i)x + a_i] \,; \quad a_i \equiv \frac{m^2(\eta^0)}{M_i^2} \,. \tag{3.1.12}$$

The exchange of the real part of η in the loop gives:

$$\frac{M_i}{16\pi^2} \left(1 + \frac{m^2(\eta^0_{\mathrm{R}})}{M_i^2 - m^2(\eta^0_{\mathrm{R}})} \log \frac{m^2(\eta^0_{\mathrm{R}})}{M_i^2} \right) \,. \tag{3.1.13}$$

The exchange of the imaginary part of η in the loop gives:

$$-\frac{M_i}{16\pi^2} \left(1 + \frac{m^2(\eta^0_{\mathrm{I}})}{M_i^2 - m^2(\eta^0_{\mathrm{I}})} \log \frac{m^2(\eta^0_{\mathrm{I}})}{M_i^2} \right) \,. \tag{3.1.14}$$

Both contributions yield

$$i\mathcal{M} = P_R (m_\nu)_{\alpha\beta} \tag{3.1.15}$$

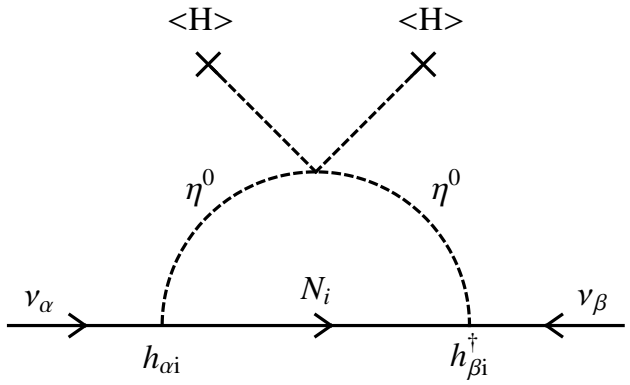

Figure 3.1.: Radiative neutrino mass generation at one-loop level.

with the effective neutrino mass:

$$(m_\nu)_{\alpha\beta} = h_{\alpha i} h^\dagger_{\beta i} \frac{M_i}{16\pi^2} \left(\frac{m^2(\eta^0_{\mathrm{R}})}{M_i^2 - m^2(\eta^0_{\mathrm{R}})} \log \frac{m^2(\eta^0_{\mathrm{R}})}{M_i^2} - \frac{m^2(\eta^0_{\mathrm{I}})}{M_i^2 - m^2(\eta^0_{\mathrm{I}})} \log \frac{m^2(\eta^0_{\mathrm{I}})}{M_i^2} \right) . \tag{3.1.16}$$

Since $m^2(\eta^0_{\mathrm{R}}) - m^2(\eta^0_{\mathrm{I}}) = \lambda_5 v^2$ and assuming $\lambda_5 v^2 \ll m_0 \equiv {}^{m^2(\eta^0_{\mathrm{R}}) + m^2(\eta^0_{\mathrm{I}})}/_2$, the final result for the radiatively generated neutrino mass is:

$$(m_\nu)_{\alpha\beta} = \frac{\lambda_5 v^2}{8\pi^2} h_{\alpha i} h^\dagger_{\beta i} \frac{M_i}{m_0^2 - M_i^2} \left(1 - \frac{M_i^2}{m_0^2 - M_i^2} \log \frac{m_0^2}{M_i^2} \right) . \tag{3.1.17}$$

For convenience, we define:

$$\Lambda_i \equiv \frac{2\lambda_5 v^2}{(4\pi)^2 M_i} \left(1 - \frac{M_i^2}{m_0^2 - M_i^2} \log \frac{m_0^2}{M_i^2} \right) , \tag{3.1.18}$$

which allows us to write:

$$(m_\nu)_{\alpha\beta} = h_{\alpha i} h^\dagger_{\beta i} \frac{M_i^2}{m_0^2 - M_i^2} \Lambda_i \, . \tag{3.1.19}$$

The assumption of a small coupling λ_5 is reasonable [106], since in the limit of $\lambda_5 \longrightarrow 0$, the symmetry of the model would increase; the model would enjoy a $U(1)$ symmetry.

If one assumes the tri-bimaximal structure of the PMNS matrix at leading order, i.e., $\theta_{12} = \sin^{-1}({}^1/\sqrt{3})$, $\theta_{23} = 45°$, $\theta_{13} = 0°$ and $\delta = 0$, equation (2.2.17) simplifies to:

$$\mathbf{U}_{\mathrm{tri}} = \begin{pmatrix} c_{12} & s_{12} & 0 \\ -\frac{s_{12}}{\sqrt{2}} & \frac{c_{12}}{\sqrt{2}} & \frac{1}{\sqrt{2}} \\ \frac{s_{12}}{\sqrt{2}} & -\frac{c_{12}}{\sqrt{2}} & \frac{1}{\sqrt{2}} \end{pmatrix} . \tag{3.1.20}$$

We diagonalize the effective neutrino mass matrix $(m_\nu)_{\alpha\beta}$ with $\mathbf{U}_{\text{tri}}$, i.e.:

$$\text{diag}\,(m_1, m_2, m_3) = \mathbf{U}_{\text{tri}}^\dagger (m_\nu)_{\alpha\beta} \mathbf{U}_{\text{tri}}^* \,. \tag{3.1.21}$$

The Yukawa couplings are written as: $h_{\alpha i} = |h_{\alpha i}| e^{i\varphi_i}$, with φ_i the phases, α the flavor ($\alpha = e, \mu, \tau$) and i the right-handed neutrinos ($i = 1, 2, 3$). The following conditions [107] result from equation (3.1.21):

$$\begin{aligned} &\sum_{i=1}^{3} (2h_{ei}^2 \sin 2\theta_{12} + 2\sqrt{2} h_{ei}(h_{\mu i} - h_{\tau i}) \cos 2\theta_{12} \\ &\quad - (h_{\tau i} - h_{\mu i})^2 \sin 2\theta_{12}) = 0 \end{aligned} \tag{3.1.22}$$

$$\sum_{i=1}^{3} h_{ei}(h_{\mu i} + h_{\tau i}) = 0 \tag{3.1.23}$$

$$\sum_{i=1}^{3} (h_{\mu i} - h_{\tau i})(h_{\mu i} + h_{\tau i}) = 0 \,.. \tag{3.1.24}$$

We realize these conditions by choosing $h_{\alpha i}$ equal to:

$$h_{\alpha i} = \begin{pmatrix} 0 & 0 & h_3' \\ h_1 & h_2 & h_3 \\ h_1 & h_2 & -h_3 \end{pmatrix} \tag{3.1.25}$$

implying that $\tan\theta_{12} = {}^1\!/\!_{\sqrt{2}} \cdot {}^{h_3'}\!/\!_{h_3}$. In a section below, we analyze the effects of the recently confirmed measurement of $\sin\theta_{13} \neq 0$. We take $\sin\theta_{13} = 0$ at leading order. In our analysis, we use the fit value $\sin^2\theta_{12} = 0.312^{+0.017}_{-0.015}$ [108]. It then follows ${}^{h_3'}\!/\!_{h_3} \approx 0.95^{+0.038}_{-0.033}$. Using the global fit value for $\sin^2\theta_{12}$ given table 2.1, we obtain ${}^{h_3'}\!/\!_{h_3} \approx 0.93^{+0.029}_{-0.026}$, i.e., within the error bars there is no significant change in the value for ${}^{h_3'}\!/\!_{h_3}$. The special form for the Yukawa couplings is discussed in [107]. It leads to one vanishing neutrino mass eigenvalue. Therefore, the measured differences of squared neutrino mass eigenvalues directly corresponds to the actual neutrino mass eigenvalues.

Neutrino masses are given in terms of the model parameters as follows:

$$|(h_1^2 + h_2^2)\Lambda_1| \simeq \frac{\sqrt{\Delta m^2_{\text{atm}}}}{2} \tag{3.1.26}$$

$$|h_3^2 \Lambda_3| \simeq \frac{\sqrt{\Delta m^2_{\text{sol}}}}{3} \,, \tag{3.1.27}$$

where use $\Delta m^2_{\text{atm}} = 2.50 \times 10^{-3}\,\text{eV}^2$ and $\Delta m^2_{\text{sol}} = 7.59 \times 10^{-5}\,\text{eV}^2$ for the differences of squared neutrino mass eigenvalues.

Again, the differences relative to the values given in table 2.1 are not severe. The mass difference of N_1 and N_2 is neglected.

From equations (3.1.18), (3.1.26) and (3.1.27), we can estimate the required sizes for the couplings h_i and λ_5. Assuming $(1 - {}^{M_i^2}/_{m_0^2 - M_i^2} \cdot \log {}^{m_0^2}/_{M_i^2}) \sim 1$ and $h_1 \sim h_2 \sim h_3 \equiv h_i$, and taking into account that $v \sim 0.05$ eV $\times\, 2 \times 10^{12}$, we obtain:

$$\frac{\lambda_5\, h_i^2}{10^{-11}} \sim \frac{M_i}{v} \left(\frac{\sqrt{\Delta m^2_{\text{atm}}}}{0.05\,\text{eV}} \right) . \tag{3.1.28}$$

Since h_i controls the DM relic density, and can therefore not be too small, λ_5 has to be tiny in order to obtain correct neutrino masses.

As will be discussed later, we impose the perturbativity condition $|h_i| < 1.5$ for the Yukawa couplings.

3.1.2. Lepton Flavor Violation

The Yukawa coupling

$$h_{\alpha i} \overline{L_\alpha} \eta^\dagger P_R N_i + \text{h.c.} \tag{3.1.29}$$

induces LFV decays at one loop level. Limits on lepton flavor violating decays then impose further constraints on the model parameters.

The branching ratios (BR) for lepton flavor violating processes $L_\alpha \longrightarrow L_\beta \gamma$ equal:

$$BR(L_\alpha \longrightarrow L_\beta \gamma) \equiv \frac{\Gamma(L_\alpha \longrightarrow L_\beta \gamma)}{\Gamma_{tot}} \tag{3.1.30}$$

$$= \frac{\Gamma(L_\alpha \longrightarrow L_\beta \gamma)}{\Gamma(L_\alpha \longrightarrow L_\beta \nu_\alpha \overline{\nu_\beta})} \frac{\Gamma(L_\alpha \longrightarrow L_\beta \nu_\alpha \overline{\nu_\beta})}{\Gamma_{tot}} \tag{3.1.31}$$

$$= \frac{\Gamma(L_\alpha \longrightarrow L_\beta \gamma)}{\Gamma(L_\alpha \longrightarrow L_\beta \nu_\alpha \overline{\nu_\beta})} BR(L_\alpha \longrightarrow L_\beta \nu_\alpha \overline{\nu_\beta}) . \tag{3.1.32}$$

The decay $L_\alpha \longrightarrow L_\beta \nu_\alpha \overline{\nu_\beta}$ is a SM process involving the exchange of a W^- gauge boson, which gives the Fermi constant G_F as an factor in the effective Fermi theory. The loop-mediated decay is possible inside the SM with a W boson and left-handed neutrinos ν_L in the loop, but it is negligible small due to the fact that $m_W \sim 10^{12}\ m_{\nu_L}$.

In the model considered here, $L_\alpha \longrightarrow L_\beta \gamma$ can also be realized with right-handed neutrinos and the charged component η^+ of the inert $SU(2)_L$ doublet η running in the loop. This loop-realization of the decay $L_\alpha \longrightarrow L_\beta \gamma$ yields sizeable branching ratios for lepton flavor violating decays:

$$BR(L_\alpha \longrightarrow L_\beta \gamma) = \frac{3\alpha_{\text{EM}}}{64\pi G_F^2 m_0^4} \left| \sum_{i=1}^{3} h^*_{\alpha i} h_{\beta i} F_2 \left(\frac{M_i^2}{m_0^2} \right) \right|^2 BR\left(L_\alpha \longrightarrow L_\beta \nu_\alpha \overline{\nu_\beta}\right) , \tag{3.1.33}$$

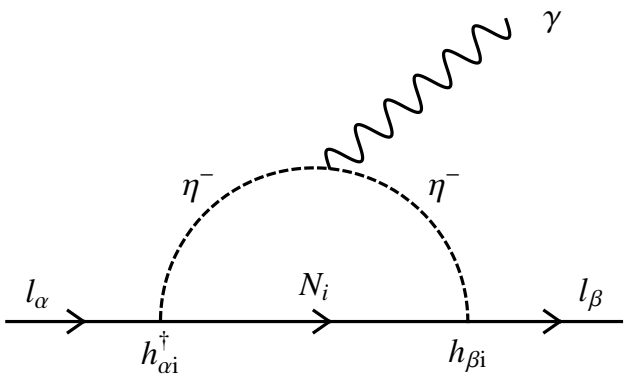

Figure 3.2.: Lepton flavor violating decay.

where $\alpha_{\rm EM} = e^2/4\pi$ is the electromagnetic fine structure constant and M_η is the mass of η^+, which we assume to be degenerate with η^0 for simplicity.

The loop involves a Dirac propagator and two scalar propagators connected through the interaction vertex with a photon, see figure 3.2. The loop function $F_2(x)$ is given by:

$$F_2(x) = \frac{1 - 6x + 3x^2 + 2x^3 - 6x^2 \log x}{6(1-x)^4}\,, \tag{3.1.34}$$

see appendix B for a detailed calculation.

With the given structure for the Yukawa couplings $h_{\alpha i}$ in equation (3.1.25), the h_3 and h'_3 elements contribute to $\mu \longrightarrow e\gamma$. The branching ratio for the decay $\mu \longrightarrow e\nu_\mu\overline{\nu_e}$ is $BR(\mu \longrightarrow e\nu_\mu\overline{\nu_e}) \approx 1$. Since $h'_3 = \sqrt{2}h_3 \tan\theta_{12}$, $\mu \longrightarrow e\gamma$ only depends on $|h_3|$ and M_3. The lepton flavor violating process $\tau \longrightarrow \mu\gamma$ depends on h_1, h_2 and the DM mass M_1. Given the current experimental situation, i.e., $BR(\mu^+ \longrightarrow e^+\gamma) < 5.7\times10^{-13}$ [109] and $BR(\tau^- \longrightarrow \mu^-\gamma) < 4.4\times10^{-8}$ [110], the most stringent constraint on the model parameters comes from the current non-observation of $\mu^+ \longrightarrow e^+\gamma$. Contours of $BR(\mu \longrightarrow e\gamma) = 5.7 \times 10^{-13}$ are shown for several $|h_3|$ values in figure 3.3. We take $M_3 = 6000\,\text{GeV}$ and $|h_3| = 0.3$ as a benchmark point in the following discussion. As it is clear from the figure, for this choice all values of m_0 are allowed, and for $m_0 \sim \mathcal{O}(100)$ GeV, we predict $\mu \longrightarrow e\gamma$ close to the present bound; equation (3.1.28) then implies $\lambda_5 \sim 10^{-9}$. With the chosen flavor structure of the Yukawa couplings $h_{\alpha i}$, we are able to relate model parameters to neutrino oscillation data. Together with the upper bounds from the LVF process, there are additional constraints on the model parameters, leaving only four independent parameters left which can be chosen as follows:

$$m_0, \quad M_1, \quad \delta \equiv M_2 - M_1, \quad \xi \equiv \text{Im}(h_2^* h_1)\,, \tag{3.1.35}$$

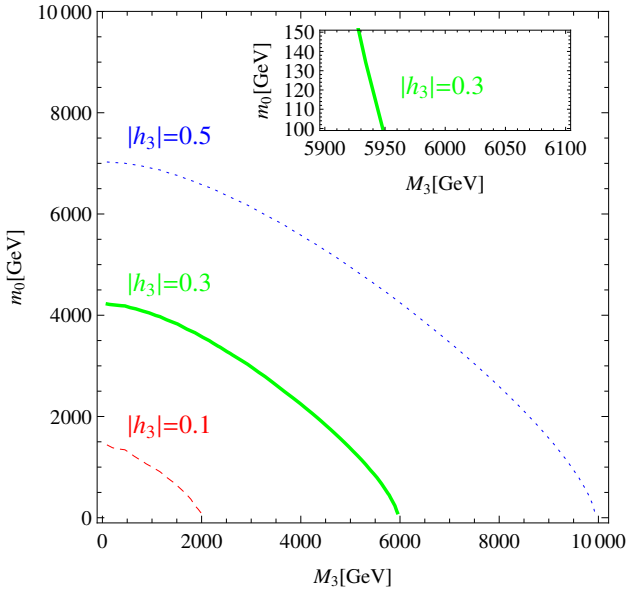

Figure 3.3.: Contours of $BR(\mu \longrightarrow e\gamma) = 5.7 \times 10^{-13}$ in the (M_3, m_0) plane for various choices of $|h_3|$. The region to the left of each contour is excluded by $\mu \longrightarrow e\gamma$ due to the behavior of $F_2(x)$. The inset zooms into the contour for $|h_3| = 0.3$.

with $\delta \ll M_1$. M_1 and δ immediately fix M_2.

Since we fix h_3 to the benchmark given point above in order to satisfy $\mu \longrightarrow e\gamma$, equation (3.1.27) determines Λ_3. Putting Λ_3 and the the benchmark value for M_3 into equation (3.1.18) fixes λ_5 for a given m_0. The λ_5 in turn determines Λ_1 via equation (3.1.18). Once Λ_1 is known, the absolute values $|h_1|$ and $|h_2|$ follow from equation (3.1.26). The still undetermined relative phase between h_1 and h_2 is defined by the parameter ξ, which will play an important role for the production of the DM relic density, which will be discussed in the following.

3.1.3. Dark Matter Relic Density

With the given $\mathbb{Z}_2$ charge assignment, DM particles in this model are, in principle, the neutral component η^0 of the inert Higgs $SU(2)_L$ doublet η and the lightest of the right-handed neutrinos N_i. We assume a mass spectrum in which N_1 is the lightest $\mathbb{Z}_2$-odd particle and hence the DM particle. It is further assumed that N_1 is almost degenerated with the second lightest right-handed neutrino N_2.

Because $\langle \eta^0 \rangle \neq 0$, the λ_3 coupling in the potential does not provide a Higgs portal, which would mediate s-channel annihilations for N_1 into SM particles. The N_i couple to the SM only via Yukawa interactions with the lepton $SU(2)_L$ doublets $\overline{L_\alpha}$, and therefore

our DM is leptophilic. The corresponding annihilation channels $N_i N_j \to L_\alpha \overline{L_\beta}$ are t-channels mediated by the inert $SU(2)_L$ doublet η.

The relic density and indirect detection of DM in the model have been investigated with the flavor structure of equation (3.1.25) in [107]. Here, we investigate the prospects for direct detection of DM in this setup for the first time in literature.

For the thermal production of DM in this model, co-annihilations between N_1 and N_2 have to be considered, since they are assumed to be degenerated. Co-annihilations are discussed in section 2.5.1. In addition to the annihilation of two N_1, the annihilation of N_1 and N_2 have also to be considered leading to an enhanced effective annihilation cross section.

The effective annihilation cross section is written as [59]:

$$\sigma_{\text{eff}} v_r = a_{\text{eff}} + b_{\text{eff}} v_r^2 + \mathcal{O}(v_r^4)\,, \tag{3.1.36}$$

see also appendix A. The DM relic density depends on the thermal average $\langle \sigma_{\text{eff}} v_r \rangle$ of the annihilation cross section σ_{eff} times relative velocity v_r. If v_r follows a Maxwell–Boltzmann distribution, then the most probable speed v is proportional to $\sqrt{T/m} = \sqrt{1/x}$. It then follows:

$$\langle \sigma_{\text{eff}} v_r \rangle = a_{\text{eff}} + \frac{b_{\text{eff}}}{x} + +\mathcal{O}(v^4)\,. \tag{3.1.37}$$

The approximate analytic solution of the Boltzmann equation, which describes the evolution of the DM density, is given by

$$\Omega h^2 \simeq \frac{1.07 \times 10^9 x_f}{\sqrt{g_{\text{eff}}(T_f)} m_{\text{pl}} \left(a_{\text{eff}} + 3\frac{b_{\text{eff}}}{x_f} \right)}\ \text{GeV}^{-1}\,, \quad \text{with} \quad x_f = \frac{M_1}{T_f}, \tag{3.1.38}$$

where $g_{\text{eff}}(T_f)$ is the number of relativistic degrees of freedom at the time of freeze-out, see appendix C, and $m_{\text{pl}} = 1.2 \times 10^{19}\,\text{GeV}$ is the Planck mass. In our analysis, we take $\Omega h^2 = 0.11260 \pm 0.0036$ [111].

Given the almost degenerate masses of N_1 and N_2, annihilations of N_1 and N_2 as well as co-annihilations between N_1 and N_2 have to be considered, which are realized by t-channel exchange of η^+ and η^0. With the structure of the Yukawa couplings $h_{\alpha i}$ in equation (3.1.25), the allowed final states are μ, τ, ν_μ, ν_τ, and their antiparticles. It is assumed that $\delta = M_2 - M_1$ is negligible small.

For the co-annihilation process, the squared amplitude $|\mathcal{M}|^2$ is proportional to:

$$|\mathcal{M}|^2 \propto \frac{s(s - 4M_l^2)}{(t - m_0^2)^2} \left(h_1 h_2^\dagger - h_1^\dagger h_2 \right)^2 = 4 \frac{s^2 - 4M_l^2 s}{(t - m_0^2)^2} \xi^2\,. \tag{3.1.39}$$

For the annihilation processes of N_1 and N_2, the squared amplitude $|\mathcal{M}|^2$ is proportional to:

$$|\mathcal{M}|^2 \propto \frac{(s - 4M_1^2)(s - 4M_l^2)}{(t - m_0^2)^2} |h_1^2 + h_2^2|^2\,. \tag{3.1.40}$$

The cross section can be calculated according to:

$$\frac{d\sigma}{dt} = \frac{1}{64\pi s}\frac{1}{|\mathbf{p}_{N_1,\mathrm{cm}}|^2}|\mathcal{M}|^2 \,. \tag{3.1.41}$$

$|\mathbf{p}_{N_1,\mathrm{cm}}|$ is the absolute value of the three momentum of the particle N_1 in the center of mass system: $|\mathbf{p}_{N_1,\mathrm{cm}}| = {}^1\!/_2\sqrt{s}v_{\mathrm{cm}} \propto \sqrt{s-4M_1^2}$. The cross section for the co-annihilation process is then proportional to ${}^{s-4M_l^2}\!/_{(s-4M_1^2)(t-m_0^2)^2}$ times phase space factors, whereas for the annihilation processes the cross section is proportional to ${}^{s-4M_l^2}\!/_{s(t-m_0^2)^2}$ times phase space factors.

The phase-space factors are the result of the t-integration of ${}^1\!/_{(t-m_0^2)^2}$, and they are equal to:

$$\frac{\sqrt{s(s-4M_1^2)}}{M_1^4 + m_0^2(s-2M_1^2+m_0^2)} \,. \tag{3.1.42}$$

Writing $s = {}^{4M_1^2}\!/_{1-v_{cm}^2}$ and expanding σv_{cm} in the the center of mass system velocity velocity v_{cm}, it is already clear that for the co-annihilation process, σv_{cm} has a velocity independent term, whereas the for the annihilation process, the leading term is proportional to v_{cm}^2; this corresponds to the helicity suppression for Majorana fermions.

Taking into account co-annihilations of N_1 and N_2 and neglecting the lepton masses, the coefficients a_{eff} and b_{eff} in the effective annihilation cross section follow from the squared amplitude for the given processes, see appendix A, and are equal to:

$$a_{\mathrm{eff}} = \frac{\xi^2}{2\pi}\frac{M_1^2}{\left(m_0^2+M_1^2\right)^2} \,, \tag{3.1.43}$$

$$b_{\mathrm{eff}} = \frac{|h_1^2+h_2^2|^2}{24\pi}\frac{M_1^2\left(m_0^4+M_1^4\right)}{\left(m_0^2+M_1^2\right)^4} + \frac{\xi^2}{2\pi}\frac{M_1^2\left(m_0^4-3m_0^2M_1^2-M_1^4\right)}{\left(m_0^2+M_1^2\right)^4} \,. \tag{3.1.44}$$

The terms proportional to ξ^2 come from the co-annihilation process $N_1N_2 \longrightarrow L_\alpha\overline{L_\beta}$, whereas the N_1N_1 and N_2N_2 annihilations lead to the terms proportional to h_1^2 and h_2^2, respectively.

We observe from Eq. (3.1.43) and (3.1.44) that the s-wave resulting from the a_{eff}-term is only present due to co-annihilations. If there is no phase difference between h_1 and h_2, the combination of the neutrino Yukawa couplings ξ vanishes and only p-wave annihilation remains. Thus, co-annihilations and a non-zero phase difference play an important role in obtaining the correct DM relic density. For the following results, we use the micrOMEGAs package [64] to calculate numerically the relic abundance of DM. In addition to $N_1 - N_2$ co-annihilations, also co-annihilations with η are important, if m_0 becomes close to M_1.

The allowed parameter region in the plane of DM mass and the Yukawa coupling ξ, which is consistent with neutrino masses and mixing, LFV, and DM relic density, is

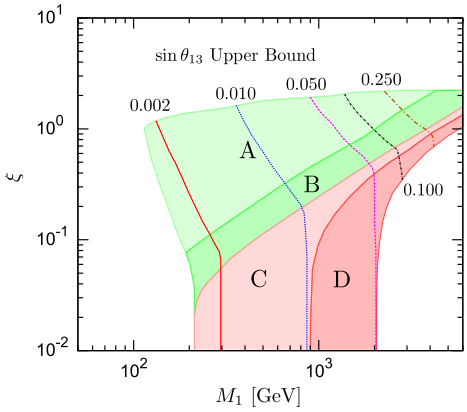

Figure 3.4.: Region in the space of DM mass M_1 and $\xi = |h_1 h_2| \sin(\varphi_1 - \varphi_2)$ consistent with neutrino masses and mixing, LFV, perturbativity, and the relic density of DM. The regions with different color shadings denoted by A, B, C, D, correspond to different assumptions on m_0, with A: $2.0 < {}^{m_0}/_{M_1} < 9.8$, B: $1.2 < {}^{m_0}/_{M_1} < 2.0$, C: $1.05 < {}^{m_0}/_{M_1} < 1.20$, D: $1.0 < {}^{m_0}/_{M_1} < 1.05$. The curves show the upper bound on $\sin\theta_{13}$ from $\mu \longrightarrow e\gamma$, see equation (3.1.52), with the Yukawa matrix from equation (3.1.49).

shown in figure 3.4. The allowed region is colored and divided into four regions A, B, C, D, corresponding to different assumptions on the ratio ${}^{m_0}/_{M_1}$. The upper bound on ξ is imposed by requiring perturbativity of the Yukawa couplings. The lower bound on M_1 in regions A and B is determined by the limit on $\tau \longrightarrow \mu\gamma$ together with the relic abundance requirement. There is no allowed parameter region if ${}^{m_0}/_{M_1} \gtrsim 9.8$, because taking into account perturbativity, as well as $\tau \longrightarrow \mu\gamma$, the annihilation cross section is suppressed by m_0^4. If ${}^{m_0}/_{M_1}$ comes close to 9.8, we are driven to the left-upper corner of the allowed region in figure 3.4. In the parameter region C and D, we have ${}^{m_0}/_{M_1} < 1.2$, and co-annihilations with η become important. Without co-annihilations with η, the parameter space C and D would not appear, and we would obtain a lower bound on $|\xi|$. However, if $N_1 - \eta$ co-annihilations are relevant, the correct relic density can be obtained even for vanishing ξ. In all cases we can conclude that the correct relic density is always obtained thanks to co-annihilations with either N_2 or η.

The charges component η^+ of the inert $SU(2)_L$ doublet η can decay into charged leptons. The allowed decays are $\eta^+ \longrightarrow N_{1,2}\mu^+$ and $\eta^+ \longrightarrow N_{1,2}\tau^+$. Given that these decays are the only possible ones for η^+ in this model, one may worry about a too long lifetime for η^+ being in conflict with light element abundances predicted by Big Bang Nucleosynthesis (BBN). Namely, η^+ can inject energy into charged leptons, which may change the predictions of BBN [112].

In the rest frame of the decaying particle η^+, the decay rate for the above listed decays is:

$$\Gamma\left(\eta^+ \longrightarrow N_{1,2}\mu^+(\tau^+)\right) = \frac{|h_1|^2+|h_1|^2}{8\pi}\left(1-\frac{M_1^2}{m_0^2}\right)^2 m_0\,. \tag{3.1.45}$$

Defining $x \equiv m_0 M_1$, the lifetime τ_η for η^+ follows to:

$$\tau_\eta = \frac{8\pi}{|h_1|^2+|h_1|^2}\left(\frac{x^2}{x^2-1}\right)^2\frac{1}{m_0}\,. \tag{3.1.46}$$

We have checked that for the parameter ranges of interest, η decays much faster than 0.01 s, unless it is degenerate with N_1 at the level of 10^{-10}, and hence the parameter region D is not in conflict with BBN.

The Yukawa couplings $h_{\alpha i}$ are chosen such that the neutrino mass matrix of the model is diagonalized by the PMNS mixing matrix with $\sin\theta_{13}=0$. However, the Double Chooz experiment measured a non-zero value for $\sin^2\theta_{13}$: $\sin^2\theta_{13} = 0.0227^{+0.0023}_{-0.0024}$, see table 2.1. Therefore, deviations from the flavor structure assumed in equation (3.1.25) have to be considered. Defining the PMNS mixing angles as $c_{ij}=\cos\theta_{ij}$ and $s_{ij}=\sin\theta_{ij}$ for $i,j=1,2,3$, the following perturbations for the PMNS matrix are introduced:

$$s_{13}=\epsilon_3, \quad c_{13}=1+\mathcal{O}(\epsilon_3^2), \tag{3.1.47}$$

$$s_{23}=\frac{1}{\sqrt{2}}+\epsilon_4, \quad c_{23}=\frac{1}{\sqrt{2}}-\epsilon_4\,. \tag{3.1.48}$$

The perturbed Yukawa coupling matrix at linear order is written as:

$$h_{\alpha i} = \begin{pmatrix} \epsilon_1 & \epsilon_2 & h_3' \\ h_1 & h_2 & h_3 \\ h_1 & h_2 & -h_3 \end{pmatrix} + \mathcal{O}(\epsilon^2)\,, \tag{3.1.49}$$

with $|\epsilon_i| \ll |h_j|$.

Diagonalizing the neutrino mass matrix in equation (3.1.19) according to equation (3.1.21) at linear order, setting $\Lambda_1 \approx \Lambda_2 \equiv \Lambda$ for the degenerated case $M_1 \approx M_2$, and using $h_3' = \sqrt{2}\tan\theta_{12}h_3$, the terms $\epsilon_1 h_1 + \epsilon_2 h_2$ and ϵ_4 depend on ϵ_3:

$$\epsilon_1 h_1 + \epsilon_2 h_2 = \sqrt{2}\left(h_1^2+h_2^2\right)\frac{\left(h_1^2+h_2^2\right)\Lambda_1 - \sec^2\theta_{12}h_3^2\Lambda_3}{\left(h_1^2+h_2^2\right)\Lambda_1 - h_3^2\Lambda_3}\epsilon_3 \equiv P\epsilon_3\,, \tag{3.1.50}$$

$$\epsilon_4 = \frac{1}{\sqrt{2}}\frac{\tan\theta_{12}h_3^2\Lambda_3}{\left(h_1^2+h_2^2\right)\Lambda_1 - h_3^2\Lambda_3}\epsilon_3\,. \tag{3.1.51}$$

The branching ratio $\mu \longrightarrow e\gamma$ depends on $\epsilon_1 h_1 + \epsilon_2 h_2$. If we assume that ϵ_1, ϵ_2 and ϵ_3 are real, we obtain from equation (3.1.33) the following expression for:

$$BR\left(\mu \longrightarrow e\gamma\right) = \frac{3\alpha_{\mathrm{EM}}}{64\pi G_F^2 m_0^4}\left|P\epsilon_3 F_2\left(\frac{M_1^2}{m_0^2}\right) + \sqrt{2}\tan\theta_{12}|h_3|^2 F_2\left(\frac{M_3^2}{m_0^2}\right)\right|^2. \tag{3.1.52}$$

Thus the non-zero θ_{13} directly gives a contribution to $\mu \longrightarrow e\gamma$ and $\epsilon_3 = \sin\theta_{13}$ is constrained by the limit on this process. Using $(h_1^2 + h_2^2)\,\Lambda_1 \approx 2.5 \times 10^{-2} < 2.9 \times 10^{-3} \approx |h_3^2 \Lambda_3|$ from equations (3.1.26) and (3.1.27), the parameter P is approximately obtained as $P \approx \sqrt{2}\,(h_1^2 + h_2^2)$, and an upper bound on ϵ_3 from $\mu \longrightarrow e\gamma$ at each point in figure 3.4 results.[1]

Contours of the upper bound on $\sin\theta_{13}$ are shown in figure 3.4. The upper bound becomes severe for small DM mass. According to figure 3.4 this requires DM masses around the TeV scale with $\xi \sim \mathcal{O}(0.1 - 1)$.

3.2. Direct Detection of Leptophilic Dark Matter in the Ma-Model

The Ma-model has been intensively studied in the literature. In the case that the lightest right-handed neutrino N_1 is the DM particle, however, detailed calculations concerning the prospects for the direct detection of N_1 have been lacking until recently. In this section, the direct detection of the leptophilic DM in the Ma-model is studied. The Majorana nature of N_1 will turn out to be crucial for the scattering process used in direct detection experiments.

3.2.1. Inelastic Scattering Cross Section

The DM particle N_1 is a Majorana fermion field defined by the property that it is even under the charge conjugation operation **C**. Hence, in the model presented here, there are neither vector current interactions $\overline{N_1}\gamma^\mu N_1$ nor tensor interactions $\overline{N_1}\sigma^{\mu\nu} N_1$. Axial-vector current interactions can be mediated by Z boson exchange, but they are suppressed by the mass of the Z boson relative to possible interactions mediated by a photon A_μ. This means that elastic scattering is suppressed.

However, for two different Majorana fields N_1 and N_2, vector and tensor interactions are possible. Inelastic scattering of N_1 off nuclei is realized at one-loop level, where the lepton $\overline{L_\alpha}$ and the inert scalar $SU(2)_L$ doublet η from equation (3.1.1) run in the loops. Since there are electric charged particles in the loops in each case, a photon A_μ can couple to the loops. Thus, the effective three particle vertex $N_2 - N_1 - A_\mu$ is possible, see figure 3.5. The kinetic term of η couples η to a photon A_μ through its covariant derivative. In the loop in which A^μ couples to η, the relevant vertex expression is therefore $-ie(p_1 + p_2)^\mu$. Here and in the following, p_1 and p_2 are the four momenta of the external right-handed neutrinos and k_μ is the four-momentum of the photon. Adding

[1] In general, the phase of P depends on the phases of the Yukawa couplings h_1 and h_2, i.e., φ_1 and φ_2, not only the phase difference $\varphi_1 - \varphi_2$. For simplicity we set the overall phase of P to zero. This phase might play a role if the two terms in equation (3.1.52) are of comparable size.

the two diagrams shown in figure 3.5, the resulting matrix element $\mathcal{M}$, which we show for completeness, has the structure:[2]

$$\mathcal{M} = \overline{u}(p_2)\gamma_\delta(1-\gamma_5)u(p_1)\left[k^2\left(\frac{1}{2}+\frac{2}{3}\log\frac{m_\alpha^2}{m_0^2}\right)g^{\mu\delta} - i(p_1+p_2)_\alpha k_\beta \epsilon^{\alpha\mu\beta\delta}\right]\epsilon_\mu^*(k)\,. \tag{3.2.1}$$

We proceed in the effective field theory approach and write the effective interactions as:

$$\mathcal{L}_{\text{eff}} = ia_{12}\overline{N_2}\gamma^\mu N_1 \partial^\nu F_{\mu\nu} + i\left(\frac{\mu_{12}}{2}\right)\overline{N_2}\sigma^{\mu\nu}N_1 F_{\mu\nu} + ic_{12}\overline{N_2}\gamma^\mu N_1 A_\mu, \tag{3.2.2}$$

where the factor i is a conventional factor to obtain real couplings a_{12}, c_{12} and μ_{12}.

Applying the Gordon identity to the term proportional to $(p_1+p_2)_\alpha k_\beta \epsilon^{\alpha\mu\beta\delta}$ in equation (3.2.1), a term proportional to $M_1\sigma^{\mu\nu}F_{\mu\nu}$ and a term proportional to $k^2 A_\mu$ results, see [113]. The first of these terms is written as the transition magnetic moment μ_{12} in equation (3.2.2) , the second one corresponds to the term proportional to c_{12}. The model considered here is a specific realization of *flavored* DM discussed in [113], where similar diagrams to the ones from figure 3.5 have been considered.

In the model considered here, the coefficients a_{12}, c_{12} and μ_{12} are calculated as:

$$a_{12} = -\sum_\alpha \frac{\text{Im}\,(h_{\alpha2}^* h_{\alpha1})\,e}{2(4\pi)^2 m_0^2} I_{\text{a}}\left(\frac{M_1^2}{m_0^2}, \frac{m_\alpha^2}{m_0^2}\right), \tag{3.2.3}$$

$$\mu_{12} = -\sum_\alpha \frac{\text{Im}\,(h_{\alpha2}^* h_{\alpha1})\,e}{2(4\pi)^2 m_0^2} 2M_1 I_{\text{m}}\left(\frac{M_1^2}{m_0^2}, \frac{m_\alpha^2}{m_0^2}\right), \tag{3.2.4}$$

$$c_{12} = \sum_\alpha \frac{\text{Im}\,(h_{\alpha2}^* h_{\alpha1})\,e}{2(4\pi)^2 m_0^2} q^2 I_{\text{c}}\left(\frac{M_1^2}{m_0^2}, \frac{m_\alpha^2}{m_0^2}\right), \tag{3.2.5}$$

where q^2 is the momentum transfer.

The explicit forms of the function $I_{\text{a}}(x,y)$, $I_{\text{m}}(x,y)$ and $I_{\text{c}}(x,y)$, which come from the loop integrals, are given in appendix B. All of the coefficients of the effective interactions are proportional to $\text{Im}\,(h_{\alpha2}^* h_{\alpha1})$, which is equal to ξ according to Eq. (3.1.25). The parameter ξ is hence responsible for $N_1 - N_2$ co-annihilations and in addition for the effective interactions of DM with nuclei. From the effective interactions in equation (3.2.2), we obtain three types of differential scattering cross sections with a nucleus that has atomic number Z, mass number A, mass m_A, spin J_A and magnetic moment μ_A, see

[2] I thank Takashi Toma for providing me with the matrix element $\mathcal{M}$.

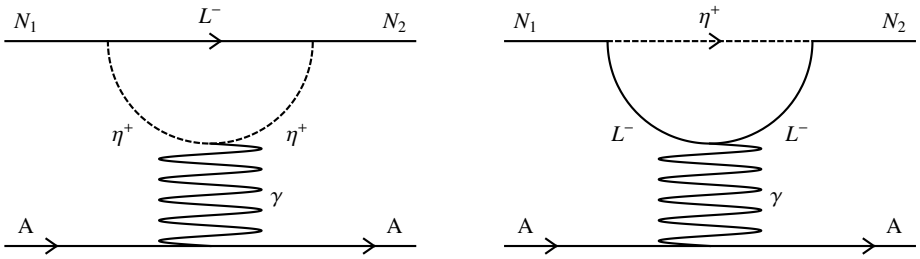

Figure 3.5.: Inelastic scattering of N_1 off a nucleus with mass number A.

e.g., [69, 113]:

$$\frac{d\sigma_{\mathrm{CC}}}{dE_R} = \frac{Z^2 b_{12}^2 m_A}{2\pi v^2} F^2(E_R), \tag{3.2.6}$$

$$\frac{d\sigma_{\mathrm{DC}}}{dE_R} = \frac{Z^2 \alpha_{\mathrm{EM}} \mu_{12}^2}{E_R} \cdot \left[1 - \frac{E_R}{v^2}\left(\frac{1}{2m_A} + \frac{1}{M_1}\right) - \frac{\delta}{v^2}\frac{1}{\mu_{\mathrm{DM}}} - \frac{\delta^2}{v^2}\frac{1}{2m_A E_R}\right] F^2(E_R), \tag{3.2.7}$$

$$\frac{d\sigma_{\mathrm{DD}}}{dE_R} = \frac{\mu_A^2 \mu_{12}^2 m_A}{\pi v^2}\left(\frac{J_A + 1}{3J_A}\right) F_D^2(E_R), \tag{3.2.8}$$

with the coefficient

$$b_{12} = \left(a_{12} + \frac{c_{12}}{q^2}\right) e\,. \tag{3.2.9}$$

The three effective cross sections are called charge-charge (CC), dipole-charge (DC), and dipole-dipole (DD) coupling, respectively. Here, E_R is the recoil energy and μ_{DM} is the DM–nucleus reduced mass, i.e., $\mu_{\mathrm{DM}} = {}^{m_{\mathrm{DM}} m_A}/_{m_{\mathrm{DM}}+m_A}$.

Magnetic moments of several nuclei are shown in Tab. 3.1, where the nuclear magneton is taken from [114].

$F(E_R)$, the so called nuclear electric form factor, is the Fourier transform of the electric charge distribution of a nucleus in the Born approximation. Parametrizing the nuclear charge distribution as $\rho(\mathbf{r}) = \int d^3\mathbf{r}'\, \rho_0(\mathbf{r}')\rho_1(\mathbf{r} - \mathbf{r}')$ [115], the nuclear form factor is:

$$F(E_R) = \frac{3\left[\sin(\kappa r) - \kappa r \cos(\kappa r)\right]}{(\kappa r)^3} e^{-\kappa^2 s^2/2}, \tag{3.2.10}$$

with $\kappa = \sqrt{2m_A E_R}$, $r = \sqrt{R^2 - 5s^2}$, $R \simeq 1.2A^{1/3}$ fm and $s \simeq 1\,\mathrm{fm}$ [116].

In addition to the electric charge, a nucleus can also possess a magnetic moment. Again, the Fourier transform of the distribution of the magnetic charge of a nucleus in

	$^{19}_{9}$F	$^{23}_{11}$Na	$^{73}_{32}$Ge	$^{127}_{53}$I	$^{131}_{54}$Xe	$^{133}_{55}$Cs	$^{183}_{74}$W
J_A	$1/2$	$3/2$	$9/2$	$5/2$	$3/2$	$7/2$	$1/2$
μ_A/μ_N	2.629	2.218	−0.879	2.813	0.692	2.582	0.118

Table 3.1.: Magnetic moments for several nuclei in units of μ_N, where $\mu_N = e/2m_p$ is the nuclear magneton.

the Born approximation is called the nuclear magnetic form factor $F_D(E_R)$. It takes into account proton orbital angular momentum as well as proton and neutron spin:

$$\mu_A = g_p^s \langle S_p \rangle + g_n^s \langle S_n \rangle + g_p^l \langle L_p \rangle + g_n^l \langle L_n \rangle \ , \tag{3.2.11}$$

see equation 2.6.13 for details.

The free particle g-factors in nuclear magnetons are given in [117]: $g_p^s = 5.586$, $g_n^s = -3.826$, $g_p^l = 1$ and $g_n^l = 0$. $F_D(E_R)$ highly depends on the nuclear shell. It is not well-known, see e.g., the discussion in ref. [69], which justifies an approximated treatment of $F_D(E_R)$: we approximate the magnetic form factor by neglecting the orbital momentum contribution.

For xenon-131, the Bonn-A calculation [117] gives $\langle S_p \rangle = -0.009$, $\langle S_n \rangle = -0.227$, $\langle L_p \rangle = 0.165$ and $\langle L_n \rangle = 1.572$. The ratio of spin and orbital contributions to the magnetic moment of $^{131}_{54}$Xe follows to $^{0.818}/_{0.165}$, which shows that the approximation is appropriate for xenon-131.

For sodium and iodine, which are also used in direct detection experiments, this approximation introduces an error of about a factor of 2, and therefore the limits derived from KIMS and DAMA should be considered accordingly.

With this approximation, the nuclear magnetic form factor can be expressed in terms of the spin form factors:

$$F_D(E_R) \approx \frac{g_p^s S_p(q^2) + g_n^s S_n(q^2)}{g_p^s S_p(0) + g_n^s S_n(0)} \, . \tag{3.2.12}$$

In addition to the CC, DC and DD interactions, also a charge-dipole coupling exists. However there is an additional suppression factor of q^2 compared to the other couplings, thus it can be neglected. The DC coupling is singular at $E_R = 0$. Therefore the predicted event rate of the DC coupling is enhanced at low recoil energies due to the singularity, and we cannot define a total cross section at the zero momentum transfer limit σ^0_{DC}. This situation is the same as in Coulomb scattering.

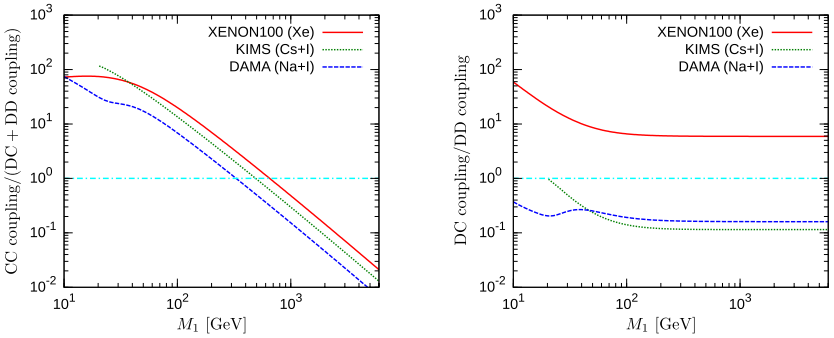

Figure 3.6.: Relative contributions of the charge-charge (CC), dipole-charge (DC), and dipole-dipole (DD) interactions to the total predicted event rate in XENON100, KIMS, and DAMA. The left panel shows the contribution from CC relative to the sum of DC and DD, the right panel shows the ratio of the DC and DD contributions. We assume m_0/M_1 and $\delta = 0$.

3.2.2. Comparison of the Predicted Event Rates with Experiments

In equation (2.6.9), we present the general expression for the event rates at DM direct detection experiments. Here, we compare the event rates calculated from the three effective cross sections CC (3.2.6), DC (3.2.7) and DD (3.2.8) with XENON100 [91], KIMS [74] and DAMA [92] data. The DD coupling might be important for KIMS or DAMA, since in these experiments, the target nuclei are iodine and cesium for KIMS, and iodine and sodium for DAMA. These nuclei have a large nuclear magnetic moment [69] as can be seen in table 3.1. In figure 3.6, we illustrate the relative importance of the the CC, DC and DD interactions for the XENON100, KIMS, and DAMA experiments by calculating the total event rate induced from each of the three interaction types separately.

We observe from the left panel that typically CC interactions are more important for small masses M_1, which follows from the different dependence on the DM mass of b_{12} and μ_{12}. The magnetic transition moment μ_{12} that generates the DC and DD interactions is proportional to the DM mass M_1, and thus subdominant for small values of M_1. The value M_1, where CC becomes subdominant, depends on the ratio m_0/M_1 that enters into the loop functions.

The right panel of figure 3.6 shows that for XENON100, the DC coupling is more important, whereas for KIMS and DAMA DD dominates. The reason for this behavior are the large magnetic moments of iodine and sodium. The features of the DAMA curves around $M_1 \simeq 20\,\text{GeV}$ in both panels are a consequence of the presence of the two elements

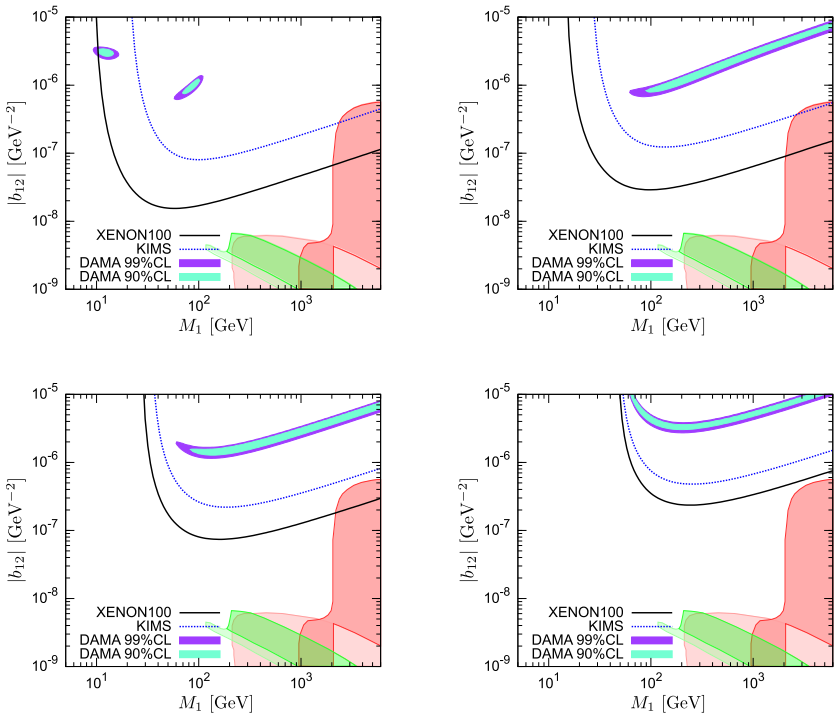

Figure 3.7.: Bounds from XENON100, KIMS and allowed regions for DAMA in the $(M_1, |b_{12}|)$ plane, i.e., charge-charge interaction. The mass difference δ is taken as 0 (the left top panel), 40 keV (the right top panel), 80 keV (the left bottom panel) and 120 keV (the right bottom panel). The shaded regions correspond to the values of b_{12} predicted in the allowed parameter space of the model, as shown in figure 3.4, with the same color shading for different values of the ratio m_0/M_1.

iodine and sodium with rather different masses. In general, the relative importance of CC, DC and DD depends on the ratio m_0/M_1 entering into the loop functions, and to a lesser extent on δ.

The main conclusion is that depending on the region in the parameter space, and depending on the considered experiment, any of the three interaction types can be important, and all of them have to be taken into account. In order to derive constraints on the model, we calculate the total event rate for XENON100 and KIMS in the energy range given in table 2.6 and require that the predicted rate is less than 0.0017 counts day^{-1} kg^{-1} for XENON100 and 0.0098 counts day^{-1} kg^{-1} KIMS. The upper bounds are obtained from the observed 3 events with 3σ of the statistical error in the 48 kg fiducial volume during 100.9 live days exposure in the signal region for XENON100 [91], and from [74] for KIMS.

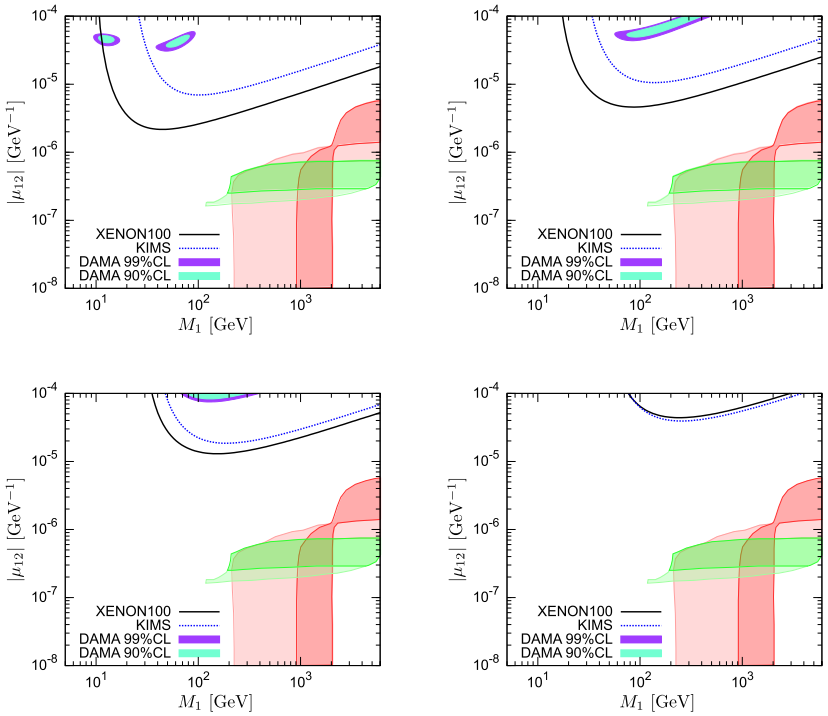

Figure 3.8.: Bounds from XENON100, KIMS and allowed regions for DAMA in the $(M_1, |\mu_{12}|)$ plane (dipole-charge and dipole-dipole interaction). The mass difference δ is taken as 0 (the left top panel), 40 keV (the right top panel), 80 keV (the left bottom panel) and 120 keV (the right bottom panel). The shaded regions correspond to the values of μ_{12} predicted in the allowed parameter space of the model, as shown in figure 3.4, with the same color shading for different values of the ratio m_0/M_1.

For DAMA, we perform a χ^2 fit to the modulation amplitude in bins of observed scintillation energy between 2 keV and 8 keV. The DAMA collaboration presents the result on the direct detection of DM as an energy distribution of the modulation amplitude A_i^{obs} with error σ_i. A_i^{obs} is the signal, the index i refers to the 36 energy bins from $E_i^- = 2\,\text{keV}$ to $E_i^+ = 8\,\text{keV}$. The question is how one can extract the DM mass and the DM scattering cross section σ_p on a proton from the energy distribution of the signal. The answer is a χ^2 fit; it works as follows: First of all, one can define a differential event rate $R(E_R)$ in counts per unit mass of a given nucleus per unit exposure time and per unit energy as a two parametric function of the recoil energy E_R. The parameters are the DM mass m_ξ and the cross section σ_p. Because the recoiling nucleus loses its energy by electromagnetic and nuclear interactions, however, the detectors measure only electromagnetic interactions, the event energy E is not equal to the recoil energy E_R, what is taken into account by a quenching factor q: $E = q \times E_R$, see section 2.6.2. Integrating $R(E_R)$ over E, one obtains the predicted modulation amplitude $A_i^{\text{pred}}(m_\xi, \sigma_p)$. A χ^2 function can then be constructed as

$$\chi^2\left(m_\xi, \sigma_p\right) = \sum_{i=1}^{36} \left(\frac{A_i^{\text{pred}}(m_\xi, \sigma_p) - A_i^{\text{obs}}}{\sigma_i} \right)^2 . \tag{3.2.13}$$

For 36 data points and 2 parameters, we have $36 - 2 = 34$ degrees of freedom.

In figure 3.7 and figure 3.8, we show the bounds from XENON100, KIMS and allowed regions from DAMA for the coefficients b_{12} and μ_{12} resulting from the CC and DC interactions. These bounds are compared to the regions as predicted in the model according to equations (3.2.9), (3.2.3) and (3.2.5) for b_{12} and equation (3.2.4) for μ_{12}. The colored regions correspond to the regions shown in figure 3.4, satisfying constraints from neutrino masses and mixing, charged LFV, the relic DM density, and perturbativity. The ratio m_0/M_1 is taken in the range $1 \leq m_0/M_1 \leq 9.8$, with the same color shading as in figure 3.4.

There is no allowed parameter space for $m_0/M_1 \gtrsim 9.8$, as discussed earlier.

We observe that the values of $|b_{12}|$ and $|\mu_{12}|$ obtained in this model are too small to account for the signal in DAMA.

For very small mass splitting δ between N_1 and N_2, some regions of the parameter space are excluded by XENON100 data. The constraints become weaker for larger δ. A larger value for δ increases the minimal velocity needed for a given nuclear recoil energy, see equation (2.6.4), which in turn decreases the scattering event rate. Relatively large values of $|b_{12}|$ are obtained for close to degenerate N_1 and η, i.e., $m_0/M_1 \lesssim 1.05$, see the dark-red region, because of the behavior of the function $I_{\text{a}}(x, y)$ near $x = 1$: $I_{\text{a}}(x, y) \sim y^{-1}$ and $y = m_\alpha^2/m_0^2$ is small. The region excluded by XENON100 for $M_1 \simeq m_0 \sim 2\,\text{TeV}$ becomes allowed for $\delta \gtrsim 120\,\text{keV}$, see bottom-right panel.

By comparing the figures 3.7 and 3.8, we observe that the model predicts values of $|\mu_{12}|$ too small to be tested by current direct detection data. The enhancement for the

transition magnetic moment $|\mu_{12}|$ for ${}^{m_0}/_{M_1} \lesssim 1.05$ is less than for $|b_{12}|$ due to a different behavior of the loop functions $I_\mathrm{a}(x,y)$ and $I_\mathrm{m}(x,y)$.

We conclude that current data from XENON100 start to exclude some parameter space of the model, in case of degenerate configurations $M_1 \simeq M_2 \simeq m_0$ of the order of a few TeV.

In figure 3.9, we show the regions excluded from XENON100 overlayed to the globally allowed regions from figure 3.4 as dark blue, by translating the $|b_{12}|$ constraint into a bound on ξ. Furthermore, we show in figure 3.9 the estimated sensitivity for XENON1T. Using the sensitivity for the elastic WIMP-nucleon scattering cross section from ref. [96], we estimate that XENON1T will constrain the event rate to be less than 1.59×10^{-5} counts day^{-1} kg^{-1}. We assume the same nuclear recoil energy range as for XENON100, see table 2.6. Then we compare this number to the event rate induced in the model assuming several values for the mass splitting δ. From figure 3.9 we find that for $\delta \lesssim 40\,\mathrm{keV}$, future data from the XENON1T experiment [96] will dig deeply into the allowed parameter region of the model. For $40\,\mathrm{keV} \lesssim \delta \lesssim 120\,\mathrm{keV}$, the degenerate region $M_1 \simeq M_2 \simeq m_0$ of the order of a few TeV will be tested.

We note, however, that no signal is guaranteed for direct detection. In the $N_1 - \eta$ co-annihilation regions, which are the dark- and light-red regions, where ${}^{m_0}/_{M_1} < 1.2$, no lower bound on the parameter $|\xi|$ is obtained, leading to arbitrarily small values of $|b_{12}|$ and $|\mu_{12}|$, which implies a vanishing signal in direct detection experiments.

3.3. Summary: Inelastic Dark Matter in the Ma-Model

The Ma-model [101], which we discussed in the previous section, is a well-known model for neutrino mass generation at one-loop level. In addition to giving masses to neutrinos, it contains candidates for a DM particle and thus combines already in its original version neutrino and DM physics.

The SM is extended by three right-handed neutrinos N_i and an inert scalar $SU(2)_L$ doublet η. The new particles transform odd under an imposed $\mathbb{Z}_2$ symmetry. Thus, the lightest of them, in our case N_1, is the DM particle. The relic density of N_1 is achieved by thermal freeze-out.

In our analysis, we take neutrino masses and mixing, LFV constraints and perturbativity into account for the DM relic density. In particular, we obtain the correct relic density without contradicting the LFV constraints due to co-annihilations.

N_1 has no direct couplings to quarks and gluons. Nevertheless, N_1 can be directly detected in inelastic scattering off nuclei, realized at one-loop level by photon exchange, which yields CC, DC and DD interactions between the DM particle N_1 and nuclei. To the best of our knowledge, these effective DM interactions in the Ma-model have not

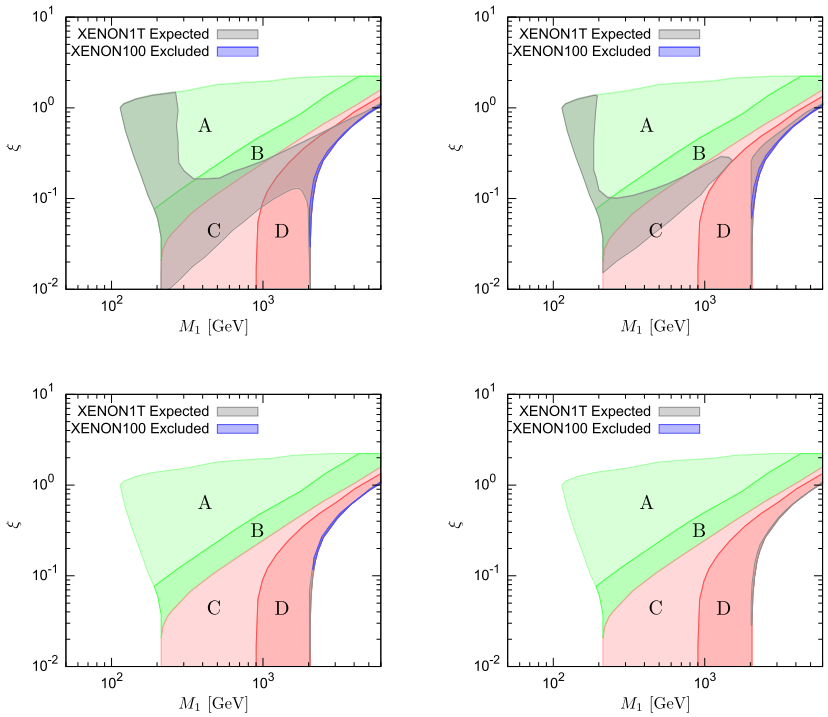

Figure 3.9.: Same as figure 3.4 with constraints from XENON100 (blue) and sensitivity from XENON1T (gray) overlayed. We assume δ =0 (left top), 40 keV (right top), 80 keV (left bottom), 120 keV (right bottom).

been considered previously. The XENON1T experiment may probe a significant part of the parameter space, given that the mass difference δ between N_1 and N_2 is small enough. A small δ is consistent with the need for co-annihilations to obtain the correct DM relic density. In the words of a famous rascals history, *This was the* model builder's *first trick, But the second follows quick*.[3]

In the next section, we increase the number of loops and study the Zee–Babu-model. There, the trick to combine neutrino and DM physics is the spontaneous breaking of a global symmetry, as we discuss in the following.

3.4. Two-Loop Example: The Zee–Babu-Model

A very predictive model to generate light neutrino masses radiatively at two loop level is the Zee–Babu-model. The particle content is that of the SM extended by two complex $SU(2)_L$ singlet scalars: a singly-charged scalar h^+ and a doubly-charged scalar k^{++}. No

[3] *Max and Moritz, a rascals history in seven tricks* by W. Busch.

right-handed neutrinos added, so neutrinos can only have Majorana masses.

Phenomenological consequences of singly- and doubly-charged scalars, especially concerning muon neutrino scattering on electrons, were first investigated by Zee [118]: the SM gauge-invariant antisymmetric Yukawa coupling of a singly-charged scalar $SU(2)_L$ singlet h to SM lepton $SU(2)_L$ doublets, i.e.,

$$f_{\alpha\beta}\, L_\alpha^T \mathbf{C}^{-1}\, i\sigma_2\, L_\beta h^+ + \text{h.c.}\,, \tag{3.4.1}$$

makes resonant muon production possible in s-channel exchange of h:

$$\nu_\mu e^- \to \nu_\tau \mu^-\,. \tag{3.4.2}$$

This process is a forbidden in the SM. In addition, Zee already considered the gauge-invariant Yukawa coupling of a doubly-charged scalar $SU(2)_L$ singlet k to SM lepton $SU(2)_L$ singlets, i.e.,

$$g_{\alpha\beta}\, e_\alpha^T \mathbf{C}^{-1} e_\beta\, k^{++} + \text{h.c.}\,. \tag{3.4.3}$$

He also noted that the lepton number violating trilinear scalar term $M k^{++} h^- h^-$ is allowed by gauge symmetry, but he did not take it into account for neutrino mass generation. The possibility to generate neutrino masses with these scalar particles was first seen by Babu [103]: Zee's Yukawa couplings of singly- and doubly-charged scalars together with the trilinear scalar coupling allow for neutrino mass generation at two-loop level. Due to the contribution of both authors, the model is referred to as the Zee–Babu-model.

Being $SU(2)_L$ singlet scalars, the electric charges of h^+ and k^{++} equal their hypercharges, respectively. Gauge invariance then allows only couplings of the scalars to leptons: h^+ couples to left-handed lepton $SU(2)_L$ doublets $L_{(i)}$ and k^{++} couples to right-handed leptons $l_{(R,i)}$. The leptonic contribution to the Lagrangian is:

$$\mathcal{L}_{\text{lept}} = f_{\alpha\beta}\, L_\alpha^T \mathbf{C}^{-1}\, i\sigma_2\, L_\beta h^+ \,+\, g_{\alpha\beta}\, e_\alpha^T \mathbf{C}^{-1} e_\beta\, k^{++} + \text{h.c.}\,, \tag{3.4.4}$$

where $\mathbf{C}$ is the charge conjugation matrix, α, β label flavor indices, and the Yukawa couplings f and g are antisymmetric and symmetric, respectively. We have omitted $SU(2)_L$ gauge indices , which enter through σ_2 in equation 3.4.4 and lead to the antisymmetric Yukawa couplings f. Yukawa couplings to quarks, which have hypercharges different from $|1/2|$ and $|1|$, are forbidden by gauge-invariance.

If both, h^+ and k^{++}, are assigned lepton number -2, lepton number is conserved by these interactions, and therefore the theory respects a global $U(1)$ symmetry. To generate Majorana neutrino masses, lepton number has to be broken by two units. In the Zee–Babu-model, lepton number is explicitly broken in the scalar sector by the trilinear term

$$\mu k^{++} h^- h^- + \text{h.c.}\,, \tag{3.4.5}$$

with μ a mass parameter. The μ coupling must be introduced by hands to generate Majorana neutrino masses at two-loop level. The relevant two-loop diagram is finite, which is the reason why Babu called his paper *model of calculable Majorana neutrino masses* [103]. The scalar potential is:

$$\begin{aligned} V_{\text{scalar}} =& \mu_H^2 H^\dagger H + \mu_k^2 k^{++}k^{--} + \mu_h^2 h^+ h^- \\ &+ \mu k^{++} h^- h^- + \text{h.c.} \\ &+ \lambda_H (H^\dagger H)^2 + \lambda_k (k^{++}k^{--})^2 + \lambda_h (h^+ h^-)^2 \\ &+ \lambda_3 (H^\dagger H)(k^{++}k^{--}) + \lambda_4 (H^\dagger H)(h^+ h^-) + \lambda_5 (k^{++}k^{--})(h^+ h^-)\,. \end{aligned} \tag{3.4.6}$$

H is the SM Higgs $SU(2)_L$ doublet. In the unitary gauge, we keep the parametrization:

$$H = \begin{pmatrix} 0 \\ \frac{1}{\sqrt{2}}(v+h) \end{pmatrix}\,. \tag{3.4.7}$$

At tree level, neutrinos are massless in the Zee–Babu-model. Due to the new particles and their interactions, neutrino masses are generated at two-loop level. The effective Majorana neutrino mass, i.e.,

$$\mathcal{L}_\nu = \frac{1}{2}\overline{\nu_L^C} m_\nu \nu_L + \text{h.c.}\,, \tag{3.4.8}$$

can be expressed as [119]:

$$(m_\nu)_{ab} = 16\mu f_{ac} m_c g^*_{cd} I_{cd} m_d f_{bd}\,. \tag{3.4.9}$$

where m_c are charged lepton masses and I_{cd} is the two-loop integral:

$$I_{cd} = \int \frac{d^4k}{(2\pi)^4}\frac{d^4q}{(2\pi)^4}\frac{1}{(k^2-m_c^2)}\frac{1}{(k^2-m_h^2)}\frac{1}{(q^2-m_d^2)}\frac{1}{(q^2-m_h^2)}\frac{1}{((k-q)^2-m_k^2}\,. \tag{3.4.10}$$

The analytic calculation of the integral in equation (3.4.10) is performed in [120].

We take an approximation for the two-loop integral into consideration, which relies on the fact that the masses of the charged leptons are much lighter than the existing lower limits on the masses of charged scalars: searches for a singly-charged particle in proton-proton (pp) collisions require a minimum reconstructed scalar mass of 120 GeV for a Drell-Yan-like production [121]. The search for a doubly-charged Higgs boson in like-sign dilepton final states are even more constraining due to the expected lower SM background. Assuming that the doubly-charged scalar decays with a branching ratio of 100% into $e^\pm e^\pm$, the expected lower mass limit at 95% confidence level is $m_{k^{\pm\pm}} > 329\,\text{GeV}$ [122].

Given that the heaviest charged SM lepton is the tau τ with a mass of $m_\tau = 1.78\,\text{GeV}$, we can neglect the masses of charged leptons compared to the masses of charged scalars. In this case, one finds:

$$I_{cd} \approx I = \frac{1}{(16\pi^2)^2}\frac{1}{M^2}\frac{\pi^2}{3}\tilde{I}\left(\frac{m_k^2}{m_h^2}\right)\,, \tag{3.4.11}$$

where $M = \max(m_k, m_h)$ and $\tilde{I}(r)$ is a dimensionless function of order unity [119]. The light neutrino mass matrix then takes the form:

$$m_\nu \simeq \frac{1}{48\pi^2}\frac{\mu}{M^2}\,\tilde{I}\,f D_\ell g^\dagger D_\ell f^T\ , \tag{3.4.12}$$

with the matrix $D_l = \mathrm{diag}(m_e, m_\mu, m_\tau)$ containing the charged-lepton masses. Due to the antisymmetry of f, we have $\det m_\nu = 0$, so one of the neutrinos is massless as long as higher-order corrections are not considered. Thus, the measured differences of squared neutrino mass eigenvalues directly corresponds to squared neutrino mass eigenvalues, i.e., in normal hierarchy: $m_2 = \sqrt{\Delta m^2_{21}}$ and $m_3 = \sqrt{\Delta m^2_{31}}$.

The neutrino masses are suppressed by the heavy scalar masses, and they are proportional to the scale of lepton-number violation μ. Assuming $\mu \sim M \sim \Lambda$, we see from (3.4.12) that for $m_\nu \sim 0.1\,\mathrm{eV}$, the scale Λ of new physics has to be of order 1 TeV, if we demand that $f \sim g \sim 0.05$. This scale Λ for generating neutrino masses is much below the scale of seesaw models due to the two loop suppression factor $1/(16\pi^2)^2 \sim 10^{-4}$ and the amount of coupling constants involved in the loops. Hence, Λ is in the range of the LHC, and may thus be probed soon. The neutrino phenomenology, as well as other signatures of the model, have been studied, e.g., in [119].

As already mentioned, the charged scalars h^+ and k^{++} induce charged LFV processes. At tree level, the doubly-charged scalar k^{--} mediates the decays $e_\alpha^- \longrightarrow e_\beta^+ e_\gamma^- e_\delta^-$. At one-loop level, both of the charged scalars contribute to the decays $L_\alpha \longrightarrow L_\beta + \gamma$ and $e_\alpha \longrightarrow e_\beta + \gamma$, respectively. The constraints given in [119] for the lepton number and lepton flavor violating processes are outdated. In particular, the sensitivity for the branching ratio of the decay $\mu \longrightarrow e + \gamma$ increased from 1.2×10^{-11} to 5.7×10^{-13} at 90% confidence level [109]. For the decay $\mu^+ \longrightarrow e^- e^+ e^+$, sensitivity to a branching fraction of $BR > 10^{-16}$ at the 90% confidence level is planned [123]. Besides lepton flavor violating decays the charged scalars also induce $\mu - e$ conversion in nuclei at the one-loop level similar to figure 3.5, where the coupling to the quarks is mediated by a photon. The upper limit on the $\mu - e$ conversion in aluminium will improve from currently 7×10^{-13} [124] to 2×10^{-17} [125], which will further constrain the Yukawa couplings of the Zee–Babu scalars. Given the current and future experimental development, we find it necessary to provide an update of the experimental constraints in table 3.2 and to discuss the resulting consequences for the charged scalars. The prospects for discovering the charged scalars of the Zee–Babu-model at the LHC have been discussed in detail in [119]. Since each doubly-charged scalar $k^{\mp\mp}$ can decay into a pair $e_\alpha^\mp e_\alpha^\mp$ of like-sign leptons, the pair production of the doubly-charged scalar in Drell-Yan-like processes will have four like-sign leptons $e_\alpha^\mp e_\alpha^\mp e_\beta^\pm e_\beta^\pm$ in the final state. The number N of events with four like-sign leptons in the final state depends on the production cross section $\sigma_{k^{\pm\pm}}$ for the doubly-charged scalar, its branching ratio $BR(k^{\mp\mp} \longrightarrow e_\alpha^\mp e_\alpha^\mp)$ into like-sign leptons

Constraint		Ref.	Bound (90% C.L.)
$\sum_{q=d,s,b} \lvert V_{uq}\rvert^2$	0.99990 ± 0.0006	[126]	$\lvert f_{e\mu}\rvert^2 < 0.014 \left(\frac{m_h}{\text{TeV}}\right)^2$
$\mu - e$ universality	$\frac{G_{\tau\to\mu}}{G_{\tau\to e}} = 1.0001 \pm 0.0020$	[126]	$\left\lvert \lvert f_{\mu\tau}\rvert^2 - \lvert f_{e\tau}\rvert^2 \right\rvert < 0.05 \left(\frac{m_h}{\text{TeV}}\right)^2$
$\mu - \tau$ universality	$\frac{G_{\tau\to e}}{G_{\mu\to e}} = 1.0004 \pm 0.0022$	[126]	$\left\lvert \lvert f_{e\tau}\rvert^2 - \lvert f_{e\mu}\rvert^2 \right\rvert < 0.06 \left(\frac{m_h}{\text{TeV}}\right)^2$
$e - \tau$ universality	$\frac{G_{\tau\to\mu}}{G_{\mu\to e}} = 1.0004 \pm 0.0023$	[126]	$\left\lvert \lvert f_{\mu\tau}\rvert^2 - \lvert f_{e\mu}\rvert^2 \right\rvert < 0.06 \left(\frac{m_h}{\text{TeV}}\right)^2$
δa_μ	$(28.7 \pm 80) \times 10^{-10}$	[126, 127]	$r(\lvert f_{e\mu}\rvert^2 + \lvert f_{\mu\tau}\rvert^2) + 4(\lvert g_{e\mu}\rvert^2 + \lvert g_{\mu\mu}\rvert^2 + \lvert g_{\mu\tau}\rvert^2) < 3.4 \left(\frac{m_k}{\text{TeV}}\right)^2$
$\mu^- \to e^+e^-e^-$	BR$< 1.0 \times 10^{-12}$	[128]	$\lvert g_{e\mu} g^*_{ee}\rvert < 2.3 \times 10^{-5} \left(\frac{m_k}{\text{TeV}}\right)^2$
$\tau^- \to e^+e^-e^-$	BR$< 2.7 \times 10^{-8}$	[129]	$\lvert g_{e\tau} g^*_{ee}\rvert < 0.009 \left(\frac{m_k}{\text{TeV}}\right)^2$
$\tau^- \to e^+e^-\mu^-$	BR$< 1.8 \times 10^{-8}$	[129]	$\lvert g_{e\tau} g^*_{e\mu}\rvert < 0.005 \left(\frac{m_k}{\text{TeV}}\right)^2$
$\tau^- \to e^+\mu^-\mu^-$	BR$< 1.7 \times 10^{-8}$	[129]	$\lvert g_{e\tau} g^*_{\mu\mu}\rvert < 0.007 \left(\frac{m_k}{\text{TeV}}\right)^2$
$\tau^- \to \mu^+e^-e^-$	BR$< 1.5 \times 10^{-8}$	[129]	$\lvert g_{\mu\tau} g^*_{ee}\rvert < 0.007 \left(\frac{m_k}{\text{TeV}}\right)^2$
$\tau^- \to \mu^+e^-\mu^-$	BR$< 2.7 \times 10^{-8}$	[129]	$\lvert g_{\mu\tau} g^*_{e\mu}\rvert < 0.006 \left(\frac{m_k}{\text{TeV}}\right)^2$
$\tau^- \to \mu^+\mu^-\mu^-$	BR$< 2.1 \times 10^{-8}$	[129]	$\lvert g_{\mu\tau} g^*_{\mu\mu}\rvert < 0.008 \left(\frac{m_k}{\text{TeV}}\right)^2$
$\mu \to e\gamma$	BR$< 5.7 \times 10^{-13}$	[109]	$r^2 \lvert f^*_{e\tau} f_{\mu\tau}\rvert^2 + 16 \lvert g^*_{e\alpha} g_{\alpha\mu}\rvert^2 < 1.6 \times 10^{-6} \left(\frac{m_k}{\text{TeV}}\right)^4$
$\tau \to e\gamma$	BR$< 3.3 \times 10^{-8}$	[110]	$r^2 \lvert f^*_{e\mu} f_{\mu\tau}\rvert^2 + 16 \lvert g^*_{e\alpha} g_{\alpha\tau}\rvert^2 < 0.52 \left(\frac{m_k}{\text{TeV}}\right)^4$
$\tau \to \mu\gamma$	BR$< 4.5 \times 10^{-8}$	[110]	$r^2 \lvert f^*_{e\mu} f_{e\tau}\rvert^2 + 16 \lvert g^*_{\mu\alpha} g_{\alpha\tau}\rvert^2 < 0.71 \left(\frac{m_k}{\text{TeV}}\right)^4$
$\mu^+e^- \to \mu^-e^+$	$G_{M\bar{M}} < 3 \times 10^{-3} G_F$	[126]	$\lvert g_{ee} g^*_{\mu\mu}\rvert < 0.2 \left(\frac{m_k}{\text{TeV}}\right)^2$

Table 3.2.: Summary of experimental constraints and the corresponding bounds on the Yukawa couplings. Here $r = m_k^2/m_h^2$, and in $g^*_{e\alpha} g_{\alpha\mu}$, α is a summation index over the flavor states.

and the integrated luminosity l as:

$$N = 2\sigma_{k^{\mp\mp}} BR(k^{\mp\mp} \longrightarrow e^\mp_\alpha e^\mp_\alpha) l \,. \tag{3.4.13}$$

For $m_k = 400\,\text{GeV}$ ($m_k = 1500\,\text{GeV}$), the production cross section at $\sqrt{s} = 14\,\text{TeV}$ is approximately $\sigma_k = 9.5\,\text{fb}$ ($\sigma_k = 0.003\,\text{fb}$) [119]. Assuming that all produced doubly-charged scalar decay solemnly into like-sign leptons, i.e., $BR(k^{\mp\mp} \longrightarrow e^\mp_\alpha e^\mp_\alpha) = 1$ and an integrated luminosity of $l = 300\,\text{fb}^{-1}$, one would expect 2850 events (0.9 events). These numbers actually will turn out smaller because the doubly-charged scalar will have other decay channels than like-sign leptons.

Current Higgs searches in the channel Higgs to four leptons are available with a dataset corresponding to an integrated luminosity of $20.7\,\text{fb}^{-1}$ at $\sqrt{s} = 8\,\text{TeV}$. The estimated number of background events in the four electron channel is approximately four [130]. A heavy doubly-charged scalar with mass $m_{k^{++}} = 1500$ GeV can then not be distinguished from a background signal. The LHC will therefore not be able to detect the doubly-charged scalar of the Zee–Babu-model if its mass is well above 1 TeV.

So far, we have discussed the original version of the Zee–Babu-model. We proceed with a dynamical generation of the trilinear μ term, which we connect to DM physics. Our extended version is based on the spontaneous breaking of a global $U(1)_{B-L}$ symmetry, which is the content of the following section.

3.4.1. Spontaneous Breaking of $B - L$ in the Zee–Babu-Model

In order to break lepton number and generate a Majorana mass term for neutrinos, the trilinear μ-term in the scalar potential, $\mu k^{++} h^- h^-$, which breaks lepton number explicitly, is strictly necessary. We write down only the leptonic part of the Lagrangian and thereby fully neglect the baryons. A complete theory has to describe leptons and baryons, i.e., lepton number L and baryon number B have to be considered at the same time. With respect to Noether's theorem, L and B are the charges of Noether currents. The Noether currents associated with L and B are, respectively:

$$j_\mu^L = \sum_\alpha \left(\overline{L^{(\alpha)}} \gamma_\mu L^{(\alpha)} + \overline{e^{(\alpha)}} \gamma_\mu e^{(\alpha)} \right) \tag{3.4.14}$$

$$j_\mu^B = \frac{1}{3} \sum_\alpha \left(\overline{Q^{(\alpha)}} \gamma_\mu Q^{(\alpha)} + \overline{u^{(\alpha)}} \gamma_\mu u^{(\alpha)} + \overline{d^{(\alpha)}} \gamma_\mu d^{(\alpha)} \right) . \tag{3.4.15}$$

The factor in front of the current associated with B takes into account that each quark comes with three colors due to $SU(3)_C$. L and B are then given by:

$$L = \int d^3x \, j_0^L = \int d^3x \, j_0^B = B \, . \tag{3.4.16}$$

In the SM, L and B are conserved at tree level, but not at loop level, where interactions with SM electroweak gauge fields yield divergences different from zero, i.e.:

$$\partial^\mu j_\mu^L = \partial^\mu j_\mu^B = \frac{N_f}{32\pi^2} \left(g^2 F_{2,\mu\nu}^a \tilde{F}_2^{a\mu\nu} - g'^2 F_{1,\mu\nu} \tilde{F}_1^{\mu\nu} \right) , \tag{3.4.17}$$

see equations (2.1.10) and (2.1.11), and the relevant discussion in [131]. N_f is the number of fermion generations, which equals three in the SM. Thus, L and B are so-called anomalous global symmetries. Since the divergence of j_μ^L equals the divergence of j_μ^B, the global symmetry $B - L$ is conserved, even by topological effects like sphalerons [132].

Motivated by this fact, we consider $B - L$ as a global symmetry of the Zee–Babu-model. This symmetry forbids the μ-term. Neutrino masses are then generated by breaking the $B - L$ symmetry. We break $B - L$ spontaneously with a complex scalar $SU(2)_L$ singlet φ,

$$\varphi = \frac{1}{\sqrt{2}} (w + \sigma + i\rho) \, , \tag{3.4.18}$$

where $\sigma = \sqrt{2}\mathrm{Re}(\varphi)$ and $\rho = \sqrt{2}\mathrm{Im}(\varphi)$ are real scalar fields. φ is assigned the lepton number -2, so the VEV of φ, i.e., $w/\sqrt{2}$, breaks $B - L$ spontaneously [133]. The scalar potential contains a term

$$V_\mu = \lambda_\mu \varphi k^{++} h^- h^- + \mathrm{h.c.} \, , \tag{3.4.19}$$

inducing the μ-term' once φ acquires its VEV, with:

$$\mu = \lambda_\mu \frac{w}{\sqrt{2}}\,, \qquad \langle\varphi\rangle = \frac{w}{\sqrt{2}}\,. \tag{3.4.20}$$

The full scalar potential of the model is:

$$\begin{aligned} V_{\text{scalar}} =& V_\mu + \mu_\varphi^2 \varphi^*\varphi + \mu_H^2 H^\dagger H + \mu_k^2 k^{++}k^{--} + \mu_h^2 h^+h^- \\ &+ \lambda_\varphi(\varphi^*\varphi)^2 + \lambda_H(H^\dagger H)^2 + \lambda_k(k^{++}k^{--})^2 + \lambda_h(h^+h^-)^2 \\ &+ \lambda(\varphi^*\varphi)(H^\dagger H) + \lambda_1(\varphi^*\varphi)(k^{++}k^{--}) + \lambda_2(\varphi^*\varphi)(h^+h^-) \\ &+ \lambda_3(H^\dagger H)(k^{++}k^{--}) + \lambda_4(H^\dagger H)(h^+h^-) \\ &+ \lambda_5(k^{++}k^{--})(h^+h^-)\,, \end{aligned} \tag{3.4.21}$$

where V_μ is given in equation (3.4.19) and μ_i are parameters of mass dimension one, and λ_i are dimensionless couplings.

The λ-coupling in the potential induces mixing between φ and H, and thus it opens the Higgs portal, as introduced in section 2.5, which connects to DM physics as discussed in section 3.4.4. Besides gauge kinetic mixing of the SM $U(1)_Y$ with an additional local abelian gauge group, the Higgs portal represents the unique renormalizable gauge invariant s-channel interaction between the SM sector and the DM sector [134].

There are two massive neutral scalars in the theory, with propagating mass eigenstates denoted by H_1 and H_2. They are related to the real part σ of φ and to the real part h of the neutral component of H by

$$\begin{pmatrix} H_1 \\ H_2 \end{pmatrix} = \begin{pmatrix} \cos\alpha & \sin\alpha \\ -\sin\alpha & \cos\alpha \end{pmatrix} \begin{pmatrix} \sigma \\ h \end{pmatrix}\,, \tag{3.4.22}$$

where the mixing angle α is given by:

$$\tan 2\alpha = \frac{\lambda w v}{\lambda_\varphi w^2 - \lambda_H v^2}\,, \tag{3.4.23}$$

and v denotes the VEV of the Higgs $SU(2)_L$ doublet H, see equation (2.1.3). The masses of H_1 and H_2 are:

$$m_{H_{1,2}}^2 = \lambda_\varphi w^2 + \lambda_H v^2 \pm \sqrt{(\lambda_\varphi w^2 - \lambda_H v^2)^2 + \lambda^2 w^2 v^2}\,. \tag{3.4.24}$$

The parameters $\mu_{\varphi,H}$ in equation (3.4.21) can be eliminated with the help of the minimum conditions for the potential. Since the true vacuum state is the global minimum of the potential, the derivatives of the potential with respect to the vacuum expectation values must vanish. $\mu_{\varphi,H}$ thus have to be equal to:

$$\mu_\varphi^2 = -\left(\lambda_\varphi w^2 + \frac{1}{2}\lambda v^2\right) \tag{3.4.25}$$

$$\mu_H^2 = -\left(\lambda_H v^2 + \frac{1}{2}\lambda w^2\right)\,. \tag{3.4.26}$$

With these minimization conditions, the masses for the fields σ and h can be expressed as:

$$m_\sigma^2 = 2\lambda_\varphi w^2 \tag{3.4.27}$$
$$m_h^2 = 2\lambda_H v^2\,, \tag{3.4.28}$$

such that the mixing angle α equals:

$$\tan 2\alpha = \frac{2\lambda w v}{m_\sigma^2 - m_h^2}\,. \tag{3.4.29}$$

With the above expressions for the mass eigenvalues, we can write λ in terms of the mass eigenvalues and the mixing angle:

$$\lambda = \frac{1}{2}\frac{(m_{H_1}^2 - m_{H_2}^2)\sin 2\alpha}{wv}\,. \tag{3.4.30}$$

Therefore the neutral scalar phenomenology depends only on three independent parameters in addition to the VEVs v, w, which can be chosen to be either $(\lambda_\varphi, \lambda_H, \lambda)$ or alternatively, $(m_{H_1}, m_{H_2}, \alpha)$. We have chosen the neutral scalar mass eigenvalues and the mixing angle as independent parameters.

The terms of the potential that are quadratic in the imaginary part ρ of the complex $SU(2)_L$ singlet φ add up to $1/2 \cdot \mu_\varphi^2 + nicefrac12 \cdot \lambda_\varphi w^2 + nicefrac14 \cdot \lambda v^2$, which results in zero due to the minimization condition for μ_φ^2. This is Goldstone's theorem [135], which dictates the appearance of a massless scalar in the spectrum due to the spontaneous breaking of the global $U(1)$ symmetry. In our model, ρ is the Goldstone boson. In writing φ in terms of its real and imaginary parts, all interactions in the Lagrangian are renormalizable, however, in this linear parametrization, it is not obvious that the Goldstone boson ρ decouples at low energies, which it does according to the Goldstone's theorem [135]. The decoupling is nevertheless guaranteed by cancellation of terms in the scattering amplitude [136]. Alternatively, the complex valued field φ can be written as:

$$\varphi = re^{i\frac{\gamma}{w}}\,. \tag{3.4.31}$$

In this parametrization, $r = \sqrt{\sigma^2 + \rho^2}$ and γ is the complex phase, which corresponds to the Majoron. The two parametrizations are equivalent, as pointed out in [136]. In this non-linear parametrization, the Majoron, for which we use again the notation ρ in the following, has derivative couplings to other particles, which directly display the vanishing interactions at low momenta and the non-renormalization of its interactions. Writing the kinetic term of φ and the λ_5 term of the potential in the non-linear parametrization, the following terms for the Goldstone boson ρ result:

$$\frac{1}{w^2} r^2 \partial_\mu \rho \partial^\mu \rho - \lambda r^2 (H^\dagger H)\,. \tag{3.4.32}$$

The SM Higgs $SU(2)_L$ doublet H couples to SM fermions f. Once the $SU(2)_L$ singlet and $SU(2)_L$ doublet vacuum expectation values are adopted, respectively, the above interactions induce a Feynman diagram with the Goldstone bosons ρ as initial particles and SM fermions f as final state particles. The scalar exchange of r and H then yields the interaction:

$$\frac{\lambda m_f}{m_r^2 m_h^2} f\overline{f}\partial_\mu\rho\partial^\mu\rho\,. \tag{3.4.33}$$

Due to the definition of r, m_r follows directly from m_σ in equation (3.4.27). Since the VEV of φ is responsible for lepton number breaking, and the generation of trilinear scalar coupling inside the two-loop, which generates light Majorana neutrino masses, we call ρ a Majoron [137], even though it does not couple directly to leptons.

Since φ is an $SU(2)_L$ singlet, there is no direct coupling of ρ to the Z boson like in $SU(2)_L$ triplet Majoron models [41]. If the Majoron is a member of a scalar $SU(2)_L$ triplet, there would be an additional invisible decay channel for the SM Z boson into the neutral component of the$SU(2)_L$ triplet and the Majoron, given that the neutral scalar is lighter than half of the Z mass. This additional contribution to the invisible decay width of the Z boson would count as $\Delta n_\nu = 2$ extra light neutrinos, which is clearly ruled out by the measurement of the number of light neutrinos that interact with the Z boson yielding the SM value of three light neutrinos, see table 2.3.

The couplings of the Majoron ρ to the Higgs mass eigenstates H_1 and H_2 are obtained from the λ_1 and λ_5 terms of the potential (3.4.21):

$$\mathcal{L}_\rho = \frac{1}{2w}\left(m_{H_1}^2\cos\alpha\, H_1 - m_{H_2}^2\sin\alpha\, H_2\right)\rho^2\,. \tag{3.4.34}$$

In addition to the charged scalar signatures, the presence of the Majoron will modify Higgs physics. As pointed out in [138], an important feature of Majoron models are invisible Higgs decays $H \to \rho\rho$, which we discuss now.

In the SM, the Higgs boson dominantly decays into bottom pairs. For a Higgs mass of 125 GeV, the central values for the leading SM Higgs branching ratios are [139]:

$$BR(H \to b\bar{b}) = 5.77 \times 10^{-1}\,, \tag{3.4.35}$$
$$BR(H \to W^+W^-) = 2.15 \times 10^{-1}\,, \tag{3.4.36}$$
$$BR(H \to gg) = 8.57 \times 10^{-2}\,, \tag{3.4.37}$$
$$BR(H \to \tau^+\tau^-) = 6.32 \times 10^{-2}\,, \tag{3.4.38}$$
$$BR(H \to c\bar{c}) = 2.91 \times 10^{-2}\,, \tag{3.4.39}$$
$$BR(H \to ZZ) = 2.64 \times 10^{-2}\,. \tag{3.4.40}$$

In our model, the corresponding decay widths for the two Higgs mass eigenstates H_1 and

H_2 are weighted with the Higgs mixing angle α:

$$\Gamma\left(H_1 \to b\bar{b}\right) = \frac{3\sqrt{2}G_F m_b^2 m_{H_1}}{8\pi}\left(1-\frac{4m_b^2}{m_{H_1}^2}\right)^{\frac{3}{2}}\sin^2\alpha\,, \tag{3.4.41}$$

$$\Gamma\left(H_2 \to b\bar{b}\right) = \frac{3\sqrt{2}G_F m_b^2 m_{H_2}}{8\pi}\left(1-\frac{4m_b^2}{m_{H_2}^2}\right)^{\frac{3}{2}}\cos^2\alpha\,. \tag{3.4.42}$$

The invisible decay modes into the Majoron ρ are obtained from the Lagrangian in equation (3.4.34):

$$\Gamma\left(H_1 \to \rho\rho\right) = \frac{\sqrt{2}G_F}{32\pi}m_{H_1}^3\left(\frac{v}{w}\right)^2\cos^2\alpha\,, \tag{3.4.43}$$

$$\Gamma\left(H_2 \to \rho\rho\right) = \frac{\sqrt{2}G_F}{32\pi}m_{H_2}^3\left(\frac{v}{w}\right)^2\sin^2\alpha\,, \tag{3.4.44}$$

and therefore [140]:

$$\frac{\Gamma\left(H_1 \to \rho\rho\right)}{\Gamma\left(H_1 \to b\bar{b}\right)} = \frac{1}{12}\left(\frac{m_{H_1}}{m_b}\right)^2\left(\frac{v}{w}\right)^2\cot^2\alpha\left(1-\frac{4m_b^2}{m_{H_1}^2}\right)^{-\frac{3}{2}} \tag{3.4.45}$$

$$\approx 250\left(\frac{m_{H_1}}{w}\right)^2\cot^2\alpha\,, \tag{3.4.46}$$

$$\frac{\Gamma\left(H_2 \to \rho\rho\right)}{\Gamma\left(H_2 \to b\bar{b}\right)} = \frac{1}{12}\left(\frac{m_{H_2}}{m_b}\right)^2\left(\frac{v}{w}\right)^2\tan^2\alpha\left(1-\frac{4m_b^2}{m_{H_2}^2}\right)^{-\frac{3}{2}} \tag{3.4.47}$$

$$\approx 250\left(\frac{m_{H_2}}{w}\right)^2\tan^2\alpha\,. \tag{3.4.48}$$

Invisible Higgs decays are searched for in associated ZH production among other channels. The produced Z decays into charged leptons and the Higgs can decay into invisible particles.

The SM contribution, which is used in the underlying analysis searches, is the decay of the produced Higgs into two Z bosons, each of which decays into two neutrinos such that the resulting channel is $ZH \to l\,l + 4\nu$. The signal for an invisibly decaying Higgs is then an excess of events over the SM channel $ZH \to l\,l + 4\nu$ plus large missing transverse energy final states.

The search [141] for invisible decays of a Higgs boson analyzed pp collision data corresponding to $13.0\,\mathrm{fb}^{-1}$ at $\sqrt{s} = 8\,\mathrm{TeV}$, and 71 signals were observed at an expected background of $78.0 \pm 2 \pm 6.5$ signals, yielding an exclusion limit of 84% for invisible branching fractions greater than 65%. Using the fixed values $m_{H_1} = 300\,\mathrm{GeV}$, $m_{H_2} = 120\,\mathrm{GeV}$, $v = 246\,\mathrm{GeV}$, $w = 1000\,\mathrm{GeV}$ and $\sin\alpha = 0.1$, the invisible decay width in our model result in $\Gamma\left(H_1 \to \rho\rho\right) \approx 0.27\,\mathrm{GeV}$ and $\Gamma\left(H_2 \to \rho\rho\right) \approx 0.17 \times 10^{-3}\,\mathrm{GeV}$. The total decay widths Γ_H of the Higgs boson measured in the decay into two gauge bosons are

$\Gamma_H(m_H = 300\,\text{GeV}) = 8.43\,\text{GeV}$ and $\Gamma_H(m_H = 120\,\text{GeV}) = 3.48 \times 10^{-3}\,\text{GeV}$. Hence, for the fixed values our model yields $\Gamma(H_1 \to \rho\rho) \approx 3.20\%\,\Gamma_H(m_H = 300\,\text{GeV})$ and $\Gamma(H_2 \to \rho\rho) \approx 4.89\%\,\Gamma_H(m_H = 120\,\text{GeV})$, which is not excluded by the current bounds from associated ZH production.

In the view of additional relativistic degrees of freedom that contribute to the number N_{eff} of effective neutrinos, the massless Majoron is also worth to study. In the next section, we investigate the role of Goldstone bosons in the context of relativistic degrees of freedom.

3.4.2. The Majoron as a Fractional Cosmic Neutrino?

The massless Majoron contributes to the radiation density ρ of the Universe given by:

$$\rho = \frac{\pi^2}{30} g_{\text{eff}}(T)\, T^4\,, \tag{3.4.49}$$

where T is the temperature of the thermal plasma. g_{eff} is the effective number of relativistic degrees of freedom contributing to the energy density. In the early Universe, when the temperature T is much larger than the masses of the particle species i in thermal equilibrium, g_{eft} follows to:

$$g_{\text{eff}} = \sum_B g_B \left(\frac{T_B}{T}\right)^4 + \frac{7}{8} \sum_F g_F \left(\frac{T_F}{T}\right)^4\,, \tag{3.4.50}$$

for details see equations (C.0.10) and (C.0.12).

As long as a particle is in thermal contact with the plasma, its temperature $T_{B,F}$ equals the temperature T of the thermal plasma. Δn_ν additional relativistic neutrinos make the contribution of $7/8 \cdot 2 \cdot \Delta n_\nu$ to g_{eff}, because particle and antiparticle contribute. Therefore the contribution of one thermalized scalar, i.e., $\Delta g_{\text{eff}} = 1$, equals the contribution of $\Delta n_\nu = 4/7$ neutrinos. Hence, a Majoron that is in thermal equilibrium contributes with $\Delta n_\nu = 4/7 \approx 0.57$ neutrinos to the effective number of relativistic degrees of freedom.

The SM neutrinos decouple from the thermal plasma at a temperature of about 1 MeV, when the weak interaction rate becomes smaller than the Hubble expansion rate. Below this temperature, electrons and positrons have not yet decoupled from the thermal equilibrium with photons. However, after they have finally decoupled, the transfer entropy to the photons and not to the neutrinos, which left equilibrium earlier. The temperature T_ν of neutrinos is therefore smaller than the temperature T_γ of the photons; the ratio of T_ν and T_γ follows from entropy conservation, which relies on an isentropic expansion of the Universe. The SM neutrino decoupling occurs just before the temperature T drops below the mass $m_e = 511\,\text{keV}$ of the electron, i.e., electron-positron annihilations are no longer in thermal equilibrium with the photons at $T \approx 1\,\text{MeV}$. The

number of effective degrees of freedom decreases from $^{11}/_{2}$, including electron, positron and photon, to 2, only including photons. Due to entropy conservation the product $(a(t_{\text{after}})T_\gamma(t_{\text{after}}))^3$ must therefore be larger than the product $(a(t_{\text{before}})T_\nu(t_{\text{before}}))^3$ at the time t_{before} just before electron-positron decoupling, when $T \approx 1\,\text{MeV}$. The outcome for the present day time radiation density ρ reads:

$$\rho = \left(1 + N_{\text{eff}} \frac{7}{8} \left(\frac{4}{11}\right)^{\frac{4}{3}}\right) \rho_\gamma \,, \tag{3.4.51}$$

see also (2.3.19). $N_{\text{eff}} = 3 + \Delta n_\nu$ is the effective neutrino number. In the SM with three generations of neutrinos, $N_{\text{eff}} = 3.046$, which does not equal three due to non-instantaneous decoupling corrections. The *Planck* 2013 result on N_{eff} is $3.36^{+0.68}_{-0.64}$ at 95% confidence level, see also table 2.3. Hence, a Majoron that is still in thermal equilibrium with the photons and therefore contributes with $\Delta n_\nu \approx 0.57$ to N_{eff} would be in conflict if the central value of $N_{\text{eff}} = 3.36$ measured by *Planck* is taken seriously. But as for the SM neutrinos, the Majoron could go out of equilibrium earlier such that due to entropy production one Majoron contributes with:

$$\Delta n_\nu = \frac{4}{7} \left(\frac{g_{\text{eff}}(T_{\text{after}})}{g_{\text{eff}}(T_{\text{before}})}\right)^{\frac{4}{3}} < \frac{4}{7} \,. \tag{3.4.52}$$

Recently, Weinberg suggested Goldstone bosons as fractional cosmic neutrinos.

If the Goldstone boson goes out of thermal equilibrium after the era of muon annihilation, it contributes $^4/_7 \cdot (^{43}/_{57})^{4/3} \approx 0.39$ to N_{eff} [142]. When the rate of interactions that keep the Goldstone boson in thermal equilibrium becomes smaller than the Hubble expansion rate $H \propto {}^{T^2}/_{m_{\text{pl}}}$, where m_{pl} is the Planck-mass, the Goldstone boson goes out of equilibrium.

In our model, we consider the interaction given in (3.4.33) as the relevant interaction, which thermalizes the Goldstone boson. The derivative couplings of the Goldstone boson are equivalent to its momentum. Being a relativistic particle, the Goldstone particle moves with the speed of light, which equals one in natural units, i.e., its velocity $v = 1$ and its average momentum scales like T. The number density n of a relativistic particle scales like T^3. The interaction rate $\Gamma_{\text{int}} = n\sigma v$ then scales like $T^3(TT)^2 = T^7$, or more accurately:

$$\Gamma_{\text{int}} \propto \frac{\lambda^2 m_f^2}{m_\sigma^4 m_h^4} T^7 \,. \tag{3.4.53}$$

Assuming that the fermion mass m_f below a temperature T scales like T, the ratio Γ_{int}/H equals one for temperatures T equal to:

$$T_{\text{eq}} = \left(\frac{m_\sigma^4 m_h^4}{\lambda^2 m_{\text{pl}}}\right)^{\frac{1}{7}} \,. \tag{3.4.54}$$

For $T < T_{\rm eq}$, the Goldstone boson goes out of thermal equilibrium. Using the relations (3.4.27) and (3.4.30), $T_{\rm eq}$ can be written as a function of the mass eigenvalues and the scalar mixing angle.

In our model, which is acknowledged by Weinberg, the Majoron typically decouples from the plasma at temperatures above the QCD phase transition, where the effective number of relativistic degrees of freedom is $\gtrsim 60$. Therefore, due to the entropy production at the QCD phase transition, the Majoron abundance gets diluted, and during BBN, ρ contributes only with

$$\Delta n_\nu \lesssim \frac{4}{7}\left(\frac{10.75}{60}\right)^{\frac{4}{3}} \approx 0.06 \tag{3.4.55}$$

to the relativistic energy density, in good agreement with the above mentioned bound.

So far, we have shown the importance of the global $B-L$ symmetry for neutrino mass generation in the Zee–Babu-model and discussed the Goldstone boson associated with its spontaneous breaking. In the following section, we use the global $B-L$ symmetry to connect to DM physics.

3.4.3. Stable Dark Matter Particle from Global $B-L$ Symmetry

Having a global $B-L$ symmetry, which is motivated by neutrino masses, it is tempting to ask if it could play also a role in stabilizing DM.

We introduce chiral fermions N_i, which are $SU(2)_L$ singlets under the SM gauge group, but charged under $U(1)_{B-L}$ in such a way that the Yukawa interaction with the SM Higgs $SU(2)_L$ doublet H, i.e.,:

$$\bar{L}_j \tilde{H} N_i \,, \tag{3.4.56}$$

where $\tilde{H} \equiv i\sigma_2 H^*$, is forbidden. Hence, our N_i cannot have lepton number $+1$, and therefore they are not right-handed neutrinos in the conventional sense. Still we want the mass term for N_i to be generated by spontaneous lepton number breaking from the term:

$$\mathcal{L}_N = \frac{1}{2} h_{ij}\, \varphi\, N_i^T \mathbf{C}^{-1} N_j + \text{h.c.}\,. \tag{3.4.57}$$

This can be achieved by introducing two N fields, N_1 and N_2, and assigning them lepton numbers q_1 and q_2, respectively, such that $q_1 + q_2 = 2$ with $q_1 \neq q_2 \neq 1$; for example $q_1 = 1/2$ and $q_2 = 3/2$. Then no Yukawa term with the lepton $SU(2)_L$ doublets is allowed and equation (3.4.57) leads to a mass matrix:

$$M_N = \begin{pmatrix} 0 & m_\chi \\ m_\chi & 0 \end{pmatrix} \quad \text{with} \quad m_\chi = \lambda_\chi \frac{w}{\sqrt{2}}\,, \tag{3.4.58}$$

and $\lambda_\chi \equiv h_{12}$. Hence, N_1 and N_2 form a Dirac particle χ, with a pair of degenerate mass eigenstates with mass m_χ and opposite CP parity:

$$\chi_1 = \frac{1}{\sqrt{2}}(N_1 + N_2)\,, \qquad \chi_2 = \frac{i}{\sqrt{2}}(N_1 - N_2)\,. \tag{3.4.59}$$

They are stable because of an accidental $\mathbb{Z}_2$ symmetry that emerges as an unbroken remnant of the global $U(1)_{B-L}$.[4] The interaction in equation (3.4.57) becomes diagonal in the χ_i fields:

$$\mathcal{L}_N = \frac{1}{2}\lambda_\chi\,\varphi(\chi_1^T\mathbf{C}^{-1}\chi_1 + \chi_2^T\mathbf{C}^{-1}\chi_2) + \text{h.c.}\,. \tag{3.4.60}$$

At this point, the question why one does consider a global symmetry instead of a local symmetry demands for discussion. From a theoretical point of view, it is conjectured that an exact quantum field theory of gravity can not have an exact global symmetry. Instead, all symmetries must be gauge symmetries, involving discrete symmetries, which could only be a symmetry if they are a remnant of a broken gauge symmetry [143]. If one starts with a global symmetry, one should then take into account that higher dimensional operators suppressed by the Planck-scale will violate the global symmetry. In our model, breaking of the global $U(1)_{B-L}$ by Planck-scale suppressed operators can provide a mass term for the Majoron [144]. In addition, if the symmetry is violated, the DM particle may not be stable any longer. A Planck-scale suppressed operator at dimension 6 is not problematic because the corresponding lifetime for the DM particle exceeds the age of the Universe. The problem might be a Planck-scale suppressed operator at dimension five, for which an estimate on the lifetime of the DM particle yields $\tau \sim m_{\text{Pl}}^2/m_\chi^3 \approx 10^7$ s for $m_\chi \sim 100\,\text{GeV}$, leaving no DM left today. It is assumed that Planck-scale suppressed operators induce DM decays only with lifetimes larger than the age of the Universe. In this perspective, the global $U(1)_{B-L}$ put forward in this work is quite reasonable. On the other hand, a gauged $U(1)_{B-L}$ suffers from an axial-vector-current anomaly. Summing over all SM fermions that run in the $[U(1)_{B-L}]^3$ triangle diagram, the result one obtains is 1 for each generation, instead of zero:

$$\sum q_{B-L}^3 = -2(-1)^3 + (-1)^3 + 3\left[-2\left(\frac{1}{3}\right)^3 + \left(\frac{1}{3}\right)^3 + \left(\frac{1}{3}\right)^3\right] = 1\,. \tag{3.4.61}$$

To make the symmetry anomaly-free in each generation, one is forced by theory to introduce a SM fermion $SU(2)_L$ singlet in each generation with $B-L$ charge -1, i.e.,

[4] Note that there are more unbroken accidental symmetries in the Lagrangian. For example there is a $\mathbb{Z}_3$ symmetry $N_1 \to \omega N_1, N_2 \to \omega^2 N_2$ with $\omega^3 = 1$. Another example is an additional $U(1)$ symmetry with opposite charges for N_1 and N_2 but all other fields uncharged. Those accidental symmetries emerge due to the $B-L$ charge assignments of $N_{1,2}$ and they ensure that no Majorana mass term is generated for them after $B-L$ breaking.

three right-handed neutrinos. In the scenario with a global $U(1)_{B-L}$, the neutrinos are added by hands without theoretical motivation, except for being a candidate particle for DM.

Obviously, the $B-L$ charges of the right-handed neutrinos needed to make the gauged $B-L$ symmetry anomaly-free in each generation are fixed to -1, and they are not free such that Yukawa couplings to the SM Higgs $SU(2)_L$ doublet emerge, which make the right-handed neutrinos unstable and thereby exclude them to be a stable DM particle. To forbid Yukawa couplings to SM particles and preserve one of the three right-handed neutrinos as DM candidate, a stabilization symmetry has to be considered in addition to the gauged $U(1)_{B-L}$. This is not needed for a global $U(1)_{B-L}$ symmetry. In that case, there are no gauge anomaly conditions to be fulfilled and the charges of the right-handed neutrinos can be chosen freely. This freedom in choosing the $B-L$ charge can be exploited to make the right-handed neutrino stable without any further additional symmetry. The stabilization symmetry in this case arises as a remnant of the spontaneously broken global symmetry.

Apart from that, for a gauged $U(1)_{B-L}$ symmetry, there is a severe constraint from electroweak precision observables on the ratio of the mass and the coupling constant of the $U(1)_{B-L}$ gauge boson. This constraint is very restricting for the DM phenomenology as will be discussed below. In the scenario with a spontaneously broken global $U(1)_{B-L}$, there is no gauge boson but a Goldstone boson and therefore the DM phenomenology in this scenario is richer. Weighing up the pro and contra arguments, we investigate the scenario of the global $U(1)_{B-L}$. It is then the spontaneous breaking of the global $U(1)_{B-L}$ symmetry that gives masses to neutrinos by generating the trilinear μ-term dynamically and at the same time gives masses to and stabilizes DM.

The only particle to which χ_i can couple is the scalar φ, with the coupling λ_χ, which is related to the DM mass via the VEV w, see equation (3.4.58). Furthermore, the coupling of φ to the SM is provided via the Higgs portal proportional to λ_5, or to the mixing angle α. Therefore the two parameters λ_χ and α will play an important role for DM phenomenology, as we are going to discuss in the following subsections.

We first point out the annihilation reactions that generate the DM relic density. All of the annihilation channels with SM particles in the final state are driven by the Higgs portal, which is the decisive communication portal in our model. Besides producing the correct amount of the DM relic density, the Higgs portal also makes the direct detection of the DM possible, which we discuss in a further subsection.

3.4.4. Relic Density of Dark Matter

The relic DM density $\Omega_{\mathrm{DM}}h^2$ is determined by the thermal freeze-out of χ_i in the early Universe. In the model presented here, the two DM particles χ_1 and χ_2 have identical couplings to φ. Hence, the annihilation cross sections are the same and they will contribute

in equal parts to the total DM density, i.e., $\Omega_{\rm DM} = \Omega_{\chi_1} + \Omega_{\chi_2}$. The numerical calculation of the relic density $\Omega_{\rm DM}$ is performed with the micrOMEGAs software package [64]. The Higgs portal is the dominant communication channel between the SM and the DM sector. It opens s-channel annihilations for the two DM particles χ_i into a quark–antiquark pair, into SM gauge bosons, into the massive scalars $H_{1,2}$, into the Zee–Babu scalars k^{++}, h^+, as well as in the Majoron ρ. As examples, the cross sections for annihilation via s-channel $H_{1,2}$ exchange into $b\,\bar{b}$, W^+W^- and $k^{++}k^{--}$, as well as the t- and u-channel annihilation into $\rho\rho$, are shown:

$$\begin{aligned}
\sigma_{b\bar{b}} v_r \approx & \lambda_\chi^2 \, \sin^2 2\alpha \, \frac{y_b^2 v_r^2}{1024\pi m_\chi} \cdot \frac{(m_{H_1}^2 - m_{H_2}^2)^2}{(s - m_{H_1}^2)^2 (s - m_{H_2}^2)^2} \\
& \times \left(s - 4m_b^2\right)^{3/2} , \qquad (3.4.62) \\
\sigma_{WW} v_r \approx & \lambda_\chi^2 \, \sin^2 2\alpha \, \frac{g^4 v^2 v_r^2}{2048\pi m_\chi} \cdot \frac{(m_{H_1}^2 - m_{H_2}^2)^2}{(s - m_{H_1}^2)^2 (s - m_{H_2}^2)^2} \\
& \times \sqrt{(s - 4m_W^2)} \left[1 + \frac{1}{2}\left(\frac{s}{2m_W^2} - 1\right)^2\right] , \qquad (3.4.63) \\
\sigma_{kk} v_r = & \lambda_1^2 \, \frac{m_\chi v_r^2}{32\pi} \, \frac{\left[(s - m_{H_2}^2)\cos\alpha - (s - m_{H_1}^2)\sin\alpha\right]^2}{(s - m_{H_1}^2)^2 \, (s - m_{H_2}^2)^2} \\
& \times \sqrt{s - 4m_k^2} \, , \qquad (3.4.64) \\
\sigma_{\rho\rho} v_r = & \lambda_\chi^4 \, \frac{v_r^2}{1536\pi m_\chi^2} \, . \qquad (3.4.65)
\end{aligned}$$

We expanded $s = {}^{4m_\chi^2}/_{1 - v_r^2/4}$ in $v_r \ll 1$ to show explicitly the velocity suppression of the annihilation. However, we keep s in the kinematical terms, as well as in the denominators, to show the resonant behavior of the s-channel cross section as a function of the DM mass m_χ. s-channel-annihilations into SM particles are controlled by the Higgs portal, and are therefore proportional to the mixing parameters $\sin^2 2\alpha$ and ${}^{(m_{H_1}^2 - m_{H_2}^2)^2}/_{((s - m_{H_1}^2)^2 (s - m_{H_2}^2)^2)}$. For simplicity, we also neglect here the width of the resonances, which are however included in the numerical calculations presented below. In equation (3.4.62), y_b and m_b are the b-quark Yukawa coupling and mass, respectively. The annihilation cross section of DM into a ZZ pair can be obtained from equation (3.4.63) by replacing $g \to g' = {}^{g}/_{\sqrt{2}\cos\theta_W}$ and $m_W \to m_Z$. The annihilation cross section into h^+h^- can be obtained from equation (3.4.64) by replacing $\lambda_1 \to \lambda_2$ and $m_{k^{++}} \to m_{h^+}$.

The full annihilation cross section $\chi\chi \longrightarrow \rho\rho$ receives also contributions from an s-channel diagram, whereas equation (3.4.65) shows only the t-and u-channel contribution for simplicity. This is the only case without the suppression by the Higgs masses $m_{H_{1,2}}$.

Annihilations into the Majoron and the Zee–Babu scalars survive even in the case of no mixing ($\sin 2\alpha = 0$, or $\lambda = 0$). Hence, these annihilation channels still provide a

mechanism to generate the correct relic abundance at the electroweak scale for $\sin 2\alpha = 0$, despite of χ_i's being completely decoupled from the SM.

All annihilation cross sections are proportional to the coupling λ_χ, because the only particle χ can directly couple to is the scalar $SU(2)_L$ singlet φ for which the corresponding coupling constant is λ_χ. In equation (3.4.64), λ_χ would appear together with the VEV w; it has been absorbed into the DM mass via equation (3.4.58). For a given set of parameters, the left column of plots in figure 3.10 shows the relative contribution of the various annihilation channels to the relic abundance. The middle and the right panels of the figure show the coupling λ_χ and the $SU(2)_L$ singlet VEV w that are needed to obtain the correct relic abundance. Note that for a given DM mass m_χ, λ_χ and w are simply related by equation (3.4.58). We have chosen representative values for the two scalar masses $m_{H_1} = 300\,\text{GeV}$ and $m_{H_2} = 120\,\text{GeV}$, but we have verified that our conclusions do not depend on this specific choice and hold within the full range of reasonable values for the Higgs masses. Taking the SM Higgs mass value of $m_{H_2} = 125.5 \pm 0.2\,(\text{stat.})^{+0.5}_{-0.6}\,(\text{sys})\,\text{GeV}$ [145], the first resonant peak in the middle and the right panels in figure 3.10 simply shift from the current position at $m_\chi = 60\,\text{GeV}$ to the new position at $m_\chi = 62.75\,\text{GeV}$. The couplings $\lambda_\mu, \lambda_{k,h,1,2,3,4,5}$ have been set to one. Again we have checked that random values in the range from 0.1 to 1 give qualitative similar results.

The upper two rows of plots in figure 3.10 correspond to a relatively large Higgs mixing angle of $\alpha = \pi/4$. For this value of the mixing angle, $\cos\alpha = \sin\alpha$. Therefore, the σ and h contribute with an equal amount to the propagating mass eigenstates H_1 and H_2, which makes two resonances at $m_\chi \simeq m_{H_{1,2}}/2$ clearly visible. Depending on the DM mass various annihilation channels are important.

In the lower two rows we use the same parameters, but a small Higgs mixing: $\sin\alpha = 0.01$, for which $\cos\alpha \approx 1$. In this case, the mass eigenstate H_1 practically coincides with the $SU(2)_L$ singlet φ, and therefore only the resonance corresponding to H_1 exchange occurs. Furthermore, the coupling to SM particles is suppressed and the relic density is provided only by annihilations into the massless Majoron or, if kinematically accessible, into H_1 and the Zee–Babu scalars $k^{\pm\pm}, h^\pm$.

In figure 3.10, we compare also two assumptions on the masses of the Zee–Babu scalars. For masses larger than the Higgs masses, annihilations into $k^{\pm\pm}$ and $h^\pm$ are subdominant, but if one of the charged scalars is lighter than one of the neutral scalars, they can dominate DM annihilations, as visible in rows b) and d).

Note also the modified shape of the curves close to the resonance if the dominant annihilation channel is into charged scalars. Whenever a pair of SM particles is in the final state, the annihilation must proceed via scalar mixing because χ only couples to φ, which is a $SU(2)_L$ singlet and has thus to mix with the SM Higgs $SU(2)_L$ doublet H in order to have a s-channel portal to SM particles. However, the annihilation channel with the pair $k^{++}k^{--}$ of doubly-charged scalars in the final state does not need a scalar

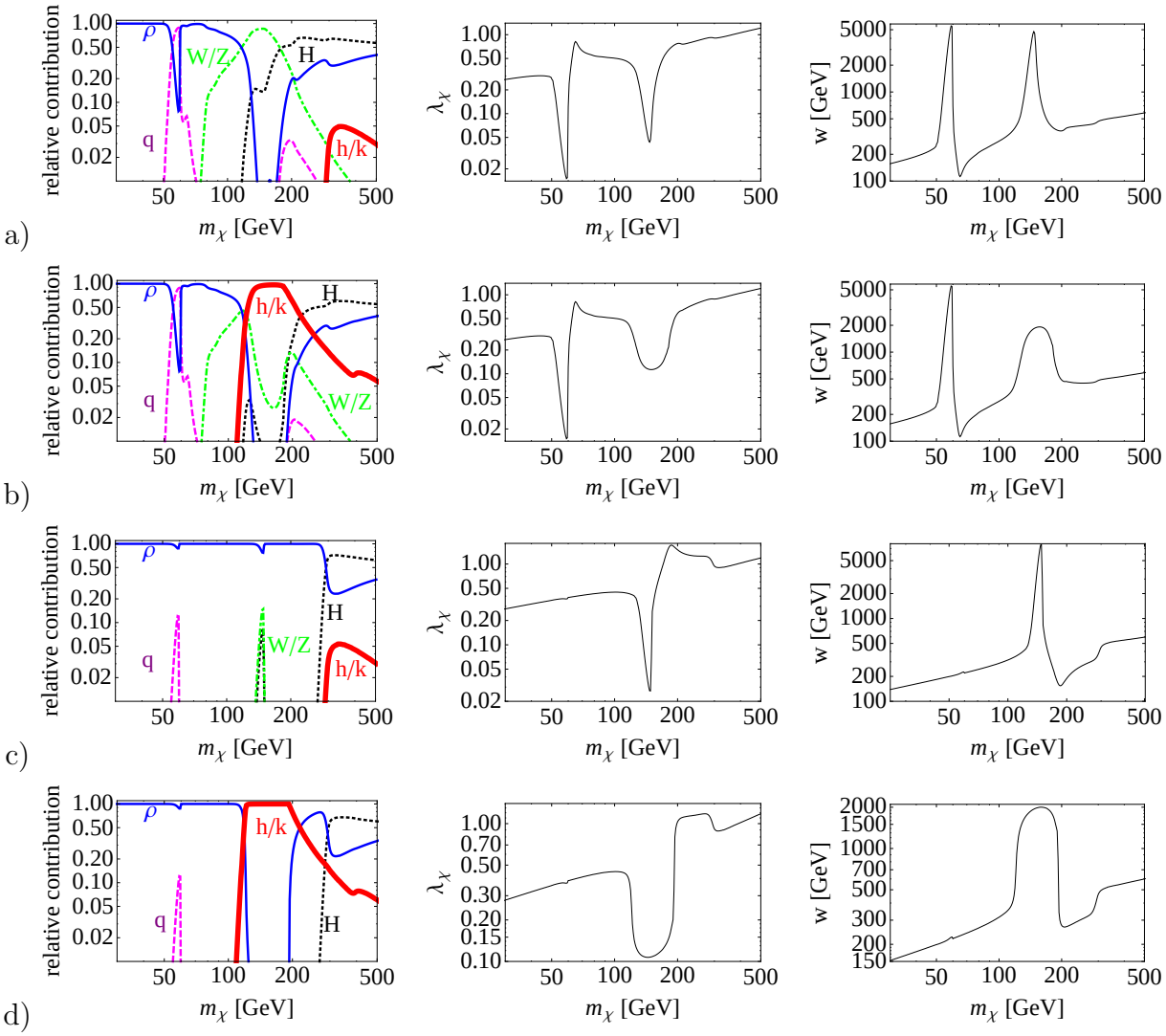

Figure 3.10.: Left: Relative contribution of annihilation channels to the relic DM abundance. Shown are annihilations into H_1 and H_2 (H), quarks (q), W and Z bosons (W/Z), Majorons (ρ) and Zee–Babu scalars (h/k). Middle and right columns show the DM scalar coupling λ_χ and $SU(2)_L$ singlet VEV, respectively, which lead to the correct relic DM density. We assume $m_{H_1} = 300\,\text{GeV}$, $m_{H_2} = 120\,\text{GeV}$, and all Zee–Babu scalar couplings are set to unity. Rows a) and b) are for a Higgs mixing angle $\sin\alpha = 0.7$, rows c) and d) for $\sin\alpha = 0.01$. Rows a) and c) are for Zee–Babu scalar masses $m_{h^+} = 300\,\text{GeV}$, $m_{k^{++}} = 800\,\text{GeV}$, rows b) and d) for $m_{h^+} = 120\,\text{GeV}$, $m_{k^{++}} = 400\,\text{GeV}$.

mixing, it is also possible if $\sin\alpha = 0$, in which case only the Higgs mass eigenstate H_2 is exchanged in the s-channel without mixing. While the shape of the resonance of the cross section itself remains the same, the different shape for λ_χ, which gives the correct relic abundance, follows from a different dependence of the annihilation cross section on λ_χ and m_χ. The amplitude of the annihilation channel $\chi\chi \longrightarrow k^{++}k^{--}$ is proportional to $\lambda_\chi w = {}^{m_\chi}/_{\sqrt{2}}$. Taking the square of the amplitude and respecting phase-space factors, the corresponding annihilation cross section is proportional to m_χ. In contrast, the cross sections for annihilation into SM particles are proportional to ${}^{\lambda_\chi^2}/_{m_\chi}$.

The middle and right columns of plots in figure 3.10 show that away from the resonances the correct relic abundance is obtained for couplings in the perturbative range, $0.5 \lesssim \lambda_\chi \lesssim 1$, and VEVs between 200 GeV and 500 GeV. Close to the resonances, the s-channel propagator develops its maximum. In order to obtain the correct relic density, the increase of the s-channel propagator has to be compensated by a small λ_χ. Since the product of λ_χ and the VEV w determines the Dark Matter mass m_χ, a small λ_χ corresponds to a large VEV for fixed m_χ, which is visible in the middle and right panel of figure 3.10.

If the symmetry of the model was gauged, there would be a Z' gauge boson with a mass set by w. Since Z' searches require the mass of such a new gauge boson to be above few TeV, e.g. [146], gauged versions of this model would be confined to the resonance regions, see ref. [147] for an example of such a model.

It is therefore an advantage of the global symmetry considered here, that the breaking scale can be lower, and therefore this model does not suffer from the need of tuning the DM mass close to half of the mass of one of the Higgs mass states, i.e., a broader range in the parameter space becomes suitable.

Once the correct DM relic density is produced, the question about the detection of the DM particle arises. In the next section, we therefore comment on the direct detection of the DM particles χ_i.

3.4.5. Direct Detection of Dark Matter

The Higgs portal, which contributes to the correct DM relic density as discussed in the previous section, also mediates DM scattering on nuclei relevant for direct detection via t-channel exchange of the Higgs mass eigenstates H_1 and H_2. Hence, scattering is spin-independent. The elastic scattering cross section σ_p of χ off a proton p is obtained as:

$$\sigma_p = \frac{\lambda_\chi^2 \sin^2 2\alpha}{4\pi}\, m_{\text{red}}^2 \left(\frac{1}{m_{H_1}^2} - \frac{1}{m_{H_2}^2}\right)^2 g_{Hp}^2\,, \tag{3.4.66}$$

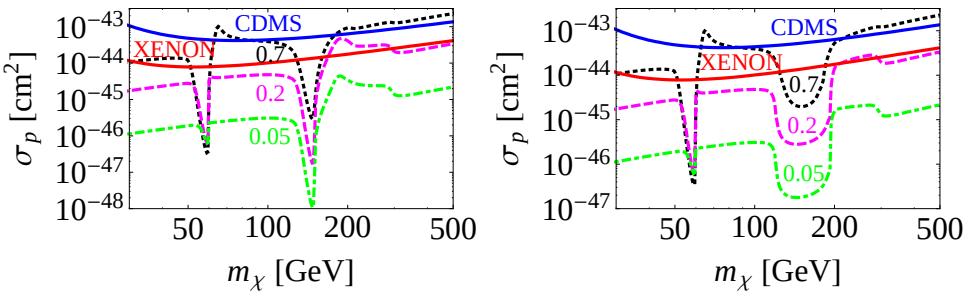

Figure 3.11.: Elastic scattering cross section σ_p of χ off a proton p for $m_{H_1} = 300\,\text{GeV}$ and $m_{H_2} = 120\,\text{GeV}$ and mixing angles $\sin\alpha = 0.7, 0.2, 0.05$, according to the label. The $SU(2)_L$ singlet VEV w has been chosen in order to obtain the correct relic DM abundance. The left (right) panel corresponds to masses of the Zee–Babu scalars of $k^{++} = 800(400)\,\text{GeV}$ and $h^+ = 300(120)\,\text{GeV}$. Also shown are the CDMS and XENON100 exclusion limits, see text for further information.

where $m_{\text{red}} = m_p m_\chi/(m_p + m_\chi)$ is the reduced mass of the DM–proton system and

$$g_{Hp} = \frac{m_p}{v}\left[\sum_{q=u,d,s} f_q^{(p)} + \frac{2}{27}\left(1 - \sum_{q=u,d,s} f_q^{(p)}\right)\right], \tag{3.4.67}$$

see equation (2.6.12) for details and table 2.5 for the values of $f^{(p)}$.

We observe from equation (3.4.66) that the cross section is proportional to the Higgs mixing, since for $\alpha = 0$, the DM particle is decoupled from the SM and therefore the scattering cross section will vanish. Figure 3.11 shows the DM cross section on a proton obtained with micrOMEGAs [64], where for given $m_{H_{1,2}}, \alpha$ and m_χ, the coupling λ_χ,or equivalently the VEV w, has been chosen such that the correct relic abundance is obtained. Therefore the resonances in the annihilation cross section appear also in the scattering cross section. Although the Zee–Babu scalars k^{++} and h^+ do not contribute directly to the scattering cross section, they affect the annihilation cross section relevant for the relic abundance, and therefore also DM–nucleus scattering depends indirectly on their masses, compare left and right panel of figure 3.11.

A part of the parameter space for large values of $\sin\alpha$ has already been excluded by previous bounds [75, 97]. But the cross section can always be suppressed by making α small. Therefore, we can make a prediction on the cross section without being in conflict with the present bounds, e.g., [95], see section 2.6.2 for further discussion. Since generically mixing should be sizable, one may expect observable signals in direct detection searches from this model, although they are not guaranteed.

3.5. Summary: $B - L$ Symmetric Zee–Babu-Model

The Zee–Babu-model [103, 118] generates neutrino masses at two loop level. A singly-charged scalar h^+ and a doubly-charged scalar k^{++} run in the loops. The loops are only closed if a lepton number violating trilinear scalar interaction $\mu k^{++} h^- h^-$ is introduced by hands. In its original version, the Zee–Babu-model does not contain a DM particle.

We generate the lepton number violating μ-term by spontaneous breaking of a global $U(1)_{B-L}$ symmetry. To realize a $B - L$ symmetric model, we extend the Zee–Babu-model by a complex scalar $SU(2)_L$ singlet ϕ, which replaces the trilinear μ-term by $\lambda_\mu \phi k^{++} h^- h^-$. We further introduce two SM $SU(2)_L$ singlet neutrinos N_i that couple to ϕ and get massive when ϕ obtains its VEV. At the same time, a remnant discrete symmetry stabilizes the neutrinos N_i, which are the DM particles in our model. The correct relic density is achieved by freeze-out through a Higgs portal $\lambda(\phi^*\phi)(H^\dagger H)$, with H the SM Higgs $SU(2)_L$ doublet. It is therefore the spontaneous breaking of the global $U(1)_{B-L}$ symmetry that combines neutrino and DM physics.

Due to the spontaneous breaking of a global symmetry, a Goldstone boson appears. We show that the contribution of this Goldstone boson to the relativistic degrees of freedom is negligible small.

Our extended Zee–Babu-model and the Ma-model discussed in section 3.1 explain the DM relic density in the freeze-out mechanism. In the following part of this thesis, the freeze-in mechanism is studied to obtain the correct DM relic density.

Part II.

keV Sterile Neutrino Dark Matter Produced by Freeze-In

4. New Production Mechanism for keV Sterile Neutrino DM

In the previous chapter, we provided two exemplary models, which at the same time explain neutrino masses and the DM relic density. The neutrino mass generation has been accomplished at one and two loop level. If not directly the DM particle itself, then at least DM related couplings have been involved in the loops. In each of the models, the corresponding DM particle has been a cold DM particle whose present relic density is achieved by the freeze-out mechanism. As the identity of the DM is still a mystery and as long as they are not verified or refused, models can only describe the possible behavior of nature, other candidates than the extensively studied weakly interacting massive cold DM particle have also to be admitted consideration on their merits.

One particularly interesting candidate particle that in most settings turns out to be warm DM is a sterile, i.e., mainly SM singlet neutrino with a mass of a few keV, as the title of this chapter already suggests. If such a particle exists, in addition to two heavier, i.e., GeV, neutrinos which are nearly degenerate in mass, the resulting setting, called the νMSM [148], can indeed simultaneously accommodate neutrino masses and DM. This thesis is aimed at a common framework for neutrino masses and DM. It is therefore interesting and well motivated to study keV sterile neutrino DM.

A frequent problem with non-standard DM candidates such as keV sterile neutrinos is that they cannot be produced easily via the generic process of thermal freeze-out. This is simple to understand, since this mechanism requires particles to be in thermal equilibrium with the plasma in the early Universe, which does not work for sterile neutrinos as their interactions are too weak.

We therefore start with a review of mechanisms for keV sterile neutrinos. As it will turn out, a very practical production mechanism is the non-thermal production of DM and, in particular, keV sterile neutrinos by the decays of particles, such as singlet scalars. This production mechanism already exists for a scalar in equilibrium with the thermal plasma, which undergoes an early or late freeze-out. However, there is an alternative way to produce the scalar particle from the thermal plasma, the so-called freeze-in mechanism [55]. The scenario in which a scalar singlet freezes-in and then decays into sterile neutrinos has to the best of our knowledge not been discussed in the literature before and thus provides a new production mechanism for keV sterile neutrino DM.

We proceed with a general description of the basic underlying idea and then move on

to the technical details.

This chapter emanates from work done in collaboration with Alexander Merle and Viviana Niro. It is based on the preprint [149] that has been submitted to JCAP and of which the author of the present thesis is the corresponding author. The author of the present thesis was mainly involved in the numerical analysis.

4.1. Known Production Mechanisms for keV Sterile Neutrino DM

Light neutrinos appear as left-handed fields in the SM lepton doublets, see section 2.1. Right-handed singlet neutrinos, which are discussed in section 2.2 and play the role of a DM particle candidate in chapter 3, are absent in the particle spectrum of the SM.

The question as to why all of the charged fermions of the SM except of neutral neutrinos appear in left-handed doublets and right-handed singlets under $SU(2)$ arises very naturally. Without going into the details, we simply assume the existence of three right-handed neutrinos N_i $(i = 1, 2, 3)$ in this section. If there are no further symmetries, then the coupling of a SM left-handed neutrino, the SM Higgs doublet H and one right-handed neutrino, i.e.:

$$-y_D^{\alpha i}\overline{L_\alpha}\tilde{H}N_i + \text{h.c.} \tag{4.1.1}$$

is unavoidable. Again, $\tilde{H} = i\sigma_2 H^*$.

As soon as the SM Higgs doublet H obtains its VEV, this coupling induces mixing between the left-handed neutrinos, which are active, and the right-handed neutrinos, which are sterile under the SM gauge group; see section 2.2.3.

Another sector where one could search for physics beyond the SM is the scalar sector. The very recently observed and established Higgs boson may not be the only neutral scalar particle. In the previous part, we studied scalar sectors with an inert scalar $SU(2)_L$ doublet, singly-and doubly charged scalar $SU(2)_L$ singlets and a complex scalar $SU(2)_L$ singlet with lepton number -2. Here, we focus on an additional real scalar $SU(2)_L$ singlet S. The right-handed neutrinos could then also have the coupling:

$$-\frac{y_i}{2}S\,\overline{N_i^C}N_i \;+\text{h.c.} \tag{4.1.2}$$

Given that the scalar is heavier than half of the mass of the right-handed neutrinos, it can produce right-handed neutrinos by the decay $S \longrightarrow N_i N_i$.

If S obtains a VEV, a Higgs portal to the SM, i.e.,

$$2\lambda(H^\dagger H)S^2 \tag{4.1.3}$$

is created. Moreover, when S obtains a VEV, a Majorana mass term for the right-handed neutrino is generated dynamically rather than being set by hand.

In this section, the implications of active-sterile neutrino mixing for DM and decays of a real scalar singlet into sterile neutrinos are reviewed.

We do not extend the gauge group of the SM. Thus, we do not consider the possibility that a right-handed neutrino is only sterile under the SM gauge group but charged under an extended gauge group. If so, the right-handed neutrinos could be produced thermally, e.g., [150]. We restrict the discussion to non-thermal production mechanisms.

4.1.1. Active-Sterile Neutrino Mixing

S. Dodelson and L. M. Widrow found that the mixing between active and sterile neutrinos can generate an appropriate value for the relic density of a sterile neutrino N_R with mass M, which is a warm DM candidate particle. From the Yukawa interaction between a SM left-handed neutrino ν_L, the SM Higgs doublet H and the right-handed neutrino N_R, i.e.,

$$\mu \left(\frac{H}{\langle H \rangle} \right) \overline{\nu_L} N_R \,, \tag{4.1.4}$$

the probability of observing N_R after a time t, given that there are only active neutrinos with an energy E, is $\sin^2 2\Theta \sin^2 {}^{vt}/_{L}$, with active-sterile mixing angle Θ and oscillation length L. Replacing $y_{\alpha i}$ in equation (2.2.19) by ${}^{\mu}/_{\langle H \rangle}$ as well as $y_i \langle S \rangle$ by M, the active-sterile mixing angle equals $\Theta = {}^{\mu}/_{M}$. The oscillation length follows to $L = {}^{4E}/_{M^2 - \mu^2}$.

In the thermal plasma of the early Universe, the high temperatures yield a relatively large interaction time for the active neutrinos compared to the oscillation time. Therefore, $\sin^2 vtL$ is replaced by its average value, which is ${}^{1}/_{2}$.

Following the discussion of equation (2.5.2), the Boltzmann equation describing the active-sterile neutrino mixing can be written as [151]:

$$\left(\frac{\partial}{\partial t} - HE \frac{\partial}{\partial E} \right) f_S(E,t) = \left[\frac{1}{2} \sin^2(2\Theta(E,t)\Gamma(E,t)) \right] f_A(E,t) \,, \tag{4.1.5}$$

with f_S and f_A the distribution functions of sterile and active neutrinos, respectively, and $\Gamma(E,t)$ the interaction rate for the active neutrinos. We consider temperatures that are larger than 1 MeV, i.e, the active neutrinos are in thermal equilibrium, see, e.g., the discussion of equation (2.3.19). Therefore f_A equals the equilibrium distribution, see equation (2.4.4).

The right-handed neutrinos do not achieve thermal equilibrium with the other particles present in the thermal bath because the relevant interaction strengths are always suppressed by the mixing angle. In that sense, the Dodelson-Widrow (DW) framework is a non-thermal production mechanism for keV sterile neutrino DM.

In [151], it is shown that the ratio of the number of sterile neutrinos and the number of active neutrinos has a maximum at the temperature $T_{\max}$ that equals:

$$T_{\max} \simeq 133 \left(\frac{M}{\text{keV}}\right)^{\frac{1}{3}} \text{MeV}\,. \tag{4.1.6}$$

For $T \ll T_{\max}$, this ratio has a T^3-behavior, and for $T \gg T_{\max}$ it behaves like T^{-9}. Thus for temperatures roughly above 100 MeV the production of keV sterile neutrinos is strongly suppressed. For temperatures $T \ll T_{\max}$, the distribution function f_S of the sterile neutrinos can be expressed as:

$$f_S = \frac{6.0}{\sqrt{h_{\text{eff}}}} \left(\frac{\mu}{\text{eV}}\right)^2 \left(\frac{\text{keV}}{M}\right) f_A\,. \tag{4.1.7}$$

The ratio of the relic density of the sterile neutrinos and the relic density of the active neutrinos is written as [151]:

$$\frac{\Omega_S}{\Omega_\nu} = \frac{M}{m_\nu}\frac{f_S}{f_A}\,. \tag{4.1.8}$$

Ω_ν is given by equation (2.4.5), i.e., $\Omega_\nu = {}^{m_\nu}/_{92h^2\,\text{eV}}$, such that:

$$\Omega_S = \frac{6.0}{\sqrt{h_{\text{eff}}}} \left(\frac{\mu}{\text{eV}}\right)^2 \frac{\text{keV}}{92h^2\,\text{eV}}\,, \tag{4.1.9}$$

which is independent of the mass scale M of right-handed neutrinos. In the derivation of this result, the number h_{eff} of relativistic degrees of freedom contributing to the entropy density is assumed to be constant: the particles that contribute tot the number of relativistic degrees of freedom are the photon, the three active neutrinos and the electron, i.e.,$h_{\text{eff}} = 10.75$. The assumption of constant h_{eff} is motivated by the fact that below the temperature of the QCD phase transition, which is at $T = 200\,\text{MeV}$, there is no abrupt change in h_{eff}. Since the maximum production of sterile neutrinos happens at $T_{\max}$, the mass scale M for the right-handed neutrinos is constrained to be $M \lesssim \text{keV}$ via equation (4.1.6), otherwise the assumption of constant h_{eff} is not valid.

Through mixing with the active neutrinos, the sterile neutrinos take part in the weak interactions. In particular, a sterile neutrino, which is a linear superposition of a left-handed mass eigenstate and a right-handed mass eigenstate, can decay at one-loop level into an active neutrino and a photon, where a charged W boson and a lepton run inside the loop, see figure 2.1. The decay rate depends on the mixing angle. The photon flux from the decay depends on $\Theta^2 M^5$, see equation (2.2.22). Since for each value of the mass the mixing angle is fixed by the demand for the correct relic density, the measured photon gives an upper bound on the mass. In the DW framework, the bound from decay $N_R \longrightarrow \nu_L \gamma$ reads [44]:

$$M \lesssim 4\,\text{keV}\,. \tag{4.1.10}$$

As already mentioned in section 2.4, warm DM suppresses small scale structures due to free streaming. The warmer the DM is, the larger its free streaming scale and the less structure is left on small scales. When the right-handed neutrinos are produced at $T_{\max} \sim 100\,\mathrm{MeV}$, their mass is therefore much smaller than the temperature of the photons; they are relativistic and stream out, thereby erasing density fluctuations at scales below the free streaming scale [152].

Above the free streaming scale, structure formation is similar to cold DM models, however, below the free streaming scale, structure formation changes. The Lyman-alpha forest is a suitable cosmological observable. Lyman series are transitions in hydrogen atoms from electron energy levels of $n \gtrsim 2$ to $n = 1$; the Lyman-alpha line results from the transition $n = 2 \to n = 1$ and has a wavelength of $\lambda_S = 1216$ angstrom. After reionization, a small fraction of hydrogen atoms are still present in neutral hydrogen clouds in the intergalactic medium at different redshifts z. Hence, the light emitted by a source is redshifted when hitting a hydrogen atom in a hydrogen cloud at a specific redshift. If the amount of redshift is such that the wavelength at the hydrogen atom equals $\lambda_S = 1216$ angstrom, then the emitted light is absorbed and an observer on the Earth sees a peak in the absorption spectrum corresponding to the redshift of that hydrogen cloud. Since the absorption can take place at different redshifts, depending on the specific wavelength of the emitter, the observer sees several absorption lines at different redshifts. Therefore, when observing the absorption spectrum of a specific source on Earth, there is a forest of Lyman alpha lines $\lambda_O(z)$ due to the redshift:

$$\lambda^O_{\mathrm{Lya}}(z_i) = (1 + z_i)\lambda_{\mathrm{Lya}}\,. \tag{4.1.11}$$

At redshifts $z = 2 - 6$ there is the right amount of neutral hydrogen among the mostly ionized hydrogen to observe Lyman-alpha absorption lines. For higher redshifts, the reionization has not yet happened and all of the hydrogen is neutral hydrogen, thus all the light emitted by an object at $z \gtrsim 6$ is absorbed by the neutral hydrogen in the line of sight; the object remains dark and is not suited for spectroscopy [153].

The observation of the Lyman alpha forest proves the existence of small scales in the form of hydrogen clouds and therefore puts a lower limit on the mass of the right-handed neutrino, which is the DM particle. In the DW framework, the bound from the Lyman-alpha forest reads [44]:

$$M > 8\,\mathrm{keV}\,. \tag{4.1.12}$$

Comparison of the X-ray bound in equation (4.1.10) and the Lyman-alpha constraint in equation (4.1.12) obviously excludes the DW framework as an explanation for keV sterile neutrino DM via mixing.

X. Shi and G.M. Fuller studied resonant active-sterile neutrino transformations where the resonance originates from a pre-existing lepton number asymmetry $\mathcal{L} \equiv 2L_{\nu_\alpha} +$

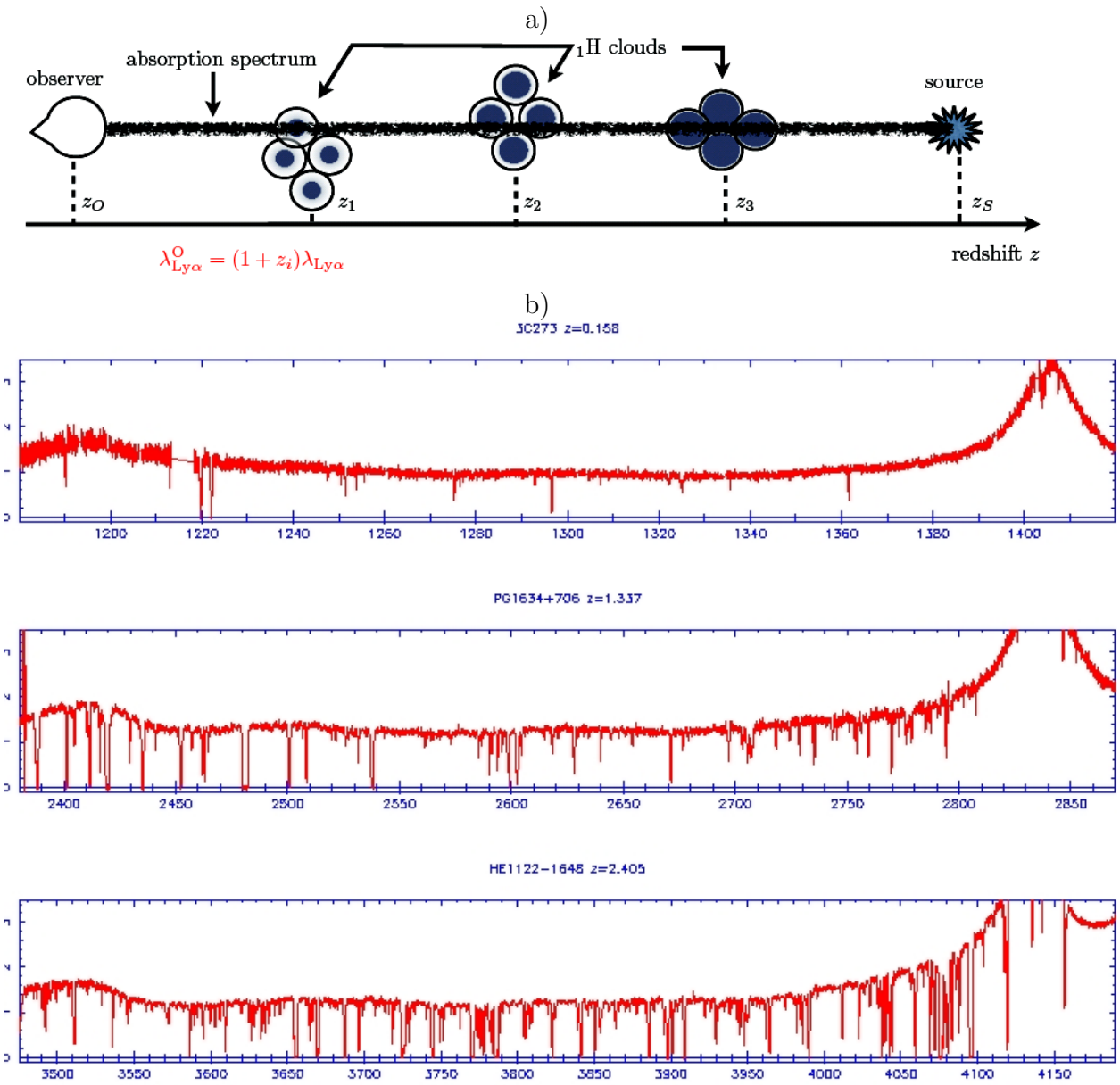

Figure 4.1.: a): Formation of the Lyman-alpha forest. b): Lyman-alpha absorption spectrum. b) is taken from http://www.ast.cam.ac.uk/%7Erfc/zevol6e.jpg

$\sum_{\alpha\neq\beta} L_{\nu_\beta}$ in the range $10^{-3} < \mathcal{L} < 10^{-1}$, where $L_{\nu_\alpha} = \#\nu_\alpha - \#\overline{\nu_\alpha}$. The Shi-Fuller (SF) framework is also a non-thermal production mechanism. A resonance in the $\nu_\alpha \leftrightarrow N_i$ oscillations is then present at a temperature $T_{\rm res}$ due to the non-zero value of $\mathcal{L}$ [154]:

$$T_{\rm res} \approx 9 \left(\frac{M}{100\text{eV}}\right)^{\frac{1}{2}} \left(\frac{\mathcal{L}}{0.1}\right)^{-\frac{1}{4}} \left(\frac{T}{E}\right)^{\frac{1}{4}} , \tag{4.1.13}$$

where E is the neutrino energy.

The oscillations $\overline{\nu_\alpha} \leftrightarrow \overline{N_i}$ are not resonantly enhanced and are therefore suppressed compared to the $\nu_\alpha \leftrightarrow N_i$ oscillations. The result is that the pre-existing lepton number asymmetry $\mathcal{L}$ is destroyed and $\mathcal{L} \to 0$. As the $E^{-1/4}$ dependence of the temperature $T_{\rm res}$ on the neutrino energy shows, the low energy neutrinos are resonantly produced before the high energy neutrinos. The high energy neutrinos reach the resonance condition when those $\nu_\alpha \leftrightarrow N_i$ oscillations for low energy neutrinos that have been resonant have already reduced the lepton number asymmetry $\mathcal{L}$. Thus, the $\nu_\alpha \leftrightarrow N_a$ oscillations for high energy neutrinos are not significant. The outcome is a sterile neutrino spectrum which is centered around low neutrino energies. It is cooler than the corresponding spectrum obtained in the DW framework, which has no pre-existing lepton number asymmetry. For the SF framework, the X-ray bound is:

$$M < 50\,\text{keV} , \tag{4.1.14}$$

and the Lyman alpha bound is:

$$M > \ 2\,\text{keV} ; \tag{4.1.15}$$

the latter depending on $\mathcal{L}$. Both of the two constraints can be satisfied at the same time, showing that the SF framework is a valid mechanism to explain sterile neutrino DM by active-sterile neutrino mixing.

4.1.2. Decay of a Real Scalar Singlet

With a scalar singlet, a Majorana mass term for right-handed neutrinos can be generated dynamically by spontaneous symmetry breaking, in analogy to the Dirac mass terms of the SM. Once it is produced, the scalar singlet may decay into two sterile neutrinos if kinematically allowed. Such decays produce sterile neutrinos in addition to the active-sterile neutrino mixing, and they can allow extra setups which would not be allowed for the mixing alone. Production by decay is a non-thermal production mechanism, because there is no thermal distribution of the decay products in the thermal plasma. If the coupling constant with which the sterile neutrinos couple to the scalar singlet is small enough, the sterile neutrinos are out of equilibrium. Since the decay of the singlet scalar

into sterile neutrinos is fixed by kinematics, the decisive point for us concerning the sterile neutrino DM is how the singlet scalar is produced.

In the picture of thermal freeze out, two scenarios have been studied in the literature, namely decay of the scalar singlet into sterile neutrinos at relative high temperatures when the scalar singlet is still in thermal equilibrium and has not yet frozen-out [155] and out of equilibrium decay of the scalar singlet into sterile neutrinos at relative low temperatures after freeze-out [156].

The two scenarios differ by the quantity $\langle p\rangle/T$, with $\langle p\rangle$ the average momentum of the sterile neutrino and T the temperature. The mass M of the sterile neutrino and its average momentum $\langle p\rangle/T$ divided by the temperature, the latter depending on the specific production mechanism, determine the free streaming horizon. Structure formation, as observed in Lyman-alpha forest surveys, constrains the free streaming horizon and thus the production mechanism for sterile neutrinos.

In a dedicated section, we calculate the free streaming horizon for our proposed novel production mechanism. At first, we present the average momentum for the known sterile neutrino production mechanism. In general, the average momentum $\langle p\rangle$ of a particle is given by:

$$\langle p(t)\rangle = \frac{\int d^3p\, p f(p,t)}{\int d^3p\, f(p,t)}\,, \tag{4.1.16}$$

with the phase-space distribution function $f(p,t)$. Phase-space distribution functions are also discussed in section (2.4). For a fermion in kinetic equilibrium, the phase-space distribution function is the Fermi–Dirac distribution, i.e.:

$$f(p,t) = \frac{1}{e^{\frac{E-\mu}{T}}+1}\,, \tag{4.1.17}$$

where the time dependence is hidden in the temperature T and μ is the chemical potential of the particle. For a nondegenerate, i.e., $\mu \ll T$, relativistic, i.e., $T \gg M$, species of fermions in kinetic equilibrium, the average momentum per particle is [45]:

$$\frac{\langle p\rangle}{T} = \frac{\langle E\rangle}{T} = \frac{7\pi^4}{180\zeta(3)} \simeq 3.15\,, \tag{4.1.18}$$

where the Riemann zeta function $\zeta(3)$ of 3 arises from phase-space integration of the Fermi–Dirac distribution function.

In the two above mentioned scenarios for sterile neutrino DM production by the decay of a scalar singlet, the phase-space distribution function of the sterile neutrinos is not a Fermi–Dirac distribution. The relevant distribution function $f(p,t)$ is found by solving the Boltzmann equation [157]:

$$\frac{\partial f(p,t)}{\partial t} - Hp\frac{\partial f(p,t)}{\partial p} = \frac{2m_\sigma\Gamma}{p^2}\int_{p+\frac{m_\sigma^2}{4p}} dE\, f_\sigma(p,t)\,. \tag{4.1.19}$$

Γ is the decay width of the decay process $\sigma \longrightarrow NN$ and $f_\sigma(p,t)$ is the phase-space distribution of the decaying scalar singlet σ. If σ is still in thermal equilibrium when it decays, its phase-space distribution function is the Bose–Einstein distribution. However, if σ has already frozen-out when it starts to decay, its phase-space distribution function has to be determined separately by solving the relevant Boltzmann equation [156].

In the scenario of scalar decay in thermal equilibrium at relative high temperatures $T \sim 100\,\mathrm{GeV}$, the average momentum per sterile neutrino is [157]:

$$\left(\frac{\langle p\rangle}{T}\right)_{T\sim 100\,\mathrm{GeV}} = \frac{\pi^6}{378\zeta(5)} \simeq 2.45\,. \tag{4.1.20}$$

Although the sterile neutrino is produced at this high temperature, it is a warm DM candidate particle and thus effects the structure formation. Structure formation starts after BBN, i.e., when the temperature is much below 1 MeV. During the time in which the Universe expands and thus cools down from the production temperature $T \sim 100\,\mathrm{GeV}$ of the sterile neutrinos to the temperature $T \ll 1\,\mathrm{MeV}$ at which structure starts to form, the momenta of the sterile neutrinos are redshifted. At the production temperature, the relativistic degrees of freedom g_{eff} for the energy density are the SM particles plus a real scalar singlet plus a Majorana neutrino, which add up to $g^i_{\mathrm{eff}} = 109.5$. If we take $T = 0.1 \ll 1$ MeV as the temperature at which structure begins to form, then $g^f_{\mathrm{eff}} = 3.36$. The redshift occurs in all three spatial dimensions, such that the average momentum per sterile neutrino decreases by a factor of $\xi^{1/3} = (g^i_{\mathrm{eff}}/g^f_{\mathrm{eff}})^{1/3}$ to:

$$\left(\frac{\langle p\rangle}{T}\right)_{T\sim 0.1\ \mathrm{MeV}} = 0.76\xi^{-\frac{1}{3}} \simeq 0.24\,. \tag{4.1.21}$$

Compared to the average momentum $\langle p\rangle/T = 2.83$ [156] of sterile neutrinos produced at low temperatures via the DW mechanism, the relatively small value in this decay scenario leads to a smaller free streaming scale. The Lyman-alpha limit changes to [155]:

$$M > 2.7\,\mathrm{keV}\,, \tag{4.1.22}$$

such that it is compatible with the X-ray bound, without the need of a pre-existing lepton number asymmetry as in the SF framework.

In the scenario of the out-of-thermal-equilibrium decay of the scalar at relative low temperatures, the average momentum per sterile neutrino can be as low as [156]:

$$\frac{\langle p\rangle}{T} \simeq \left(\frac{2.5}{\xi^{\frac{1}{3}}}\right)_{T\ll 1\,\mathrm{MeV}} = 0.8\,. \tag{4.1.23}$$

At this stage it is worth pointing out that the identifiers cold, warm and hot DM are not solely referring to the mass of the DM, but to the free streaming horizon of the DM

candidate particle defined in equation (2.4.8), which in turn depends on the product of the DM mass and its average momentum distribution. Therefore, in principle, a particle with a mass of the order of keV can also be a cold DM particle, as long as its average momentum divided by the relevant temperature is relatively small compared to that one for usual keV warm DM.

4.2. The Basic Idea: Decays of Scalar FIMPs

We illustrate the proposed mechanism before entering into the technical details. The keV neutrinos emerge as daughter particles of a decaying scalar singlet particle. Thus, in the first place, the parent particle has to be produced. All in all, we then have two production stages: the production of the decaying particle followed by the production of keV sterile neutrinos as decay products. Since different constraints may hold for the two particles involved, two production stages may have advantages over mechanisms with only one production stage. For example, the keV sterile neutrino cannot be produced from the thermal plasma only: in case it enters thermal equilibrium, it is typically overproduced since it is relativistic at freeze-out [150]. If it does not enter thermal equilibrium and is only produced non-resonantly by small admixtures, its spectrum is too warm, if the correct abundance is produced. The constraints from structure formation [158] can then only be realized for relatively large keV sterile neutrino masses, which are in conflict with the constraints from the non-observation of the decay of the keV neutrino into a light neutrino and a photon [159], as outlined above. The singlet scalar, instead, can be produced via thermal freeze-out, and its decay leads to a suitable abundance of keV sterile neutrino DM, while at the same time being compatible with all bounds [155, 156], as we already have discussed.

We pursue a different path to produce the singlet scalar σ: if the Higgs portal coupling is small enough, $\lambda \ll 10^{-6}$ [155,156], the scalar particle does not enter thermal equilibrium because its feeble interaction rate with the thermal bath is always smaller than the Hubble expansion rate. However, it can still be produced by the plasma. This opens up a new region in the parameter space where a non-negligible abundance can be produced, which actually increases for increasing λ, contrary to what would happen in thermal freeze-out. This is the freeze-in mechanism which is not new, see, e.g., [54], but has been recently summarized and systematized in [55], where also the term FIMP, i.e., feebly interacting massive particle, has been introduced. See also the discussion in section 2.5.2. Furthermore, a scalar that has been produced via freeze-in has not been studied before for the case of the production of keV sterile neutrinos.

The frozen-in physical singlet scalar σ will have a spectrum with approximately thermal shape, but with an overall suppression factor. This scalar σ will then fully decay into keV neutrinos N_1 via the reaction $\sigma \longrightarrow N_1 N_1$. We assume the decays into the heavier

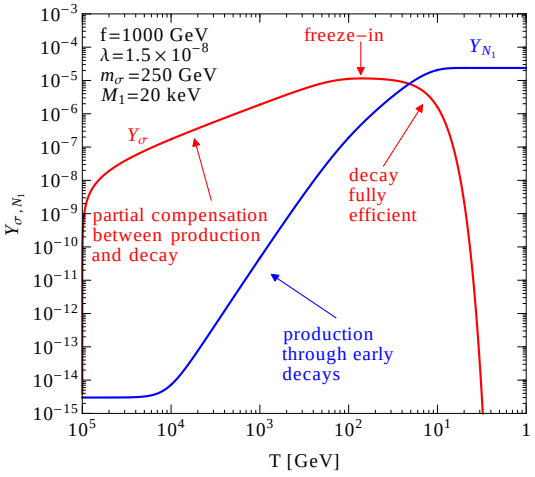

Figure 4.2.: Example variation of yields Y_{N_1} and Y_σ as a function of the temperature T, see section 4.3.1 for details. As can be seen from the figure, a significant abundance of σ gradually builds up due to freeze-in, before the decays $\sigma \longrightarrow N_1 N_1$ set in and, at the same time, a significant amount of keV sterile neutrinos N_1 is produced.

sterile neutrinos $N_{2,3}$ to be kinematically forbidden, since we consider $M_{2,3} \gg m_\sigma$. Thus, the decisive decay mode is $\sigma \longrightarrow N_1 N_1$. We always assume $M_1 \ll m_\sigma \ll M_{2,3}$, keeping in mind that there are several models and mechanisms which can indeed generate such a mass pattern for Majorana sterile neutrinos [160]. An example evolution of the yields Y of σ and N_1 with decreasing temperature T is displayed in figure 4.2. As can be seen, we essentially start with a zero abundance of both particles, the precise value of the initial abundance plays no role as long as it is negligibly small, but with decreasing temperature the abundance of σ increases before reaching a plateau at the freeze-in temperature $T \sim m_\sigma$, which is typical for the freeze-in process as discussed above. However, this abundance decreases again later, due to the decays $\sigma \longrightarrow N_1 N_1$. Since every scalar σ decays into exactly two N_1's, this implies $Y_{N_1}(\text{late times}) = 2Y_\sigma(\text{early times})$ as long as no N_1's are produced from other sources. If the N_1's are fully non-relativistic at late times, this also implies the relation $\Omega_{N_1} h^2 = 2 \cdot {}^{M_1}\!/_{m_\sigma} \cdot \Omega_\sigma h^2$ between the final abundances, which makes it evident that this mechanism is useful to correct an overabundance of σ by a suitable mass ratio ${}^{M_1}\!/_{m_\sigma}$. However, since the N_1's can also be semi-relativistic, i.e., warm, at least for times close to their production, the above relation could receive a correction factor in case the yield Y_{N_1} is not evaluated at a late enough time. Nevertheless, the above formula can be applied as an estimate.

Finally, note that the assumption that the keV neutrinos N_1 are produced exclusively by the described scalar decays does not always need to be true. In particular, in a setting

where there is a non-negligible active-sterile mixing between N_1 and the light neutrinos ν_i, a certain contribution to the abundance of N_1's produced by the DW mechanism is unavoidable. We will take this contribution into account by estimating the maximal amount of keV neutrinos which can be produced by DW, without violating the X-ray bound or overproducing the DM. However, we would like to stress that our production mechanism does not need active-sterile mixing. While such a mixing may or may not be desirable from a phenomenological perspective, there are settings known in which it is exactly zero due to a discrete symmetry, see, e.g., [161]. In such a scenario, the production of keV neutrinos by a combination of the standard DW and SF mechanisms would fail, while our mechanism, as well as the version where σ does enter thermal equilibrium, could still be valid.

This is the general idea behind our proposal; we will now present the more technical aspects of our mechanism.

4.3. Details of the Production Mechanism

4.3.1. The Model

The particle content of the SM is extended by three right-handed sterile neutrinos N_i ($i = 1, 2, 3$) and one real scalar $SU(2)_L$ singlet S [156]. The Lagrangian is:

$$\begin{aligned}\mathcal{L} =& \mathcal{L}_{\mathcal{SM}} + \left[i\overline{N_i}\partial\!\!\!/ N_i + \frac{1}{2}(\partial_\mu S)(\partial^\mu S) - \frac{y_i}{2} S\, \overline{N_i^C} N_i \ + \text{h.c.} \right] - V_{\text{scalar}} \\ &+ \mathcal{L}_\nu \,, \end{aligned} \tag{4.3.1}$$

which consists of the SM, kinetic terms of the sterile neutrinos N_a, Yukawa interactions f_a of the singlet S with N_a, and a scalar potential V_{scalar}. Finally, $\mathcal{L}_\nu$ is the part of the Lagrangian giving mass to the light neutrinos. In the simplest setting, we would have $\mathcal{L}_\nu = -y_D^{\alpha i}\overline{L_\alpha}\tilde{H}N_i + \text{h.c.}$, where $\tilde{H} = i\sigma_2 H^*$. Then, a type-I seesaw mechanism could be at work using the right-handed Majorana masses for N_i arising from a VEV $f = \langle S \rangle$, as long as the Yukawa couplings respect the observational X-ray bound [162]. Alternatively, there could exist more complicated seesaw-type mechanisms, or radiative light neutrino mass generation as discussed in part part:one. Since we do not rely on a specific mechanism, we will leave the mass generation of light neutrinos unspecified. Any realistic setting must provide a way to generate a viable light neutrino mass and mixing pattern, but the details do not play a decisive role in our production mechanism.

We restrict our considerations to a potential V_{scalar} that only depends on the absolute value of the SM Higgs doublet H and on even powers of the real scalar singlet S. Such a potential results from a global symmetry, e.g., lepton number, and does not impose a

severe restriction. Assuming a $\mathbb{Z}_4 = \{\pm 1, \pm i\}$ symmetry [1] such that $L_\alpha \to iL_\alpha$, $e_\alpha \to ie_\alpha$, $N_i \to N_i$ and $S \to -S$, while all other fields transform trivially, the most general potential is:

$$V_{\text{scalar}} = -\mu_H^2 H^\dagger H - \frac{1}{2}\mu_S^2 S^2 + \lambda_H (H^\dagger H)^2 + \frac{1}{4}\lambda_S S^4 + 2\lambda (H^\dagger H) S^2. \tag{4.3.2}$$

The Higgs doublet H and the scalar singlet S are parametrized as:

$$H = \begin{pmatrix} h^+ \\ \frac{1}{\sqrt{2}}(v + \tilde{h} e^{i\rho}) \end{pmatrix} \to \begin{pmatrix} 0 \\ \frac{1}{\sqrt{2}}(v + \tilde{h}) \end{pmatrix} \quad \text{and} \quad S = f + \tilde{\sigma}. \tag{4.3.3}$$

We use the unitary gauge as in equations (2.1.3), (3.1.3) and equation (3.4.7). The Goldstone bosons $h^\pm$ are eaten by $W^\pm$ to make them massive, similar to the neutral boson ρ being eaten by the Z^0. All other components are physical: $\tilde{h}$ is the SM-like Higgs and $\tilde{\sigma}$ is a physical singlet scalar, see equation (2.1.3). The VEVs are given by $\langle H \rangle = {}^1/\sqrt{2} \cdot v$, where $v = 246\,\text{GeV}$, and $\langle S \rangle = f$. Note that f could potentially be large.

Inserting the VEVs, $H^\dagger H \to {}^{v^2}/_2$ and $S^2 \to f^2$, and differentiating the potential with respect to v^2 and f^2, respectively, gives the minimum conditions:

$$\mu_H^2 = \lambda_H v^2 + 2\lambda f^2, \tag{4.3.4}$$

$$\mu_S^2 = \lambda_S f^2 + 2\lambda v^2. \tag{4.3.5}$$

The Higgs portal coupling λ results in mixing of the physical scalar fields. Concentrating on the potential terms which are proportional to $\tilde{\sigma}^2$, $\tilde{h}^2$, and $\tilde{\sigma}\tilde{h}$, and inserting the minimum conditions, equation (4.3.4) and equation (4.3.5), the mass matrix in the interaction basis $(\tilde{h}, \tilde{\sigma})^T$ reads:

$$\begin{pmatrix} \lambda_H v^2 & 2\lambda v f \\ 2\lambda v f & \lambda_S f^2 \end{pmatrix}. \tag{4.3.6}$$

[1] Note that this discrete $\mathbb{Z}_4$ symmetry might potentially be problematic, since its breaking by a non-zero VEV $f = \langle S \rangle$ could lead to so-called domain walls [163], which would considerably alter the history of the Universe but are not observed. There are arguments for how this problem could be evaded, see e.g., [164–166]. We will not enter this discussion here and simply assume that this problem is solved in a model containing the framework presented here. Nevertheless, we would like to point out that the most obvious solution of taking S to be complex and promoting the symmetry to a global $U(1)$ rotation, for which no domain walls would appear, is not a straightforward solution to pursue. In that case, our production mechanism would suffer considerably from the existence of a Goldstone boson [135], more precisely a singlet Majoron [137] which would also couple to N_1 and considerably modify the DM production. In general, there can be a non-trivial interplay between the abundances of the different scalar fields in the early Universe, which makes the model with a complex scalar S considerably different from the freeze-in of a real scalar, the latter case being addressed in this paper.

In the basis $(h, \sigma)^T$ of mass eigenstates we have, in the limit of small λ:

$$\frac{1}{2}(h,\sigma)\begin{pmatrix} m_h^2 & 0 \\ 0 & m_\sigma^2 \end{pmatrix}\begin{pmatrix} h \\ \sigma \end{pmatrix}, \quad \text{where} \quad \left.\begin{matrix} m_h^2 \\ m_\sigma^2 \end{matrix}\right\} \simeq \left\{\begin{matrix} \lambda_H v^2 \\ \lambda_S f^2 \end{matrix}\right\} \mp \frac{(2\lambda f v)^2}{\lambda_S f^2 - \lambda_H v^2}\,. \tag{4.3.7}$$

Interpreting the transition from the interaction to the mass basis as an abstract rotation similar to equation (3.4.22),

$$\begin{pmatrix} \tilde{h} \\ \tilde{\sigma} \end{pmatrix} = \begin{pmatrix} \cos\alpha & -\sin\alpha \\ \sin\alpha & \cos\alpha \end{pmatrix}\begin{pmatrix} h \\ \sigma \end{pmatrix}, \tag{4.3.8}$$

equations (4.3.6) and (4.3.7) yield:

$$\lambda_S = \frac{m_h^2 \sin^2\alpha + m_\sigma^2 \cos^2\alpha}{2f^2}\,, \quad \lambda_H = \frac{m_h^2 \cos^2\alpha + m_\sigma^2 \sin^2\alpha}{2v^2}\,, \tag{4.3.9}$$

$$\lambda = \frac{(m_h^2 - m_\sigma^2)\cos\alpha\sin\alpha}{4fv}\,. \tag{4.3.10}$$

The independent parameters are the singlet mass m_σ, the Higgs portal λ, and the VEV f of the singlet. Since the Higgs portal λ is small, we can practically identify h with $\tilde{h}$ and σ with $\tilde{\sigma}$. We will use the notation h and σ in the following.

In our numerics, we have fixed the SM Higgs mass to 125 GeV in accordance with the experimental results by the ATLAS and the CMS collaborations. In addition we assume $m_\sigma > m_h$ for definiteness and $m_\sigma < f$ in order to avoid being in danger of entering a non-perturbative regime, i.e., we vary m_σ between the 1σ upper limit of $m_h < 126.4\,\text{GeV}$ [167] and f.

4.3.2. Dark Matter Relic Density

The relic density of our DM candidate particle N_1 is produced by the decays of a frozen-in real scalar singlet particle σ. The Boltzmann equations for the annihilation and decay processes are given in equations (E.0.2) and (E.0.12), respectively. To calculate the relic density of N_1, we have to solve a system of coupled equations simultaneously describing the annihilation and decay processes as it is done in, e.g, [168].

We have to solve the following two coupled Boltzmann equations:

$$\frac{d}{dT}Y_\sigma = \frac{d}{dT}Y_\sigma^{\mathcal{A}} + \frac{d}{dT}Y_\sigma^{\mathcal{D}}\,, \tag{4.3.11}$$

$$\frac{d}{dT}Y_{N_1} = \frac{d}{dT}Y_{N_1}^{\mathcal{D}}\,, \tag{4.3.12}$$

with

$$\frac{d}{dT}Y_{\sigma}^{\mathcal{A}} = -\sqrt{\frac{\pi}{45G_N}}\sqrt{g_*}\langle\sigma_{\rm ann}v_r\rangle\, Y_{\sigma,eq}^2\,, \quad \frac{d}{dT}Y_{\sigma}^{\mathcal{D}} = -\frac{1}{2}\frac{d}{dT}Y_{N_1}^{\mathcal{D}}\,, \tag{4.3.13}$$

$$\frac{d}{dT}Y_{N_1}^{\mathcal{D}} = -\sqrt{\frac{45}{\pi^3 G_N}}\frac{1}{T^3}\frac{1}{\sqrt{g_{\rm eff}}}\langle\Gamma(\sigma\to N_1N_1)\rangle\, Y_{\sigma}\,, \tag{4.3.14}$$

see appendix E, in particular equations (E.0.6) and (E.0.13), for detailed information. The equilibrium yield is given by:

$$Y_{\sigma,\rm eq} = \frac{45g_\sigma}{4\pi^4}\frac{x^2K_2(x)}{h_{\rm eff}(T)}\,, \tag{4.3.15}$$

with $g_\sigma = 1$ being the spin degrees of freedom for the particle σ, $x \equiv {}^{m_\sigma}/_{T}$, and

$$\sqrt{g_*} \equiv \frac{h_{\rm eff}}{\sqrt{g_{\rm eff}}}\left(1 + \frac{1}{3}\frac{T}{h_{\rm eff}}\frac{dh_{\rm eff}}{dT}\right)\,. \tag{4.3.16}$$

For the definitions of $h_{\rm eff}$, $g_{\rm eff}$ and of the Bessel function $K_2(x)$, see appendices C and D. Building on our verified results obtained in the calculation of the relic density for the singlet scalar FIMP, we have further developed our numeric treatment of the freeze-in scenario. Thus we are able to numerically solve the system of the coupled Boltzmann equations (4.3.11) and (4.3.12).

Equation (C.0.7) and equation (C.0.6) for the effective relativistic degrees of freedom $h_{\rm eff}$ and $g_{\rm eff}$ are implemented in our Mathematica procedure and summed over as in equations (C.0.9) and (C.0.8). Thus we are able to correctly account for the contribution of the singlet scalar to the relativistic degrees of freedom. In addition, we obtain $\sqrt{g_*}$ of equation (4.3.16) as a function of the temperature T. The system of Boltzmann equations in equations (4.3.11) and (4.3.12) is numerically solved for each combination of integer valued m_σ and M_1 in the range we have scanned, see below. For each parameter pair, we check that the equilibrium condition $n_{\rm eq}\langle\sigma v_r\rangle > H$ is satisfied for each temperature T.

As already explained, the DM particle is the lightest sterile neutrino N_1 that is produced by the frozen-in real scalar singlet σ due to out-of-equilibrium decays, $\sigma \longrightarrow N_1N_1$. The thermally averaged cross section times relative velocity $\langle\sigma_{\rm ann}v_r\rangle$ for the real scalar singlet σ is calculated numerically using the micrOMEGAs package [64]. $\langle\Gamma(\sigma \longrightarrow N_1N_1)\rangle$ is the thermally averaged decay rate for the decay $\sigma \longrightarrow N_1N_1$ and the analytically determined decay width in the rest frame of the decaying particle σ is:

$$\Gamma(\sigma \longrightarrow N_1N_1) = \frac{y_1^2}{16\pi}m_\sigma\left[1 - \frac{4M_1^2}{m_\sigma^2}\right]\,. \tag{4.3.17}$$

See equations (E.0.9) and (E.0.11) for the definition of $\langle\Gamma(\sigma \longrightarrow N_1N_1)\rangle$. The relic density is obtained from formula (2.3.21).

4.3.3. Existing Constraints on the Free Streaming Horizon

In this section, we determine the free streaming horizon r_{FS} for the sterile neutrinos produced through our new mechanism. In a spatial flat universe, the curvature constant k is zero. Assuming isotropy, i.e., $d\Theta = d\phi = 0$, the Robertson–Walker metric, see equation (2.3.4), reads:

$$ds^2 = c^2 dt^2 - a^2(t) dr^2 \,. \tag{4.3.18}$$

Note that t and r are the comoving coordinates. A freely propagating particle with velocity v then moves on a geodesic $ds^2 = 0$ and satisfies:

$$v(t) dt = a(t) dr \,. \tag{4.3.19}$$

The free streaming horizon r_{FS} is the comoving distance a freely moving particle propagates between a time t_{in} and t_0 and is thus given by:

$$r_{\mathrm{FS}} = \int_{t_{\mathrm{in}}}^{t_0} dt \, \frac{v(t)}{a(t)} \,, \tag{4.3.20}$$

where t_{in} is the initial time at which the integration starts, t_0 is the current time, $v(t)$ is the mean velocity of the DM particles, and $a(t)$ is the scale factor, see also equation (2.4.8).

The first step is to calculate the average momentum $\langle p \rangle$. Therefore, the phase-space distribution function is needed, see discussion of equation (2.4.1) The sterile neutrinos are produced at the time t_{in} after the singlet scalar σ has frozen-in, which happens at the time t_{prod}, and then decays, i.e., $t_{\mathrm{in}} = t_{\mathrm{prod}} + \tau$ where τ is the lifetime of σ given by $\tau = 1/\Gamma$. The freeze-in of σ happens when the temperature of the photons equals the mass of σ, which is of order $\mathcal{O}(100)\,\mathrm{GeV}$. At that time, σ is clearly non-relativistic. Since matter radiation equality occurs much later on at t_{eq}, the decays of σ and thus the production of the sterile neutrinos take place in the radiation dominated era. Under these circumstances, the phase space distribution of the sterile neutrinos is given by [169]:

$$f(p,t) = \frac{\beta}{\frac{p}{T_{\mathrm{DM}}}} \exp\left(-\frac{p^2}{T_{\mathrm{DM}}^2}\right) \,, \tag{4.3.21}$$

where β is a normalization factor that will turn out to be irrelevant for our purposes, p is the co-moving momentum, and the DM temperature is defined as $T_{\mathrm{DM}} = T_{\mathrm{DM}}(t) = p_{cm}{}^{a(t_d)}/_{a(t)}$. Here, $p_{cm} = \sqrt{m_\sigma^2 - M_1^2}/2 \simeq m_\sigma/2$ is the DM momentum in the center-of-mass frame and the decay time t_d is defined as $H(t = t_d) = 1/2t_{\mathrm{in}}$ [170]. Since the particle production happens in the radiation dominated era, the Hubble expansion rate H scales like $H(t) = 1/2t$. Therefore, $H(t_d) = 1/2t_d$ and we can identify $t_d \equiv t_{\mathrm{in}}$.

The average momentum $\langle p \rangle$ follows after integrating the phase space distribution function to:

$$\langle p(t) \rangle = \frac{\sqrt{\pi}}{2} T_{\mathrm{WDM}}(t) \simeq \frac{\sqrt{\pi}}{2} \frac{m_\sigma}{2} \frac{a(t_{\mathrm{in}})}{a(t)} \,. \tag{4.3.22}$$

The mean velocity $v(t)$ of the sterile neutrinos can be set to 1 as long as they are relativistic. After the non-relativistic transition, which sets in at the time $t_{\rm nr}$, the sterile neutrinos are non-relativistic and their mean velocity simply follows from the determined average momentum $\langle p(t)\rangle$, i.e., $v(t) = {}^{\langle p(t)\rangle}/_{M}$.

In a second step, we answer the question about the time when the non-relativistic transition happens. The non-relativistic transition will set in when $\langle p(t)\rangle \simeq {}^{\sqrt{\pi}}/_{2} \cdot {}^{m_\sigma}/_{2} \cdot {}^{a(t_{\rm in})}/_{a(t)} = M$. The scale factor $a(t)$ can be approximated as $a(t) \propto t^{1/2}$ ($a(t) \propto t^{2/3}$) for radiation (matter) dominance. Since the scale factor has a different time dependence in the radiation and matter dominated era, respectively, one has to distinguish between the cases of non-relativistic transition happening before, i.e., $t_{\rm nr}^{\rm early} < t_{\rm eq}$, or after the matter radiation equality, i.e., $t_{\rm nr}^{\rm late} > t_{\rm eq}$.

One finds:

$$t_{\rm nr}^{\rm early} = \left(\frac{\sqrt{\pi}}{2}\frac{m_\sigma}{2M_1}\right)^2 t_{\rm in}\,, \tag{4.3.23}$$

$$t_{\rm nr}^{\rm late} = \left(\frac{\sqrt{\pi}}{2}\frac{m_\sigma}{2M_1}\right)^{\frac{3}{2}} t_{\rm in}^{\frac{3}{4}} t_{\rm eq}^{\frac{1}{4}}\,. \tag{4.3.24}$$

With the outcomes of steps one and two, the free streaming horizon can now be calculated. In the case $t_{\rm nr}^{\rm early} < t_{\rm eq}$, the interval $[t_{\rm in}; t_0]$ can be split into three pieces yielding:

$$r_{\rm FS} = \int_{t_{\rm in}}^{t_0} dt\,\frac{\langle v(t)\rangle}{a(t)} = \int_{t_{\rm in}}^{t_{\rm nr}} \frac{dt}{a(t)} + \int_{t_{\rm nr}}^{t_{\rm eq}} dt\,\frac{\langle v(t)\rangle}{a(t)} + \int_{t_{eq}}^{t_0} dt\,\frac{\langle v(t)\rangle}{a(t)} \tag{4.3.25}$$

$$\simeq \frac{2\sqrt{t_{\rm eq}t_{\rm nr}}}{a_{\rm eq}} + \frac{\sqrt{t_{\rm eq}t_{\rm nr}}}{a_{\rm eq}}\ln\left(\frac{t_{\rm eq}}{t_{\rm nr}}\right) + \frac{3\sqrt{t_{\rm eq}t_{\rm nr}}}{a_{\rm eq}} = \frac{\sqrt{t_{eq}t_{\rm nr}}}{a_{\rm eq}}\left[5 + \ln\left(\frac{t_{\rm eq}}{t_{\rm nr}}\right)\right]. \tag{4.3.26}$$

For the case $t_{\rm nr}^{\rm late} > t_{\rm eq}$, the result reads:

$$r_{\rm FS} = \int_{t_{\rm in}}^{t_0} dt\,\frac{\langle v(t)\rangle}{a(t)} = \int_{t_{\rm in}}^{t_{\rm eq}} \frac{dt}{a(t)} + \int_{t_{\rm eq}}^{t_{\rm nr}} dt\,\frac{\langle v(t)\rangle}{a(t)} + \int_{t_{\rm nr}}^{t_0} dt\,\frac{\langle v(t)\rangle}{a(t)} \tag{4.3.27}$$

$$\simeq \frac{2t_{\rm eq}}{a_{\rm eq}} + \left(\frac{3t_{\rm eq}^{\frac{2}{3}}t_{\rm nr}^{\frac{1}{3}}}{a_{\rm eq}} - \frac{3t_{\rm eq}}{a_{\rm eq}}\right) + \frac{\sqrt{\pi}}{2}\frac{m_\sigma/2}{M_1}\sqrt{\frac{t_{\rm in}}{t_{\rm eq}}}\frac{3\ t_{\rm eq}^{\frac{4}{3}}}{a_{\rm eq}t_{\rm nr}^{\frac{1}{3}}} \tag{4.3.28}$$

$$= \frac{3t_{\rm eq}^{\frac{2}{3}}t_{\rm nr}^{\frac{1}{3}}}{a_{\rm eq}} - \frac{t_{\rm eq}}{a_{\rm eq}} + \frac{\sqrt{\pi}}{2}\frac{m_\sigma/2}{M_1}\sqrt{\frac{t_{\rm in}}{t_{\rm eq}}}\frac{3\ t_{\rm eq}^{\frac{4}{3}}}{a_{\rm eq}t_{\rm nr}^{\frac{1}{3}}}\,. \tag{4.3.29}$$

We have assumed matter-dominance until t_0, since very late times practically do not have any effect on the result [158]. Both expressions exactly coincide in the limit $t_{\rm nr} \to t_{\rm eq}$. One still has to take into account the entropy dilution between the time of production, which happens at a very high temperature, and the current time. This amounts to a

further factor of $\xi^{-1/3}$ [156], with an entropy dilution factor given by:

$$\xi = \frac{g_{\text{eff}}(\text{high } T)}{g_{\text{eff}}(t_0)} \approx \frac{109.5}{3.36}, \tag{4.3.30}$$

where we have taken both the real scalar σ and the keV Majorana neutrino N_1 to contribute to radiation at high temperatures.[2] Since the scalar σ has been produced in a significant amount at the time of its decay, this should not be a bad approximation, and for the same reason also a significant amount of N_1's should be produced. The final result for the free streaming horizon is:

$$r_{\text{FS}} \simeq \left\{ \begin{array}{ll} \frac{\sqrt{t_{\text{eq}} t_{\text{nr}}}}{a_{\text{eq}}} \left[5 + \ln\left(\frac{t_{\text{eq}}}{t_{\text{nr}}}\right) \right] \xi^{-1/3} & \text{if } t_{\text{nr}} < t_{\text{eq}}, \\ \left[\frac{3 t_{\text{eq}}^{\frac{2}{3}} t_{\text{nr}}^{1/3}}{a_{\text{eq}}} - \frac{t_{\text{eq}}}{a_{\text{eq}}} + \frac{\sqrt{\pi}}{2} \frac{m_\sigma/2}{M_1} \sqrt{\frac{t_{\text{in}}}{t_{\text{eq}}}} \frac{3\ t_{\text{eq}}^{\frac{4}{3}}}{a_{\text{eq}} t_{\text{nr}}^{\frac{1}{3}}} \right] \xi^{-1/3} & \text{if } t_{\text{nr}} > t_{\text{eq}}, \end{array} \right\} . \tag{4.3.31}$$

One can define a free-streaming horizon of 0.1 Mpc [172], which is about the size of a dwarf galaxy, as the separation between HDM (r_{FS} >0.1 Mpc) and WDM (r_{FS} ¡ 0.1 Mpc). In turn, free-streaming horizons which are considerably smaller typically correspond to CDM. Note that this is in some sense an artificial definition, as we will explain in detail in section 4.4, but it nevertheless gives a good orientation in practice. As we will see, the condition r_{FS} <0.1 Mpc will lead to a lower bound on the mass M_1 of the keV sterile neutrino.

We have used equation (4.3.31) to mark the excluded region of HDM (r_{FS} >0.1 Mpc) later on in figure 4.4 and in figure 4.5. We will furthermore indicate the CDM regions (r_{FS} <0.01 Mpc), which are not excluded and instead reveal that a keV-mass particle can also act as CDM, depending on the details of its production.

4.3.4. Collider Bounds on the Production of Dark Matter

In colliders, a DM signal can be detected through monojet or cascade events. If the DM particle is stable, it does not decay inside the detector volume and thus leaves its track as missing energy, which can be reconstructed. Comparing simulated DM events with data analysis allows to constrain the DM interaction and its mass. Bounds exist on DM masses around 1 GeV. Specific collider constraints on Majorana fermion DM can be found in [173]; for Dirac fermion, complex scalar, and real scalar DM, see [174].

Because a Majorana field is its own charge conjugate, only operators which are even under charge conjugation are allowed for Majorana fermions. Therefore, in contrast to the case of Dirac fermions, there are neither vector nor tensor field bilinears for Majorana

[2] At this step, we disagree with [156], where the number of degrees of freedom at a high temperature has been taken to be 110.5. This corresponds to one Majorana neutrino and a complex scalar [171]. However, the resulting numerical difference is tiny and would in no case affect the results significantly.

fermions. However, note that the constraints cited above are not relevant in our case, since the DM is a sterile neutrino N_1 with a mass in the keV range, produced by the decay of a frozen-in scalar singlet FIMP.

The scalar singlet FIMP itself is produced via the Higgs portal. In [175], the allowed region for the Higgs portal coupling λ and the mass of the scalar singlet is presented. Through the Higgs portal, the SM Higgs could decay invisibly into two scalar singlets. By demanding that the invisible decay width is less than 20% of the SM decay width, the strongest upper bound on the Higgs portal coupling is $\lambda < 0.01$, but for scalar singlet masses $m_\sigma \gtrsim 60$ GeV there is essentially no constraint. In the mechanism we propose, the Higgs portal coupling is of order $\lambda \sim \mathcal{O}(10^{-8})$, i.e., given the mass range of our scalar singlet and its feeble interactions, the constraints in [175] for the allowed $\lambda - m_S$ region are not relevant for us.

To conclude, all existing collider bounds on the production of DM are not relevant for our mechanism and do not constrain the parameters we are considering in our numerical analysis.

4.4. Numerical Analysis

We have numerically solved equations (4.3.11) and (4.3.12) in order to determine the final abundance of keV sterile neutrinos N_1.

First of all we scanned over a range of values for the Higgs portal coupling λ in order to identify the successful region to obtain the correct relic abundance. The only requirement we impose on λ is that $\lambda \lesssim 10^{-6}$ in order not to enter thermal equilibrium [156]. The result of this scan can be found in figure 4.3, where we plot the abundance regions for different values of the coupling, $\lambda = 10^{-7,8,9}$, as a function of the keV neutrino mass M_1. The broadening of the corresponding bands originates from the variation over the scalar mass m_σ. For definiteness, we assume that the singlet scalar mass is always larger than the SM-like Higgs mass $m_h \approx$125 GeV, corresponding to the upper end of the bands in the plot. Furthermore, in order to avoid entering a potentially non-perturbative regime, we also assume that $m_\sigma < f$ corresponding to the lower ends of the bands in the plot, where f is the VEV of the singlet field S.

In figure 4.3, we present the plots for the two example values f =500 GeV and f =1 TeV, which are perfectly compatible with all bounds. As can be seen from figure 4.3, the successful value of the Higgs portal coupling λ should be around 10^{-8}, more or less independently of the value of the VEV f. Accordingly, we will focus on the region $\lambda \approx 10^{-8}$ in what follows and investigate this region in greater detail in what concerns the relic abundance and in particular the experimental and observational bounds.A more detailed investigation of the successful regions in parameter space can be found in figures 4.4 and 4.5, where we have indicated the region of the correct abundance, i.e., within the 3σ

ranges of the *Planck* data [5], as generated by scalar FIMP production only, by the orange band in the plot. The parameter values for the plots are chosen as $f \in [500; 1000]$ GeV, with $\lambda \in [1.0 \cdot 10^{-8}; 1.2 \cdot 10^{-8}]$ for figure 4.4 and $\lambda \in [1.5 \cdot 10^{-8}; 2.0 \cdot 10^{-8}]$ for figure 4.5.

As can be seen from the plots, the iso-abundance lines reveal a more or less linear dependence of the keV sterile neutrinos mass M_1 on the scalar singlet mass m_σ. This feature can be understood easily by observing that the final DM energy density must be equal to the initial energy density in scalar σ particles, which can at most be redshifted. Since this initial energy density is non-relativistic, it can be written as $\rho_\sigma = m_\sigma n_\sigma$, where n_σ is the number density of σ-particles. Similarly, the energy density in N_1 can be computed by the non-relativistic expression for late times, see the discussion in section 4.2, since in the successful regions in the parameter space the DM particles become non-relativistic within the age of the Universe. In addition, we have indicated some important bounds. As explained, we have assumed that $m_\sigma > m_h$, and we indicate the corresponding regions left of the upper 1σ bound on m_h of 126.4 GeV [167] by gray rectangles. Furthermore, we know that HDM is excluded or, rather, bound to make up at most 1% of the DM in the Universe [176, 177] by considerations of cosmological structure formation.

A rough way to quantify when DM particles are HDM, WDM, or CDM is the co-moving free-streaming horizon r_{FS}, see section 4.3.3. Since it is a bit crude to attribute the property of a whole velocity spectrum of DM particles to one single number, it is to some extent a question of definition where to draw the lines between the three DM categories. A relatively common choice, which somewhat representatively reflects the use of the three terms in the literature [178, 179] is to take the border between HDM and WDM at a free-streaming horizon of roughly $r_{\mathrm{FS}} = 0.1\,\mathrm{Mpc}$, where larger values signal HDM which is forbidden. Note that this value is physically motivated due to the size of dwarf satellite galaxies being in that range. However, between CDM and WDM, there is not a very well-defined boundary, since it is not easy to unambiguously define at which value of r_{FS} the structure formation on small scales starts to depart from the pure CDM case [158, 180]. However, it is clear that the free-streaming horizon for CDM should be "significantly smaller" than the one for WDM. For definiteness, we have therefore decided to simply take a value that is by one order of magnitude smaller than the one for the HDM–WDM boundary. Keeping in mind that this distinction between WDM and CDM is also a matter of definition, the values of r_{FS} which we used are:

$$\begin{aligned} \text{Cold DM (CDM)} &\quad :\Longleftrightarrow \quad r_{\mathrm{FS}} < 0.01\,\mathrm{Mpc}, \\ \text{Warm DM (WDM)} &\quad :\Longleftrightarrow \quad 0.01\,\mathrm{Mpc} < r_{\mathrm{FS}} < 0.1\,\mathrm{Mpc}, \\ \text{Hot DM (HDM)} &\quad :\Longleftrightarrow \quad 0.1\,\mathrm{Mpc} < r_{\mathrm{FS}}. \end{aligned}$$

Thus, in the plots displayed in figures 4.4 and 4.5, the thick red line at the bottom of the plots marks the transition between WDM and HDM, and the light red region below

this line is excluded by structure formation. The light blue region in the upper part of the plots, bounded by the thick blue line, corresponds to CDM and the white region marks the WDM sector. Here, it is worth pointing out that in a considerable region of the parameter space, keV sterile neutrinos with large enough masses can be cold DM, or, more precisely, indistinguishable from CDM according to our definition, in contrast to most of the scenarios for keV sterile neutrino DM. To some extent, this is a simple reflection of the fact that our DM production happens in the early Universe, but the more crucial point is that the mass ratio m_σ/M_1 happens to be in the correct region to allow for a sufficient cooling time. Figures 4.4 and 4.5 reveal that the region of the correct DM relic abundance lies in the cold or warm DM parameter space, depending on the specific value of λ, respectively. We also have the possibility to produce part of the DM as keV sterile neutrinos by the ordinary DW-mechanism [151], in addition to the production by the mechanism proposed here. This contribution depends on the active-sterile mixing angle θ_1 of the keV sterile neutrino N_1, and it can be estimated by the approximate formula [181]:

$$\Omega_{N_1,\mathrm{DW}}h^2 \approx 0.2 \cdot \frac{\sin^2\theta_1}{3\cdot 10^{-9}} \left(\frac{M_1}{3\ \mathrm{keV}}\right)^{1.8} . \tag{4.4.1}$$

Note that, if the keV sterile neutrino makes up all of the DM in the Universe and if it is unstable under and decays into photons, then there is a strong bound from the non-observation of the corresponding X-ray line, see [159,182,183] for recent collections of bounds. In the plots, we have represented the corresponding maximal, i.e., for the largest allowed value of $\sin^2\theta_1$ addition of particle production due to the DW mechanism by the purple bands. As can be seen from the plots, this would shift the allowed regions, i.e., the regions where the total abundance of keV neutrinos, as produced by both mechanisms together, is within the 3σ regions of *Planck* data, towards slightly larger values of m_σ. For very low M_1, there is a considerable DW-production resulting from the comparatively weak X-ray bound in this mass region. In this region, nearly all the DM can be produced by the DW-mechanism, which for these masses completely dominates the production by frozen-in scalars, if the maximum possible value is taken for the active-sterile mixing. However, from studies of the Lyman-alpha forest, the corresponding lower bound on the keV sterile neutrino mass, when the DW-mechanism is at work, is between 8 keV and 10 keV [158]. Note that this accidentally coincides with the light red HDM region in our plots. Thus, this region of the parameter space is excluded. On the other hand, depending on the exact value of the active-sterile mixing, the combined abundance of keV sterile neutrinos produced by both mechanisms could also lie in between the orange and purple bands, which we indicate in the plots.

We want to stress that the orange bands correspond to production by scalar FIMPs only, i.e., this is the region of correct abundance for a vanishing active-sterile mixing, $\theta_1 \equiv 0$. While this may not be desirable from a phenomenological point of view, e.g., for

a possible detection of the X-ray line [184], or for a potential detection of modifications of neutrino-less double beta decay [183, 185]), vanishing active-sterile mixing may be very natural in certain settings [186]. In such frameworks it would be impossible to produce keV sterile neutrinos via the DW and/or SF mechanisms, but our mechanism as well as the version in which the scalar freezes out could be easily used as an alternative.

Finally, we have also indicated possible mass limits arising from the X-ray bound. For example, if the bound on the active-sterile mixing is taken to be $\sin^2(2\theta_1) < 10^{-13}$, this excludes keV sterile neutrino masses M_1 above 64.5 keV, while the values below are consistent with the X-ray bound, but not necessarily with the HDM bound. If active-sterile mixing is not present, then there is no fixed upper bound on M_1, and alternative scenarios with stable, e.g., MeV or GeV sterile neutrino DM could be found, too. The general message of our plots is that there is considerable room for keV sterile neutrinos to be produced by scalar FIMPs and to be compatible with all bounds. Accordingly, if in a certain setting the Higgs portal coupling of a singlet scalar is bound to be very small, it could still be used to produce sterile neutrino DM.

4.5. Summary: Freeze-In Production of keV Sterile Neutrino Dark Matter

Many models beyond the SM include three right-handed neutrinos as counterparts to the left-handed neutrinos. As $SU(2)_L$ singlets, right-handed neutrinos do not directly take part in weak interactions, or in other words, they are sterile. For an appropriate mass hierarchy of the three right-handed neutrinos, two of these can generate the measured neutrino oscillation parameters, the remaining lightest one, given that it is stable, can be a DM particle. If its mass is in the keV range, this right-handed neutrino can be a warm DM. On large scales, warm DM behaves as cold DM, but on small scales warm DM describes the structures of the Universe even better than cold DM. These arguments turn keV sterile neutrino DM into a are very interesting candidate for warm DM, offering at the same time a common framework for neutrino mass generation and DM physics.

Numerous mechanisms to produce keV sterile neutrino DM are discussed in the literature. As examples, we discussed oscillations between active and sterile neutrinos and the production of sterile neutrinos by decays of scalar particles. In the latter case, scenarios had been studied in which the scalar particle freezes out from thermal equilibrium.

We presented a new and successful mechanism for the production of keV sterile neutrino DM. The underlying principle is the freeze-in of a scalar particle σ that never enters thermal equilibrium. A significant abundance of σ is produced by a feeble mixing with the SM Higgs doublet H. If σ is unstable, it can decay into pairs of keV sterile neutrinos N_1. Thus, the correct DM relic density is achieved by the decay of a frozen in feebly

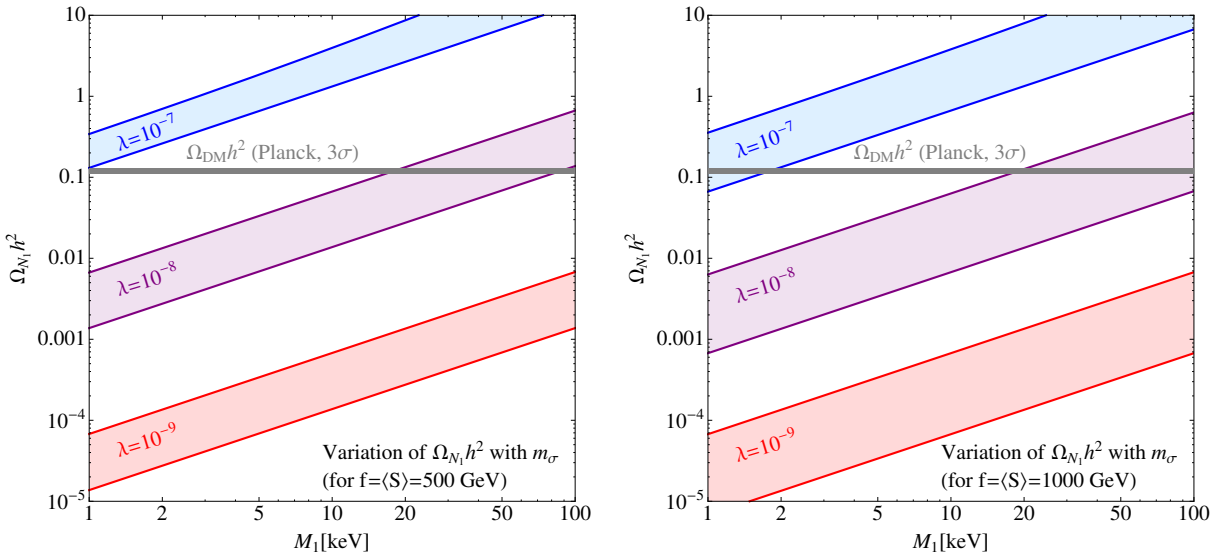

Figure 4.3.: Relic density $\Omega_{N_1}h^2$ as a function of the sterile neutrino mass M_1, for Higgs portal coupling $\lambda = 10^{-7,8,9}$. In the left panel we show the results considering f =500 GeV, while in the right panel the results with f =1 TeV.

interacting scalar particle.

The corresponding system of coupled Boltzmann equations was solved numerically. The relevant bounds for keV sterile neutrinos were discussed emphasizing the new parameter regions of our mechanism.

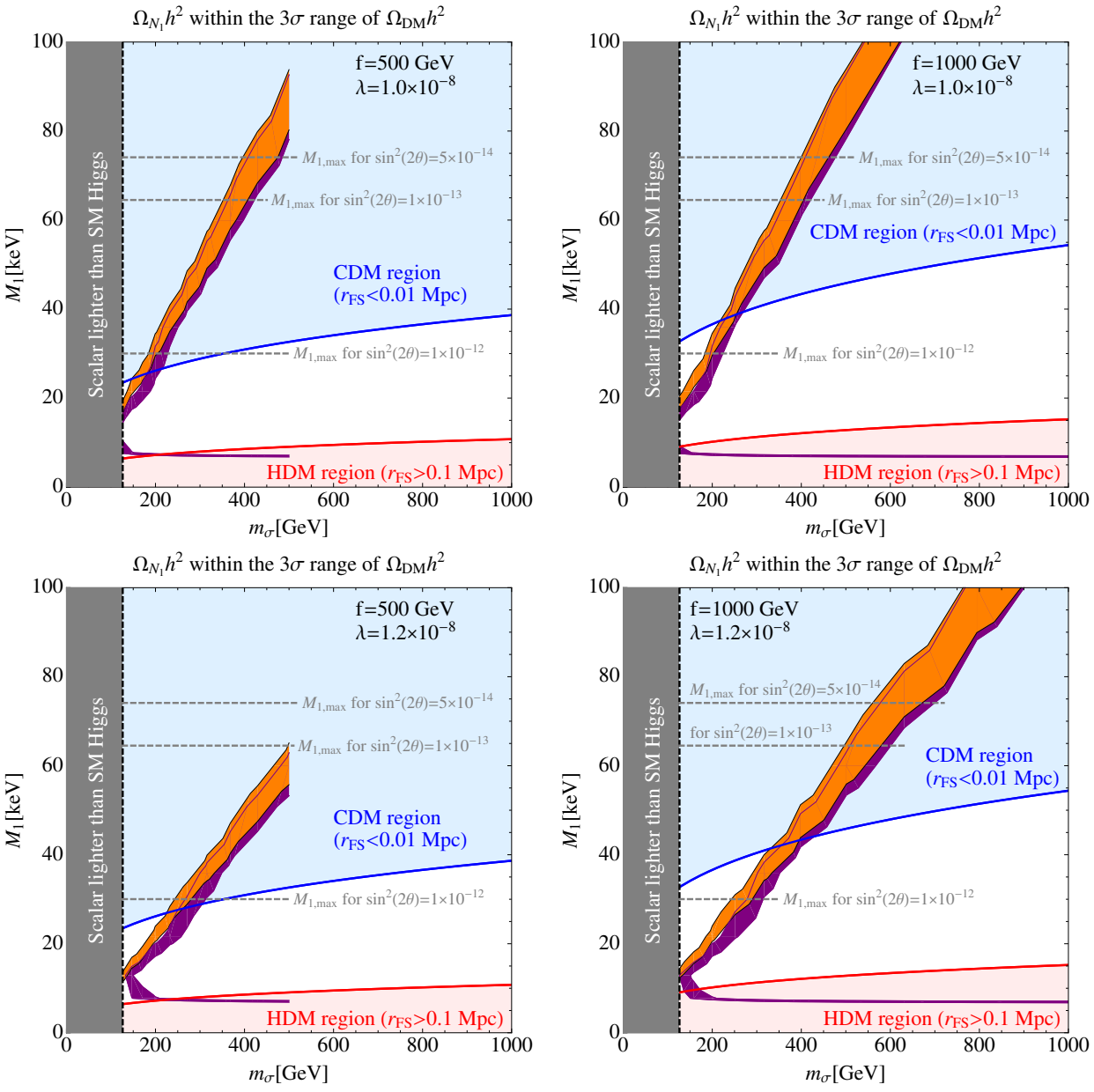

Figure 4.4.: We show the results using $\lambda = 1.0\cdot10^{-8},\ 1.2\cdot10^{-8}$, as well as f =500 GeV and f =1 TeV. The orange (purple) bands represent the regions of the parameter space with a sterile neutrino relic abundance $\Omega_{N_1}h^2$ within the 3σ observed value, obtained only through the decay of a freeze-in scalar, considering also the DW mechanism, see text for more details. The red and blue areas denote the HDM and CDM regions, respectively.

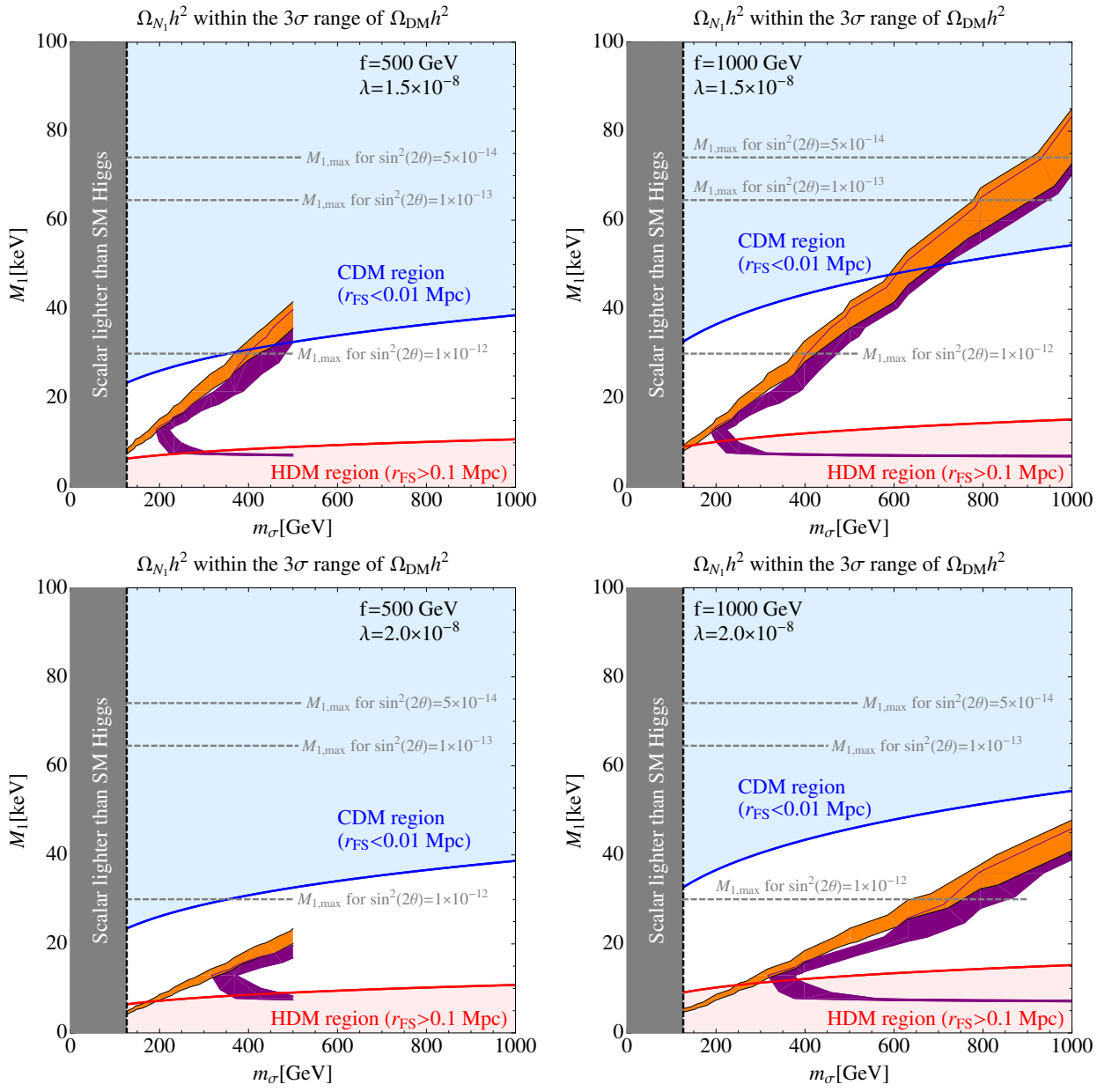

Figure 4.5.: Same as figure 4.4, but for $\lambda = 1.5 \cdot 10^{-8},\ 2.0 \cdot 10^{-8}$.

5. Conclusions

Neutrino flavor oscillation experiments have precisely measured the neutrino mixing angles and the difference of squared mass eigenvalues, which are all different from zero. However, the SM does not contain a mass term for neutrinos. Apart from that, cosmological observations that probe the energy density of the Universe have shown that the matter content of the SM does only contribute with approximately 15.50% to the whole matter content of the Universe. That is, 84.50% of the matter content is not described by SM particle physics. Since up to now only gravitational interactions of this missing mass component have manifest themselves in the structure formation of the Universe, but no electromagnetic interactions, in particular, this lion share of matter is called DM. In the introductory section 1 of this thesis, we outlined the importance of neutrino masses and DM.

It is tempting to ask if neutrino masses and DM physics could be explained by a common theoretical principle, thus providing a unified framework for these two issues. In that sense, models which generate neutrino masses radiatively are one possible answer; the loops needed to make neutrinos massive could connect to DM physics such that neutrino masses and a DM particle have a common energy scale. In most of these kinds of frameworks, the DM relic density is produced by freeze-out, which starts with a DM particle that is in thermal equilibrium. An alternative to obtain the correct DM relic density is the freeze-in scenario, which starts with a particle that is never in thermal equilibrium. This thesis contributes to unified frameworks for neutrino mass generation and to DM physics.

In part I, DM freeze-out production is considered in two exemplarily models which generate neutrino masses at loop-level; these are the Ma-model discussed in sections 3.1 and 3.2 and the Zee–Babu-model in section 3.4.

The Ma-model is a one-loop radiative neutrino mass model in which the DM particle runs in the loop. Therefore, neutrino masses and DM physics are directly linked in the neutrino mass generation. The particles beyond the SM are a complex scalar doublet η and three right-handed Majorana neutrinos $N_i (i = 1, 2, 3)$. In principle, the Ma-model has two candidates for a DM particle: either the neutral component η or the lightest of the N_i. In section 3.1.3, we chose N_1, which is the lightest of the right-handed Majorana neutrinos, as the DM particle. Also, we chose a small mass splitting δ of N_1 to the second lightest right-handed Majorana neutrino N_2. With this choice, we have to include co-annihilations of N_1 and N_2. Our result is that these co-annihilations are essential for

producing the correct DM relic density: the $N_1 - N_1$, $N_2 - N_2$ and $N_1 - N_2$ annihilations depend on Yukawa coupling constants that are constrained by LFV processes. In many cases, these Yukawa coupling constants have to be tiny yielding a too large relic density in the freeze-out scenario. In our case, the co-annihilations $N_1 - N_2$ have a term independent of the relative velocity at lowest order and thus give a relative large cross section for relative small Yukawa coupling constants, i.e., a small enough DM relic density. In addition, in some regions of the parameter space, co-annihilations between N_1 and η become important. N_1 has no direct couplings to quarks or gluons that are necessarily for its possible direct detection. However, via one-loop photon exchange, N_1 can effectively couple to a nucleus realizing inelastic scattering. To the best of our knowledge, we have calculated for the first time the inelastic scattering cross sections in an effective field theory approach, see section 3.2.1. We have determined charge-charge, dipole-charge and dipole-dipole interactions. We have found that the mass splitting δ has to be small in order to obtain a sizable signal in direct detection experiments, which is consistent with the need of co-annihilations relying on a small δ. The XENON1T experiment could have sensitivity to most of our parameter space.

The Zee–Babu-model is a two-loop neutrino mass model. In its original version, it has no right-handed neutrinos and no candidate for a DM particle. The particles beyond the SM are a singly charged scalar h^+ and a doubly charged scalar k^{++}. To close the loops, a lepton number violating trilinear scalar interaction term $\mu k^{++} h^- h^-$ has to be introduced by hands. To connect neutrino mass generation with DM physics in the Zee–Babu model, we have used the spontaneous breaking of a global $U(1)_{B-L}$ symmetry. Therefore, the model is extended by a complex scalar singlet ϕ driving the symmetry breaking and two right handed neutrinos for DM. The μ term and thus neutrino masses as well as the mass of the DM arise when ϕ obtains its vacuum expectation value. After the spontaneous symmetry breaking, a remnant discrete symmetry stabilizes the DM. We have used a global symmetry and not a local one. If one uses a local $B - L$ symmetry, the $B - L$ charges of the three right-handed neutrinos are fixed by gauge anomaly conditions and Yukawa interactions to SM lepton doublets are allowed. To have the lightest of the three right-handed neutrinos stable, an additional $\mathbb{Z}_2$ symmetry has to be introduced. This is not the case for a global symmetry: the $B - L$ charges of the right-handed neutrinos can be chosen with more freedom and the stability of the DM is automatically guaranteed by a remnant stabilization symmetry. Also, in the global case, there are no bounds coming from a Z' gauge boson, which would decrease the allowed parameter space for the correct DM relic density. But in the global case, there is a Goldstone boson which contributes to the DM relic density in contrast to the local case.

In part II, we have presented an alternative to freeze-out of DM: a new production mechanism for keV sterile neutrino DM is introduced that is based on the freeze-in of a scalar particle σ. Although it never enters thermal equilibrium, a significant abundance of σ is produced due to its feeble interactions with the SM Higgs doublet. If it is unstable,

it can decay into a pair of keV sterile neutrinos which are the proposed DM particles. Thus, the relic density of DM is produced by the decay of a frozen-in feebly interacting massive particle. Similar mechanisms had already been proposed previously for early and late freeze-out and subsequent decay of the scalar. Our proposal opens up a new window in a region of the parameter space where freeze-out is not at all possible. This is particularly interesting for models which predict a very small Higgs portal coupling between σ and the SM-like Higgs. Our mechanism is applicable to many models including neutrino mass generation by seesaw scenarios or at loop level.

Appendix

A. Expansion of the Annihilation Cross Section

In chapter 3, we express the $2 \to 2$ effective annihilation cross section σ_{eff} times relative velocity v_r as an expansion in v:

$$\sigma_{\text{eff}} v_r = a_{\text{eff}} + b_{\text{eff}} v_r^2 + \mathcal{O}(v_r^4)\,. \tag{A.0.1}$$

In this appendix, we provide a detailed explanation for this expansion. We rely on the argumentation of [59].

As initial states, we consider N_1N_1, N_2N_2, N_1N_2 and $N_1\eta$. The mass differences between the intial particles either vanish or is almost zero in the cases we consider. Therefore, it is justified to set the masses of the initial particles to M_1. p_1 and p_2 are the incoming momenta. p_α and p_β are the outgoing momenta. The masses of the final state particles are m_α and m_β, respectively. The differential cross section σ_{eff} with respect to the solid angle Ω is written as:

$$\frac{d\sigma_{\text{eff}}}{d\Omega} = \frac{|\mathcal{M}|^2}{64\pi^2 s} \frac{|\mathbf{p}_\alpha|}{|\mathbf{p}_\beta|}\,. \tag{A.0.2}$$

$\mathcal{M}$ is the corresponding amplitude. Here and in the following, s, t and u are the Mandelstam variables. Since $u = \sum(M_i^2 + m_\alpha^2) - s - t$, where the sum includes all final and initial state particles, the amplitude does in general depend on s and t, i.e., $|\mathcal{M}|^2 = J(s,t)$. Due to kinematics, $|\mathbf{p_1}| = {}^{M_1 v_{\text{cm}}}/\sqrt{1-v_{\text{cm}}^2}$ with the center of mass system velocity $v_{\text{cm}} = {}^1\!/_2 v_r$ and $|\mathbf{p}_\alpha| = \sqrt{(s-(m_\alpha+m_\beta)^2)(s-(m_\alpha-m_\beta)^2)}/2\sqrt{s}$. We further introduce the s-depending function $K(s) = {}^{\mathbf{p}_\alpha}\!/_{16\pi M_1 s}$ such that the differential cross section σ_{eff} with respect to the solid angle Ω, into which the final state products are produced, equals:

$$v_{\text{cm}} \frac{d\sigma_{\text{eff}}}{d\Omega} = \frac{J(s,t)}{4\pi} K(s) \sqrt{1 - v_{\text{cm}}^2}\,. \tag{A.0.3}$$

The Mandelstam variable s equals $s = {}^{4M_1^2}\!/\!/1 - v_{\text{cm}}^2$. Since $v_{\text{cm}} \ll 1$, s can be Taylor expanded in v_{cm} yielding:

$$s = 4M_1^2(1 + v_{\text{cm}}^2 + v_{\text{cm}}^4 + \mathcal{O}(v_{\text{cm}}^6))\,. \tag{A.0.4}$$

The Mandelstam variable t equals $t = M_1^2 + m_\alpha^2 - 2(E_1 E_\alpha - \mathbf{p_1 p}_\alpha)$. E_1 can be written as $E_1 = \sqrt{s}/2$ and $E_\alpha = \sqrt{s}/2 \cdot (1 + {}^{m_\alpha^2 - m_\beta^2}/_s)$. The scalar product $\mathbf{p_1 p}_\alpha$ equals $\mathbf{p_1 p}_\alpha = |\mathbf{p_1}||\mathbf{p}_\alpha| \cos\Theta$. For $|\mathbf{p_1}|$ and $|\mathbf{p}_\alpha|$ we can write: $|\mathbf{p_1}| = \sqrt{s}/2 \cdot v_{\mathrm{cm}}$ and

$$|\mathbf{p}_\alpha| = \frac{\sqrt{s}}{2} \sqrt{\left(1 - \frac{(m_\alpha + m_\beta)^2}{s}\right)\left(1 - \frac{(m_\alpha - m_\beta)^2}{s}\right)}\,. \tag{A.0.5}$$

Thus the Mandelstam t equals:

$$\begin{aligned} t =& M_1^2 + m_\alpha^2 - \frac{s}{2}\left(1 + \frac{m_\alpha^2 - m_\beta^2}{s}\right. \\ & \left. - \cos\Theta v_{\mathrm{cm}} \sqrt{\left(1 - \frac{(m_\alpha + m_\beta)^2}{s}\right)\left(1 - \frac{(m_\alpha - m_\beta)^2}{s}\right)}\right)\,. \end{aligned} \tag{A.0.6}$$

Expressing s again via v_{cm}, a Taylor expansion of t yields:

$$\begin{aligned} t =& \frac{-2M_1^2 + m_\alpha^2 + m_\beta^2}{2} \\ & + \frac{1}{2}\cos\Theta v_{\mathrm{cm}} \sqrt{(4M_1^2 - (m_\alpha - m_\beta)^2)(4M_1^2 - (m_\alpha + m_\beta)^2)} \\ & - 2M_1 v_{\mathrm{cm}}^2 \\ & + \cos\Theta v_{\mathrm{cm}}^3 \frac{2M_1^2(4M_1^2 - m_\alpha^2 - m_\beta^2)}{\sqrt{(4M_1^2 - (m_\alpha - m_\beta)^2)(4M_1^2 - (m_\alpha + m_\beta)^2)}} \\ & - 2M_1^2 v_{\mathrm{cm}}^4 + \mathcal{O}(v_{\mathrm{cm}}^5)\,. \end{aligned} \tag{A.0.7}$$

In the Taylor expansion of $K(s)$, only even powers of v_{cm} remain:

$$K(s) = K_0 + K_2 v_{\mathrm{cm}}^2 + K_4 v_{\mathrm{cm}}^4 + \mathcal{O}(v_{\mathrm{cm}}^6)\,. \tag{A.0.8}$$

The coefficients K_i do depend only on the masses M_1, m_α and m_β.

Using the expansions of s and t, the quantity $J(s,t)/4\pi$ can be Taylor expanded around $s_0 \equiv 4M_1^2$ and $t_0 \equiv (-2M_1^2 + m_\alpha^2 + m_\beta^2)/2$:

$$\begin{aligned} J(s,t) \approx & J(s,t)|_{s=s_0;t=t_0} + \left.\frac{\partial J}{\partial s}\right|_{s=s_0;t=t_0} (s - s_0) + \left.\frac{\partial J}{\partial t}\right|_{s=s_0;t=t_0} (t - t_0) \\ & + \frac{1}{2}\left.\frac{\partial^2 J}{\partial s^2}\right|_{s=s_0;t=t_0} (s - s_0)^2 + \frac{1}{2}\left.\frac{\partial^2 J}{\partial t^2}\right|_{s=s_0;t=t_0} (t - t_0)^2 \\ & + \frac{1}{2}\left.\frac{\partial^2 J}{\partial s \partial t}\right|_{s=s_0;t=t_0} (s - s_0)(t - t_0) \end{aligned} \tag{A.0.9}$$

To obtain the cross section, the integration over the solid angle $d\Omega = \sin\Theta d\Theta d\phi$ has to be performed. The only angle dependence is $\cos\Theta$ in the expansion of t. Since

$J(s,t)|_{s=s_0;t=t_0}$ and $\partial^{m+n}J/\partial^m s\partial^n t|_{s=s_0;t=t_0}$ do not depend on $\cos\Theta$ after inserting s_0 and t_0, the only $\cos\Theta$ dependence is in $(t-t_0)^n$. Because $\int_0^\pi d\Theta \sin\Theta\cos\Theta^{2n+1} = 0$, only even powers of $\cos\Theta$ and therefore only even powers of v_{cm} contribute. Due to the dependence of the Mandelstam variables s and t on $\cos\Theta$ and v_{cm}, the cross section thus depends only on even powers of v_{cm}. Integrating the expanded $J(s,t)$ over the solid angle Ω, the result can therefore be written as:

$$\int d\Omega \, \frac{J(s,t)}{4\pi} = J(s,t)|_{s=s_0;t=t_0} + J_2 v_{\mathrm{cm}}^2 + J_4 v_{\mathrm{cm}}^4 + \mathcal{O}\left(v_{\mathrm{cm}}^6\right) . \tag{A.0.10}$$

The coefficients J_i only depend on the involved masses and derivatives of $J(s,t)|_{s=s_0;t=t_0}$. The outcome for the cross section can then be expressed as:

$$\sigma_{\mathrm{eff}} v_{\mathrm{cm}} = a_{\mathrm{eff}} + b_{\mathrm{eff}} v_{\mathrm{cm}}^2 + c_{\mathrm{eff}} v_{\mathrm{cm}}^4 + \mathcal{O}(v_{\mathrm{cm}}^6) . \tag{A.0.11}$$

The involved coefficients are given in terms of M_1, m_α, m_β and derivatives of $|\mathcal{M}|^2$.

B. Loop Integrals

We present the calculation for the loop function $F_2(x)$ involved in the lepton flavor violating decay $L_\alpha \longrightarrow L_\beta\gamma$, see (3.1.34). The loop integral is:

$$\int \frac{d^dq}{(2\pi)^d}\,\overline{u}\,(p')\,P_R\frac{\not{p}+\not{q}+M_i}{(p+q)^2-M_i^2}\,\frac{(2q+k)^\mu}{((q+k)^2-M_\eta^2)(q^2-m_0^2)}P_L u\,(p)\ . \tag{B.0.1}$$

Using Feynman parametrization, the denominator D of (B.0.1) can be expressed as $(D)^{-\frac{1}{3}} = l^2 - \overline{\Lambda_i}$ with $l = q + Q$, $\overline{\Lambda_i} \approx xM_i^2 + (1-x)m_0^2$ and $Q = xp + yk$. We have neglected the masses of the muon and electron compared to the masses of N_i and η.We keep trace of the additional factor $(3-1)! = 2$. In dimensional regularization, the denominator of (B.0.1) results to:

$$\begin{aligned}&\int_0^1 dx\int_0^{1-x} dy 2\int\frac{d^dl}{(2\pi)^d}\,\frac{1}{(l^2-\overline{\Lambda_i})^3} = \int_0^1 dx\int_0^{1-x} dy\,2\frac{(-1)^3 i}{(4\pi)^2}\frac{\Gamma(1)}{\Gamma(3)}\left(\frac{1}{\overline{\Lambda_i}}\right)\\ &= \int_0^1 dx\int_0^{1-x} dy\,\frac{-i}{(4\pi)^2}\frac{1}{xM_i^2+(1-x)M_\eta^2}\,.\end{aligned} \tag{B.0.2}$$

In the numerator, terms that are odd in l vanish by the symmetric integration in l. The Dirac equation yields $\overline{u}\,(p')\not{p}' = m_e\overline{u}\,(p') \approx 0$ and $\not{p}u\,(p) = m_\mu u\,(p)$. Since the polarization tensor ϵ_μ^* of the outgoing photon is involved in the amplitude, terms in the numerator that are proportional to k^μ vanish. Thus, the outcome for the numerator is $-m_\mu x(1-x-y)\overline{u}\,(p')\,(p^\mu + p'^\mu)P_R u(p)$.

Combining the numerator and the denominator expressions, respectively, yields the loop function $F_2(x)$:

$$\int_0^1 dx\int_0^{1-x} dy\,\frac{x(1-x-y)}{xM_i^2+(1-x)m_0^2} \tag{B.0.3}$$

$$= \frac{1-6\frac{M_i^2}{m_0^2}+3\left(\frac{M_i^2}{m_0^2}\right)^2+2\left(\frac{M_i^2}{m_0^2}\right)^3-6\left(\frac{M_i^2}{m_0^2}\right)^2\log\left(\frac{M_i^2}{m_0^2}\right)}{12\left(1-\frac{M_i^2}{m_0^2}\right)^4} \tag{B.0.4}$$

$$= \frac{1}{2}F_2\left(\frac{M_i^2}{m_0^2}\right)\ . \tag{B.0.5}$$

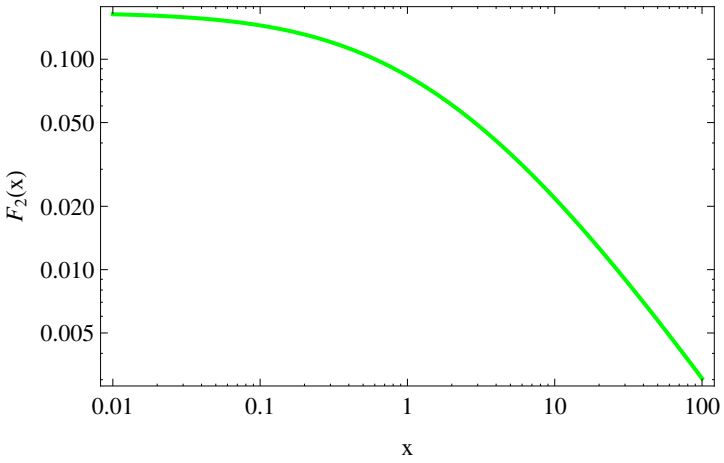

Figure B.1.: The loop function $F_2(x)$.

Next, we give the explicit functions involved in the effective interactions in equations (3.2.3), (3.2.4) and (3.2.5). The functions $I_a(x,y)$ and $I_m(x)$ are given as follows:

$$I_a(x,y) = \frac{1}{3}\int_0^1 \frac{3u^2-6u+1}{xu^2-(1+x-y)u+1}, \tag{B.0.6}$$

$$I_m(x,y) = -\int_0^1 \frac{u(1-u)}{xu^2-(1+x-y)u+1}. \tag{B.0.7}$$

The analytic formulas [1] of these integrations are written as:

(i) If $(1+x-y)^2-4x>0$,

$$\begin{aligned} I_a(x,y) =& \frac{1}{x}\left[1+\frac{3A_+^2-6A_++1}{3(A_+-A_-)}\log\left|\frac{A_+-1}{A_+}\right|\right. \\ &\left.-\frac{3A_-^2-6A_-+1}{3(A_+-A_-)}\log\left|\frac{A_--1}{A_-}\right|\right], \end{aligned} \tag{B.0.8}$$

$$\begin{aligned} I_m(x,y) =& \frac{1}{x}\left[1+\frac{A_+(A_+-1)}{A_+-A_-}\log\left|\frac{A_+-1}{A_+}\right|\right. \\ &\left.-\frac{A_-(A_--1)}{A_+-A_-}\log\left|\frac{A_--1}{A_-}\right|\right]. \end{aligned} \tag{B.0.9}$$

(ii) If $(1+x-y)^2-4x=0$,

[1] I am indebted to Takashi Toma for providing me the analytic formulas.

$$I_a(x,y) = \frac{1}{x}\left[1 + 2(A_0-1)\log\left|\frac{A_0-1}{A_0}\right| + \frac{3A_0^2-6A_0+1}{3A_0(A_0-1)}\right], \tag{B.0.10}$$

$$I_m(x,y) = \frac{1}{x}\left[2 + (2A_0-1)\log\left|\frac{A_0-1}{A_0}\right|\right]. \tag{B.0.11}$$

(iii) If $(1+x-y)^2 - 4x < 0$,

$$\begin{aligned} I_a(x,y) =& \frac{1}{x}\left[1 + \frac{B_+ + B_- - 2}{2}\log\left|\frac{(B_+-1)^2+(B_--1)^2}{B_+^2+B_-^2}\right|\right. \\ &\left. + \frac{6(B_+-1)(B_--1)-4}{3(B_+-B_-)}\tan^{-1}\left(\frac{B_+-B_-}{B_+^2+B_-^2-B_+-B_-}\right)\right], \end{aligned} \tag{B.0.12}$$

$$\begin{aligned} I_m(x,y) =& \frac{1}{x}\left[1 + \frac{B_+ + B_- - 1}{2}\log\left|\frac{(B_+-1)^2+(B_--1)^2}{B_+^2+B_-^2}\right|\right. \\ &\left. + \frac{(2B_+-1)(2B_--1)-1}{2(B_+-B_-)}\tan^{-1}\left(\frac{B_+-B_-}{B_+^2+B_-^2-B_+-B_-}\right)\right]. \end{aligned} \tag{B.0.13}$$

$A_\pm$, A_0 and $B_\pm$ are defined as

$$A_\pm \equiv \frac{1+x-y \pm \sqrt{(1+x-y)^2-4x}}{2x}, \tag{B.0.14}$$

$$A_0 \equiv \frac{1+x-y}{2x}, \tag{B.0.15}$$

$$B_\pm \equiv \frac{1+x-y \pm \sqrt{4x-(1+x-y)^2}}{2x}. \tag{B.0.16}$$

The function $I_c(x,y)$ is the same as $I_m(x,y)$.

These functions are continuous and smooth for $0 \le x, y \le 1$. For $0 \simeq y \ll x \ll 1$, these functions approach to

$$I_a(x,y) \to \frac{1}{2} + \frac{2}{3}\log y, \tag{B.0.17}$$

$$I_m(x,y) \to -\frac{1}{2}. \tag{B.0.18}$$

Therefore the obtained parameters $|b_{12}|$ and $|\mu_{12}|$ at lowest order agree with the result of [113] where the parameter λ^2 corresponds to $\mathrm{Im}(h^*_{\alpha 2}h_{\alpha 1})/2$ in our notation. The difference of the relative sign comes from the definition of the effective operators.

C. Degrees of Freedom

A particle species i with mass m_i, momentum p_i, energy $E_i = \sqrt{m_i^2 + p_i^2}$ and temperature T_i that is in kinetic equilibrium has the following energy ρ_i and entropy density s_i [187]:

$$\rho_i\left(T_i\right) = \int_0^\infty d^3p\, E_i f_i(T_i, E_i)\,, \tag{C.0.1}$$

$$s_i\left(T_i\right) = \int_0^\infty d^3p\, \frac{3m_i^2 + 4p_i^2}{3E_iT_i} f_i(T_i, E_i)\,. \tag{C.0.2}$$

The phase-space distribution function $f_i(T_i, E_i)$ is:

$$f_i(T_i, E_i) = \frac{g_i}{(2\pi^3)} \frac{1}{e^{E_i/T_i} + \eta_i}\,, \tag{C.0.3}$$

with g_i the number of internal degrees of freedom and $\eta_i = 1$ for Fermi–Dirac, $\eta_i = -1$ for Bose–Einstein and $\eta = 0$ for Maxwell–Boltzmann statistics. We write ρ_i and s_i as:

$$\rho_i\left(T_i\right) = g^i_{\text{eff}}\left(T_i\right) \frac{\pi^2}{30} T_i^4\,, \tag{C.0.4}$$

$$s_i\left(T_i\right) = h^i_{\text{eff}}\left(T_i\right) \frac{2\pi^2}{45} T_i^3\,, \tag{C.0.5}$$

with the effective T-dependent degrees of freedom g^i_{eff} and h^i_{eff} for a species i for energy and entropy density, respectively. g^i_{eff} and h^i_{eff} follow from equations (C.0.1) and (C.0.2) to:

$$g^i_{\text{eff}}\left(T_i\right) = \frac{15 g_i}{\pi^4} x_i^4 \int_1^\infty dy\, y^2 \sqrt{y^2 - 1} \frac{1}{e^{y x_i} + \eta_i}\,, \tag{C.0.6}$$

$$h^i_{\text{eff}}\left(T_i\right) = \frac{45 g_i}{12\pi^4} x_i^4 \int_1^\infty dy\, \left(4y^2 - 1\right) \sqrt{y^2 - 1} \frac{1}{e^{y x_i} + \eta_i}\,, \tag{C.0.7}$$

with $x_i \equiv m_i/T_i$ and $y \equiv E_i/m_i$.

In our numerics in chapter 4, we account for the contribution of the real scalar singlet σ and the sterile neutrino N using equations (C.0.6) and (C.0.7). The total energy and entropy effective degrees of freedom, which enter into the calculation of the total entropy

density and DM relic density, are given as:

$$g_{\text{eff}}(T) = \sum_i g^i_{\text{eff}}(T_i)\frac{T_i^4}{T^4}\,, \tag{C.0.8}$$

$$h_{\text{eff}}(T) = \sum_i h^i_{\text{eff}}(T_i)\frac{T_i^3}{T^3}\,. \tag{C.0.9}$$

The total energy and entropy densities equal:

$$\rho = g_{\text{eff}}\,(T)\,\frac{\pi^2}{30}T^4\,, \tag{C.0.10}$$

$$s = h_{\text{eff}}\,(T)\,\frac{2\pi^2}{45}T^3\,. \tag{C.0.11}$$

In the early Universe, all existing particle species i are in thermal equilibrium, such that their temperatures T_i are equal to the photon temperature T. In that limit, $T \gg m_i$ for each species i. Equations (C.0.4) and (C.0.5) then yield:

$$\rho = \sum_i \rho_i\,(T_i) = \left[\sum_B g_B\left(\frac{T_B}{T}\right)^4 + \frac{7}{8}\sum_F g_F\left(\frac{T_F}{T}\right)^4\right]\frac{\pi^2}{30}T^4\,, \tag{C.0.12}$$

$$s = \sum_i s_i\,(T_i) = \left[\sum_B g_B\left(\frac{T_B}{T}\right)^3 + \frac{7}{8}\sum_F g_F\left(\frac{T_F}{T}\right)^3\right]\frac{2\pi^2}{45}T^3 \tag{C.0.13}$$

where g_B is the number of internal degrees of freedom of a boson and the sum over bosons takes all bosonic particle species i into account; analog for g_F.

D. Modified Bessel Functions

The modified Bessel functions $K_n(x)$ of the second kind obey the identity:

$$K_n\left(x\right) = \frac{\sqrt{\pi}}{\left(n-\frac{1}{2}\right)!}\left(\frac{1}{2}x\right)^n \int\limits_1^\infty dy\, \frac{(y^2-1)^{n-\frac{1}{2}}}{e^{xy}}\,. \tag{D.0.1}$$

Assuming a Maxwell– Boltzmann distribution with zero chemical potential, the equilibrium number density $n_{\rm eq}$ of a particle with g internal degrees of freedom can, therefore, be written as:

$$n_{\rm eq} = \frac{g}{(2\pi)^3}\int\limits_0^\infty d^3p\, e^{-\frac{E}{T}} \tag{D.0.2}$$

$$= \frac{g}{2\pi^2}\int\limits_m^\infty dE\, E\sqrt{E^2-m^2}\frac{1}{e^{\frac{E}{T}}} \tag{D.0.3}$$

$$= m^3\frac{g}{2\pi^2}\int\limits_1^\infty dy\, \frac{y\sqrt{y^2-1}}{e^{xy}} \tag{D.0.4}$$

$$= m^3\frac{g}{2\pi^2}\frac{1}{x}K_2(x)\,. \tag{D.0.5}$$

In terms of the abundance

$$Y = \frac{n}{s} \tag{D.0.6}$$

with the entropy density

$$s = 2\pi^2/45\cdot h_{\rm eff}T^3\,, \tag{D.0.7}$$

it follows:

$$Y_{\rm eq} = \frac{45g}{4\pi^4}\frac{x^2}{h_{\rm eff}}K_2(x)\,. \tag{D.0.8}$$

E. Annihilation and Decay Reactions

In the Robertson–Walker metric, the Boltzmann equation for the number density n of a particle species can be written as:

$$\frac{d}{dt}n + 3Hn = C[n]\,, \tag{E.0.1}$$

where C is the collision operator expressing the number of particles per phase space volume that are lost or gained per unit time due to interactions with other particles.

For the standard annihilation process $\sigma\,\sigma \rightleftharpoons SM\ \ SM$ of a real scalar singlets σ into SM particles, the Boltzmann equation for the number density n_σ reads as:

$$\frac{d}{dt}n_\sigma + 3Hn_\sigma = -\langle\sigma_{\rm ann}v_r\rangle(n_\sigma^2 - n_{\sigma,\rm eq}^2) \simeq \langle\sigma_{\rm ann}v_r\rangle n_{\sigma,\rm eq}^2\,, \tag{E.0.2}$$

where the last approximation is valid for the freeze-in case for which the initial number density and thus the initial abundance can be neglected [55]. Furthermore, $\langle\sigma_{\rm ann}v_r\rangle$ is the relativistic thermally averaged annihilation cross section and v_r is the relative velocity. Following the discussion of [187], it is possible to write:

$$\langle\sigma_{\rm ann}v_r\rangle = \frac{1}{8m^4TK_2^2(m/T)}\int\limits_{4m^2}^{\infty} ds\sigma\cdot(s-4m^2)\sqrt{s}\;K_1\left(\frac{\sqrt{s}}{T}\right)\,, \tag{E.0.3}$$

where we have made the assumption that the initial particles have masses equal to m. We have generated the correct Feynman rules using LanHEP [63] and we have used micrOMEGAs [64] for the calculation of Eq. (E.0.3).

In the radiation dominated era, the Hubble expansion rate can be expressed as:

$$H = \sqrt{\frac{4\pi^3 G_N g_{\rm eff}}{45}}T^2\,. \tag{E.0.4}$$

Furthermore, in the radiation dominated era the expansion age t of the Universe with $\Omega_{\rm tot} = 1$ equals:

$$t = \frac{1}{2H}\,. \tag{E.0.5}$$

In terms of the abundance $Y = {}^{n}/_{s}$ with the entropy density $s = {}^{2\pi^2}/_{45} \cdot h_{\rm eff} T^3$, it follows:

$$\frac{d}{dT} Y_\sigma^{\mathcal{A}} = -\sqrt{\frac{\pi}{45 G_N}} \sqrt{g_*} \langle \sigma_{\rm ann} v_r \rangle Y_{\sigma,eq}^2 \,, \tag{E.0.6}$$

with the definition

$$\sqrt{g_*} \equiv \frac{h_{\rm eff}}{\sqrt{g_{\rm eff}}} \left(1 + \frac{1}{3} \frac{T}{h_{\rm eff}} \frac{dh_{\rm eff}}{T} \right) . \tag{E.0.7}$$

The superscript $\mathcal{A}$ serves as indication of the annihilation process. The decay processes $\sigma \longrightarrow N_1 N_1$ of a real scalar singlet σ into two sterile neutrinos N_1 is described by the following phase space integration:

$$\int \frac{d^3 p_\sigma}{(2\pi)^3 2E_\sigma} \frac{d^3 p_{N_1}}{(2\pi)^3 2E_{N_1}} \frac{d^3 p_{N_1}}{(2\pi)^3 2E_{N_1}} (2\pi)^4 \delta^{(4)}(p_{N_1} + p_{N_1} - p_\sigma) |\mathcal{M}|^2_{\sigma \to N_1 N_1} f_\sigma (1 - f_{N_1})(1 - f_{N_1}) . \tag{E.0.8}$$

Neglecting, as usual, the Pauli blocking and enhancing factors, we can define:

$$\int \frac{d^3 p_{N_1}}{(2\pi)^3 2E_{N_1}} \frac{d^3 p_{N_1}}{(2\pi)^3 2E_{N_1}} (2\pi)^4 \delta^{(4)}(p_{N_1} + p_{N_1} - p_\sigma) |\mathcal{M}|^2_{\sigma \to N_1 N_1} \equiv 2 E_\sigma \Gamma^*(\sigma \to NN) \,, \tag{E.0.9}$$

with $\Gamma^*(\sigma \to N_1 N_1)$ the decay width for the particle at energy E_σ. The above phase space integration yields:

$$\int dn_\sigma \, \Gamma^*(\sigma \to N_1 N_1) = n_\sigma \, \langle \Gamma(\sigma \to N_1 N_1) \rangle \,, \tag{E.0.10}$$

where

$$\langle \Gamma(\sigma \to N_1 N_1) \rangle = \frac{\int d^3 p_\sigma \Gamma^*(\sigma \to N_1 N_1) e^{-\frac{E_\sigma}{T}}}{\int d^3 p_\sigma e^{-\frac{E_\sigma}{T}}} = \frac{K_1(x)}{K_2(x)} \Gamma(\sigma \to N_1 N_1) \,, \tag{E.0.11}$$

with $\Gamma(\sigma \to N_1 N_1)$ the decay width in the rest frame of the decaying particle σ, i.e., $\Gamma(\sigma \to N_1 N_1) = {}^{E_\sigma}/_{m_\sigma} \cdot \Gamma^*(\sigma \to N_1 N_1)$. Thus, for the decay process $\sigma \to N_1 N_1$ of a real scalar singlet σ into two sterile neutrinos N_1, the Boltzmann equation for the number density n_{N_1} reads as:

$$\frac{d}{dt} n_{N_1} + 3 H n_{N_1} = 2 \frac{K_1(x)}{K_2(x)} \Gamma(\sigma \to N_1 N_1) \, n_\sigma \,. \tag{E.0.12}$$

The factor 2 accounts for the fact that two sterile neutrinos N_1 are produced per decay. In terms of the abundance $Y = {}^{n}/_{s}$ with the entropy density $s = {}^{2\pi^2}/_{45} \cdot h_{\rm eff} T^3$, it follows:

$$\frac{d}{dT} Y_{N_1}^{\mathcal{D}} = -\sqrt{\frac{45}{\pi^3 G_N}} \frac{1}{T^3} \frac{1}{\sqrt{g_{\rm eff}}} \frac{K_1(x)}{K_2(x)} \Gamma(\sigma \to N_1 N_1) \, Y_\sigma \,, \tag{E.0.13}$$

where the superscript $\mathcal{D}$ serves as indication of the decay process.

Bibliography

References to publications in scientific journals include the corresponding journal and eprint number wherever possible. Books, conference contributions and talks are marked appropriately.

[1] J. Keats, "*On First Looking into Chapman's Homer, Poems 1817*", 1817.

[2] A. Bouvard, *"Tables Astronomiques Publiees par le Bureau des Longitudes de France"*. 1821.

[3] G. M. Clemence, "*The Relativity Effect in Planetary Motions*", Rev. Mod. Phys. **19** (1947) 361–364.

[4] L. Iorio, "*On the Possibility of Measuring the Solar Oblateness and some Relativistic Effects from Planetary Ranging*", Astron.Astrophys. **433** (2005) 385–393, arXiv:gr-qc/0406041.

[5] **Planck Collaboration** , P. A. R. Ade *et al.*, "*Planck 2013 Results. XVI. Cosmological Parameters*", arXiv:1303.5076 .

[6] J. H. Oort, "*The Force Exerted by the Stellar System in the Direction Perpendicular to the Galactic Plane and some Related Problems*", Bull. Astron. Inst. Netherlands **6** (1932) 249–287.

[7] F. Zwicky, "*Spectral Displacement of Extra Galactic Nebulae*", Helv. Phys. Acta **6** (1933) 110–127.

[8] V. C. Rubin and J. Ford, W. Kent, "*Rotation of the Andromeda Nebula from a Spectroscopic Survey of Emission Regions*", Astrophys.J. **159** (1970) 379–403.

[9] M. Milgrom, "*A Modification of the Newtonian Dynamics as a Possible Alternative to the Hidden Mass Hypothesis*", Astrophys. J. **270** (1983) 365–370.

[10] J. D. Bekenstein, "*Relativistic Gravitation Theory for the MOND Paradigm*", Phys.Rev. **D70** (2004) 083509, arXiv:astro-ph/0403694.

[11] S. Dodelson, "*The Real Problem with MOND*", Int.J.Mod.Phys. **D20** (2011) 2749–2753, arXiv:1112.1320.

[12] A. Klypin and F. Prada, "*Testing Gravity with Motion of Satellites Around Galaxies: Newtonian Gravity Against Modified Newtonian Dynamics*", Astrophys. J. **690** (2009) 1488–1496, arXiv:0706.3554.

[13] **ATLAS Collaboration** , G. Aad *et al.*, "*Evidence for the Spin-0 Nature of the Higgs Boson Using ATLAS Data*", arXiv:1307.1432.

[14] **CMS Collaboration** , S. Chatrchyan *et al.*, "*Observation of a New Boson at a Mass of 125 GeV with the CMS Experiment at the LHC*", Phys.Lett. **B716** (2012) 30–61, arXiv:1207.7235.

[15] **Double Chooz Collaboration** , Y. Abe *et al.*, "*Reactor $\overline{\nu_e}$ Disappearance in the Double Chooz Experiment*", Phys. Rev. **D86** (2012) 052008, arXiv:1207.6632.

[16] S. Glashow, "*Partial-Symmetries of Weak Interactions*", Nucl.Phys. **22** (1961) 579–588.

[17] S. Weinberg, "*A Model of Leptons*", Phys.Rev.Lett. **19** (1967) 1264–1266.

[18] J. Goldstone, A. Salam, and S. Weinberg, "*Broken Symmetries*", Phys.Rev. **127** (1962) 965–970.

[19] A. Salam and J. C. Ward, "*Electromagnetic and Weak Interactions*", Phys.Lett. **13** (1964) 168–171.

[20] P. W. Higgs, "*Broken Symmetries, Massless Particles and Gauge Fields*", Phys.Lett. **12** (1964) 132–133.

[21] F. Englert and R. Brout, "*Broken Symmetry and the Mass of Gauge Vector Mesons*", Phys.Rev.Lett. **13** (1964) 321–323.

[22] G. Guralnik, C. Hagen, and T. Kibble, "*Global Conservation Laws and Massless Particles*", Phys.Rev.Lett. **13** (1964) 585–587.

[23] N. Cabibbo, "*Unitary Symmetry and Leptonic Decays*", Phys. Rev. Lett. **10** (1963) 531–533.

[24] M. Kobayashi and T. Maskawa, "*CP-Violation in the Renormalizable Theory of Weak Interaction*", Prog. Theor. Phys. **49** (1973) 652–657.

[25] W. Pauli, "*Dear Radioactive Ladies and Gentlemen*", Phys.Today **31N9** (1978) 27.

[26] J. Bahcall, W. A. Fowler, J. Iben, I., and R. Sears, "*Solar Neutrino Flux*", Astrophys.J. **137** (1963) 344–346.

[27] J. N. Bahcall, M. Pinsonneault, and S. Basu, "*Solar Models: Current Epoch and Time Dependences, Neutrinos, and Helioseismological Properties*", Astrophys.J. **555** (2001) 990–1012, arXiv:astro-ph/0010346.

[28] J. Davis, Raymond, D. S. Harmer, and K. C. Hoffman, "*Search for Neutrinos from the Sun*", Phys.Rev.Lett. **20** (1968) 1205–1209.

[29] **Super-Kamiokande Collaboration** , J. Hosaka *et al.*, "*Solar Neutrino Measurements in Super-Kamiokande-I*", Phys.Rev. **D73** (2006) 112001, arXiv:hep-ex/0508053.

[30] **KAMIOKANDE-II Collaboration** , K. Hirata *et al.*, "*Experimental Study of the Atmospheric Neutrino Flux*", Phys.Lett. **B205** (1988) 416.

[31] **Double Chooz Collaboration** , Y. Abe *et al.*, "*First Measurement of θ_{13} from Delayed Neutron Capture on Hydrogen in the Double Chooz Experiment*", Phys.Lett. **B723** (2013) 66–70, arXiv:1301.2948 .

[32] Z. Maki, M. Nakagawa, and S. Sakata, "*Remarks on the Unified Model of Elementary Particles*", Prog.Theor.Phys. **28** (1962) 870–880.

[33] B. Pontecorvo, "*Mesonium and Anti-Mesonium*", Sov.Phys.JETP **6** (1957) 429.

[34] **LSND Collaboration** , A. Aguilar-Arevalo *et al.*, "*Evidence for Neutrino Oscillations from the Observation of $\overline{\nu_e}$ in a $\overline{\nu_\mu}$ Beam*", Phys.Rev. **D64** (2001) 112007, arXiv:hep-ex/0104049 .

[35] **MiniBooNE Collaboration** , A. Aguilar-Arevalo *et al.*, "*Improved Search for $\overline{\nu}_\mu \to \overline{\nu}_e$ Oscillations in the MiniBooNE Experiment*", Phys.Rev.Lett. **110** (2013) 161801, arXiv:1207.4809 .

[36] G. Mention, M. Fechner, T. Lasserre, T. Mueller, D. Lhuillier, *et al.*, "*Reactor Antineutrino Anomaly*", Phys.Rev. **D83** (2011) 073006, arXiv:1101.2755 .

[37] M. Gonzalez-Garcia, M. Maltoni, J. Salvado, and T. Schwetz, "*Global Fit to Three Neutrino Mixing: Critical Look at Present Precision*", JHEP **1212** (2012) 123, arXiv:1209.3023.

[38] S. Weinberg, "*Baryon- and Lepton-Nonconserving Processes*", Phys. Rev. Lett. **43** (1979) 1566–1570.

[39] E. Ma, "*Pathways to Naturally Small Neutrino Masses*", Phys. Rev. Lett. **81** (1998) 1171–1174, arXiv:hep-ph/9805219.

[40] P. Minkowski, "$\mu \to e\gamma$ *at a Rate of One Out of* 10^9 *Muon Decays?*", Phys. Lett. **B67** (1977) 421.

[41] G. B. Gelmini and M. Roncadelli, "*Left-Handed Neutrino Mass Scale and Spontaneously Broken Lepton Number*", Phys. Lett. **B99** (1981) 411.

[42] R. Foot, H. Lew, X. He, and G. C. Joshi, "*See-Saw Neutrino Masses Induced by a Triplet of Leptons*", Z.Phys. **C44** (1989) 441.

[43] T. Asaka, S. Eijima, and H. Ishida, "*Mixing of Active and Sterile Neutrinos*", JHEP **1104** (2011) 011, arXiv:1101.1382.

[44] A. Boyarsky, J. Lesgourgues, O. Ruchayskiy, and M. Viel, "*Realistic Sterile Neutrino Dark Matter with keV Mass Does Not Contradict Cosmological Bounds*", Phys. Rev. Lett. **102** (2009) 201304, arXiv:0812.3256.

[45] E. W. Kolb and M. S. Turner, *The Early Universe*. Westview Press, 1990.

[46] D. Hilbert, "*Die Grundlagen der Physik*", Konigl. Gesell. d. Wiss. Goettingen, Nachr. Math.-Phys. Kl. (1915) 395.

[47] S. Blondin, T. Davis, K. Krisciunas, B. Schmidt, J. Sollerman, *et al.*, "*Time Dilation in Type Ia Supernova Spectra at High Redshift*", Astrophys.J. **682** (2008) 724–736, arXiv:0804.3595 .

[48] P. Peebles, *Principles of Physical Cosmology*. Princeton University Press, 1993.

[49] V. Springel, S. D. White, A. Jenkins, C. S. Frenk, N. Yoshida, *et al.*, "*Simulations of the Formation, Evolution and Clustering of Galaxies and Quasars*", Nature **435** (2005) 629–636, arXiv:astro-ph/0504097.

[50] B. Moore, S. Ghigna, F. Governato, G. Lake, T. R. Quinn, *et al.*, "*Dark Matter Substructure Within Galactic Halos*", Astrophys.J. **524** (1999) L19–L22, arXiv:astro-ph/9907411.

[51] S. Colombi, S. Dodelson, and L. M. Widrow, "*Large-Scale Structure Tests of Warm Dark Matter*", Astrophys.J. **458** (1996) 1, arXiv:astro-ph/9505029.

[52] A. Djouadi, O. Lebedev, Y. Mambrini, and J. Quevillon, "*Implications of LHC Searches for Higgs–Portal Dark Matter*", Phys.Lett. **B709** (2012) 65–69, arXiv:1112.3299 .

[53] S. Wolfram, "*Abundances of New Stable Particles Produced in the Early Universe*", Phys.Lett. **B82** (1979) 65.

[54] J. McDonald, "*Thermally Generated Gauge Singlet Scalars as Self-Interacting Dark Matter*", Phys.Rev.Lett. **88** (2002) 091304, arXiv:hep-ph/0106249.

[55] L. J. Hall, K. Jedamzik, J. March-Russell, and S. M. West, "*Freeze-In Production of FIMP Dark Matter*", JHEP **1003** (2010) 080, arXiv:0911.1120.

[56] C. E. Yaguna, "*The Singlet Scalar as FIMP Dark Matter*", JHEP **1108** (2011) 060, arXiv:1105.1654.

[57] M. Frigerio, T. Hambye, and E. Masso, "*Sub-GeV Dark Matter as Pseudo-Nambu-Goldstone from the Seesaw Scale*", Phys. Rev. **X1** (2011) 021026, arXiv:1107.4564.

[58] B. W. Lee and S. Weinberg, "*Cosmological Lower Bound on Heavy-Neutrino Masses*", Phys. Rev. Lett. **39** (1977) 165–168.

[59] J. D. Wells, "*Annihilation Cross Sections for Relic Densities in the Low Velocity Limit*", arXiv:hep-ph/9404219.

[60] K. Griest and D. Seckel, "*Three Exceptions in the Calculation of Relic Abundances*", Phys. Rev. **D43** (1991) 3191–3203.

[61] J. McDonald, "*Gauge Singlet Scalars as Cold Dark Matter*", Phys.Rev. **D50** (1994) 3637–3649, arXiv:hep-ph/0702143 .

[62] C. Burgess, M. Pospelov, and T. ter Veldhuis, "*The Minimal Model of Nonbaryonic Dark Matter: A Singlet Scalar*", Nucl.Phys. **B619** (2001) 709–728, arXiv:hep-ph/0011335.

[63] A. Semenov, "*LanHEP- A Package for Automatic Generation of Feynman Rules in Gauge Models*", arXiv:hep-ph/9608488.

[64] G. Belanger, F. Boudjema, P. Brun, A. Pukhov, S. Rosier-Lees, *et al.*, "*Indirect Search for Dark Matter with micrOMEGAs_2.4*", Comput.Phys. Commun. **182** (2011) 842–856, arXiv:1004.1092 .

[65] **AMS Collaboration** , M. Aguilar *et al.*, "*First Result from the Alpha Magnetic Spectrometer on the International Space Station: Precision Measurement of the Positron Fraction in Primary Cosmic Rays of 0.5-350 GeV*", Phys.Rev.Lett. **110** (2013) no. 14, 141102.

[66] **Fermi-LAT Collaboration** , "*Fermi-LAT Observations of the Diffuse γ-Ray Emission: Implications for Cosmic Rays and the Interstellar Medium*", Astrophys.J. **750** (2012) 3, arXiv:1202.4039.

[67] M. W. Goodman and E. Witten, "*Detectability of Certain Dark-Matter Candidates*", Phys.Rev. **D31** (1985) 3059.

[68] D. Tucker-Smith and N. Weiner, "*Inelastic Dark Matter*", Phys. Rev. **D64** (2001) 043502, arXiv:hep-ph/0101138.

[69] S. Chang, N. Weiner, and I. Yavin, "*Magnetic Inelastic Dark Matter*", Phys.Rev. **D82** (2010) 125011, arXiv:1007.4200.

[70] G. Angloher, S. Cooper, R. Keeling, H. Kraus, J. Marchese, *et al.*, "*Limits on WIMP Dark Matter Using Sapphire Cryogenic Detectors*", Astropart.Phys. **18** (2002) 43–55.

[71] **DAMA Collaboration** , R. Bernabei *et al.*, "*The DAMA/LIBRA Apparatus*", Nucl.Instrum.Meth. **A592** (2008) 297–315, arXiv:0804.2738.

[72] **CoGeNT Collaboration** , C. Aalseth *et al.*, "*Results from a Search for Light-Mass Dark Matter with a p-type Point Contact Germanium Detector*", Phys.Rev.Lett. **106** (2011) 131301, arXiv:1002.4703.

[73] **XENON100 Collaboration** , E. Aprile *et al.*, "*The XENON100 Dark Matter Experiment*", Astropart.Phys. **35** (2012) 573–590, arXiv:1107.2155.

[74] **KIMS Collaboration** , S.-C. Kim, "*The Recent Results from KIMS Experiment*", J.Phys.Conf.Ser. **384** (2012) 012020.

[75] **CDMS-II Collaboration** , Z. Ahmed *et al.*, "*Dark Matter Search Results from the CDMS II Experiment*", Science **327** (2010) 1619–1621, arXiv:0912.3592.

[76] E. A. Baltz, M. Battaglia, M. E. Peskin, and T. Wizansky, "*Determination of Dark Matter Properties at High-Energy Colliders*", Phys. Rev. **D74** (2006) 103521, arXiv:hep-ph/0602187.

[77] J. F. Navarro, C. S. Frenk, and S. D. M. White, "*The Structure of Cold Dark Matter Halos*", Astrophys. J. **462** (1996) 563–575, arXiv:astro-ph/9508025.

[78] R. Catena and P. Ullio, "*A Novel Determination of the Local Dark Matter Density*", JCAP **1008** (2010) 004, arXiv:0907.0018.

[79] P. Salucci, F. Nesti, G. Gentile, and C. Martins, "*The Dark Matter Density at the Sun's Location*", Astron.Astrophys. **523** (2010) A83, arXiv:1003.3101.

[80] **LAT Collaboration** , M. Ackermann *et al.*, "*Fermi LAT Search for Dark Matter in Gamma-Ray Lines and the Inclusive Photon Spectrum*", Phys.Rev. **D86** (2012) 022002, arXiv:1205.2739.

[81] **Fermi-LAT Collaboration** , "*Search for Gamma-Ray Spectral Lines with the Fermi Large Area Telescope and Dark Matter Implications*", arXiv:1305.5597 .

[82] T. Bringmann, X. Huang, A. Ibarra, S. Vogl, and C. Weniger, "*Fermi LAT Search for Internal Bremsstrahlung Signatures from Dark Matter Annihilation*", JCAP **1207** (2012) 054, arXiv:1203.1312.

[83] C. Weniger, "*A Tentative Gamma-Ray Line from Dark Matter Annihilation at the Fermi Large Area Telescope*", JCAP **1208** (2012) 007, arXiv:1204.2797.

[84] G. Jungman, M. Kamionkowski, and K. Griest, "*Supersymmetric Dark Matter*", Phys. Rept. **267** (1996) 195–373, arXiv:hep-ph/9506380.

[85] J. Gasser and H. Leutwyler, "*Quark Masses*", Phys.Rept. **87** (1982) 77–169.

[86] R. Catena and P. Ullio, "*The Local Dark Matter Phase-Space Density and Impact on WIMP Direct Detection*", JCAP **1205** (2012) 005, arXiv:1111.3556.

[87] J. Lewin and P. Smith, "*Review of Mathematics, Numerical Factors, and Corrections for Dark Matter Experiments Based on Elastic Nuclear Recoil*", Astropart.Phys. **6** (1996) 87–112.

[88] C. McCabe, "*The Astrophysical Uncertainties Of Dark Matter Direct Detection Experiments*", Phys.Rev. **D82** (2010) 023530, arXiv:1005.0579 .

[89] A. L. Fitzpatrick and K. M. Zurek, "*Dark Moments and the DAMA-CoGeNT Puzzle*", Phys.Rev. **D82** (2010) 075004, arXiv:1007.5325.

[90] J. Lindhard and M. Scharff, "*Energy Dissipation by Ions in the kev Region*", Phys.Rev. **124** (1961) 128–130.

[91] **XENON100 Collaboration** , E. Aprile *et al.*, "*Dark Matter Results from 100 Live Days of XENON100 Data*", Phys.Rev.Lett. **107** (2011) 131302, arXiv:1104.2549 .

[92] **DAMA Collaboration, LIBRA Collaboration** , R. Bernabei *et al.*, "*New Results from DAMA/LIBRA*", Eur.Phys.J. **C67** (2010) 39–49, arXiv:1002.1028.

[93] R. Bernabei, P. Belli, S. d'Angelo, A. Di Marco, F. Montecchia, *et al.*, "*Dark Matter Investigation by DAMA at Gran Sasso*", Int.J.Mod.Phys. **A28** (2013) 1330022, arXiv:1306.1411.

[94] E. Aprile and T. Doke, "*Liquid Xenon Detectors for Particle Physics and Astrophysics*", Rev.Mod.Phys. **82** (2010) 2053–2097, arXiv:0910.4956.

[95] **XENON100 Collaboration** , E. Aprile *et al.*, "*Dark Matter Results from 225 Live Days of XENON100 Data*", Phys. Rev. Lett. **109** (2012) 181301, arXiv:1207.5988.

[96] **XENON1T Collaboration** , E. Aprile, "*The XENON1T Dark Matter Search Experiment*", arXiv:1206.6288.

[97] **XENON100** , E. Aprile *et al.*, "*First Dark Matter Results from the XENON100 Experiment*", Phys. Rev. Lett. **105** (2010) 131302, arXiv:1005.0380.

[98] "*Search for Dark Matter Pair Production in Events with a Hadronically Decaying W or Z Boson and Missing Transverse Momentum in pp Collision Data at $\sqrt{s} = 8$ TeV with the ATLAS Detector*", Tech. Rep. ATLAS-CONF-2013-073, CERN, Geneva, Jul, 2013.

[99] L. M. Krauss, S. Nasri, and M. Trodden, "*Model for Neutrino Masses and Dark Matter*", Phys. Rev. **D67** (2003) 085002, arXiv:hep-ph/0210389.

[100] M. Aoki, S. Kanemura, and O. Seto, "*Neutrino Mass, Dark Matter and Baryon Asymmetry via TeV- Scale Physics without Fine-Tuning*", Phys. Rev. Lett. **102** (2009) 051805, arXiv:0807.0361.

[101] E. Ma, "*Verifiable Radiative Seesaw Mechanism of Neutrino Mass and Dark Matter*", Phys. Rev. **D73** (2006) 077301, arXiv:hep-ph/0601225.

[102] D. Schmidt, T. Schwetz, and T. Toma, "*Direct Detection of Leptophilic Dark Matter in a Model with Radiative Neutrino Masses*", Phys.Rev. **D85** (2012) 073009, arXiv:1201.0906.

[103] K. S. Babu, "*Model of 'Calculable' Majorana Neutrino Masses*", Phys. Lett. **B203** (1988) 132.

[104] M. Lindner, D. Schmidt, and T. Schwetz, "*Dark Matter and Neutrino Masses from Global $U(1)_{B-L}$ Symmetry Breaking*", Phys.Lett. **B705** (2011) 324–330, arXiv:1105.4626.

[105] N. G. Deshpande and E. Ma, "*Pattern of Symmetry Breaking with Two Higgs Doublets*", Phys.Rev. **D18** (1978) 2574.

[106] G. 't Hooft, "*Naturalness, Chiral Symmetry, and Spontaneous Chiral Symmetry Breaking*", NATO Adv.Study Inst.Ser.B Phys. **59** (1980) 135.

[107] D. Suematsu, T. Toma, and T. Yoshida, "*Reconciliation of CDM Abundance and $\mu \to e\gamma$ in a Radiative Seesaw Model*", Phys.Rev. **D79** (2009) 093004, arXiv:0903.0287.

[108] T. Schwetz, M. Tortola, and J. Valle, "*Where We Are on θ_{13}: Addendum to 'Global Neutrino Data and Recent Reactor Fluxes: Status of Three-Flavour Oscillation Parameters'*", New J.Phys. **13** (2011) 109401, arXiv:1108.1376.

[109] **MEG Collaboration** , J. Adam *et al.*, "*New Constraint on the Existence of the $\mu^+ \to e^+\gamma$ Decay*", arXiv:1303.0754.

[110] **BaBar Collaboration** , B. Aubert *et al.*, "*Searches for Lepton Flavor Violation in the Decays $\tau^\pm \to e^\pm\gamma$ and $\tau^\pm \to \mu^\pm\gamma$* ", Phys.Rev.Lett. **104** (2010) 021802, arXiv:0908.2381.

[111] **WMAP Collaboration** , E. Komatsu *et al.*, "*Seven-Year Wilkinson Microwave Anisotropy Probe (WMAP) Observations: Cosmological Interpretation*", Astrophys.J.Suppl. **192** (2011) 18, arXiv:1001.4538 .

[112] M. Kawasaki, K. Kohri, and T. Moroi, "*Big-Bang Nucleosynthesis and Hadronic Decay of Long-Lived Massive Particles*", Phys.Rev. **D71** (2005) 083502, arXiv:astro-ph/0408426.

[113] P. Agrawal, S. Blanchet, Z. Chacko, and C. Kilic, "*Flavored Dark Matter, and Its Implications for Direct Detection and Colliders*", Phys.Rev. **D86** (2012) 055002, arXiv:1109.3516.

[114] J. R. Ellis and R. A. Flores, "*Elastic Supersymmetric Relic-Nucleus Scattering Revisited*", Phys.Lett. **B263** (1991) 259–266.

[115] R. H. Helm, "*Inelastic and Elastic Scattering of 187-MeV Electrons from Selected Even-Even Nuclei*", Phys.Rev. **104** (1956) 1466–1475.

[116] J. Engel, "*Nuclear Form Factors for the Scattering of Weakly Interacting Massive Particles*", Phys.Lett. **B264** (1991) 114–119.

[117] M. Ressell and D. Dean, "*Spin-Dependent Neutralino-Nucleus Scattering for a $A \sim 127$ nuclei*", Phys.Rev. **C56** (1997) 535–546, arXiv:hep-ph/9702290.

[118] A. Zee, "*Charged Scalar Field and Quantum Number Violations*", Phys. Lett. **B161** (1985) 141.

[119] M. Nebot, J. F. Oliver, D. Palao, and A. Santamaria, "*Prospects for the Zee–Babu-Model at the CERN LHC and low energy experiments*", Phys.Rev. **D77** (2008) 093013, arXiv:0711.0483 .

[120] K. L. McDonald and B. H. J. McKellar, "*Evaluating the Two Loop Diagram Responsible for Neutrino Mass in Babu's Model*", arXiv:hep-ph/0309270.

[121] **CMS Collaboration** , S. Chatrchyan *et al.*, "*Searches for Long-Lived Charged Particles in pp Collisions at $\sqrt{s}$=7 and 8 TeV*", arXiv:1305.0491.

[122] **ATLAS Collaboration** , G. Aad *et al.*, "*Search for Doubly-Charged Higgs Bosons in Like-Sign Dilepton Final States at $\sqrt{s} = 7$ TeV with the ATLAS Detector*", Eur.Phys.J. **C72** (2012) 2244, arXiv:1210.5070.

[123] S. e. a. Bachmann, "*Research Proposal for an Experiment to Search for the Decay Mu3e*", tech. rep., Univesitaet Heidelberg et al., 2012.

[124] **SINDRUM II Collaboration** , W. H. Bertl *et al.*, "*A Search for $\mu - e$ Conversion in Muonic Gold*", Eur.Phys.J. **C47** (2006) 337–346.

[125] A. Gaponenko, "*The Mu2e Experiment: A New High-Sensitivity Muon to Electron Conversion Search at Fermilab*", in *CIPANP 2012*. 2012.

[126] **Particle Data Group** , J. Beringer *et al.*, "*Review of Particle Physics (RPP)*", Phys.Rev. **D86** (2012) 010001.

[127] **Muon G-2 Collaboration** , G. Bennett *et al.*, "*Final Report of the E821 Muon Anomalous Magnetic Moment Measurement at BNL*", Phys.Rev. **D73** (2006) 072003, arXiv:hep-ex/0602035 .

[128] **SINDRUM Collaboration** , U. Bellgardt *et al.*, "*Search for the Decay $\mu^+ \to e^+e^+e^-$*", Nucl.Phys. **B299** (1988) 1.

[129] K. Hayasaka, K. Inami, Y. Miyazaki, K. Arinstein, V. Aulchenko, *et al.*, "*Search for Lepton Flavor Violating τ Decays into Three Leptons with 719 Million Produced $\tau^+\tau^-$ Pairs*", Phys.Lett. **B687** (2010) 139–143, arXiv:1001.3221 .

[130] "*Measurements of the Properties of the Higgs-like Boson in the Four Lepton Decay Channel with the ATLAS Detector Using 25 fb^{-1} of Proton-Proton Collision Data*", Tech. Rep. ATLAS-CONF-2013-013, CERN, Geneva, Mar, 2013.

[131] A. Ringwald, "*Rate of Anomalous Baryon and Lepton Number Violation at Finite Temperature in Standard Electroweak Theory*", Phys.Lett. **B201** (1988) 510.

[132] V. Kuzmin, V. Rubakov, and M. Shaposhnikov, "*On the Anomalous Electroweak Baryon-Number Non-Conservation in the Early Universe*", Phys.Lett. **B155** (1985) 36.

[133] D. Chang, W.-Y. Keung, and P. B. Pal, "*Spontaneous Lepton-Number Breaking at Electroweak Scale*", Phys. Rev. Lett. **61** (1988) 2420–2423.

[134] R. Schabinger and J. D. Wells, "*A Minimal Spontaneously Broken Hidden Sector and its Impact on Higgs Boson Physics at the Large Hadron Collider*", Phys. Rev. **D72** (2005) 093007, arXiv:hep-ph/0509209.

[135] J. Goldstone, "*Field Theories with Superconductor Solutions*", Nuovo Cim. **19** (1961) 154–164.

[136] C. P. Burgess, "*Goldstone and Pseudo-Goldstone Bosons in Nuclear, Particle and Condensed-Matter Physics*", Phys. Rept. **330** (2000) 193–261, arXiv:hep-th/9808176.

[137] Y. Chikashige, R. N. Mohapatra, and R. D. Peccei, "*Are There Real Goldstone Bosons Associated with Broken Lepton Number?*", Phys. Lett. **B98** (1981) 265.

[138] R. E. Shrock and M. Suzuki, "*Invisible Decays of Higgs Bosons*", Phys. Lett. **B110** (1982) 250.

[139] S. Dittmaier, S. Dittmaier, C. Mariotti, G. Passarino, R. Tanaka, *et al.*, "*Handbook of LHC Higgs Cross Sections: 2. Differential Distributions*", arXiv:1201.3084 .

[140] A. S. Joshipura and J. W. F. Valle, "*Invisible Higgs Decays and Neutrino Physics*", Nucl. Phys. **B397** (1993) 105–122.

[141] "*Search for Invisible Decays of a Higgs Boson Produced in Association with a Z Boson in ATLAS*", Tech. Rep. ATLAS-CONF-2013-011, CERN, Geneva, Mar, 2013.

[142] S. Weinberg, "*Goldstone Bosons as Fractional Cosmic Neutrinos*", Phys.Rev.Lett. **110** (2013) 241301, arXiv:1305.1971 .

[143] T. Banks and N. Seiberg, "*Symmetries and Strings in Field Theory and Gravity*", Phys.Rev. **D83** (2011) 084019, arXiv:1011.5120 .

[144] E. K. Akhmedov, Z. G. Berezhiani, R. N. Mohapatra, and G. Senjanovic, "*Planck Scale Effects on the Majoron*", Phys. Lett. **B299** (1993) 90–93, arXiv:hep-ph/9209285.

[145] "*Combined Measurements of the Mass and Signal Strength of the Higgs-Like Boson with the ATLAS Detector Using up to 25 fb^{-1} of Proton-Proton Collision Data*", Tech. Rep. ATLAS-CONF-2013-014, CERN, Geneva, Mar, 2013.

[146] M. S. Carena, A. Daleo, B. A. Dobrescu, and T. M. P. Tait, "*Z' Gauge Bosons at the Fermilab Tevatron*", Phys. Rev. **D70** (2004) 093009, arXiv:hep-ph/0408098.

[147] N. Okada and O. Seto, "*Higgs portal dark matter in the minimal gauged $U(1)_{B-L}$ model*", Phys.Rev. **D82** (2010) 023507, arXiv:1002.2525 .

[148] T. Asaka, S. Blanchet, and M. Shaposhnikov, "*The νMSM, Dark Matter and Neutrino Masses*", Phys. Lett. **B631** (2005) 151–156, arXiv:hep-ph/0503065 .

[149] A. Merle, V. Niro, and D. Schmidt, "*New Production Mechanism for keV Sterile Neutrino Dark Matter by Decays of Frozen-In Scalars*", arXiv:1306.3996.

[150] F. Bezrukov, H. Hettmansperger, and M. Lindner, "*keV Sterile Neutrino Dark Matter in Gauge Extensions of the Standard Model*", Phys. Rev. **D81** (2010) 085032, arXiv:0912.4415 .

[151] S. Dodelson and L. M. Widrow, "*Sterile Neutrinos as Dark Matter*", Phys. Rev. Lett. **72** (1994) 17–20, arXiv:hep-ph/9303287 .

[152] A. Boyarsky, O. Ruchayskiy, and M. Shaposhnikov, "*The Role of Sterile Neutrinos in Cosmology and Astrophysics*", Ann. Rev. Nucl. Part. Sci. **59** (2009) 191–214, arXiv:0901.0011.

[153] J. E. Gunn and B. A. Peterson, "*On the Density of Neutral Hydrogen in Intergalactic Space*", Astrophys. J. **142** (1965) 1633.

[154] X.-D. Shi and G. M. Fuller, "*A New Dark Matter Candidate: Nonthermal Sterile Neutrinos*", Phys. Rev. Lett. **82** (1999) 2832–2835, arXiv:astro-ph/9810076 .

[155] A. Kusenko, "*Sterile Neutrinos, Dark Matter, and the Pulsar Velocities in Models with a Higgs Singlet*", Phys. Rev. Lett. **97** (2006) 241301, arXiv:hep-ph/0609081 .

[156] K. Petraki and A. Kusenko, "*Dark-Matter Sterile Neutrinos in Models with a Gauge Singlet in the Higgs sector*", Phys. Rev. **D77** (2008) 065014, arXiv:0711.4646 .

[157] M. Shaposhnikov and I. Tkachev, "*The νMSM, Inflation, and Dark Matter*", Phys. Lett. **B639** (2006) 414–417, arXiv:hep-ph/0604236 .

[158] A. Boyarsky, J. Lesgourgues, O. Ruchayskiy, and M. Viel, "*Lyman-α constraints on warm and on warm-plus-cold dark matter models*", JCAP **0905** (2009) 012, arXiv:0812.0010 .

[159] L. Canetti, M. Drewes, T. Frossard, and M. Shaposhnikov, "*Dark Matter, Baryogenesis and Neutrino Oscillations from Right-Handed Neutrinos*", Phys. Rev. **D87** (2013) 093006, arXiv:1208.4607 .

[160] J. Barry, W. Rodejohann, and H. Zhang, "*Light Sterile Neutrinos: Models and Phenomenology*", JHEP **1107** (2011) 091, arXiv:1105.3911 .

[161] E. Ma, "*Radiative Scaling Neutrino Mass and Warm Dark Matter*", Phys. Lett. **B717** (2012) 235–237, arXiv:1206.1812.

[162] A. Merle, "*Constraining Models for keV Sterile Neutrinos by Quasidegenerate Active Neutrinos*", Phys. Rev. **D86** (2012) 121701(R), arXiv:1210.6036 .

[163] Y. B. Zeldovich, I. Y. Kobzarev, and L. B. Okun, "*Cosmological Consequences of the Spontaneous Breakdown of Discrete Symmetry*", Zh. Eksp. Teor. Fiz. **67** (1974) 3–11.

[164] G. R. Dvali and G. Senjanovic, "*Is There a Domain Wall Problem?*", Phys. Rev. Lett. **74** (1995) 5178–5181, arXiv:hep-ph/9501387 .

[165] G. R. Dvali, A. Melfo, and G. Senjanovic, "*Nonrestoration of Spontaneously Broken P and CP at High Temperature*", Phys. Rev. **D54** (1996) 7857–7866, arXiv:hep-ph/9601376 .

[166] S. E. Larsson, S. Sarkar, and P. L. White, "*Evading the Cosmological Domain Wall Problem*", Phys. Rev. **D55** (1997) 5129–5135, arXiv:hep-ph/9608319 .

[167] M. Narain, "*The Higgs Boson Discovery and its Implications*",. Talk given at the Rencontres de Moriond, *QCD and High Energy Interactions*, 13 March 2013, La Thuile, Italy, http://moriond.in2p3.fr/QCD/2013/WednesdayAfternoon/Narain.pptx.

[168] A. Adulpravitchai, B. Batell, and J. Pradler, "*Non-Abelian Discrete Dark Matter*", Phys.Lett. **B700** (2011) 207–216, arXiv:1103.3053 .

[169] M. Kaplinghat, "*Dark Matter from Early Decays*", Phys. Rev. **D72** (2005) 063510, arXiv:astro-ph/0507300 .

[170] A. Kamada, N. Yoshida, K. Kohri, and T. Takahashi, "*Structure of Dark Matter Halos in Warm Dark Matter Models and in Models with Long-Lived Charged Massive Particles*", JCAP **1303** (2013) 008, arXiv:1301.2744.

[171] I. Vilja, "*Baryogenesis in the Singlet Majoron Model*", Phys. Lett. **B324** (1994) 197–200, arXiv:hep-ph/9312283 .

[172] P. Colin, V. Avila-Reese, and O. Valenzuela, "*Substructure and Halo Density Profiles in a Warm Dark Matter Cosmology*", Astrophys. J. **542** (2000) 622–630, arXiv:astro-ph/0004115 .

[173] J. Goodman, M. Ibe, A. Rajaraman, W. Shepherd, T. M. Tait, *et al.*, "*Constraints on Light Majorana Dark Matter from Colliders*", Phys.Lett. **B695** (2011) 185–188, arXiv:1005.1286 .

[174] J. Goodman, M. Ibe, A. Rajaraman, W. Shepherd, T. M. Tait, *et al.*, "*Constraints on Dark Matter from Colliders*", Phys.Rev. **D82** (2010) 116010, arXiv:1008.1783 .

[175] J. F. Kamenik and C. Smith, "*Could a light Higgs Boson Illuminate the Dark Sector?*", Phys.Rev. **D85** (2012) 093017, arXiv:1201.4814 .

[176] K. Abazajian, E. R. Switzer, S. Dodelson, K. Heitmann, and S. Habib, "*The Nonlinear Cosmological Matter Power Spectrum with Massive Neutrinos: The Halo Model*", Phys. Rev. **D71** (2005) 043507, arXiv:astro-ph/0411552 .

[177] R. de Putter, O. Mena, E. Giusarma, S. Ho, A. Cuesta, *et al.*, "*New Neutrino Mass Bounds from SDSS-III Data Release 8 Photometric Luminous Galaxies*", Astrophys. J. **761** (2012) 12, arXiv:1fig:f201.1909 .

[178] K. Sigurdson, "*Hidden Hot Dark Matter as Cold Dark Matter*", arXiv:0912.2346 .

[179] S. Das and K. Sigurdson, "*Cosmological Limits on Hidden Sector Dark Matter*", Phys.Rev. **D85** (2012) 063510, arXiv:1012.4458 .

[180] A. Schneider, R. E. Smith, and D. Reed, "*Halo Mass Function and the Free Streaming Scale*", arXiv:1303.0839 .

[181] A. Kusenko, "*Sterile Neutrinos: The Dark Side of the Light Fermions*", Phys. Rept. **481** (2009) 1–28, arXiv:0906.2968 .

[182] L. Canetti, M. Drewes, and M. Shaposhnikov, "*Sterile Neutrinos as the Origin of Dark and Baryonic Matter*", Phys. Rev. Lett. **110** (2013) 061801, arXiv:1204.3902 .

[183] A. Merle and V. Niro, "*Influence of a keV Sterile Neutrino on Neutrino-Less Double Beta Decay – How Things Changed in the Recent Years*", arXiv:1302.2032 .

[184] A. Boyarsky, O. Ruchayskiy, D. Iakubovskyi, M. G. Walker, S. Riemer-Sorensen, *et al.*, "*Searching for Dark Matter in X-Rays: How to Check the Dark Matter Origin of a Spectral Feature*", Mon.Not.Roy.Astron.Soc. **407** (2010) 1188–1202, arXiv:1001.0644.

[185] F. L. Bezrukov, "*Neutrino Minimal Standard Model for Neutrinoless Double Beta Decay*", Phys. Rev. **D72** (2005) 071303, arXiv:hep-ph/0505247 .

[186] K. Allison, "*Dark Matter, Singlet Extensions of the νMSM, and Symmetries*", JHEP **1305** (2013) 009, arXiv:1210.6852 .

[187] P. Gondolo and G. Gelmini, "*Cosmic Abundances of Stable Particles: Improved Analysis*", Nucl. Phys. **B360** (1991) 145–179.